UNIVERSITY OF LIVERPOOL

Understanding the Role of the Solid Tumour Microenvironment in Brain Tumour Progression

Thesis submitted in accordance with the requirements of the

University of Liverpool

For the degree of Doctor in Philosophy by

Rosalie Richards

September 2016

Acknowledgements

I would like to thank my supervisor, Violaine Sée, for being a constant source of guidance, support, and motivation throughout my PhD. Thank you to Naseem's Manx Brain Tumour Charity, whose fundraising made this PhD possible. Thanks to Sarah, Carol, and Anne for welcoming me into the Sée group and giving up their time to help me get started. During my time in Liverpool, lab meetings were always something to look forward to; I would like to say this was because of the interesting scientific discourse but mainly it was because of the baking! So thank you to everyone who contributed, with a special mention to Anne, Violaine and Dave for the seemingly endless supply of wonderful German, French and Canadian baked goods. Thank you to Marco and the rest of team CCI for coming to the rescue whenever I had a microscopy problem. Special thanks go to Dave for making the light sheet imaging analyses possible, and for always having time to answer my questions. Thank you to Sophie for the tissue culture room chats, which restored my sense of sanity on more than one occasion! To all of the members of the Sée group, past and present: thank you for being a pleasure to work with. Finally, thank you to all of the wonderful friends I have made in Liverpool.

Abstract

Glioblastoma (GBM) is the most common malignant brain tumour and has an extremely poor prognosis. The invasion of tumour cells into normal brain tissue makes complete surgical removal impossible; GBM is also resistant to treatment with chemotherapy and radiotherapy. Our aim was to investigate how GBM cell proliferation, survival and invasion is affected by the solid tumour microenvironment. Although GBM is highly vascularised, the abnormal structure and function of tumour blood vessels results in an inadequate supply of oxygen (hypoxia). Hypoxia is known to promote tumour progression; however, the effect of hypoxia on cell proliferation has not been well characterised. We performed a systematic investigation into the effects of different oxygen levels on the cell cycle. In contrast to the prevailing hypothesis, we found that long-term exposure to pathophysiological levels of hypoxia (1–8% O_2) does not affect cell proliferation and viability and that even severe hypoxia (0.1% O_2) has only minimal effects. We next sought to characterise the effect of hypoxia in multicellular tumour spheroids: 3D cell clusters that replicate important aspects of the tumour microenvironment. We characterised spheroids in terms of proliferation, survival and oxygenation and found that, in this more complex model, hypoxia was associated with reduced proliferation. We then used spheroids to develop a novel method for imaging cellular migration and invasion in 3D using lightsheet fluorescence microscopy (LSFM). We imaged spheroids over 24 h and then quantified the movements of up to 1200 cells per spheroid in terms of speed and straightness of movement. We were able to compare the movement of cells in different regions of spheroids, gaining insight into the behaviour of quiescent cells in the core of large (~500 μm), heterogeneous spheroids that had been exposed to hypoxia. This technique can be used to investigate the effect of the tumour microenvironment on cell motility and to gain insight into the mechanism of drugs that hinder the process of invasion.

Table of contents

Abbreviations

(*R*)-2HG	(*R*)2-hydroxyglutarate
2D	Two-dimensional
3D	Three-dimensional
ABCB1	ATP binding cassette subfamily B member 1
Acetyl-CoA	Acetyl coenzyme A
APS	Ammonium persulfate
ATP	Adenosine triphosphate
BABB	Benzyl alcohol/benzyl benzoate
BBB	Blood brain barrier
BCNU	1, 3-bis (2-chloroethyl)-1-nitrosourea
BSA	Bovine serum albumin
CAC	Citric acid cycle
CAIX	Carbonic anhydrase-IX
CDK	Cyclin-dependent kinase
CDKI	Cyclin-dependent kinase inhibitor
cDNA	Complementary DNA
CMOS	Complementary metal–oxide–semiconductor
CNS	Central nervous system
CPU	Central processing unit
CTCs	Circulating tumour cells
diSPIM	Dual-view illumination SPIM
DMEM	Dulbecco's modified eagle's medium
DNA	Deoxyribonucleic acid
E2F1	E2F Transcription Factor 1
ECM	Extracellular matrix
EdU	5-ethynyl-2′-deoxyuridine
EGFR	Epidermal growth factor receptor
ETC	Electron transport chain
FAD	Flavin adenine dinucleotide

FBS	Foetal bovine serum
FEP	Fluorinated Ethylene Propylene
FITC	Fluorescein isothiocyanate
FTIR	Fourier transform infrared
GA	General anaesthetic
GB	Gigabyte
GBM	Glioblastoma
GDNF	Glial cell derived neurotrophic factor
GFAP	Glial fibrillary acid protein
GLUT	Glucose transporter
GPGPU	General-purpose processing on graphics processing units
H2B	Histone H2B
HBSS	Hank's balanced salt solution
HIF	Hypoxia-inducible factor
HK	Hexokinase
HRE	Hypoxia response elements
HSP-90	Heat shock protein 90
HTS	High-throughput screening
IDH1	Isocitrate dehydrogenase 1
IDH1mt	Isocitrate dehydrogenase 1 mutated
iSPIM	Inverted SPIM
LDHA	Lactate dehydrogenase A
LSFM	Lightsheet fluorescence microscopy
M	Mean
MCT4	Monocarboxylate transporter
MEM	Minimal essential media
MFI	Mean fluorescence intensity
MFI	Mean fluorescence intensity
MGMT	O6-methylguanine-DNA methyltransferase
MMPs	Matrix metalloproteinases
mRFP	Monomeric red fluorescent protein

MRI	Magnetic Resonance Image
mRNA	Messenger RNA
NA	Numerical aperture
NAD	Nicotinamide adenine dinucleotide
NaPyr	Sodium pyruvate
NEAA	Non-essential amino acids
NHS	National health service
NLGN3	Neuroligin-3
NPC	Neural precursor cells
OxPhos	Oxidative phosphorylation
P13K	Phosphoinositide 3-kinase
PBS	Phosphate-buffered saline
PCR	Polymerase chain reaction
PEI	Polyethylenimine
Pen-strep	Penicillin-streptomycin
PES	Polyethersulfone
PET	Positron-emission tomography
PFA	Paraformaldehyde
PHD	Prolyl-hydroxylase domain protein
PI	Propidium iodide
PIMO	Pimonidazole hydrochloride
PTEN	Phosphatase and tensin homolog
qPCR	Real-time polymerase chain reaction
RAM	Random access memory
RNA	Ribonucleic acid
ROI	Region of interest
RT	Room temperature
SD	Standard deviation
SDF1	Stromal cell-derived factor 1
SDS	Sodium dodecyl sulfate
SEM	Standard error of the mean

SGZ	Subgranular zone
SPIM	Single-plane illumination microscopy
SVZ	Subventricular zone
TB	Terabyte
TEMED	Tetramethylethylenediamine
TGF-α	Transforming growth factor alpha
TP53	Tumour protein p53
VEGF	Vascular endothelial growth factor
VHL	Von Hippel-Lindau tumour suppressor protein
α-KG	α-ketoglutarate

Chapter 1:
Introduction

1.1 Cancer

Cancer is a major contributor to global disease burden, with 14 million new cases and 8 million cancer deaths occurring each year (*1*). In the UK, cancer is the responsible for 29% of all deaths (*2*). In nearly all cancers, death is caused by the spread of cancer to other parts of the body (metastasis), where it interferes with normal organ function. While cancer remains a major contributor to mortality, intensive research into the causes of cancer over the last 40 years has led to the development of more effective treatments and significant improvements in survival. In 1971, only 24% of patients diagnosed with cancer were alive 10 years later, but by 2011 the 10 year survival rate had increased to 49% (*3*). However, while the outlook for many cancers is now favourable, for others the survival rate remains extremely poor (Fig 1.1). Environmental and lifestyle factors such as smoking, drinking, diet, and obesity are implicated in the majority of cancers. The biggest preventable cause of cancer is smoking, which is responsible for 20% of new cancer cases in the UK (*4*). Infection is also an important cause of cancer, particularly in developing nations (*5*).

Cancer is a disease caused by uncontrolled cellular proliferation coupled with the ability of cells to invade away from the primary tumour, either by invading neighbouring tissue or by spreading to distant organs. Tumours that lack the the ability to invade are benign and not cancerous. All cancers share a number of acquired hallmarks that underlie their malignant properties; these properties are discussed in detail in Hanahan and Weinberg's seminal paper 'The Hallmarks of Cancer' (*6*). Cancer cells are able to generate their own proliferative signals and are insensitive to the anti-growth signals that regulate proliferation in normal cells. While normal cells have limited replicative capability, cancer cells have unlimited replicative potential and are resistant to apoptosis. Cancer cells are also able to stimulate the formation of new blood vessels from existing blood vessels

(angiogenesis), which provides the oxygen and nutrients that are essential for tumour expansion. As our knowledge of cancer has improved, two additional hallmarks have emerged: reprogramming of cellular energetics and the avoidance of immune destruction (*7*). The acquisition of these hallmarks is a result of genetic mutations that enhance the activity of tumour-promoting genes (oncogenes) and reduce the effectiveness of tumour suppressor genes. Mutations in genes which normally keep genetic alterations to a minimum, such as DNA-repair genes, increases the likelihood that oncogenes and tumour suppressor genes will become mutated (*8*). To gain further insights into tumourigenesis, it is becoming increasingly clear that tumours need to be considered in the context of their microenvironment. The role of the tumour microenvironment in tumour progression is a topic that will be discussed throughout this thesis.

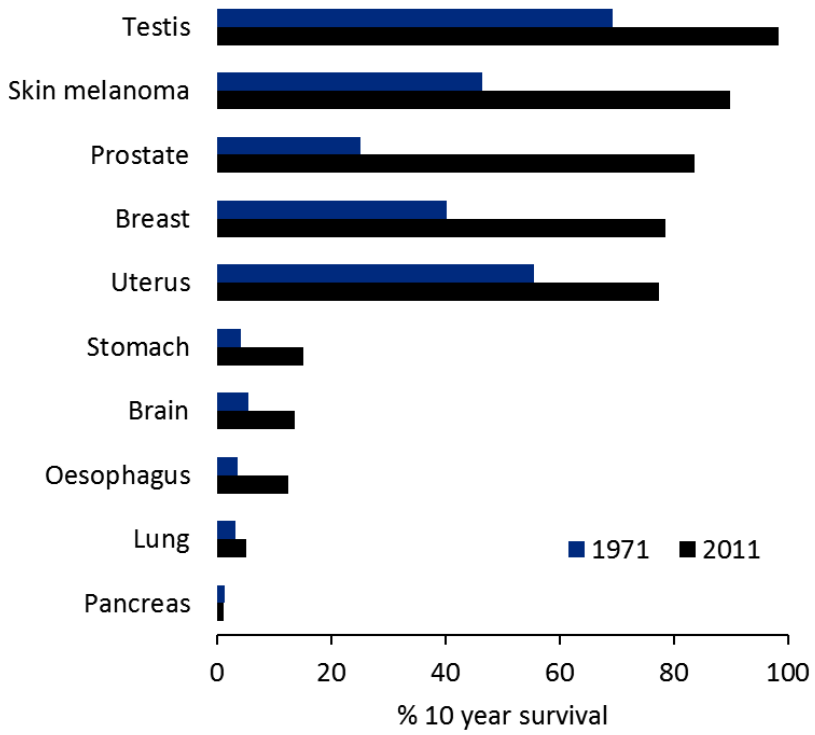

Figure 1.1. Changes in cancer survival rates from 1971–2011. The figure shows the percentage of people who survive for 10 years after being diagnosed with cancer in the indicated tissues. Survival data were obtained from (*3*).

1.2 Central nervous system tumours

The central nervous system (CNS) comprises the brain and spinal cord. CNS tumours can occur due to the abnormal growth of cells originating in the CNS (primary tumours) or because of metastatic dissemination from a tumour in another location in the body (metastatic tumours). Primary tumours can arise from any tissue in the CNS, including neuroepithelial tissue, the meninges, cranial nerves and pituitary gland (*9*). The most common tumour is the meningioma, a typically benign tumour that develops in the meninges. The second most common tumour is the glioma, a type of neuroepithelial tumour that develops from glial cells. Gliomas are the most common malignant CNS tumours, accounting for 80% of cases (*10*). Gliomas are categorised by the World Health Organisation as grades I-IV, with a higher grade indicating increased malignancy (*9*). Glial cells are electrically non-excitable cells that perform a number of supportive functions for neurons. Four main types of glial cells are found in the mature CNS: astrocytes, oligodendrocytes, microglia and ependymal cells. Oligodendrocytes form an electrically insulating layer around neurons known as the myelin sheath, ependymal cells line the ventricles and the spinal canal, and microglia have immunological functions (*11*). The normal functions of astrocytes include providing mechanical, metabolic and neurotrophic support to neurons, regulating blood flow, synaptic transmission and ion concentrations in the extracellular space, and responding to tissue damage. Once thought to provide only supportive functions, it is now known that astrocytes participate in CNS signalling through Ca^{2+} signalling and the release of gliotransmitters (*12-14*). Glioma cells have inherited many of the biological traits of their glial ancestors, which make important contributions to disease progression (*15*).

1.3 Glioblastoma

Glioblastoma (GBM) is a Grade IV astrocytic tumour that accounts for over half of all gliomas. It is an extremely aggressive tumour with a poor prognosis; even with the best available treatments, median survival is just 14 months after diagnosis and most patients die within two years (*16*). Around three cases per 100,000 people occur every year, making it the most common primary malignant brain tumour. GBM can occur *de novo* without any evidence of a less malignant precursor (primary GBM), or due to progression from a lower grade glioma (secondary GBM). Primary GBM occurs most frequently, accounting for 95% of all cases. Unless otherwise specified, all future references to GBM refer to primary GBM. While GBM can occur at any age, it occurs most frequently in patients between 50 and 70 years of age and in men (*17*). Headache is the most common presenting symptom, followed by memory loss, deficits in language and motor skills and cognitive changes. Other common symptoms include personality changes, seizures, nausea and visual problems (*18*).

1.3.1 Pathology

Seventy percent of GBMs occur in the frontal and temporal lobes of the cerebral cortex, with the remainder occurring in the parietal and occipital lobes and deeper brain structures (Fig 1.2A, B) (*19*). Although GBMs can also develop in the brainstem, cerebellum and spinal cord, this is extremely rare**.** GBMs are both cellularly and molecularly heterogeneous tumours. Histopathologically, they are characterised by heterogeneous cell morphology, abnormal nuclei, a high mitotic rate, vascular thrombosis, microvascular proliferation and necrosis. The last two features are essential diagnostic criteria for GBM, distinguishing it from grade III anaplastic astrocytoma (*20*). The only established environmental risk factor for GBM is

therapeutically administered X-irradiation (*21*). The origin of GBM is controversial; it could develop from the malignant transformation of neural stem cells, neural precursor cells (NPCs), or mature differentiated cells. In the adult brain, neurogenesis is restricted to the subventricular zone (SVZ) of the lateral ventricles and the subgranular zone of the hippocampus (*22*). The bulk of the evidence tends to support NPCs as the cell of origin; however, there is currently not enough evidence to rule out the involvement of neural stem cells or differentiated cells (*22, 23*). A further possibility, consistent with the heterogeneous nature of GBM, is that it originates from different pathways in multiple cellular sources (*24*).

The most frequent genetic alteration in GBM is loss of heterozygosity on the long arm of chromosome 10, which occurs in 70% of patients. *EGFR* amplifications, *p16INK4a* deletion, *TP53* and *PTEN* mutations are also common, occurring in 25–36 % of patients (*25*). *EGFR* is an oncogene that encodes the epidermal growth factor receptor (EGFR), a transmembrane protein that promotes cell proliferation (*26*). *P16INK4a*, *TP53* and *PTEN* are all tumour suppressor genes involved in the control of cell proliferation and survival (*27-29*). Based on gene expression profiles, GBM has been classified into four molecular subtypes: pro-neural, neural, mesenchymal and classical (*30*). These subtypes are associated with the expression of markers associated with different neural lineages. For example, the mesenchymal subtype is characterised by *PTEN* mutations and the expression of mesenchymal and astrocytic markers, while the classical group is characterised by *EGFR* mutations and the expression of NPC and stem cell markers. Treatment efficacy also varies by subtype; aggressive treatment significantly improves survival in the classical and mesenchymal types, but not the proneural type, which is more common in patients with secondary GBM. The finding that different subtypes are associated with different neural lineages supports the hypothesis that GBM can arise from more than one cell type. There is considerable intratumoural heterogeneity in GBM and spatially distinct

samples from the same tumour have been found to fall into different subtypes. Furthermore, multiple cell lineages have been found to co-exist within a single sample (*31*). This heterogeneity presents significant challenges for the treatment of GBM.

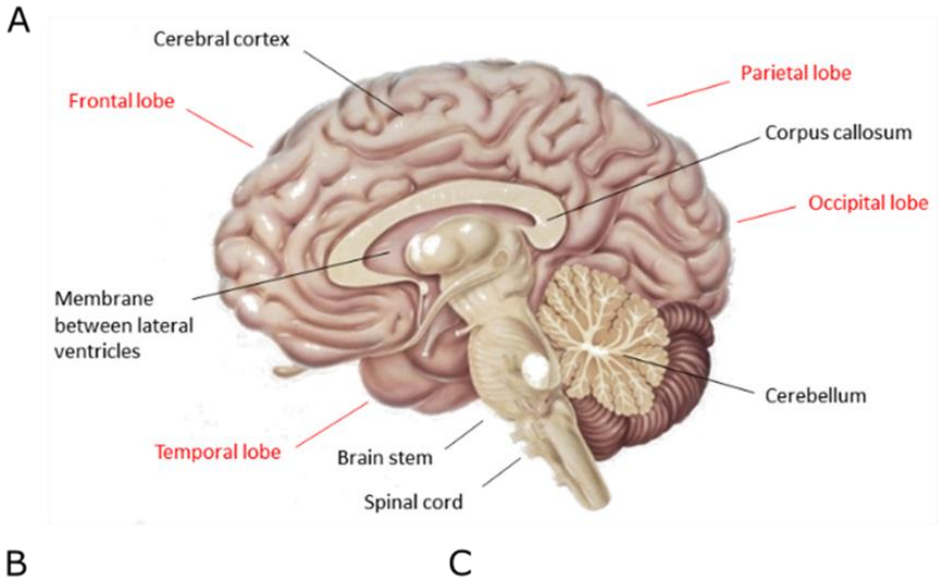

Figure 1.2. Location and characteristics of glioblastoma (GBM). (A). Cross-sectional view of the right cerebral hemisphere of the brain; relevant structures are indicated. This image is under a CC-BY licence from Wellcome Images but has been altered into a Derivative Work by the addition of text (*32*). **(B)**. GBM commonly occurs in the frontal lobes of the cerebral cortex, as seen in this MRI image. Image was adapted from (*33*). **(C).** GBM cells show a characteristic pattern of invasion along existing structures such as (a) under the meninges (b), perivascularly and (c) along white matter tracts such as the corpus callosum; (d) indicates a characteristic region of necrosis. Tumour cells are illustrated in blue, mitotic tumour cells in black, neurons in green and blood vessels in red. Adapted from (*34*).

1.3.2 Treatment

The gold standard of treatment for GBM is maximal surgical resection of the tumour followed by radiotherapy and chemotherapy with temozolomide (*16, 35*). However, the survival of patients has shown little improvement in the past thirty years and treatment remains palliative. The main obstacles to curative treatment are the invasion of GBM cells into neighbouring tissue (Fig 1.2C), which makes total surgical resection impossible, and their resistance to treatment with chemotherapy and radiotherapy (*15, 36-39*). Even when gross total surgical resection has been achieved (determined by the removal of enhancing regions on MRI), 85% of tumours recur within the resection cavity margin in macroscopically normal tissue; despite treatment with radiotherapy and chemotherapy. The other 15% of tumours recur at more distal sites (*38*). Treatment with temozolomide is only of benefit to patients with epigenetic silencing of the O^6-methylguanine-DNA methyltransferase (MGMT) gene by promoter methylation (*35, 40*). MGMT is a DNA-repair protein that repairs the temozolomide-induced alkylation of the O^6 position of guanine by transferring the alkyl group to a cysteine acceptor residue within its own sequence (*41*). Around half of GBM patients have tumours with *MGMT* methylation (*35*).

While molecularly targeted therapies have been successful in improving the outlook for many types of cancer, to date this approach has proved unsuccessful in GBM (*42, 43*). The difficulty of getting therapeutic compounds across the blood-brain barrier (BBB) presents a significant challenge (Fig 1.3) (*44*). One approach that has been trialled to improve local drug delivery is the implantation of biodegradable wafers containing 1, 3-bis (2-chloroethyl)-1-nitrosourea (BCNU), also known as carmustine. BCNU wafers are associated with a modest increase in survival; however, their use is controversial and reports of high complication rates have led some clinicians to conclude that they should not be used in the treatment of GBM

because the risks outweigh the benefits (*45-47*). While some investigations have reported a lower incidence of adverse events, the controversy surrounding the use of BCNU wafers means that they have not been widely adopted as a treatment for GBM (*48*).

Figure 1.3. The blood-brain barrier (BBB). Image shows a cross-section of an arteriole in the cerebral cortex from a modified merged confocal image obtained from (*49*). Neurons are depicted in green and astrocytes in red. The arteriole consists of endothelial, smooth muscle and leptomeningeal cells. Brain endothelial cells have reduced caveolae and are connected by tight junctions. The tight junctions act as a physical barrier, forcing most molecules to move transcellularly. Small gaseous and lipophilic molecules can freely diffuse through the cell membrane while the traffic of small hydrophilic molecules is either permitted or excluded by membrane transport systems. However, large hydrophilic molecules are generally excluded from the brain. Astrocyte endfeet encompass >99% of the vascular surface (*12, 49, 50*).

1.4 Regulation of proliferation

Cellular proliferation is the result of an ordered set of events termed the cell cycle, which is tightly regulated in normal cells. The cell cycle is composed of four sequential phases: G_1, S, G_2 and M phase (Fig 1.3). During G_1 phase, cells are sensitive to extracellular signals and, ordinarily, will only progress to S phase if stimulated to do so by mitogenic growth factors (*51*). However, one of the hallmarks of cancer is that cells are able to proliferate in the absence of growth factors (*6, 52*). Once the cell passes a restriction point in late G_1, cell cycle progression is no longer dependent on growth factors but is controlled by cyclin-dependent kinases (CDKs) that phosphorylate and inactivate cell cycle genes (*51*). CDKs only become active when they have formed a complex with cyclin proteins, the levels of which oscillate throughout the cell cycle. The activity of CDKs is regulated by cyclin-dependent kinase inhibitors (CDKIs) such as p16, p21 and p27, which inhibit the cyclin-CDK complexes and cause cell cycle arrest (*53*).

Genetic mutations that interfere with cell cycle regulation occur frequently in cancer, resulting in one of its defining features: uncontrolled cell proliferation. As previously mentioned, one of the most common genetic mutations in GBM is the deletion of *p16INK4a*, which encodes p16. *TP53* is one of the most commonly mutated genes in all cancers, including GBM (*54*). *TP53* encodes the tumour suppressor protein p53, an important regulator of the cell cycle, which is activated in response to cell stress or DNA damage. P53 prevents the accumulation of DNA damage during cell division either by activating the expression of p21, which causes cell cycle arrest, or by initiating apoptosis. The level of p53 expression dictates whether cell cycle arrest or apoptosis is initiated (*55, 56*). Therefore, mutations in *TP53* contribute to two of the hallmarks of cancer: insensitivity to growth suppressors and the evasion of apoptosis.

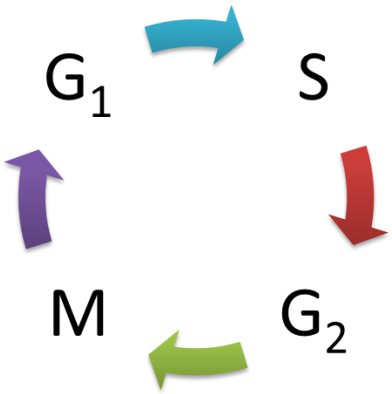

Figure 1.4. The cell cycle. G_1 phase is a period of growth in preparation for S phase, in which DNA replication occurs. G_2 phase is a further period of growth. The cell cycle culminates in M phase, in which mitosis occurs.

1.5 Tumour microenvironment

The tumour microenvironment can be defined as the molecules and parenchymal or stromal cells that surround tumour cells *in vivo*. Tumours are characterised by an environment depleted of oxygen and nutrients, with high extracellular levels of lactate and acidosis (*57*). The tumour microenvironment contributes to the acquisition of many of the hallmarks of cancer and is recognised as a critical factor throughout tumourigenesis (*7*). Therapies targeting the tumour microenvironment are considered to be a promising alternative to the traditional approach of targeting tumour cells directly (*58*). The complex interactions between tumour cells and different components of the microenvironment have led to the concept of the tumour as an organ (*59*). In the brain, the parenchyma is comprised of neurons and glia, while the stromal compartment is made up of the cells that form blood vessels and the meninges. Many of these cells develop abnormal characteristics as a result of their proximity to tumour cells.

1.5.1 Interactions with parenchymal cells

Under normal conditions in the adult CNS, mature astrocytes do not proliferate; however, astrocytes undergo a number of changes in response to injury or disease, termed reactive astrogliosis. The expression of the intermediate filament protein glial fibrillary acid protein (GFAP) is increased and astrocytes can become hypertrophic and proliferate. In more severe cases, this can result in the formation of a glial scar (*13*). Reactive astrocytes are present around the periphery of gliomas and can be difficult to distinguish from tumour cells, which also express GFAP (*60*). Astrocytes are known to secrete neurotrophic factors such as TGF-α, SDF1 and GDNF, which can promote glioma proliferation (*61*). The unique biology of gliomas means that, unlike epithelial cancers, gliomas are surrounded by 'normal' cells derived from the same lineage as tumour cells. Therefore, the secretion of factors that promote glioma growth may have similar effects on glial cells (*62*). Tumour-associated astrocytes develop changes in gene expression, a subset of which are associated with a poorer prognosis in the proneural subtype of GBM (*63*). Furthermore, gliomas are able to recruit glial progenitor cells that become transformed and develop a similar gene expression pattern to glioma cells. These cells take on many of the properties of tumour cells and can become the predominant cell type in gliomas (*62*). GBMs also attract NPCs, which migrate from the SVZ to surround both the main tumour mass and individual cells that are infiltrating the parenchyma. In contrast to astrocytes and progenitor cells, NPCs exert anti-tumour activity and are associated with a survival advantage in animal models (*64, 65*). The number of NPCs peaks 14 days after tumour cell implantation and then begins to decline, possibly due to glioma-induced differentiation. The peritumoural accumulation of NPCs is most profound in the young brain and declines with age, in line with the decline in NPC population, which may provide an explanation for the increased incidence of GBM in older adults.

Only a few studies have investigated interactions between neurons and glioma cells. Excitatory neuronal activity has been shown to support glioma growth through the secretion of growth factors and mitogens such as neuroligin-3. Mitogenic signalling by neurons provides a potential explanation for perineuronal satellitosis - the clustering of invading GBM cells around neuronal cell bodies. The expression of *NLGN3*, the gene encoding neuroligin-3, is associated with a shorter survival time in patients with GBM, suggesting that interactions between neurons and tumour cells can play an important role in tumour progression (*66*). Glutamate is the main excitatory neurotransmitter in the CNS and extracellular levels are normally tightly regulated to ensure proper synaptic function and prevent toxicity to neurons. While normal astrocytes take up excess glutamate from the extracellular space, this activity is reversed in glioma cells, which release high concentrations of glutamate. This causes the excitotoxic death of surrounding neurons and provides a growth advantage to gliomas (*67, 68*). Unlike other soft tissue tumours, which have unlimited physical growth capacity, brain tumour growth is limited by the skull. While brain tissue can be displaced, it cannot be compressed and its macroscopic structure is typically unaltered despite tumour expansion and widespread tissue invasion. The excessive release of glutamate allows glioma cells to create the necessary room to expand by destroying existing tissue, and is thought to be the cause of epileptic seizures in patients with GBM (*69*).

1.5.2 Tumour vasculature and oxygenation

As the diffusion limit of oxygen in tissue is only around 150 µm, tumours need to need to develop new blood vessels in order to expand (*70, 71*). GBMs are among the most highly vascularised solid tumours and microvascular proliferation is a defining feature of GBM (*20, 72*). However, these blood vessels are typically enlarged, thickened, tortuous and deformed,

with evidence of degeneration and frequent thrombosis (*60, 73*). They are also hyperpermeable, leading to oedema and increased interstitial fluid pressure. This causes an increase in intracranial pressure that necessitates the routine use of corticosteroids for symptomatic relief in patients with GBM (*74-76*). Intuitively, vessel hyperpermeability seems advantageous for drug delivery, which is especially difficult in the brain due to the BBB. However, the resulting increased interstitial pressure interferes with vascular pressure gradients and blood flow and is detrimental to drug delivery (*77, 78*). Gliomas are initially able to expand by co-opting existing vessels; however, vessel regression and further tumour expansion result in cell death and the induction of angiogenesis (*79*). The abnormal structure and function of these new blood vessels result in inadequate perfusion and an insufficient supply of oxygen (hypoxia) (*80*).

Hypoxia contributes to the acquisition of many of the hallmarks of cancer and is associated with poor patient prognosis in the majority of solid tumours (*81, 82*). In gliomas, hypoxia is associated with higher grade tumours and decreased patient survival time (*83, 84*). Hypoxia contributes to treatment resistance in tumours by reducing the effects of radiotherapy, which requires molecular oxygen to be fully effective, and by increasing the expression of drug efflux transporters (*85, 86*). The cellular response to hypoxia is orchestrated by the transcription factor hypoxia-inducible factor (HIF), which increases the expression of genes that promote cell survival in low oxygen conditions. Many of HIF's target genes are known to contribute to tumour progression by enhancing pro-tumour processes such as angiogenesis, glycolysis, cell survival, invasion and metastasis (*87*).

1.5.2.1 Therapeutic targeting of angiogenesis

Vascular endothelial growth factor (VEGF) is the principle mediator of hypoxia-induced angiogenesis. Pre-clinical studies have shown that anti-VEGF treatment can normalise tumour vasculature, reduce interstitial fluid pressure and improve oxygen supply, allowing for increased drug delivery and an enhanced response to radiotherapy (*88-91*). It was hoped that treatment with bevacizumab, a humanised monoclonal antibody against the VEGF-A ligand, would improve the prognosis for patients with GBM. The results of phase III clinical trials showed that the addition of bevacizumab to standard treatment significantly improved progression-free survival and reduced the need for treatment with corticosteroids. However, there was no improvement in overall survival and, over time, treatment with bevacizumab was associated with neurocognitive decline, worsening symptoms and a reduction in quality of life (*92, 93*). These results indicate that treatment with bevacizumab has only transient benefits and may even be harmful in the longer term. The recurrence pattern of GBM in patients treated with bevacizumab suggests an increase in infiltrative growth (*94, 95*). Anti-VEGF treatment has been shown to induce hypoxia and increase the expression of multiple factors that act to promote both angiogenesis and invasion (*96*). Anti-angiogenesis therapy can also increase alternative methods of neovascularisation, such as vascular co-option and the development of new blood vessels from circulating bone marrow-derived cells (*97*). The disappointing failure of bevacizumab highlights the complexity of the tumour microenvironment and the ability of tumour cells to adapt to changes in this environment.

1.5.2.2 Normal and pathological oxygen levels in the brain

In vitro, cells are typically cultured in 20% O_2, which is representative of the level of oxygen in the atmosphere. However, the oxygenation of biological tissues varies throughout the body in a tissue-specific manner, ranging from

around 1% O_2 in the skin to 8% O_2 in the intestines. The normal level of oxygen in the human brain is 5–6% O_2 (*98-100*). In brain tumours, there is considerable variability in the level of oxygen both within and between tumours due to micro-regional heterogeneity in the supply of oxygen (*98*). This variability can make it challenging to draw conclusions about brain tumour oxygenation; however, at least two studies have reported significantly lower oxygen levels in brain tumours compared to the surrounding tissue (*101, 102*). The results of a number of studies that have investigated the oxygen levels in gliomas using oxygen sensitive probes are summarised in Table 1.1. The reported mean oxygen values in these studies range from 0.97–4.35%, with an overall mean of 1.43% O_2. These results support the conclusion that the oxygen levels in GBM are lower than in normal brain tissue.

Table 1.1 | Mean values for intra-tumoural oxygen levels in patients with gliomas. The partial pressure (mmHg) of O_2 is reported alongside the equivalent O_2 percentage. GA = General Anaesthetic.

Author	N	O_2 mmHg	O_2 %	GA	Glioma type
Beppu *et al*. (*102*)	16	9.2 ± 5.8	1.21	N	High grade
Whittle *et al*. (*103*)	12	21 ± 7.9	2.76	N	GBM
Collingridge *et al*. (*104*)	10	5.6 ± 2	0.74	Y	High grade
	7	10.3 ± 4.9	1.35	Y	Low grade
	3	11.1 ± 9.6	1.46	N	High grade
	3	33.1 ± 4.6	4.35	N	Low grade
Rampling et al. (*105*)	10	7.25 ± 8.12	0.97	Y	GBM

1.5.2.3 Spatial and temporal aspects of hypoxia

Within tumours, there is both spatial and temporal heterogeneity in oxygenation. The regular temporal variation in oxygen supply is referred to as cycling hypoxia. At least two timescales are known to co-exist: a short timescale, which has a frequency of several cycles per hour, and a longer timescale that operates over hours to days. The short timescale is due to fluctuations in microvessel red blood cell flux, while the longer timescale is thought to be caused by vascular remodelling (*106-108*). Several studies have reported that cycling hypoxia is more potent than chronic hypoxia, as evidenced by increased HIF-1α stabilisation, cellular invasion and resistance to radiotherapy (*109, 110*). Cycling hypoxia contributes to tumour malignancy by increasing the expression of HIF target genes such *ABCB1*, which encodes p-glycoprotein: a well-known drug efflux transporter that increases resistance to chemotherapy (*111*). Tumours are also characterised by spatial heterogeneity in oxygen levels. Pistollato *et al.* used image-guided surgery to characterise the distribution of hypoxia in GBM and found evidence for an intratumoural hypoxic gradient, consisting of a peripheral oxygenated layer, an intermediate mildly hypoxic layer and a highly hypoxic core. They found that cell phenotype correlated with the level of hypoxia, with more immature cells concentrated in the highly hypoxic core. Cells derived from the core and intermediate layers of tumours also showed increased protein expression of MGMT and resistance to temozolomide (*112*).

1.5.2.4 Regulation of HIF activity

HIF is a heterodimer consisting of α and β subunits. The α subunit exists as several different isoforms: HIF-1α, HIF-2α and HIF-3α (*113-115*). HIF-1α is ubiquitously expressed and HIF-1α protein levels are upregulated in the majority of tumours (*116*). The expression of HIF-2α and HIF-3α is more restricted and their role in tumour hypoxia has not been extensively

investigated. While HIF-β is constitutively expressed, HIF-α is constantly degraded under normal oxygen conditions (normoxia) (*117*). This oxygen-dependent degradation is regulated by the prolyl-hydroxylase domain (PHD) proteins (PHD1, PHD2 and PHD3) which hydroxylate HIF-α. Hydroxylation leads to the recognition of HIF-α by the von Hippel-Lindau tumour suppressor protein (VHL), which ubiquitinates HIF-α's oxygen-dependent degradation domain and tags it for proteasomal degradation (Fig 1.5) (*118-121*). Under hypoxic conditions, as the PHD proteins lack the oxygen required to hydroxylate HIF-α, itis not recognised by VHL and escapes degradation (*122*). This allows HIF-α and HIF-β to heterodimerise in the nucleus where HIF-α is predominantly located (*117, 123, 124*). Once dimerised, HIF binds to hypoxia response elements (HREs) and initiates the transactivation of its target genes (*121*). In addition to this oxygen-dependent degradation, HIF is also subject to oxygen-independent regulation by growth factors, metabolites, reactive oxygen species and transition metals (*125, 126*).

1.6 Tumour metabolism

1.6.1 Cellular respiration

It has been known that tumours display altered cellular metabolism since the first half of the 20th century; however, a detailed understanding of this phenomenon has only emerged over the last decade (*127*). In normal aerobic tissue, cellular respiration consists of three stages that result in the production of adenosine triphosphate (ATP) from glucose (Fig 1.6). The first stage, glycolysis, occurs in the cytosol. During this stage, one molecule of glucose is converted into two molecules of pyruvate, with a net gain of two molecules of ATP. Pyruvate enters the mitochondria where it is converted into CO_2 and acetyl-CoA, which enters the citric acid cycle (CAC). In this second stage, the carbons in acetyl-CoA are oxidised to CO_2, reducing NAD+

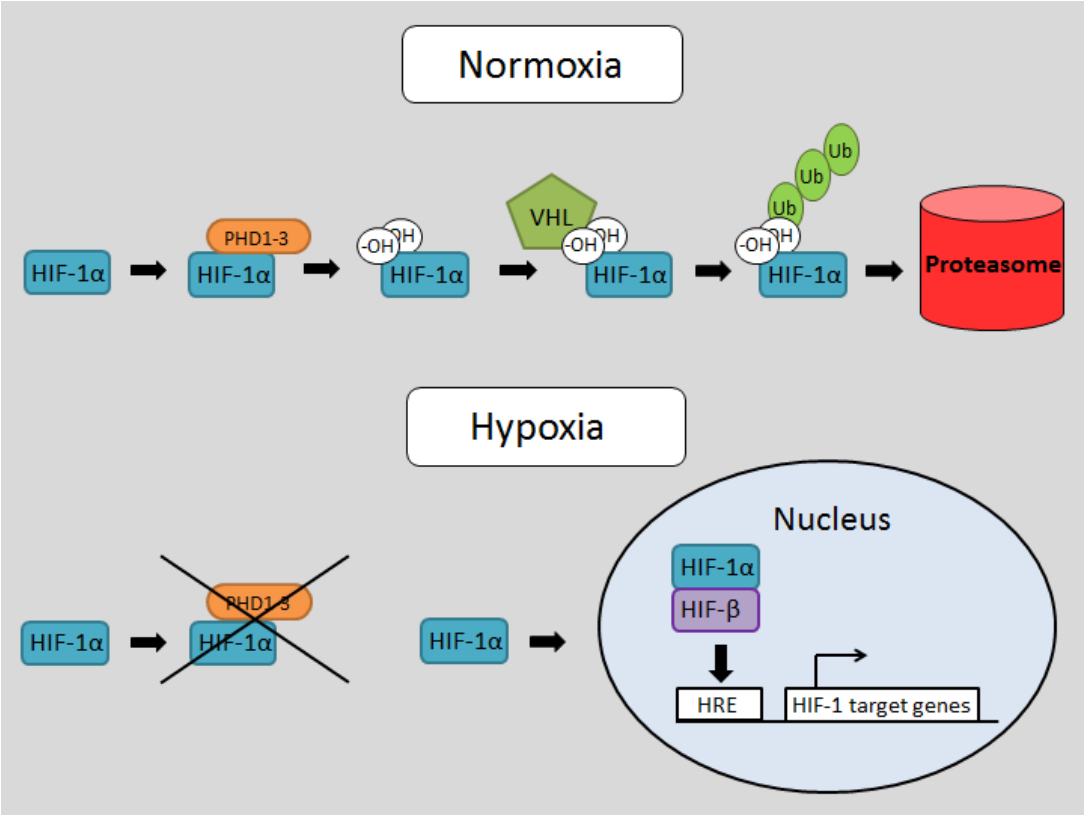

Figure 1.5. The oxygen-dependent regulation of HIF-1α. Under normal oxygen conditions, HIF-1α is hydroxylated by the PHD proteins, leading to its recognition and ubiquitination by VHL and subsequent degradation by the proteasome. In low oxygen conditions, HIF-1α is able to accumulate in the nucleus and dimerise with HIF-β. The dimerised protein binds to hypoxia response elements (HREs) where it initiates transactivation of its target genes.

to NADH and FAD to $FADH_2$. The final stage of respiration is oxidative phosphorylation (OxPhos), in which electrons are transferred from NADH and $FADH_2$, along the electron transport chain (ETC) in the inner mitochondrial membrane, to O_2. The ETC creates a proton gradient which is used to drive the production of ATP by ATP synthase (*128*). These three stages of cellular respiration result in the net total gain of 38 molecules of ATP per molecule of glucose (*129*).

1.6.2 The Warburg effect

As the final electron donor in the ETC is O_2, in conditions where O_2 is limited OxPhos is not possible and cellular metabolism halts at glycolysis. In this scenario, pyruvate stays in the cytosol where it is converted to lactate by lactate dehydrogenase, regenerating NAD^+ in the process and allowing further cycles of glycolysis (*128*). Many tumours show a preference for glycolytic metabolism under aerobic conditions (aerobic glycolysis). This phenomenon is termed the Warburg effect, after Otto Warburg who was the first to document it (*130, 131*). The Warburg effect is exploited clinically by the use of positron-emission tomography (PET) to detect tumours, which show increased uptake of the radiolabelled glucose analogue 2-[^{18}F]fluoro-2-deoxy-D-glucose (*132*). Tumour metabolism is an attractive therapeutic target and there are several glycolysis inhibitors under various stages of development (*133*). Otto Warburg's central hypothesis (the Warburg hypothesis) was that injured respiration, followed by an increase in glycolysis, is the cause of all cancers (*130*). However, subsequent research has challenged this theory. Cell lines derived from a number of tumours have been shown to predominantly utilise OxPhos as a source of energy (*134, 135*). Furthermore, the metabolism of tumour cells is highly dependent on the availability of energy substrates. When glucose is not available, HeLa cervical cancer cells remodel their mitochondrial structure and protein composition to derive energy exclusively from OxPhos (*136*). Similarly, breast cancer cells increase OxPhos in response to glucose deprivation and decrease OxPhos in response to hypoxia. However, when hypoxia occurs concomitantly with aglycemia, OxPhos is not decreased as, under these conditions, ATP can only be produced by the mitochondria (*137*). It is clear that cancer cells can coordinate nutrient and oxygen sensing and adapt their metabolism accordingly. Therefore, cellular metabolism is sensitive to cell culture conditions. The high level of glucose routinely used in cell culture inhibits respiration and OxPhos in cancer cells (the Crabtree effect). Static

monolayer culture has also been shown to increase glycolysis, compared to rotary cell culture, due to decreased O_2 diffusion (*138*). In glioma cells, the *in vitro* growth environment has been shown to cause a shift towards glycolysis, creating lipid and ETC abnormalities (*137, 139, 140*).

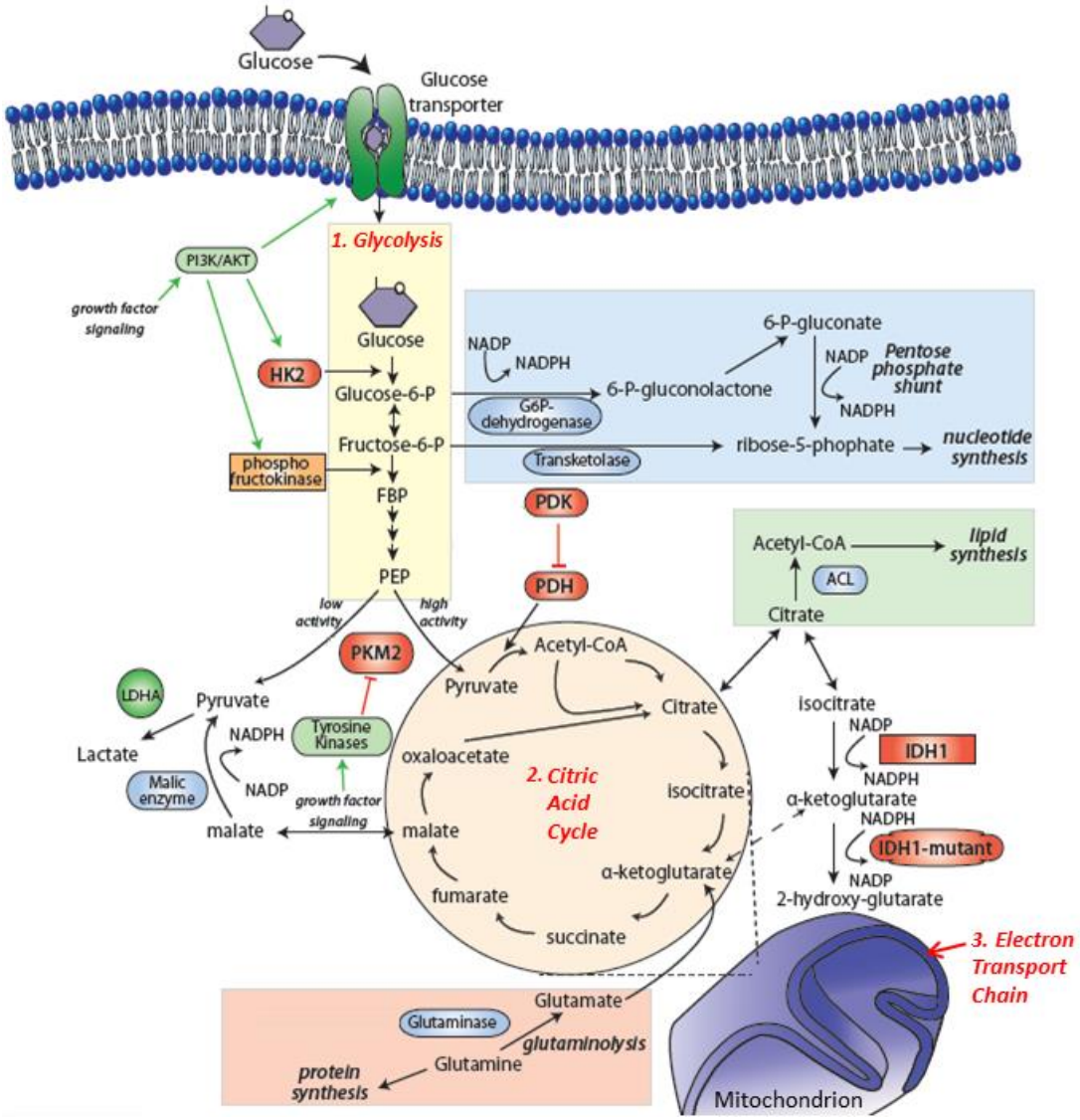

Figure 1.6. Regulation of cellular metabolism. Key enzymes involved in glycolysis, the citric acid cycle, lipid, protein and nucleotide synthesis are illustrated. Growth factor signalling can activate phosphoinositide 3-kinase (PI3K) signalling, increasing glycolysis through hexokinase 2 (HK2) and phosphofructokinase activity. Mutations in isocitrate dehydrogenase 1 (*IDH1*) prevent the enzyme from catalysing the production of α-ketoglutarate from isocitrate, resulting in the production of (R)2-hydroxy-glutarate instead, reducing cytosolic NADPH production. Adapted from (*141*).

1.6.3 The role of hypoxia in cellular metabolism

Hypoxia is a potent inducer of glycolysis that also causes the active downregulation of OxPhos, reducing oxygen demand and ensuring the continued supply of ATP. HIF-1α plays an essential role in the regulation of cellular metabolism under hypoxic conditions. HIF target genes are found at almost every step of glycolysis; from the entry of glucose into the cell via GLUT1 and GLUT3, through to the removal of lactate from the cell by the monocarboxylate transporter MCT4 (*142*). In partnership with Christophe Sandt's group at the synchrotron SOLEIL, our group carried out an investigation into hypoxia-induced metabolic changes in GBM cell lines and primary cells using fourier transform infrared (FTIR) microspectroscopy. Although there was metabolic variability between cell lines, all cells showed an increase in lipids when incubated in hypoxia, and U87 cells showed an increase in glycogen. These changes were harder to detect when cells had been exposed to long-term hypoxia, suggesting that they had begun to adapt to the changes in their environment (*143*). Hypoxia has also been shown to cause an increase in the storage of lipids in lipid droplets (*144*).

1.6.4 Normal metabolism in the brain

The human brain is an energetically costly organ, comprising just 2% of body weight but consuming 20% of the energy supply (*145*). The adult brain predominantly utilises glucose for OxPhos; however, around 10-12% is used for aerobic glycolysis and there are significant regional variations in metabolism. Compared with the rest of the brain, aerobic glycolysis is significantly elevated in the medial and lateral parietal and prefrontal cortices (*146*). Aerobic glycolysis plays an important role in normal brain function; it is increased during brain activation and is associated with synaptic plasticity (*147, 148*). While most tissues are able to derive energy

from different substrates depending on their availability, the brain derives its energy almost exclusively from glucose, on which it is reliant to maintain normal function. As the entry of neuroactive compounds, such as glutamate and aspartate, is restricted by the BBB, the brain is forced to synthesise these compounds from glucose (*149*).

1.6.5 Metabolic alterations in GBM

The metabolomic profile of GBM is characterised by accelerated anabolic metabolism, reflecting the need for the increased production of nucleotides, proteins and lipids in rapidly dividing cells (*150, 151*). *In vitro*, the metabolism of glioma cells has been found to be cell line dependent, with some cell lines displaying an OxPhos-dependent phenotype while others display a glycolytic-dependent phenotype with functional OxPhos. The OxPhos-dependent cell lines are extremely resistant to glucose starvation, suggesting that OxPhos dependency may have developed as a result of the need to cope with nutrient deficiency (*152*). A microdialysis study carried out in patients with GBM found a significantly higher lactate:pyruvate ratio in tumour tissue than peritumoural tissue, suggesting that aerobic glycolysis is increased in gliomas (*153*). *In vivo* studies in mice and humans using ^{13}C-labelled glucose have revealed that GBMs are metabolically complex, utilising glucose for the CAC, aerobic glycolysis and the synthesis of macromolecular precursors (*154, 155*). The oxidation of blood-borne glucose was found to contribute to less than 50% of the total acetyl-CoA, indicating that gliomas are able to oxidise alternative substrates. Stored lipid supplies are one possible alternative; altered lipid metabolism is a feature of many tumours including gliomas, which display increased lipid levels and fatty acid synthesis (*156*).

Metabolic remodelling in tumours can occur as a result of changes in the microenvironment, such as hypoxia, or because of the deregulated signalling that occurs during malignant transformation (Fig 1.5) (*141*). Hexokinase (HK), the enzyme that catalyses the first step of glycolysis, exists as four different isoforms (HK1, HK2, HK3, HK4). While HK1 is ubiquitously expressed, the expression of HK2 is more restricted. HK2 is aberrantly expressed in many tumours (*157*). In GBM, its expression is associated with decreased OxPhos and increased lactate production, increased cellular proliferation, and a reduction in patient survival time. HK2 activity is regulated by growth-factor induced phosphoinositide 3-kinase (PI3K) signalling (*158*). PI3K is negatively regulated by phosphatase and tensin homolog (PTEN); however, the *PTEN* gene is frequently deleted in GBM, resulting in overactive PI3K signalling. The induced expression of PTEN in PTEN-null cells is associated with increased aerobic glycolysis (*159*). Mutations in the gene encoding isocitrate dehydrogenase 1 (IDH1), the enzyme that catalyses the oxidative decarboxylation of isocitrate to produce α-ketoglutarate (α-KG), occur in the majority of secondary GBMs but in only 7% of primary GBMs (*160*). *IDH1* mutations occur early in tumorigenesis and are a favourable prognosis factor, associated with a doubling in survival time (*161, 162*). Mutations in the *IDH1* gene (*IDH1*^{mt}) cause the enzyme to lose the ability to catalyse the production of α-KG from isocitrate, and gain the ability to reduce α-KG to the suspected oncometabolite (*R*)2-hydroxyglutarate [(*R*)-2HG] (Fig 1.6) (*163*). (*R*)-2HG has been found to potentiate PHD activity, promoting HIF-1α degradation (*164*). HIF1-α target genes, including many essential for glycolysis such as *LDHA*, are downregulated in *IDH1*^{mt} gliomas. These findings suggest that a reduced glycolytic capacity may contribute to slower tumour growth and a better prognosis in *IDH1*^{mt} tumours. However, the inhibition of *IDH1*^{mt} impairs the growth of *IDH1*^{mt} glioma cells and increases the expression of glial differentiation markers (*165*). Although this area of research has generated a great deal of interest, the consequences of *IDH1* mutation for tumorigenicity are still poorly understood (*166*).

1.7 Cellular invasion

1.7.1 Patterns of invasion

The diffusely infiltrative nature of GBM is a major reason for treatment failure. It follows that cellular invasion is of crucial importance in GBM despite the fact that, in contrast to other malignant tumours, the occurrence of metastasis is extremely rare. In a review of the literature, Kalokhe *et al*. identified only 79 case reports of GBM metastasis in the last 50 years. To put this into perspective, between 10,000 and 12,000 cases of GBM occur each year in the United States alone (*167*)**.** Unlike solid tumours in other areas of the body, or tumours that have metastasised to the brain, GBM is not reliant on intravascular or lymphatic spread. Rather, GBM shows a unique pattern of invasion, with single cells invading throughout the extracellular space (*15, 168*). The margins of GBM are poorly delineated and invading cells are capable of migrating long distances. Early attempts to cure patients by the complete removal of the affected brain hemisphere were unsuccessful due to tumour recurrence in the remaining hemisphere (*169*). Hans-Joachim Scherer's careful histological examination of gliomas in 1938 has contributed much to our knowledge of the invasive behaviour of these tumours (*170*). Scherer coined the phrase 'secondary structures' to refer to the structures formed by glioma cells as they invaded the pre-existing tissue architecture. These include perineural and perivascular growth as well as growth in and around white matter tracts (Fig 1.2C). The migration of glioma cells along existing structures closely mimics neuronal migration during embryonic development, in which immature neurons travel along radial glia and neuronal axons, and adult neurogenesis, in which neuroblasts migrate along the vasculature to reach their final destination (*171*). *In vivo* imaging studies and studies using slice cultures generated from rat brains have shown that GBM cells preferentially invade along blood vessels, along which they move faster and more efficiently (*172, 173*). This causes astrocyte endfeet to be

displaced from the vasculature and disrupts the BBB. Astrocyte-vascular coupling is lost, allowing GBM cells to seize control of vascular tone (*174*). Single invading GBM cells can also induce vascular remodelling and angiogenesis (*173*). The preference of GBM cells for perivascular migration is thought to be explained in part by the release of bradykinin by endothelial cells, which acts as a chemoattractant and enhances invasion by increasing matrix metalloproteinase (MMP) activity (*175*).

1.7.2 Metastatic dissemination

One possible explanation for the extremely low incidence of metastasis in GBM is that the cells are unable to invade into blood vessels (intravasation) and enter the circulatory system. In studies using animal models, GBM cells have been seen to invade along the surface of blood vessels; however, invasion into the vessels has not been observed (*172, 176, 177*). It has been suggested that GBM cells may be unable to breach the BBB; however, this is frequently disrupted in GBM due to the abnormal nature of the vasculature (*178*). While tissue disruption during surgery may well be responsible for cells seeding into the circulation in a proportion of cases, extracranial metastases are also documented in patients who have not undergone any surgical intervention (*179*). Other explanations for why GBM typically does not metastasise include the short survival of patients, which means metastases may not have time to develop or may not be detected, and the absence of a lymphatic system in the brain (*167, 180*). However, in 2015 two labs independently reported the discovery of a lymphatic vessel network in the dura of the meninges, overturning the long-held belief that the brain does not have a lymphatic system (*181, 182*).

The most common sites for metastasis to occur outside the CNS are bone, lymph nodes and the lung (*167*). Due to the rarity of metastasis in GBM,

patients are able to become organ donors after their death. However, there are 11 reports of recipients developing GBM metastasis in donated organs following transplantation (*183*). This suggests that the historical view of GBM being confined to the CNS is untrue. Muller *et al.* recently investigated the existence of circulating tumour cells (CTCs) in the peripheral blood of patients with GBM. They found that CTCs were present in 21% of patients and that there was no relationship between surgery and detection of CTCs (*184*). The discrepancy between the proportion of patients with CTCs and the proportion that develop metastasis suggests that GBM cells are able to enter the circulation, but find their new extraneural environment to be unfavourable to growth. It is possible that tumour cells lodge in distant organs in a dormant state until immunosuppression, caused by radiotherapy and chemotherapy or, in organ donor recipients, immunosuppressive drugs, renders the environment more favourable and allows cells to proliferate (*180, 184*).

1.7.3 Molecular mechanisms of invasion

In order to invade away from the tumour mass, cells need to move through the extracellular matrix (ECM): the secreted molecules of the extracellular space. The ECM of the adult human brain is mainly composed of proteoglycans, hyaluronic acid and tenascin. It is densely packed, with pore sizes of just 38-64 nm. The matrix proteins that are common in other tissues, such as collagen, fibronectin, and laminin, are almost absent in brain parenchymal ECM; however, they are present in the vascular and subpial basement membranes (*185-187*). Integrins are transmembrane receptors that link the interior of the cell to the ECM. They provide a mechanical link, through the actin cytoskeleton, and a sensory link, through signal transduction pathways. Integrins are key regulators of numerous cellular processes including adhesion, migration, proliferation and survival (*188*).

Integrin αVβ3 is mainly expressed on angiogenic endothelial cells and promotes tumour angiogenesis alongside αVβ5 (*189*). However, in gliomas, αVβ3 is also expressed in tumour cells and its expression correlates with tumour grade, with increased expression in GBM compared to low-grade gliomas (*190*). Inhibition of αVβ3 has been shown to reduce glioma migration and invasion, suggesting that it may play an important role in contributing to the invasive phenotype of GBM (*191, 192*).

The activity of proteinases, which degrade the ECM and create space for tumour cells to migrate, is essential for invasion. The MMPs are a large family of proteinases that, collectively, are capable of degrading a broad range of substrates including all ECM components. They are overexpressed in almost all human tumours and their activity is correlated with increased tumour aggressiveness and a poorer prognosis (*193*). MMP-2, MMP-9 and MMP-14 are overexpressed in GBM compared to lower grade gliomas and normal brain tissue (*194*). As well as promoting migration and invasion, MMPs have also been shown to regulate proliferation, survival and angiogenesis (*193*). The tumour microenvironment is an important regulator of glioma invasion and MMP expression. Multiple studies have demonstrated that hypoxia increases glioma invasion and that this effect is mediated by HIF-1α (*195-197*). HIF-1α increases the expression of numerous factors that facilitate invasion, such as MMP-2, MMP-9, integrin αVβ3 and αVβ5 (*196, 198, 199*). Cell-cell interactions are also important in regulating invasion: astrocytes produce active MMP-2 when cultured with glioma cells and the inhibition of gap junctions in astrocyte-glioma co-cultures has been shown to prevent glioma migration (*200-202*). Although MMP inhibitors reduce glioma invasiveness *in vitro*, they have performed poorly in clinical trials (*203, 204*).

1.8 Three-dimensional cell culture

The majority of *in vitro* cancer research has been conducted using cells cultured as two-dimensional monolayers on plastic or glass surfaces. However, these conditions fail to replicate important aspects of the cellular environment that occur *in vivo*, such as cell-cell and cell-matrix interactions, matrix stiffness and gradients in soluble factors such as oxygen, nutrients, growth factors and cytokines (*205*). Three-dimensional (3D) cell culture systems have been established in an attempt to more faithfully reproduce characteristics of the tumour environment. Broadly, these culture systems fall into two categories: those that rely on exogenous support from a matrix or scaffold, and those that are independent of exogenous support. Cells can be grown in hydrogels derived from components of the ECM, such as collagen, or in hydrogels made from agarose or synthetic polymers. A popular choice of matrix for mimicking the ECM is Matrigel: a reconstituted basement membrane extract from the Engelbreth-Holm-Swarm mouse sarcoma, composed of approximately 60% laminin, 30% collagen IV and 8% entactin plus numerous growth factors. A number of commercial companies have developed pre-fabricated hard scaffolds made from substances such as polystyrene. These provide structural support for cells but are engineered to be highly porous, allowing for cell-cell contact and migration throughout the scaffold (*206*).

Important considerations when choosing a 3D cell culture method include how well it represents the *in vivo* environment, how practical and reproducible the method is, and how well it has already been characterised. The choice of matrix has been shown to strongly influence cell behaviour and response to drugs, with cells cultured in synthetic scaffolds more closely resembling monolayer cultures than cells cultured in biologically-derived matrixes (*207*). When embedding cells in hydrogels, it is important to mitigate the effects of growth inhibition by solid stress. Solid stress can occur

in gels containing just 0.3% agarose, and markedly increases when higher concentrations of agarose are used (*70*). A further challenge of growing cells in scaffolds of matrixes is that the cells can be difficult to retrieve for biochemical analyses.

1.8.1 The multicellular tumour spheroid model

The multicellular tumour spheroid model is a well-characterised model in which cells are grown as a 3D cluster in the absence of any exogenous support. The model was developed in the 1970s by Sutherland to mimic nodular carcinomas and avascular regions of tumours (Fig 1.7) (*208, 209*). Spheroids show a spatial gradient in oxygen availability, which mimics the intratumoural hypoxic gradient reported in GBM, as well as gradients in nutrients and pH (*210-214*). These gradients can cause a metabolic switch, resulting in enhanced glycolytic metabolism in spheroids compared to monolayer cultures (*215*). Spheroids also show a characteristic concentric pattern of cell proliferation and viability. Typically, spheroids consist of a necrotic core, an intermediate layer of quiescent cells, and an outer layer of proliferating cells concentrated around the periphery of the spheroid (*214, 216, 217*). Gradients in soluble factors begin to occur in spheroids when they reach around 200 µm, and central necrosis at 500 µm; however, the size at which necrosis develops is cell line dependent. Changes in metabolism have also been observed in small spheres, before the onset of nutrient or oxygen gradients. Santini *et al*. compared osteosarcoma cells grown as a monolayer and as very small spheroids (50-80 µm) using high-resolution proton nuclear magnetic resonance spectroscopy. The cells cultured as spheroids displayed different metabolic characteristics, suggesting an effect of spatial arrangement on cellular metabolism (*218*).

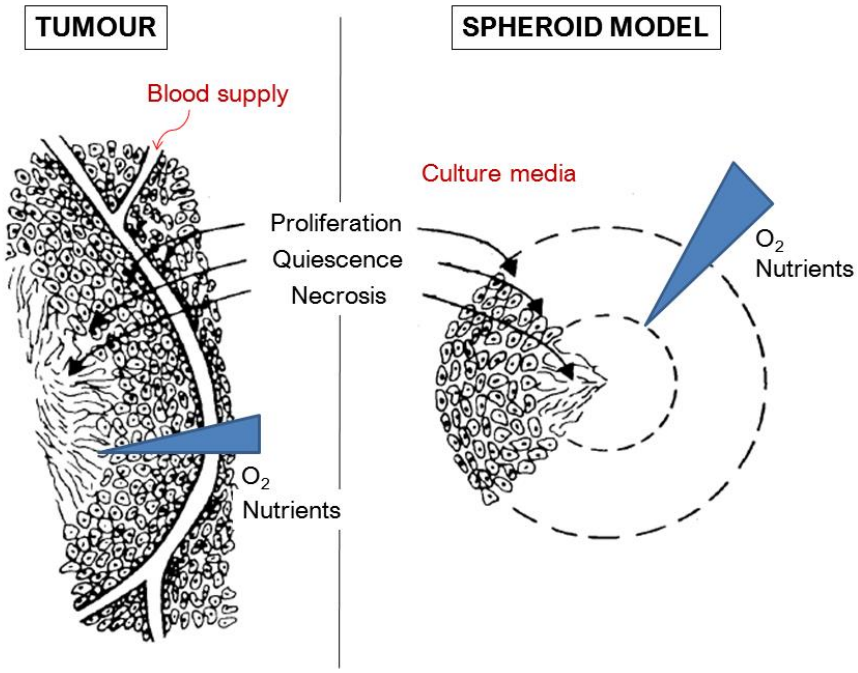

Figure 1.7. The multicellular tumour spheroid model. Tumour spheroids share important characteristics with solid tumours, such as gradients in oxygen and nutrients. Like tumours, they contain a mixture of proliferating, quiescent and necrotic cells. Adapted from (*209*).

The cellular and molecular heterogeneity of spheroids makes them a better model for solid tumours than homogeneous monolayer cultures. Spheroid culture preserves the genomic profile of primary GBM cells, which is rapidly altered when the cells are subjected to standard cell culture conditions (*219*). The results of *in vitro* drug screening often only poorly correlate with the results of *in vivo* tests; for this reason, drug testing in spheroids is emerging as a necessary intermediate between testing in monolayer cultures and testing in animals (*220*). Drug diffusion in spheroids closely replicates diffusion in tumour tissue, furthermore, the hypoxic core of spheroids contains higher levels of p-glycoprotein, mimicking the hypoxic drug resistant areas found in solid tumours (*221, 222*). Typically, the effects of therapeutic drugs are reduced in the 3D environment; however, in some cases, their activity is increased (*223-225*). Spheroids can also be used to screen for drugs that target dormant tumour regions, which are resistant to treatment with cytostatic drugs. An investigation by Wenzel *et al.* revealed that respiratory chain inhibitors are most effective in the quiescent centre of

spheroids, while the proliferating outer region of spheroids is more sensitive to cytostatic drugs (*226*).

The 3Rs of animal research refer to the principles of replacement, reduction and refinement (*227*). According to these principles, every effort should be made to develop experimental methods that replace the use of animals (replacement), minimise the number of animals used (reduction), and cause animals the minimum amount of distress (refinement). The use of 3D cell cultures, such as multicellular tumour spheroids, can help to fulfil the principles of replacement and reduction. The increased physiological relevance of these models over 2D cell cultures offers an alternative option to *in vivo* experiments. Furthermore, the use of spheroids in drug screening assays can lead to more effective selection of compounds, reducing the number of compounds that need to be tested in animals (*220*).

1.9 Aims of the project

The overall aim of this project was to investigate the effect of the solid tumour microenvironment on GBM cells. Firstly, we aimed to investigate the effect of different levels of oxygen on cell proliferation in cells cultured as a monolayer. Next, we aimed to explore the effects of hypoxia in a more physiologically relevant model of GBM. We wished to establish a multicellular tumour spheroid model, which we aimed to characterise in terms of cell proliferation, survival, oxygenation and energetic status. We further aimed to assess the effects of hypoxia on these characteristics. Finally, we aimed to carry out live cell imaging of spheroid invasion using lightsheet microscopy. We wished to quantify the movements of cells moving within spheroids, as well as the movements of cells invading into ECM. We also aimed to assess the suitability of this technique as a 3D invasion assay for characterising the effects of drugs that target the invasion process.

Chapter 2:
Materials and Methods

2.1 Chemicals and reagents

Unless otherwise stated, cell culture reagents were purchased from Gibco (USA), plasticware from Corning (USA), RNA extraction and qPCR reagents from Roche (Switzerland), and all other chemicals and reagents from Sigma-Aldrich (USA).

2.2 Cell culture

2.2.1 Cell lines and propagation

U251 cells were obtained from CLS (Germany, #300385), U87 cells from ATCC (UK, #HTB-14), HeLa cells from ECACC (UK, #93021013) and HEK 293TN cells from System Biosciences (USA, #LV900A-1). D566 cells were a generous gift from Professor DD Bigner (Duke University Medical Centre, USA). The shPHD2 HeLa cells were a gift from D Hoogewijs, D Stiehl and R Wenger (University of Zürich, Switzerland) and the shPHD3 HeLa cells were a gift from Sarah Taylor (University of Liverpool, UK). Cells were maintained in culture medium as listed in Table 2.1. Cells were cultured in T-75 flasks and subcultured every 2–3 days when they had reached 80-90% confluence. Cells were counted using a Bio-Rad (UK) TC20 automated cell counter and seeded at the required density. Cells were maintained in a humidified incubator at 37 °C, 5% CO2 (Sanyo, Japan).

Table 2.1 Cell lines and culture medium.

Cell line	Origin	Culture medium
U251, D566	GBM	10% v/v FBS, 1% v/v NaPyr & 1% v/v NEAA in MEM
U87	GBM	10% v/v FBS & 1% v/v NaPyr in MEM
Primary GBM (GBM03, GBM04)	GBM	20% v/v FBS, 1% v/v NaPyr, 1% v/v NEAA & 1% pen-strep in MEM
HeLa	Cervical carcinoma	10% v/v FBS & 1% v/v NEAA in MEM
HeLa shPHD2 & shPHD3	HeLa cells stably knocked down for PHD2/PHD3 via small hairpin RNA (shRNA)	10% v/v FBS, 1% v/v NEAA & 10 μg/mL puromycin (Invitrogen, USA) in MEM
HEK 293TN	Human embryonic kidney	10% v/v FBS & 1% v/v NEAA in DMEM

2.2.2 Tumour dissection and primary culture

Samples of primary GBM tumours were received from patients undergoing craniotomy and resection. All patients gave informed written consent to donate their tissue to the Walton Research Tissue Bank, Walton Centre NHS Foundation Trust, which has full approval of the National Research Ethics Service (11/WNo03/2). Primary cell culture was carried out in accordance with the approved guidelines.

Tumour samples were transported in MEM plus 1% (v/v) penicillin-streptomycin (pen-strep) and then mechanically dissected in a petri dish using a disposable scalpel (Swann-Morton, UK). The dissected samples were incubated in dissociation medium (10% (v/v) trypsin 10X, 1% (v/v) DNase and 1% (v/v) pen-strep in MEM) at 37 °C and triturated every 5 min (up to a maximum of 30 min) until a cell suspension was obtained. The trypsin reaction was stopped by the addition of growth medium (see Table 2.1 for details). Cells were centrifuged for 5 min at 3000 rpm; the supernatant was aspirated and the pellet resuspended in growth medium and seeded into a T-75 flask. The resulting cell lines (designated GBM03 and GBM04) were maintained in culture for a maximum of three passages.

2.2.3 Hypoxic incubation

For experiments requiring hypoxia, cells were incubated in a Don Whitley Scientific (UK) H35 Hypoxystation (1% O_2) or a New Brunswick Galaxy 48R hypoxic incubator (Eppendorf, Germany; 0.1% and 8% O_2). Cells were maintained at 37 °C, 5% CO_2 and the air humidified.

2.2.4 Etoposide treatment

Cells were treated with 10–20 μM etoposide for 24 h.

2.2.5 Spheroid culture

To generate multicellular tumour spheroids, 2.4×10^4 U87 cells were seeded in 1 mL of filtered growth media. Media was filtered through a 0.22 μm PES filter using a bottle-top vacuum filter system. The cell suspension was pipetted (50 μl per well) into a 96-well Perfecta3D Hanging Drop plate (3D Biomatrix, USA) where it formed a hanging droplet. After three days, the cells had compacted from a loose aggregate and formed a compact spheroid. Spheroids were transferred to a 35 mm non-treated culture dish using a P1000 pipette and media was exchanged every 2-3 days.

2.3 Flow cytometry

Cells were seeded into 6 cm tissue culture dishes (1×10^5 cells per dish) and incubated in different levels of O_2 for up to five days.

2.3.1 Cell viability analyses

Adherent cells were washed with phosphate-buffered saline (PBS), trypsinised and suspended in Hank's balanced salt solution (HBSS) together with the floating fraction of cells. The cell suspension was pipetted into a 96-well plate, stained with FITC Annexin V (Invitrogen, 1:500) and incubated for 15 min in the dark at room temperature (RT). Propidium iodide (PI) was added at a final concentration of 4 μg/mL immediately prior to analyses. Samples were analysed using a Guava EasyCyte Flow Cytometer and cell viability was established using GuavaSoft software (EMD Millipore, USA).

2.3.2 Cell cycle analyses

Cells were washed with PBS, trypsinised and resuspended in 0.1% (v/v) Triton X-100 in PBS. PI and ribonuclease A were added at a final concentration of 10 μg/mL. Cells were analysed by flow cytometry and the percentage of viable and apoptotic cells was established using GuavaSoft software. The proportion of cells in G_0/G_1, S and G_2/M phases was established using Modfit software (Verity Software House, USA).

2.4 Real-time reverse transcription PCR (qRT-PCR)

RNA was extracted using a High Pure RNA Isolation Kit according to the manufacturer's instructions. RNA was eluted in 30 μl elution buffer and quantified using a Nanodrop 1000 spectrophotometer (Thermo Scientific, USA). Reverse transcription of 1 μg mRNA to cDNA was carried out using a

SuperScript VILO cDNA synthesis kit (Invitrogen, USA). cDNA was diluted 1:20 in DNase/RNase-free water and stored at -20 °C until required. Reactions were performed in triplicate using 10 µl LightCycler SYBR Green I Master, 6 µl DNase/RNase-free H_2O, 2 µl cDNA and 0.5 µM of each primer. Primers are detailed in Table 2.2. qPCR was performed using a LightCycler 480 and results were analysed using LightCycler 480 software (version 1.5.0.39). For qPCR parameters, see Chapter 3. The values for target genes were normalised to cyclophilin A and expressed as fold change from the control values (20% O_2).

Table 2.2 Primers used for qPCR

Primer name	Forward sequence	Reverse sequence
Cyclophillin A	gctttgggtccaggaatgg	gttgtccacagtcagcaatggt
p21	agctgccgaagtcagttcctt	gttctgacatggcgcctcct
p27	tccggctaactctgaggaca	gaagaatcgtcggttgcagg
E2F1	ccgccatccaggaaaaggtg	gtgatgtcatagatgcgccg

2.5 Western blotting

2.5.1 Sample preparation

Cells were seeded in 6 cm tissue culture dishes and subjected to various treatments. Seeding density was adjusted so that cells would be almost confluent at the time of harvesting. Cells were washed with PBS, placed on ice, and lysed using 150 µl RIPA buffer (50 mM Tris-HCl ph 7.5, EDTA 1 mM, EGTA 1 mM, Na_3VO_4 1 mM, 1% (v/v) Triton X-100, 50 mM sodium fluoride, 5 mM sodium pyrophosphate, 19 mM sodium B-glycerophosphate and

0.1 mM phenylmethylsulfonyl fluoride) plus phosphatase inhibitor cocktail (1:1000). The cells were detached using a cell scraper and transferred into a 1.5 mL Eppendorf tube. Samples were rotated at 4 °C for 45 min and centrifuged for 15 min at 14 000 x g, 4 °C. The supernatant was collected and protein content quantified using a Thermo Scientific Pierce BCA Protein Assay Kit.

2.5.2 Protein separation and transfer

Protein samples were mixed in a 4:1 ratio with 5x Laemmli buffer (final concentration: 60 mM Tris-Cl [pH 6.8], 2% (w/v) SDS, 10% (v/v) glycerol, 5% (v/v) β-mercaptoethanol, 0.01% (w/v) bromophenol blue) and denatured by heating at 100 °C for 5 min. Proteins were resolved on 4% stacking gels (0.4 M Tris base [pH 6.8], 4% (v/v) acrylamide, 0.65 ng/µl APS and 0.325% (v/v) Temed) and 10% SDS-polyacrylamide gels (0.4 M Tris base [pH 8.8], 0.1% (w/v) SDS, 10% (v/v) acrylamide, 0.25 ng/µl APS and 0.125% (v/v) Temed). Thirty to forty micrograms of protein were loaded per well and 8 µl of protein ladder (Precision Plus Protein All Blue Standards, Bio-Rad) was loaded into the end well. Gels were submerged in running buffer (25 mM Tris, 192 mM glycine and 3.4 mM SDS) and ran at 100–130 V until adequate separation was achieved. Proteins were transferred onto a 0.2 µm nitrocellulose membrane (Bio-Rad) by electroblotting transfer with a tank system. The transfer was carried out for 1.5 h at 300 mA, 4 °C using transfer buffer (20% (v/v) ethanol, 25 mM Tris and 192 mM glycine).

2.5.3 Detection of protein

Membranes were blocked with 5% (w/v) non-fat milk in TBST (0.2 M Tris [pH 7.6], 0.14 M NaCl and 0.1% (v/v) Tween-20) for 1 h at RT. Primary antibodies were applied following three washes with TBST and membranes were incubated overnight at 4 °C in a 50 mL falcon tube on a roller mixer. Secondary antibodies were applied after three washes in TBST and

membranes were incubated for 1 h at RT on an orbital shaker. All antibodies were prepared in 5% (w/v) BSA in TBST; see Table 2.3 for details of primary and secondary antibodies used. Following a further three washes in TBST, membranes were incubated with Super Signal West Pico Chemiluminescent substrate (Thermo Scientific) for 2 min and imaged using a Syngene Gel Imaging G-box (Geneflow, UK). Images were taken every 2 min and were integrated into previous images for up to 40 min.

Table 2.3 Antibodies used for immunoblotting

Antibody	Dilution	Host species	Source	Cat No
HIF-1α	1:1000	Mouse	BD Biosciences, USA	610959
p21	1:500	Rabbit	Santa Cruz, USA	sc-397
p53	1:1000	Mouse	Santa Cruz	sc-126
β-actin	1:1000	Mouse	Abcam, UK	ab8226
Cyclophilin A	1:1000	Rabbit	Abcam	ab3563
Anti-mouse HRP conjugated	1:5000	Horse	Cell Signalling Technology, USA	7073
Anti-rabbit HRP conjugated	1:3000	Goat	Cell Signalling Technology	7074

2.6 Live cell imaging of cell cycle length

In the hypoxic condition, D566 cells were incubated in 1% O_2 for 72 h prior to imaging. Twenty-four hours prior to imaging, 75 x 10^4 cells were seeded in a

35 mm glass-bottomed dish (Greiner Bio-One, UK). The dish was mounted on a PeCon CO_2-O_2 controller incubator (PeCon, Germany) on the stage of an LSM 510 confocal microscope (Zeiss, Germany). Cells were maintained at 37 °C, 5% CO_2 and either 1% or 20% O_2 and imaged using a Plan-Neofluar 10x objective (NA 0.3) for 48 h. The sample was illuminated with a 543 nm laser and transmitted light was detected. Images were captured using Zen 2012 software (Zeiss). Cell cycle length was determined by tracking individual cells manually using the open source image analyses software Icy, version 1.5.4.2, and recording the length of time between the first and second observed cell divisions.

2.7 Stable cell line production

The U87-H2BmRFP and U87-PercevalHR stable cell lines were made using lentiviral transduction. HEK 293TN cells were seeded into six 10 cm dishes at a density of 1.5 x 10^6 cells per dish. Cells were transfected with the lentiviral construct the following day using a vector:packaging:env ratio of 4:2:1 (see Table 2.4). The plasmids were transfected using polyethylenimine (PEI) at a ratio of 2:1 PEI:DNA in DMEM. A media change was performed three days after seeding. Three days after transfection, the supernatant was harvested, centrifuged at 500 x g for 10 min and filtered through a 0.45 µm PES filter. Ultracentrifugation was carried out following the protocol described by Kutner *et al*. (*228*). Viral particles were resuspended in 600 µl PBS, aliquoted into screw cap microfuge tubes, frozen in crushed dry ice and stored at -80 °C for future use. For transduction, 2 x 10^5 U87 cells were seeded into a T-25 flask and 250 µl (H2B-mRFP) or 10 µl (PercevalHR) of the concentrated virus was applied. A media change was performed after 24 h.

Table 2.4 Plasmid information

Plasmid	Addgene plasmid no.	Mass (ng) for 1 x 10 cm^2 dish
pHIV-H2BmRFP	18982	9 714
FUGW-PercevalHR	49083	9 714
psPAX2	12259	4 857
pMD2.G	12260	2 428

2.8 Spheroid characterisation

2.8.1 Pimonidazole hydrochloride (PIMO, Hypoxyprobe™-1) staining

PIMO was added to spheroids in growth media at a final concentration of 200 μM 24 h prior to fixation.

2.8.2 Spheroid fixation and sectioning

Spheroids were washed three times with PBS and fixed in 4% paraformaldehyde (PFA) for 45 min at RT. Spheroids were washed again three times and then transferred into 20% sucrose for 72 h at 4 °C. After this cryoprotective step, spheroids were transferred into Peel-A-Way disposable embedding moulds (Polysciences, USA) and the sucrose was aspirated and replaced with cryomatrix (Thermo Scientific). Samples were centrifuged at 700 rpm for 3 min before being snap frozen on dry ice and transferred to -80 °C. Samples were cut into 10 μm sections using a CM1860 Cryostat (Leica, Germany). Sample sections were transferred onto Superfrost Plus microscope slides (Thermo Scientific) and stored at -20 °C.

2.8.3 Immunofluorescence

Slides were allowed to thaw for 10 min at RT and a Dako PAP pen was used to draw a hydrophobic barrier around the circumference of the sample sections. Samples were washed three times with PBS and then incubated in 50 mM NH_4CL for 20 min to quench autofluorescence. Samples were blocked and permeablised with 1% (v/v) Triton X-100 and 0.4% (v/v) Tween20 in 1% (w/v) BSA in PBS for 20 min and then incubated with primary antibody for 1 h. Samples were washed three times with blocking solution and then incubated in secondary antibody for 30 min in the dark. All antibodies were diluted in blocking solution; for details of primary and secondary antibodies see Table 2.4. Samples were washed again three times with blocking solution, stained with Hoechst 33342 (1:1000, Invitrogen) for 20 min, and then washed three times with PBS and once with water. Dako fluorescent mounting medium was used to mount 50 mm glass cover slides (VWR) onto the sections.

Table 2.4 Antibodies used for immunofluorescence.

Antibody	Dilution	Host species	Source	Cat No
CA IX	1:500	Rabbit	Abcam	ab15086
GLUT1	1:500	Rabbit	Abcam	ab652
MCT4	1:500	Rabbit	Santa Cruz	Sc-50329
PIMO	1:1000	Mouse	Hypoxyprobe	HP1-100Kit
Alexa Fluor 488 anti-rabbit	1:500	Goat	Invitrogen	a-11008

2.8.4 EdU staining and detection

5-ethynyl-2'-deoxyuridine (EdU, Invitrogen) was added to spheroids in growth media at a final concentration of 20 nM 24 h prior to spheroid fixation. Following the fixation and sectioning steps already described, samples were washed with 3% (w/v) BSA in PBS followed by a 20 min incubation in 0.5% (v/v) Triton X-100 in PBS. EdU was detected using the Click-iT EdU Alexa Fluor 647 Imaging Kit (Invitrogen) according to the manufacturer's instructions.

2.8.5 Confocal microscopy

Spheroid sections were imaged using an LSM 780 confocal microscope (Zeiss, Germany) with an EC Plan-Neofluar 20x objective (NA 0.5). Alexa Fluor 488 was excited using a 488 nm laser and emitted light detected using a 473–597 nm bandpass filter (MBS 488/561/633, DBS1 mirror). Hoechst was excited using a 405 nm laser and emitted light detected using a 415 nm longpass filter (MBS 405, DBS1 mirror). Alexa Fluor 647 and PI were excited using a 561 nm laser and emitted light detected using a 620 nm longpass filter (MBS 458/561, DBS1 mirror). Samples expressing PercevalHR were excited with 488 nm and 405 nm lasers and emitted light was collected using a 499–552 nm bandpass filter. Images were captured using Zen 2012 software.

2.8.6 Quantification of spheroid immunofluorescence

Spatial intensity analysis was carried out on background-subtracted images using the open-source platform for biological-image analyses, Fiji (*229*). For each spheroid, ten concentric regions of interest (ROI) were selected, each 10% smaller than the last (Fig 2.1). As each of these ROIs overlapped, the integrated density for the non-overlapping regions was calculated by subtracting the integrated density of the next smallest ROI from the total for

every ROI, except the smallest. This gave us integrated density values for ten separate regions of the spheroid. The mean fluorescence intensity (MFI) was calculated by dividing the integrated density for each region by its area. MFI was normalised to the centre (GLUT-1, MCT4 and PIMO) or the periphery of the sphere (EdU) by dividing the MFI for each ROI by the MFI of the central ROI. The fractional distance was calculated by dividing the average radius of each ROI, measured in pixels, by the average radius of the largest ROI. Normalised MFI values were plotted against fractional distance to show the distribution of fluorescence within each spheroid.

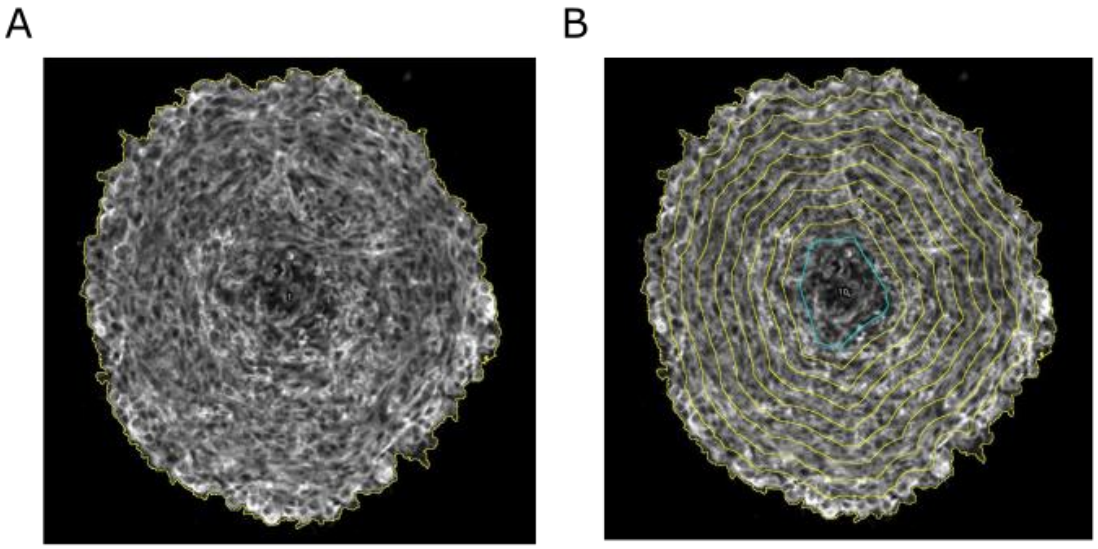

Figure 2.1. Spatial intensity analyses. An analysis of the distribution of fluorescence intensity in spheroid sections was carried out using Fiji. **(A).** The initial region of interest (ROI), shown as a yellow line, was selected so that it encompassed the entire spheroid**. (B).** The size of the initial ROI was measured so that the subsequent ROIs, each 10% smaller than the last, could be created. Mean fluorescence intensities were calculated for the non-overlapping regions between ROIs as described above.

2.9 Lightsheet fluorescent microscopy

2.9.1 Sample preparation

Spheroids were prepared for imaging by aspirating the growth media and replacing it with 50% ice-cold Matrigel and 50% growth media plus 25 mM Hepes. For drug treated spheroids, 0.5 μM 17-AAG (Abcam) or 2 μM cilengitide (Adooq Bioscience, US) was added to the growth media. A Teflon plunger (Zeiss) was used to draw the spheroid into a fluorinated ethylene propylene (FEP) tube (S 1815-04, BOLA, Germany). The tube was cut with scissors to release it from the plunger and one end was sealed with a small amount of parafilm. A glass capillary (inner diameter 1.5 mm) was mounted in the lightsheet sample holder and the FEP tube placed partially inside the capillary. The sample holder was mounted in the Lightsheet Z.1 (Zeiss) sample chamber, where the sample was immersed in water at 37 °C for the duration of the experiment.

2.9.2 Image acquisition

Samples were excited with a 561 nm laser and 10x excitation objectives; emitted light was collected through a 576–615 band pass filter using a 20x W Plan-Apochromat objective and 1 x zoom. Images were acquired every 3 min with a z-step of 1.66 μm, starting approximately 50 μm in front of the spheroid. Lightsheet Z.1 Zen software (Zeiss) was used to acquire images using online dual side fusion with pivot scan. Images were detected using a pco.edge scientific complementary metal–oxide–semiconductor (sCMOS) camera.

2.9.3 Image processing

Image processing was carried out using a HP Z640 computer workstation (Hewlett-Packard, US) equipped with six central processing units (CPUs; Intel Xeon E5-2620v3 2.4 GHz) and 128 GB of DDR4 random access memory

(RAM). We devised a method of reducing the size of the lightsheet data prior to analyses, using a macro written in Fiji by Dr. David Mason, image analyst in the Liverpool Centre for Cell Imaging (Appendix 1.1). This was essential due to the extremely large file sizes produced (up to 0.75 TB for one experiment). The macro loads one time point at a time and downsamples the data by decreasing bit depth from 16 bit to 8 bit and performing 2 x binning. A further processing step was carried out prior to analyses in order to deal with sample drift. This was carried out in Fiji, using the descriptor-based series registration plugin developed by Preibisch *et al.* (*230*). Registration was carried out using a translational transformation model and consecutive matching of images with a range for all-to-all matching of two.

2.9.4 Cell tracking and data analyses

Segmentation and tracking were carried out using Imaris 8.2.0 (Bitplane, Belfast). Tracking was carried out using an autoregressive motion algorithm, with a maximum distance of 6 μm and a maximum gap size of zero. A filter was applied to remove any tracks that were shorter than eight time points (24 min). Once tracking was complete, track and spot statistics were exported into excel files. MATLAB (Mathworks, US) was used to further process these statistics. A wrapper script (Appendix 1.2.1) was used to batch process files using the data processing script (Appendix 1.2.2) or the figure plotting script (Appendix 1.2.3). All MATLAB scripts were written by Dr. David Mason.

The data processing script calculates spot speed and straightness as a function of radial distance from the centre of the spheroid. When the script is run, the user is asked to input the coordinates of the centre of the spheroid. Spot position, spot speed, track position, track straightness and mean track speed are then imported from the excel files generated using Imaris. For each spot, the Euclidian distance from the centre of the spheroid is calculated using the spot position information. This allows spot speed and straightness to be calculated as a function of radial distance from the centre of the

spheroid. Spot straightness was calculated by dividing the sum of displacements between the preceding and proceeding two spots by the distance between the first and last spot. Spots located outside of the initial spheroid outer boundary were categorised as invading, while spots inside the boundary were categorised as non-invading. The spatial location of the outer boundary of each spheroid was defined by taking the mean of the ten furthest out spots present in the first frame of the experiment and adding 5%. For the large spheroids, the region inside the spheroid boundary was divided by three to calculate the inner, middle and outermost region of the spheroid. The data processing script was also used to determine the cumulative distribution of spot speeds by distance from the centre of the spheroid, over time.

The figure plotting script was used to plot histograms and beehive plots for the output variables for each condition. A representative selection of these graphs are included in Chapter 5, section 5.2. As so many graphs were generated, it would have been impractical to include them in the appendix. Instead, we have made them available online using the image management software Zegami (Zegami, UK). Using Zegami, it is possible to view all of the graphs that were generated and sort them by condition and graph type. The Zegami database has been made available with the help of Dr. David Mason.

2.10 Statistical analyses

Statistical significance was determined by Analysis of Variance (ANOVA) followed by Dunnett's test or Fisher's LSD test, where appropriate, using SPSS statistical software (IBM, USA).

Chapter 3:

The effects of low oxygen levels on glioblastoma cell proliferation and survival

3.1 Introduction

The level of oxygen is recognised as a critical aspect of the tumour microenvironment. Hypoxia is associated with tumour aggressiveness and is known to increase angiogenesis, treatment resistance and invasion (*81*). However, the effect of hypoxia on cell proliferation is less well characterised. We aimed to address this gap in the literature by performing a systematic investigation into the effect of different oxygen levels on GBM cell proliferation and survival. Next, we wished to use live single-cell imaging to gain quantitative information on the dynamic relationship between HIF-1α and the cell cycle. We planned to transfect GBM cells with fluorescent ubiquitination-based cell cycle indicators (Fucci). These are cell cycle reporters that have been formed by fusing proteins whose expression levels oscillate during the cell cycle with fluorescent proteins (*231*). We have the facilities to perform time-lapse confocal fluorescence microscopy in an oxygen-controlled environment, allowing us to compare cell cycle characteristics under different oxygen conditions. We aimed to further explore the relationship between HIF-1α and the cell cycle using mathematical modelling and a systems biology approach. This approach has been successfully used by our group to examine the temporal regulation of HIF-1α expression, revealing the existence of a HIF-PHD negative feedback loop with important consequences for cell fate (*232*). To increase the relevance of our findings, we hoped to replicate the results obtained in cell lines in primary GBM cells. We were successful in characterising the relationship between different oxygen levels and cell proliferation and survival; this work has been published as an article in PeerJ (*233*), which has been included in this chapter. Unexpectedly, the results of flow cytometry experiments revealed that hypoxia has only minimal effects on cell proliferation. As such, we decided not to pursue our original aims relating to single-cell imaging and mathematical modelling of the relationship between HIF-1α and the cell cycle.

3.2 Cell cycle progression in glioblastoma cells in unaffected by pathophysiological levels of hypoxia

(Published paper)

Authors: Rosalie Richards, Michael D. Jenkinson, Brian J. Haylock and Violaine See

PeerJ, March 2016

Author contributions

Rosalie Richards

- Conceived and designed the experiments
- Performed the experiments
- Analysed the data
- Prepared figures and tables
- Wrote the paper

Michael D. Jenkinson

- Reviewed drafts of the paper

Brian J. Haylock

- Reviewed drafts of the paper

Violaine Sée

- Conceived and designed the experiments
- Wrote the paper
- Reviewed drafts of the paper

PeerJ

Cell cycle progression in glioblastoma cells is unaffected by pathophysiological levels of hypoxia

Rosalie Richards[1], Michael D. Jenkinson[2], Brian J. Haylock[3] and Violaine See[1]

[1] Institute of Integrative Biology, Department of Biochemistry, University of Liverpool, Liverpool, United Kingdom
[2] Institute of Translational Medicine, Clinical Science Centre, University of Liverpool, Liverpool, United Kingdom
[3] Department of Clinical Oncology, Clatterbridge Cancer Centre, Bebington, United Kingdom

ABSTRACT

Hypoxia is associated with the increased malignancy of a broad range of solid tumours. While very severe hypoxia has been widely shown to induce cell cycle arrest, the impact of pathophysiological hypoxia on tumour cell proliferation is poorly understood. The aim of this study was to investigate the effect of different oxygen levels on glioblastoma (GBM) cell proliferation and survival. GBM is an extremely aggressive brain tumour with a heterogeneous oxygenation pattern. The effects of a range of oxygen tensions on GBM cell lines and primary cells were assessed using flow cytometry. Results indicate that cell cycle distribution and viability are unaffected by long term exposure (24–96 h) to pathophysiological levels of oxygen (1–8% O_2). Both transient cell cycle arrest and small amounts of cell death could only be detected when cells were exposed to severe hypoxia (0.1% O_2). No significant changes in p21 protein expression levels were detected. These findings reinforce the importance of using physiologically relevant oxygen tensions when investigating tumour hypoxia, and help to explain how solid tumours can be both hypoxic and highly proliferative, as is the case with GBM.

Subjects Biochemistry, Cell Biology, Oncology
Keywords Hypoxia, Cell cycle, HIF, Glioblastoma, Cell death, Tumour microenvironment, Brain tumours

Submitted 14 January 2016
Accepted 12 February 2016
Published 3 March 2016

Corresponding author
Violaine See, violaine@liverpool.ac.uk

Academic editor
Giulia Piaggio

Additional Information and Declarations can be found on page 10

DOI **10.7717/peerj.1755**

INTRODUCTION

As tumour growth is dependent on the formation of new blood vessels, tumours are often highly vascularised. However, the vasculature is poorly organised and exhibits severe structural and functional abnormalities. This leads to regions of the tumour experiencing a reduced supply of oxygen, known as hypoxia (*Folkman, 1990*; *Vaupel, Kallinowski & Okunieff, 1989*; *Dewhirst, Cao & Moeller, 2008*). Hypoxia is a fundamentally important hallmark of solid tumours and is associated with tumour progression and poor patient prognosis across a broad range of tumour types (*Ruan, Song & Ouyang, 2009*; *Semenza, 2010*). Paradoxically, hypoxia has also been reported to induce cell cycle arrest (*Box & Demetrick, 2004*). This reduction in proliferation could reduce tumour burden, or alternatively it may increase tumour aggressiveness due to the central role of the cell cycle in mediating sensitivity to both chemo- and radiotherapy (*Shah & Schwartz, 2001*;

How to cite this article Richards et al. (2016), Cell cycle progression in glioblastoma cells is unaffected by pathophysiological levels of hypoxia. **PeerJ 4:e1755; DOI 10.7717/peerj.1755**

Pawlik & Keyomarsi, 2004). To resolve the apparent contradiction between the pro-tumorigenic role of hypoxia and its reported anti-proliferative effects, we performed a systematic investigation into the effect of different oxygen levels on glioblastoma (GBM) cell proliferation and survival.

GBM is the most common primary malignant brain tumour with 3 per 100,000 people diagnosed every year (*Ostrom et al., 2013*). Despite advances in neurosurgery and radiotherapy over the past 40 years, the prognosis remains poor with an average survival time of just 14 months (*Anderson et al., 2008*). GBM is a diffusely infiltrative Grade IV astrocytic tumour, characterised histopathologically by brisk mitotic activity, cellular and nuclear atypia, vascular thrombosis, microvascular hyperproliferation and necrosis (*Reifenberger et al., 2010*). As with many solid tumours, GBM is characterised by a heterogeneous pattern of oxygenation. Investigations using oxygen-sensitive electrodes have shown the normal level of oxygen in human brain tissue to be 5–8%. In contrast, mean oxygen levels in high-grade gliomas range from 0.75% to 2.76% (*Meixensberger et al., 1993*; *Kayama et al., 1991*; *Beppu et al., 2002*; *Whittle et al., 2010*; *Collingridge et al., 1999*; *Rampling et al., 1994*), and the larger the hypoxic tumour volume, the poorer the prognosis (*Spence et al., 2008*).

There are a number of mechanisms through which hypoxia promotes tumour malignancy, including resistance to radio- and chemotherapy (*Haar et al., 2012*; *Harrison & Blackwell, 2004*), increased cell migration and invasion (*Herrmann et al., 2015*), reprogramming towards a cancer stem cell (CSC) phenotype and expansion of CSC populations (*Soeda et al., 2009*; *Fujiwara et al., 2007*; *Heddleston et al., 2009*). At a cellular level, the master regulator of oxygen homeostasis is the transcription factor hypoxia-inducible factor (HIF). HIF promotes cell survival in low oxygen conditions by activating the transcription of genes that regulate processes such as angiogenesis, glycolysis and invasion (*Semenza, 2003*). HIF-1α expression is correlated with tumour grade in gliomas, with the highest expression found in high-grade gliomas (*Zagzag et al., 2000*; *Sondergaard et al., 2002*).

In contrast to other aspects of tumour malignancy, the effects of hypoxia on cell cycle regulation are poorly characterised. It is often stated that hypoxia induces cell cycle arrest, however these observations have been made in severe hypoxia ($\leq$0.1% O_2) or anoxia (*Box & Demetrick, 2004*; *Graeber et al., 1994*; *Amellem & Pettersen, 1991*). Investigations using the 2-nitroimidazole EF5, an agent which forms macromolecular adducts in low-oxygen levels as a result of its reductive metabolism (*Koch, 2002*), have established that the proportion of severely hypoxic cells in brain tumours is low. Rather, the majority of cells are exposed to moderate hypoxia (>0.5% O_2) (*Evans et al., 2004*). Research into the effect of more physiologically relevant oxygen tensions on tumour growth is lacking.

The aim of this study was to investigate the effects of physiological (8% O_2), pathophysiological (1% O_2) and severe (0.1% O_2) levels of hypoxia on GBM cell proliferation and survival. We demonstrate that cell cycle progression in GBM cells is unaffected by pathophysiological levels of hypoxia, and only severe hypoxia is capable of causing transient cell cycle arrest or cell death.

METHODS

Cell culture and hypoxic treatment

All reagents were purchased from Life Technologies, unless otherwise stated. U87 cells (ATCC, HTB-14), U251 cells (CLS, 300385) and D566 cells (a kind gift from Professor DD Bigner, Duke University Medical Centre, USA) were maintained in MEM supplemented with 1% sodium-pyruvate and 10% foetal bovine serum (FBS). U251 and D566 cells were supplemented with 1% non-essential amino acids (NEAA). HeLa cells (ECACC, 93021013) were maintained in MEM plus 10% FBS and 1% NEAA. All cells were maintained at 37 °C in 5% CO_2. For flow cytometry experiments, 1×10^5 cells were seeded in 6 cm tissue culture dishes (Corning). For hypoxic experiments, cells were incubated in a Don Whitley H35 Hypoxystation (1% O_2) or a New Brunswick Galaxy 48R hypoxic incubator (0.1% and 8% O_2). A media change was performed after 48 h.

Tumour dissection and primary culture

Samples of primary GBM tumours were received from patients undergoing craniotomy and resection. All patients gave informed written consent to donate their tissue to the Walton Research Tissue Bank, Walton Centre NHS Foundation Trust, which has full approval of the National Research Ethics Service (11/WNo03/2). Primary cell culture was carried out in accordance with the approved guidelines. Tumour samples were transported in MEM plus 1% penicillin-streptomycin (pen-strep), mechanically dissected, and transferred into dissociation medium (10% trypsin 10X and 1% DNase [Sigma] in MEM plus 1% pen-strep). Samples were incubated for 15–30 min at 37 °C and triturated every 5 min. The trypsin reaction was stopped by adding growth medium (MEM plus 20% FBS, 1% sodium-pyruvate and 1% pen-strep). Cells were centrifuged for 5 min at 3,000 rpm, resuspended in growth medium and seeded into a 75 cm^2 tissue culture flask.

Flow cytometry

For the viability analyses, adherent cells were washed with phosphate buffered saline (PBS), trypsinised and suspended in Hank's balanced saline solution (HBSS) together with the floating fraction of cells. The cell suspension was pipetted into a 96 well plate, stained with FITC Annexin V (1:500) and incubated for 15 min in the dark at room temperature (RT). Propidium iodide (PI) was added at a final concentration of 4 μg/mL immediately prior to analyses. Samples were analysed using a Guava EasyCyte Flow Cytometer and cell viability was established using GuavaSoft software (Millipore). For the cell cycle analyses, cells were washed with PBS, trypsinised and resuspended in PBS with 0.1% TritonX-100. PI and ribonuclease A were added at a final concentration of 10 μg/mL. Cells were analysed by flow cytometry and the percentage of cells in G_0/G_1, S and G_2/M phases was established using ModFit LT (Verity Software House).

Western blotting

30–40 μg protein was resolved on a 10% SDS-polyacrylamide gel, transferred onto a nitrocellulose membrane, and probed with primary antibodies against HIF-1α (BD Biosciences 610959, 1:1000), β-actin (Abcam ab8226, 1:1000) and p21 (Santa Cruz sc-396,

1:500) at 4 °C overnight. Membranes were incubated with either an anti-mouse (1:5000) or anti-rabbit (1:3000) horseradish peroxidase-linked secondary antibody (Cell Signalling) for 1 h at RT. Amersham ECL Prime Western Blotting Detection Reagent (GE Healthcare) was used according to the manufacturer's instructions prior to detection using a G:BOX gel imaging system (Syngene, UK).

Real time reverse transcription polymerase chain reaction (qRT-PCR)

RNA was extracted using a HP RNA isolation kit (Roche) according to the manufacturer's instructions. Reverse transcription of 1 μg mRNA to cDNA was carried out using a SuperScript VILO cDNA synthesis kit. Real time polymerase chain reaction (qPCR) was performed in triplicate using 10 μl LightCycler® 480 SYBR Green I Master (Roche), 6 μl DNase/RNase-free H_2O, 2 μl cDNA and 0.5 μM of each primer. Primers used were as follows: cyclophilin A forward: GCTTTGGGTCCAGGAATGG, reverse: GTTGTCCACAGTCAGCAATGGT; p21 forward: AGCTGCCGAAGTCAGTTCCTT, reverse: GTTCTGACATGGCGCCTCCT; p27 forward: TCCGGCTAACTCTGAGGACA, reverse: GAAGAATCGTCGGTTGCAGG; E2F1 forward: CCGCCATCCAGGAAAAGGTG, reverse: GTGATGTCATAGATGCGCC. qPCR was performed using a LightCycler 480 (Roche); for parameters see Table S1. Results were analysed using LightCycler 480 software (version 1.5.0.39, Roche). The values for target genes were normalised to cyclophillin A and expressed as fold change from control values (20% O_2).

Statistical analyses

Statistical significance was determined by ANOVA using SPSS statistical software (IBM).

RESULTS

Pathophysiological hypoxia has minimal effects on GBM cell proliferation and survival, while long-term exposure to severe hypoxia results in cell death

To investigate the effect of different oxygen levels on cell survival, three GBM cell lines (D566, U87 and U251 cells) were exposed to atmospheric (20% O_2), physiological (8% O_2) and pathophysiological (1% O_2) levels of oxygen for up to 96 h. Cell proliferation and survival were measured using Annexin V/PI staining and cell counting using flow cytometry. D566 and U87 cell proliferation was not affected at any time, while U251 cells only displayed a reduction in cell number after 96 h in 1% O_2 (Fig. 1A). The viability of all three cell lines was not affected by the different levels of oxygen (Fig. 1B). These results suggest that pathophysiological levels of hypoxia do not significantly affect cell proliferation or survival.

We investigated whether severe hypoxia (0.1% O_2) could have a more pronounced effect on cell fate. In both D566 and U251 cells, a significant reduction in cell number was evident after 48 h in 0.1% O_2, while a significant decrease in U87 cell number could only be observed after 96 h (Fig. 2A). A reduction in cell number can be due to a reduction in proliferation or an increase in cell death. The latter was the case for U251 and U87 cells, which showed a significant decrease in viability after 48 h exposure to 0.1% O_2 (Fig. 2B).

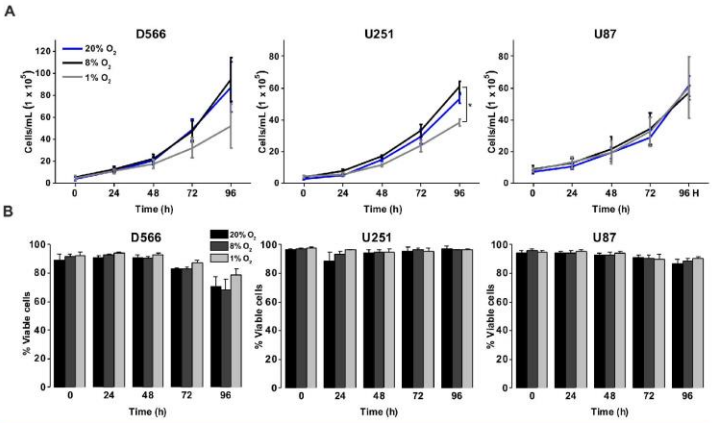

Figure 1 Exposure to physiological and pathophysiological levels of hypoxia has minimal effects on GBM cell proliferation and survival. GBM cell lines were exposed to 1%, 8% and 20% O_2 for the indicated time points. (A) Cell proliferation was assessed by cell counting using flow cytometry. (B) Cell survival was assessed by Annexin/PI staining and flow cytometry. Figure shows mean of three experiments + SEM. $^*p < 0.05$ $^{**}p < 0.01$.

In both U251 cells (Fig. 2C) and U87 cells (Fig. S1), cell death was predominantly due to necrosis. In contrast, the viability of D566 cells was unaffected by exposure to 0.1% O_2, suggesting that the reduction in D566 cell number may be due to cell cycle arrest.

Pathophysiological hypoxia has no effect on cell cycle distribution, while severe hypoxia induces a transient cell cycle arrest in D566 cells only

As a more direct assessment of the effect of hypoxia on cell proliferation, cells were exposed to 0.1%, 1% or 20% O_2 prior to cell cycle analyses by flow cytometry. There was no difference in cell cycle distribution between cells exposed to 1% O_2 and 20% O_2 in any of the cell lines tested (Fig. 3A). In U87 and U251 cells there were no significant differences in cell cycle distribution between cells exposed to 0.1% and 20% O_2 (Fig. 3A). However, after 48 h in 0.1% O_2 D566 cells displayed a 13% increase ($p = .002$) in the proportion of cells in G_1 phase. Interestingly, this cell cycle arrest was only transient and was lost in chronic hypoxia ($\geq$72 h) (Fig. 3A, Fig. S2). To confirm that resistance to hypoxia-induced cell cycle arrest is not an acquired characteristic of cell lines maintained in culture, we conducted the same experiment with primary GBM cells isolated from tumour samples obtained at resection (designated GBM03 and GBM04). We saw no evidence of cell cycle arrest in 1% or 0.1% O_2 (Fig. 3B). These results show that only severe hypoxia has the potential to induce cell cycle arrest in GBM cells and, furthermore, this arrest is only transient.

As GBM cells are known to harbour mutations in a number of genes involved in cell cycle control (Catalogue of somatic mutation in cancer (COSMIC),

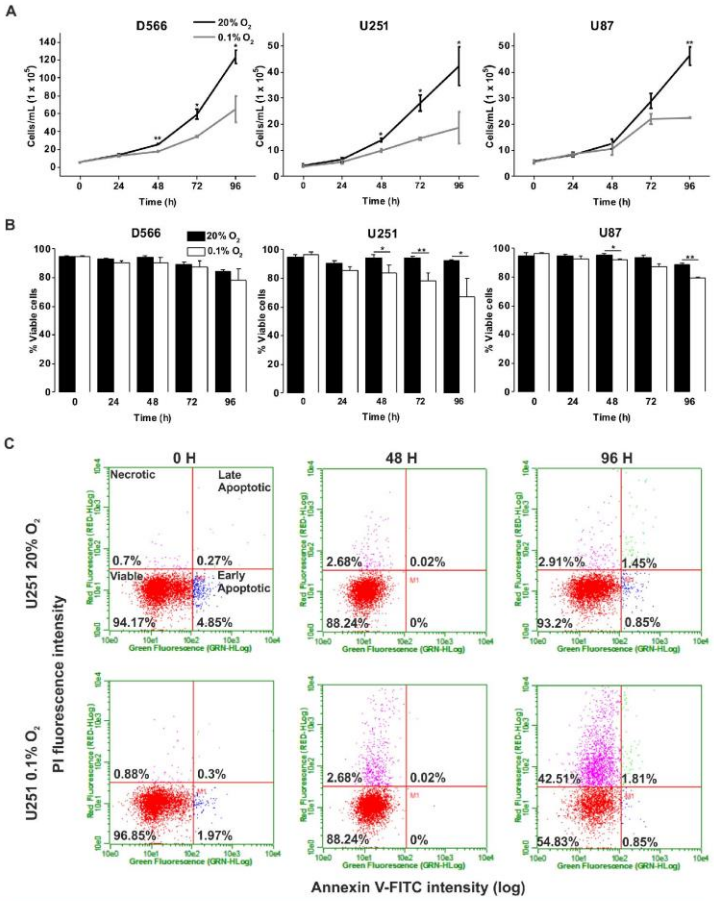

Figure 2 Long-term exposure to severe hypoxia causes cell death. GBM cell lines were exposed to 0.1% and 20% O_2 for the indicated time points. (A) Cell proliferation was assessed by cell counting using flow cytometry. (B) Cell survival was assessed by Annexin/PI staining and flow cytometry. (C) Representative example of U251 flow cytometry profile. Figure shows mean of three experiments + SEM. $*p < 0.05$ $**p < 0.01$.

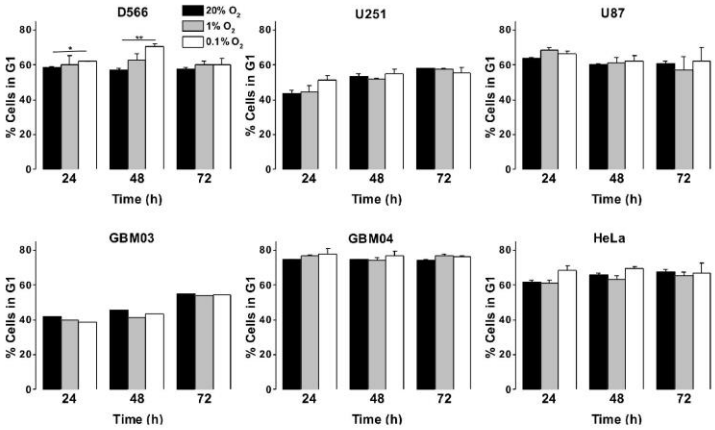

Figure 3 Severe hypoxia causes a transient G_1 phase arrest in D566 cells only. Cells were exposed to 0.1%, 1% and 20% O_2 for the indicated time points and cell cycle distribution was assessed using flow cytometry. The histograms show mean of three experiments + SEM, with the exception of primary cell lines GBM03 ($N = 1$), and GBM04 ($N = 2$), where mean + SD are plotted. $^*p < 0.05$, $^{**}p < 0.01$.

http://cancer.sanger.ac.uk/cosmic), we verified that these cells were capable of undergoing cell cycle arrest by exposing them to 10 μM etoposide for 24 h. All three cell lines displayed a profound S phase arrest (Fig. S3). To investigate whether the observed cell cycle response was specific to GBM cells or common to other cancer cells, we exposed HeLa cells to 0.1%, 1% and 20% O_2 for up to 72 h. As with the GBM cells, HeLa cell cycle distribution was unaffected by exposure to 1% O_2. An increase in cells in G_1 phase was observed following 48 h in 0.1% O_2; however, this increase was not significant and cell cycle distribution returned to normal after 72 h, as previously observed in D566 cells (Fig. 3B).

The effect of hypoxia on the expression of HIF-1α and cell cycle regulatory proteins

We confirmed the ability of GBM cells to respond to hypoxia by measuring HIF-1α stabilisation using western blot (Fig. 4A). In all three cell lines, HIF-1α was stabilised in hypoxia, with increased protein levels in 0.1% compared to 1% O_2 (Fig. 4B). To confirm that hypoxia does not have a significant effect on cell cycle regulation, mRNA levels of the cyclin-dependent kinase inhibitors p21, p27 and the well described transcription factor involved in G_1/S transition, E2F1, were measured by qRT-PCR following up to 96 h in 0.1% O_2 (Fig. 4C). No significant changes in p21, p27, or E2F1 expression were observed in any of the cell lines. D566 cells showed a non-significant increase in p21 expression at 24 h, with expression levels peaking at 48 h and decreasing after 72 h, consistent with the temporary G_1 phase accumulation observed in D566 cells exposed to 0.1% O_2 (Fig. 3A). Western blotting was used to investigate whether this transient increase in p21 mRNA

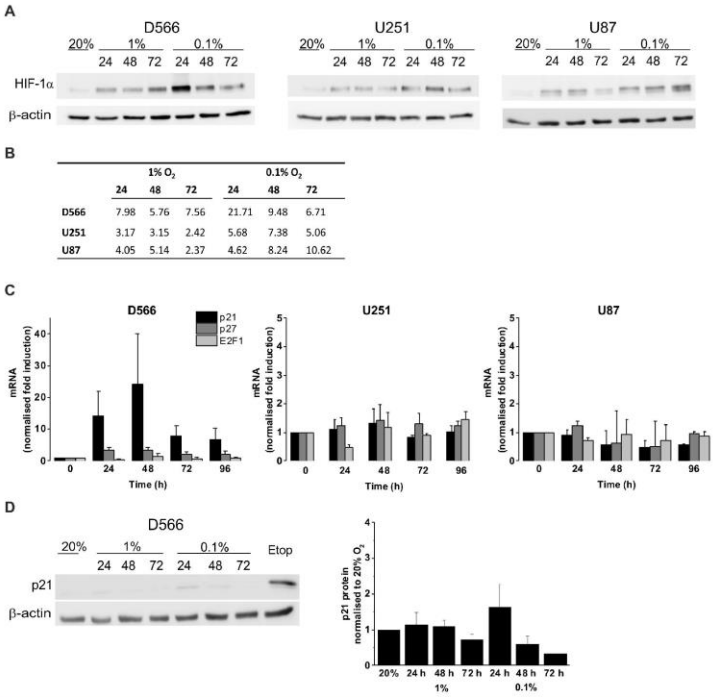

Figure 4 Hypoxia increases HIF-1α but does not change p21 protein expression. Protein expression was examined by western blot following incubation in 20%, 1% or 0.1% O_2 for 24, 48 or 72 h. Blots are representative examples taken from three experiments. (A) Western blots of HIF-1α protein expression. (B) Densitometry of HIF-1α protein expression shown in (A). (C) qRT-PCR was used to assess mRNA levels of p21, p27 and E2F1 following exposure to 0.1% O_2. Values were normalised to cyclophilin A and expressed as fold change from 20% O_2. Figure shows mean of three experiments + SEM. (D) Western blot of p21 protein expression. Cell exposed to the chemotherapeutic etoposide (Etop) were included as a control. The densitometry analysis, measured as the mean background subtracted integrated density for three experiments + SEM, has been plotted.

was translated at the protein level. Only a small increase in protein was detected after 24 h exposure to 0.1% O_2 (Fig. 4D). Furthermore, this increase was negligible compared to the amount of p21 detected following treatment with etoposide, a potent inducer of cell cycle arrest (see Fig. S3).

DISCUSSION

Our results show that GBM cells survive and proliferate following chronic exposure to 1% O_2, which is typical of the oxygen levels found in brain tumours. We have shown that only

severe hypoxia (0.1% O_2) is capable of inducing GBM cell cycle arrest and, furthermore, this arrest is only transient. Previous research has indicated that hypoxia causes cell cycle arrest; however, in the majority of these experiments cells were exposed to severe hypoxia or anoxia, which is not representative of the oxygen levels found within tumours (*Box & Demetrick, 2004*; *Graeber et al., 1994*; *Amellem & Pettersen, 1991*; *Gardner et al., 2001*). Although a change in cell cycle distribution has been reported in U87 cells exposed to 1% O_2, no changes were observed in the growth curve (*Li et al., 2013*). Furthermore, as previous investigations have used short-term exposures ($\leq$48 h) it is not clear whether the reported cell cycle changes are transient, as we have observed in D566 cells.

While none of the cell lines tested showed any changes to cell cycle distribution following exposure to pathophysiological levels of oxygen (1% O_2) U251 cells displayed a reduction in cell number after 96 h. This suggests that in certain cell lines progression through each phase of the cell cycle may be slowed following long-term exposure to hypoxia. A G_1 cell cycle arrest was only observed in one cell line (D566 cells) following exposure to severe hypoxia. This transient arrest was associated with a parallel increase in p21 mRNA; however, the increase was not significant and not translated at the protein level.

No changes in p27 or E2F1 gene expression were detected. Previous investigations have demonstrated an association between the cell cycle arrest induced by severe hypoxia and the expression of p21 and p27, although there is controversy as to whether these proteins are essential (*Gardner et al., 2001*; *Goda et al., 2003*; *Graff et al., 2005*). *Goda et al. (2003)* reported that HIF-1α mediated induction of p21 and p27 is essential for hypoxia-induced G_1 cell cycle arrest. *Gardner et al. (2001)* also reported that hypoxia induces p27; however, in contrast to Goda et al. they found no involvement of HIF-1α in hypoxia-induced G_1 arrest. The reason for these discrepancies is unclear but may be due to differences in cell lines and methods.

When we compared cell proliferation under physiological oxygen levels (8% O_2, 'physioxia') to standard cell culture conditions (20% O_2), no changes were detected. These findings contrast with previous research which has suggested a pro-proliferative role for physioxia. Fibroblasts display an elevated growth rate and a delayed onset of replicative senescence when cultured in 3% O_2. These effects are a result of the reduction in oxidative damage accumulated under low oxygen conditions (*Chen et al., 1995*; *Parrinello et al., 2003*). Although HIF-1α is only present in small amounts above 1% O_2, increasing evidence suggests that it plays a pro-proliferative role in physiological oxygen conditions. Neural progenitor cells display increased proliferation in 10% O_2 in an effect mediated by HIF-1α, and the moderate induction of HIF-1α in 5% O_2 has been shown to promote proliferation of both cancer and non-cancer cell lines, suggesting an important role in normal cell physiology (*Carrera et al., 2014*; *Zhao et al., 2008*).

After 48 h exposure to severe hypoxia (0.1% O_2), we found that U251 and U87 cells underwent cell death. This observation is in line with the well-established finding that cell survival *in vitro* is compromised by exposure to extreme hypoxia (*Hall, Bedford & Oliver, 1966*). In GBM, the most severe regions of hypoxia (as indicated by high EF5 binding) are adjacent to regions of necrosis (*Evans et al., 2004*). One of the defining characteristics of GBM is pseudopalisading necrosis: an area of necrosis that often arises following a

vaso-occlusive event, surrounded by a dense arrangement of cells organised into parallel rows (*Rong et al., 2006*). The surviving cells on the periphery express high levels of HIF-1α and matrix metalloproteinases and are thought to be actively migrating outward towards a more favourable environment (*Sondergaard et al., 2002*; *Zagzag et al., 2006*; *Brat et al., 2004*). As such, regions of necrosis are associated with higher grade tumours and a poorer prognosis (*Hammoud et al., 1996*).

One mechanism by which hypoxia is thought to increase resistance to chemotherapy is the induction of cell cycle arrest. As traditional chemotherapeutics target rapidly diving cells, this is thought to allow hypoxic cells to escape cell death (*Harrison & Blackwell, 2004*). Our research suggests that only a small proportion of cells will be exposed to hypoxia severe enough to cause cell cycle arrest, and of these cells a proportion will undergo cell death. It is therefore likely that other mechanisms play a more important role in hypoxia-mediated chemoresistance, such as the increased expression of the ABCB1 and p-glycoprotein drug transporters (*Chou et al., 2012*). Tumour hypoxia is also associated with increased expression of O6-methylguanine-DNA-methyltransferase (MGMT), a DNA repair protein involved in resistance to temozolomide (*Pistollato et al., 2010*). Decreased diffusion of drugs to hypoxic areas due to an increase in distance from blood vessels is also likely to play a major role (*Tredan et al., 2007*).

In conclusion, our results indicate that GBM cell proliferation and survival is not affected by pathophysiological levels of hypoxia, and that even severe hypoxia has only minimal effects on cell cycle. As such, the proliferation of the majority of cells in high-grade gliomas will not be affected by the reduced oxygen supply that is characteristic of these tumours. These findings illustrate the importance of using physiologically relevant oxygen concentrations before drawing conclusions about the effects of hypoxia on cell fate.

ACKNOWLEDGEMENTS

We thank Dr. Carol Walker for coordinating access to patient tumour samples through the Walton Research Tissue Bank. We also extend our thanks to Mr Andrew Brodbelt of the Walton Centre NHS Foundation Trust for obtaining the samples.

ADDITIONAL INFORMATION AND DECLARATIONS

Funding

This work was funded by Naseem's Manx Brain Tumour Charity. The funders had no role in study design, data collection and analysis, decision to publish, or preparation of the manuscript.

Grant Disclosures

The following grant information was disclosed by the authors:
Naseem's Manx Brain Tumour Charity.

Competing Interests

Violaine See is an Academic Editor for PeerJ.

Author Contributions

- Rosalie Richards conceived and designed the experiments, performed the experiments, analyzed the data, wrote the paper, prepared figures and/or tables, reviewed drafts of the paper.
- Michael D. Jenkinson and Brian J. Haylock contributed reagents/materials/analysis tools, reviewed drafts of the paper.
- Violaine See conceived and designed the experiments, wrote the paper, reviewed drafts of the paper.

Human Ethics

The following information was supplied relating to ethical approvals (i.e., approving body and any reference numbers):

The Walton Research Tissue Bank, Walton Centre NHS Foundation Trust. National Research Ethics Service (11/WNo03/2).

Data Availability

The following information was supplied regarding data availability:

figshare; https://figshare.com/s/6bfd585c89dd5c321f03.

Supplemental Information

Supplemental information for this article can be found online at http://dx.doi.org/10.7717/peerj.1755#supplemental-information.

REFERENCES

Amellem O, Pettersen EO. 1991. Cell inactivation and cell-cycle inhibition as induced by extreme hypoxia: the possible role of cell-cycle arrest as a protection against hypoxia-induced lethal damage. *Cell Proliferation* **24**:127–141 DOI 10.1111/j.1365-2184.1991.tb01144.x.

Anderson E, Grant R, Lewis SC, Whittle IR. 2008. Randomized Phase III controlled trials of therapy in malignant glioma: where are we after 40 years? *British Journal of Neurosurgery* **22**:339–349 DOI 10.1080/02688690701885603.

Beppu T, Kamada K, Yoshida Y, Arai H, Ogasawara K, Ogawa A. 2002. Change of oxygen pressure in glioblastoma tissue under various conditions. *Journal of Neuro-Oncology* **58**:47–52 DOI 10.1023/A:1015832726054.

Box AH, Demetrick DJ. 2004. Cell cycle kinase inhibitor expression and hypoxia-induced cell cycle arrest in human cancer cell lines. *Carcinogenesis* **25**:2325–2335 DOI 10.1093/carcin/bgh274.

Brat DJ, Castellano-Sanchez AA, Hunter SB, Pecot M, Cohen C, Hammond EH, Devi SN, Kaur B, Van Meir EG. 2004. Pseudopalisades in glioblastoma are hypoxic, express extracellular matrix proteases, and are formed by an actively migrating cell population. *Cancer Research* **64**:920–927 DOI 10.1158/0008-5472.CAN-03-2073.

Carrera S, Senra J, Acosta MI, Althubiti M, Hammond EM, De Verdier PJ, Macip S. 2014. The role of the HIF-1alpha transcription factor in increased cell division at

physiological oxygen tensions. *PloS ONE* **9**:e97938 DOI 10.1371/journal.pone.0097938.

Chen Q, Fischer A, Reagan JD, Yan LJ, Ames BN. 1995. Oxidative DNA damage and senescence of human-diploid fibroblast cells. *Proceedings of the National Academy of Sciences USA* **92**:4337–4341 DOI 10.1073/pnas.92.10.4337.

Chou C-W, Wang C-C, Wu C-P, Lin Y-J, Lee Y-C, Cheng Y-W, Hsieh C-H. 2012. Tumor cycling hypoxia induces chemoresistance in glioblastoma multiforme by upregulating the expression and function of ABCB1. *Neuro-Oncology* **14**:1227–1238 DOI 10.1093/neuonc/nos195.

Collingridge DR, Piepmeier JM, Rockwell S, Knisely JPS. 1999. Polarographic measurements of oxygen tension in human glioma and surrounding peritumoural brain tissue. *Radiotherapy and Oncology* **53**:127–131 DOI 10.1016/S0167-8140(99)00121-8.

Dewhirst MW, Cao Y, Moeller B. 2008. Cycling hypoxia and free radicals regulate angiogenesis and radiotherapy response. *Nature Reviews Cancer* **8**:425–437 DOI 10.1038/nrc2397.

Evans SM, Judy KD, Dunphy I, Jenkins WT, Nelson PT, Collins R, Wileyto EP, Jenkins K, Hahn SM, Stevens CW, Judkins AR, Phillips P, Geoerger B, Koch CJ. 2004. Comparative measurements of hypoxia in human brain tumors using needle electrodes and EF5 binding. *Cancer Research* **64**:1886–1892 DOI 10.1158/0008-5472.CAN-03-2424.

Folkman J. 1990. What is the evidence that tumors are angiogenesis dependent. *JNCI Journal of the National Cancer Institute* **82(1)**:4–6.

Fujiwara S, Nakagawa K, Harada H, Nagato S, Furukawa K, Teraoka M, Seno T, Oka K, Iwata S, Ohnishi T. 2007. Silencing hypoxia-inducible factor-1 alpha inhibits cell migration and invasion under hypoxic environment in malignant gliomas. *International Journal of Oncology* **30**:793–802 DOI 10.3892/ijo.30.4.793.

Gardner LB, Li Q, Park MS, Flanagan WM, Semenza GL, Dang CV. 2001. Hypoxia inhibits G(1)/S transition through regulation of p27 expression. *Journal of Biological Chemistry* **276**:7919–7926 DOI 10.1074/jbc.M010189200.

Goda N, Ryan HE, Khadivi B, McNulty W, Rickert RC, Johnson RS. 2003. Hypoxia-inducible factor 1 alpha is essential for cell cycle arrest during hypoxia. *Molecular and Cellular Biology* **23**:359–369 DOI 10.1128/MCB.23.1.359-369.2003.

Graeber TG, Peterson JF, Tsai M, Monica K, Fornace AJ, Giaccia A. 1994. Hypoxia induces accumulation of p53 protein, but activation of a G(1)-phase checkpoint by low-oxygen conditions is independent of p53 status. *Molecular and Cellular Biology* **14**:6264–6277 DOI 10.1128/MCB.14.9.6264.

Graff P, Amellem O, Seim J, Stokke T, Pettersen EO. 2005. The role of p27 in controlling the oxygen-dependent checkpoint of mammalian cells in late G(1). *Anticancer Research* **25**:2259–2267.

Haar CP, Hebbar P, Wallace GC, Das A, Vandergrift WA, Smith JA, Giglio P, Patel SJ, Ray SK, Banik NL. 2012. Drug resistance in glioblastoma: a mini review. *Neurochemical Research* **37**:1192–1200 DOI 10.1007/s11064-011-0701-1.

Hall EJ, Bedford JS, Oliver R. 1966. Extreme hypoxia its effect on survival of mammalian cells irradiated at high and low dose-rates. *The British Journal of Radiology* **39**:302–307 DOI 10.1259/0007-1285-39-460-302.

Hammoud MA, Sawaya R, Shi WM, Thall PF, Leeds NE. 1996. Prognostic significance of preoperative MRI scans in glioblastoma multiforme. *Journal of Neuro-Oncology* **27**:65–73 DOI 10.1007/BF00146086.

Harrison L, Blackwell K. 2004. Hypoxia and anemia: Factors in decreased sensitivity to radiation therapy and chemotherapy? *The Oncologist* **9**:31–40 DOI 10.1634/theoncologist.9-90005-31.

Heddleston JM, Li Z, McLendon RE, Hjelmeland AB, Rich JN. 2009. The hypoxic microenvironment maintains glioblastoma stem cells and promotes reprogramming towards a cancer stem cell phenotype. *Cell Cycle* **8**:3274–3284 DOI 10.4161/cc.8.20.9701.

Herrmann A, Rice M, Lévy R, Pizer BL, Losty PD, Moss D, Sée V. 2015. Cellular memory of hypoxia elicits neuroblastoma metastasis and enables invasion by non-aggressive neighbouring cells. *Oncogenesis* **4**:e138 DOI 10.1038/oncsis.2014.52.

Kayama T, Yoshimoto T, Fujimoto S, Sakurai Y. 1991. Intratumoral oxygen-pressure in malignant brain-tumor. *Journal of Neurosurgery* **74**:55–59 DOI 10.3171/jns.1991.74.1.0055.

Koch CJ. 2002. Measurement of absolute oxygen levels in cells and tissues using oxygen sensors and 2-nitroimidazole EF5. *Methods in Enzymology* **352**:3–31 DOI 10.1016/S0076-6879(02)52003-6.

Li P, Zhou C, Xu L, Xiao H. 2013. Hypoxia enhances stemness of cancer stem cells in glioblastoma: An *in vitro* study. *International Journal of Medical Sciences* **10**:399–407 DOI 10.7150/ijms.5407.

Meixensberger J, Dings J, Kuhnigk H, Roosen K. 1993. Studies of tissue PO2 in normal and pathological human brain cortex. *Acta Neurochirurgica* **59**:58–63.

Ostrom QT, Gittleman H, Farah P, Ondracek A, Chen Y, Wolinsky Y, Stroup NE, Kruchko C, Barnholtz-Sloan JS. 2013. CBTRUS statistical report: primary brain and central nervous system tumors diagnosed in the United States in 2006–2010. *Neuro-Oncology* **15**:1–56 DOI 10.1093/neuonc/nos333.

Parrinello S, Samper E, Krtolica A, Goldstein J, Melov S, Campisi J. 2003. Oxygen sensitivity severely limits the replicative lifespan of murine fibroblasts. *Nature Cell Biology* **5**:741–747 DOI 10.1038/ncb1024.

Pawlik TM, Keyomarsi K. 2004. Role of cell cycle in mediating sensitivity to radiotherapy. *International Journal of Radiation Oncology* **59**:928–942 DOI 10.1016/j.ijrobp.2004.03.005.

Pistollato F, Abbadi S, Rampazzo E, Persano L, Della Puppa A, Frasson C, Sarto E, Scienza R, D'Avella D, Basso G. 2010. Intratumoral hypoxic gradient drives stem cells distribution and MGMT expression in glioblastoma. *Stem Cells* **28**:851–862.

Rampling R, Cruickshank G, Lewis AD, Fitzsimmons SA, Workman P. 1994. Direct measurement of pO_2 distribution and bioreductive enzymes in human malignant brain tumors. *International Journal of Radiation Oncology* **29**:427–431 DOI 10.1016/0360-3016(94)90432-4.

Reifenberger G, Blümcke I, Pietsch T, Paulus W. 2010. Tonn J-C, Westphal M, Rutka JT, eds. *Oncology of CNS tumours*. 2nd edition. Springer, 12–14.Ch. 1.

Rong Y, Durden DL, Van Meir EG, Brat DJ. 2006. Pseudopalisading' necrosis in glioblastoma: a familiar morphologic feature that links vascular pathology, hypoxia, and angiogenesis. *Journal of Neuropathology and Experimental Neurology* **65**:529–539 DOI 10.1097/00005072-200606000-00001.

Ruan K, Song G, Ouyang G. 2009. Role of hypoxia in the hallmarks of human cancer. *Journal of Cellular Biochemistry* **107**:1053–1062.

Semenza GL. 2010. Defining the role of hypoxia-inducible factor 1 in cancer biology and therapeutics. *Oncogene* **29**:625–634.

Semenza GL. 2003. Targeting HIF-1 for cancer therapy. *Nature Reviews Cancer* **3**:721–732.

Shah MA, Schwartz GK. 2001. Cell cycle-mediated drug resistance: an emerging concept in cancer therapy. *Clinical Cancer Research* **7**:2168–2181.

Soeda A, Park M, Lee D, Mintz A, Androutsellis-Theotokis A, McKay RD, Engh J, Iwama T, Kunisada T, Kassam AB, Pollack IF, Park DM. 2009. Hypoxia promotes expansion of the CD133-positive glioma stem cells through activation of HIF-1 alpha. *Oncogene* **28**:3949–3959 DOI 10.1038/onc.2009.252.

Sondergaard KL, Hilton DA, Penney M, Ollerenshaw M, Demaine AG. 2002. Expression of hypoxia-inducible factor 1 alpha in tumours of patients with glioblastoma. *Neuropathology and Applied Neurobiology* **28**:210–217.

Spence AM, Muzi M, Swanson KR, O'Sullivan F, Rockhill JK, Rajendran JG, Adamsen TCH, Link JM, Swanson PE, Yagle KJ, Rostomily RC, Silbergeld DL, Krohn KA. 2008. Regional hypoxia in glioblastoma multiforme quantified with F-18 fluoromisonidazole positron emission tomography before radiotherapy: correlation with time to progression and survival. *Clinical Cancer Research* **14**:2623–2630 DOI 10.1158/1078-0432.CCR-07-4995.

Tredan O, Galmarini CM, Patel K, Tannock IF. 2007. Drug resistance and the solid tumor microenvironment. *JNCI Journal of the National Cancer Institute* **99**:1441–1454 DOI 10.1093/jnci/djm135.

Vaupel P, Kallinowski F, Okunieff P. 1989. Blood-flow, oxygen and nutrient supply, and metabolic microenvironment of human-tumors: a review. *Cancer Research* **49**:6449–6465.

Whittle IR, Stavrinos N, Akil H, Yau Y, Lewis SC. 2010. Assessment of physiological parameters within glioblastomas in awake patients: A prospective clinical study. *British Journal of Neurosurgery* **24**:447–453.

Zagzag D, Lukyanov Y, Lan L, Ali MA, Esencay M, Mendez O, Yee H, Voura EB, Newcomb EW. 2006. Hypoxia-inducible factor 1 and VEGF upregulate CXCR4

in glioblastoma: implications for angiogenesis and glioma cell invasion. *Laboratory Investigation* **86**:1221–1232 DOI 10.1038/labinvest.3700482.

Zagzag D, Zhong H, Scalzitti JM, Laughner E, Simons JW, Semenza GL. 2000. Expression of hypoxia-inducible factor 1 alpha in brain tumors: association with angiogenesis, invasion, and progression. *Cancer* **88**:2606–2618 DOI 10.1002/1097-0142(20000601)88:11<2606::AID-CNCR25>3.0.CO;2-W.

Zhao T, Zhang CP, Liu ZH, Wu LY, Huang X, Wu HT, Xiong L, Wang X, Wang XM, Zhu LL, Fan M. 2008. Hypoxia-driven proliferation of embryonic neural stem/progenitor cells—role of hypoxia-inducible transcription factor-1 alpha. *FEBS Journal* **275**:1824–1834 DOI 10.1111/j.1742-4658.2008.06340.x.

3.2.1 Supplemental information

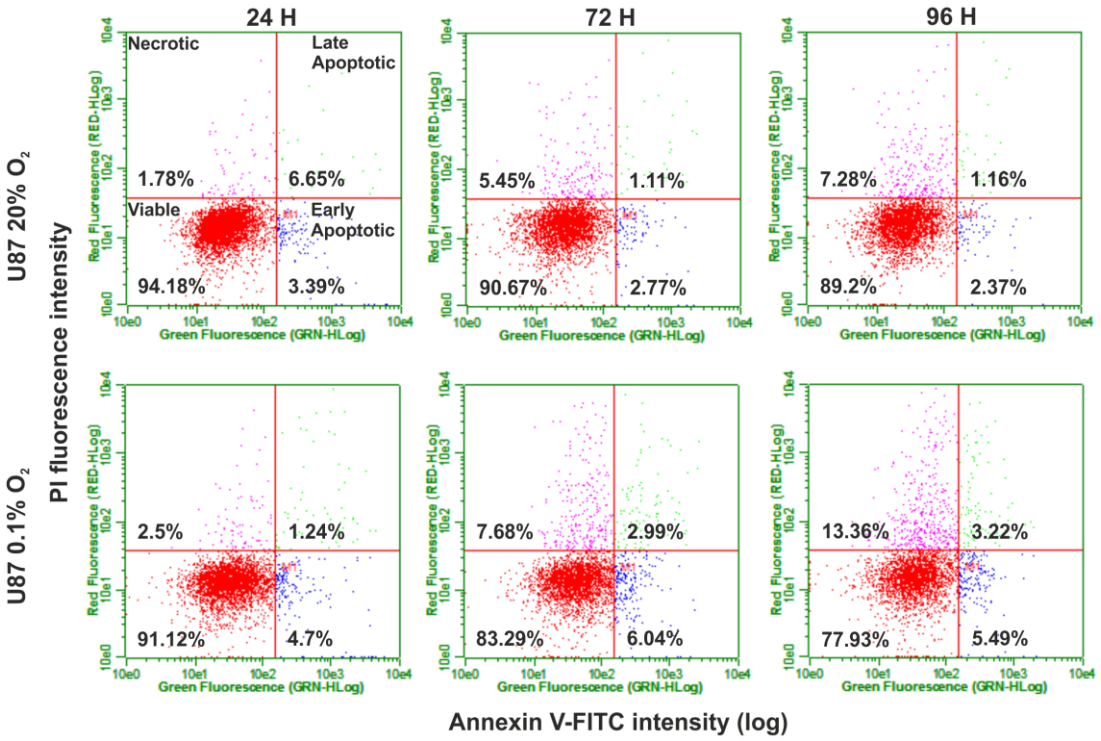

Figure S1. Severe hypoxia causes a reduction in U87 cell viability. U87 cells were exposed to 0.1% and 20% O_2 for the indicated time points. Cell survival was assessed by Annexin/PI staining and flow cytometry.

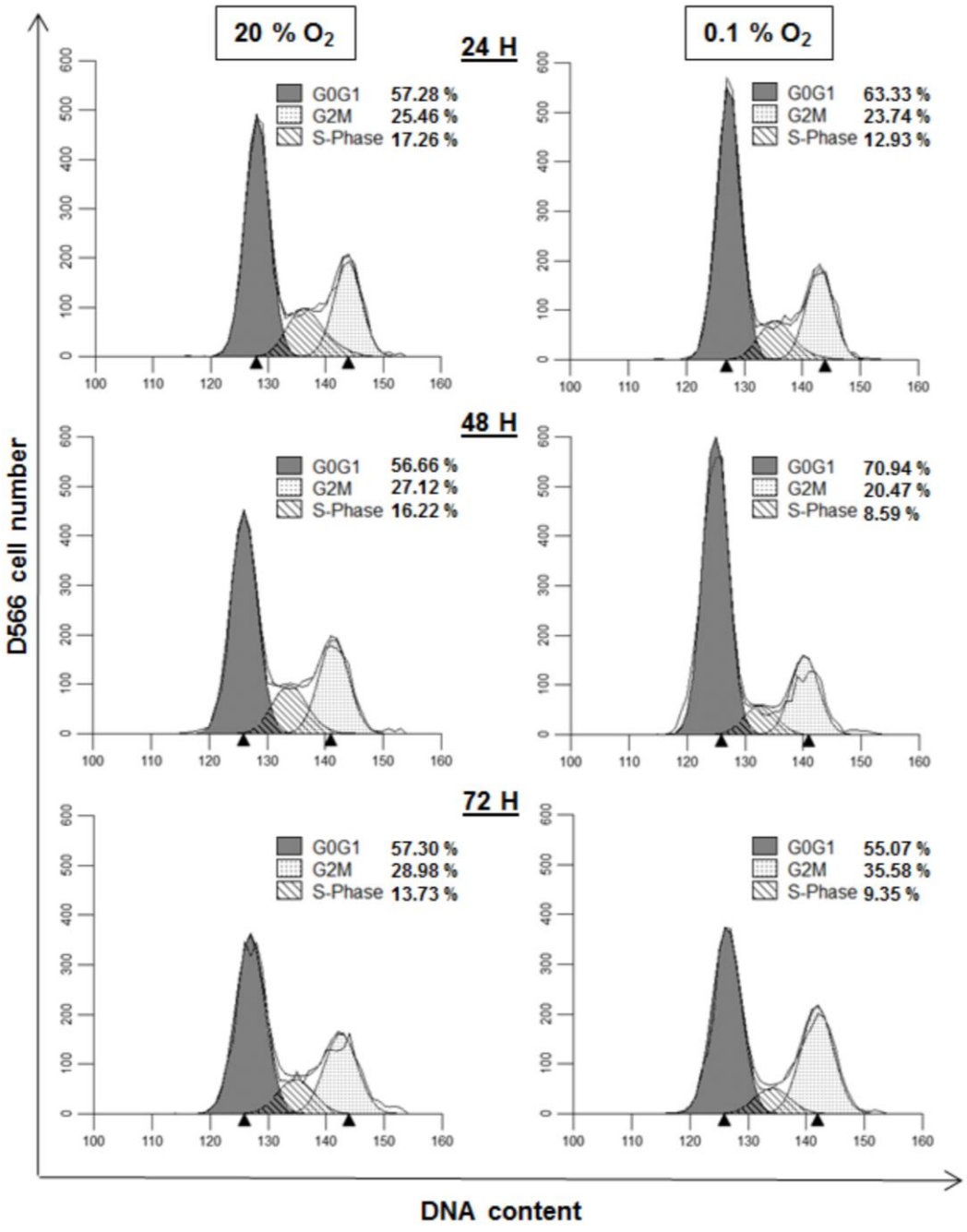

Figure S2. Severe hypoxia causes a transient G_1 phase arrest in D566 cells. Representative histograms of D566 cell cycle following exposure to 0.1% and 20% O_2 for the indicated time points. Cell cycle distribution was analysed using flow cytometry.

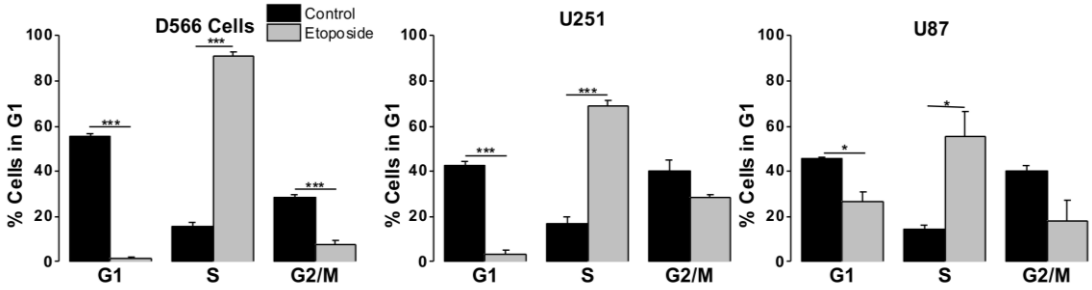

Figure S3. Cell cycle arrest can be induced in GBM cells. Cells were incubated in 20% O_2 and exposed to 10μM etoposide for 24 h. Cell cycle distribution was analysed using flow cytometry.

3.3 Additional results

3.3.1 Live cell imaging of cell cycle length

The results of the previously described flow cytometry experiments indicated that 1% O_2 does not alter cell cycle distribution. However, we wanted to confirm that there was not an overall lengthening of the cell cycle in hypoxia, which would not be detected by flow cytometry. To determine the effect of hypoxia on cell cycle length, we pre-incubated D566 cells in 1% O_2 for 72 h and then imaged them in 1% O_2 over the course of 48 h. We found that cell cycle length was similar between cells incubated in 20% O_2 and cells incubated in 1% O_2 (Fig 3.1). These preliminary results were in line with our previous findings, indicating that cell proliferation is unaffected by 1% O_2. As such, we decided not to carry out any further live cell imaging experiments relating to the relationship between the cell cycle and hypoxia.

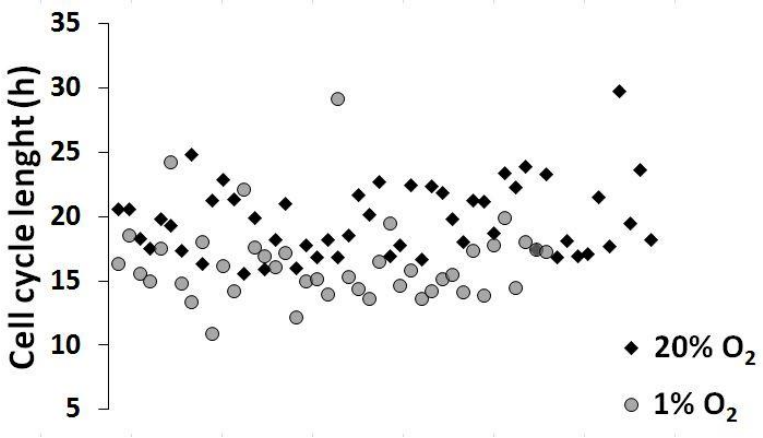

Figure 3.1. Cell cycle length. D566 cells were either incubated and imaged in 20% O_2 (52 cells, *N* = 1; M = 19.71, SD = 2.83), or pre-incubated in 1% O_2 for 72 h prior to imaging in 1% O_2 for 48 h (42 cells, *N* = 1; M = 16.37, SD = 3.20). Cell cycle length was determined by measuring the time that had elapsed between two subsequent cell divisions.

3.3.2 The expression of p53 is not altered by hypoxia

We were interested in whether the cell death observed in U251 and U87 cells after 48 h in 0.1% O_2 was associated with an increase in p53, as p53 is known to regulate both cell cycle progression and cell survival (*28*). P53 protein expression was assessed after 24–72 h exposure to hypoxia. However, neither 1% O_2 nor 0.1% O_2 altered the level of p53 in any of the cell lines tested (Fig 3.2). We next wished to assess whether p53 was active in our cell lines, as both U251 and D566 cells harbour *TP53* mutations (*234*). To assess whether p53 was active, we treated cells with etoposide; a topoisomerase II inhibitor used for the treatment of cancer which causes DNA damage and p53 activation (*235*). We found that only U87 cells responded to etoposide with an increase in p53 protein, confirming that p53 is non-functional in D566 and U251 cells. These results indicate that the response to hypoxia is similar in *TP53* wild type and *TP53* mutated GBM cells, and that the cell death observed in severe, long-term hypoxia is not related to p53 activation.

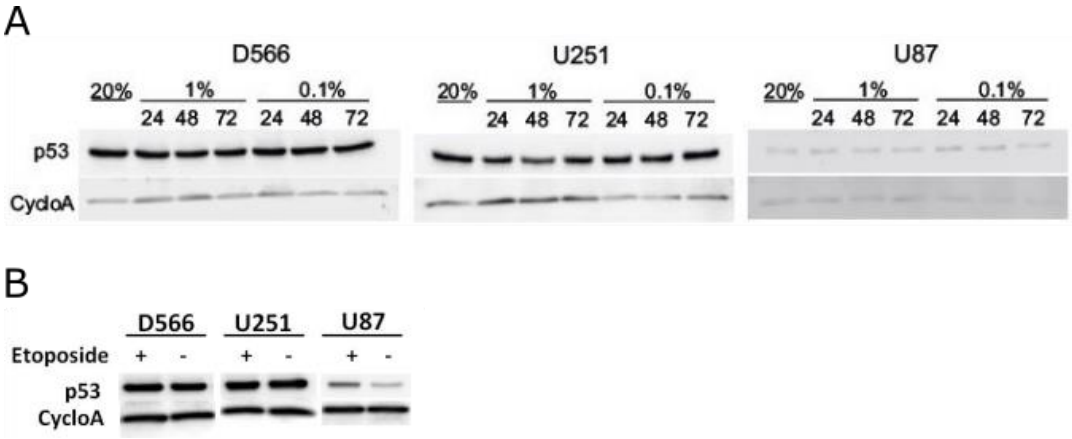

Figure 3.2. Western blots of p53 protein expression. (A). Cells were incubated 20%, 1% and 0.1% O_2 for the indicated time points. Protein expression was measured by western blot. Images are representative examples of three experiments. **(B).** Cells were treated with 20 μM etoposide for 24 h. Images are representative of two (U251 cells) or three (U87 and D566 cells) experiments.

3.3.3 The relationship between PHD proteins and the cell cycle response to hypoxia

We were interested in whether we could alter the cellular response to hypoxia by knocking down PHD2 and PHD3, which regulate the oxygen-dependent degradation of HIF-1α. Previous work by our group has demonstrated the existence of a HIF-PHD negative feedback loop (Fig 3.3). The initial sharp increase in HIF-1α expression under low oxygen conditions is followed by a decrease, caused by the transactivation of PHD2 by HIF-1α. When PHD2 is expression is silenced, the result is a steady accumulation in HIF-1α. In contrast, when PHD3 is silenced, HIF-1α accumulation is unaltered (*232*). Previous research has suggested that PHD3 may promote cell cycle progression in hypoxia, while PHD1 has been shown to regulate progression through mitosis (*236-238*).

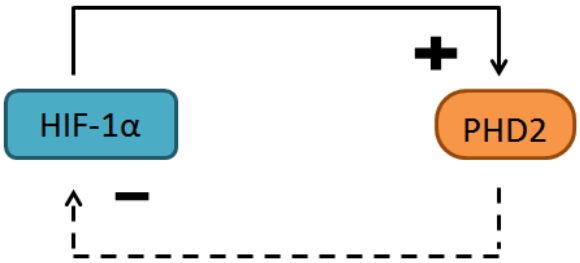

Figure 3.3. HIF-1α–PHD2 negative feedback loop. HIF-1α increases the expression of PHD2, which, under normal oxygen conditions, hydroxylates HIF-1α leading to its degradation.

We examined the effects of low oxygen levels on the cell cycle of wild type (WT) HeLa cells, shPHD2 HeLa cells (a gift from D Hoogewijs, D Stiehl and R Wenger, University of Zürich) and shPHD3 HeLa cells (a gift from Sarah Taylor, University of Liverpool). Firstly, we compared the cell cycle profiles of all three cell lines under normal oxygen conditions. Compared with WT HeLa cells, shPHD2 cells had significantly fewer cells in G_1 phase and more cells in S phase (Fig 3.4A). However, the proliferation rate of the cell lines was similar (Fig 3.4B). We then assessed the effects of 1% and 0.1% O_2 on cell cycle distribution. In WT HeLa cells we saw a non-significant increase in cells

in G_1 phase after 24 h and 48 h in 0.1% O_2, but by 72 h the cell cycle profile had returned to normal (Fig 3 in the PeerJ paper). In shPHD2 HeLa cells, there was a significant reduction in cells in G_1 phase after 24 h in 1% O_2; however, this effect was only transient. In shPHD3 HeLa cells, there was a significant increase in cells in G_1 phase after 24 h and 48 h in 0.1% O_2. However, as with the WT cells, this difference had disappeared by 72 h (Fig 3.4C). While shPHD3 cells are more sensitive to hypoxia, these results indicate that cell cycle response to hypoxia is similar in WT, shPHD2 and shPHD3 HeLa cells.

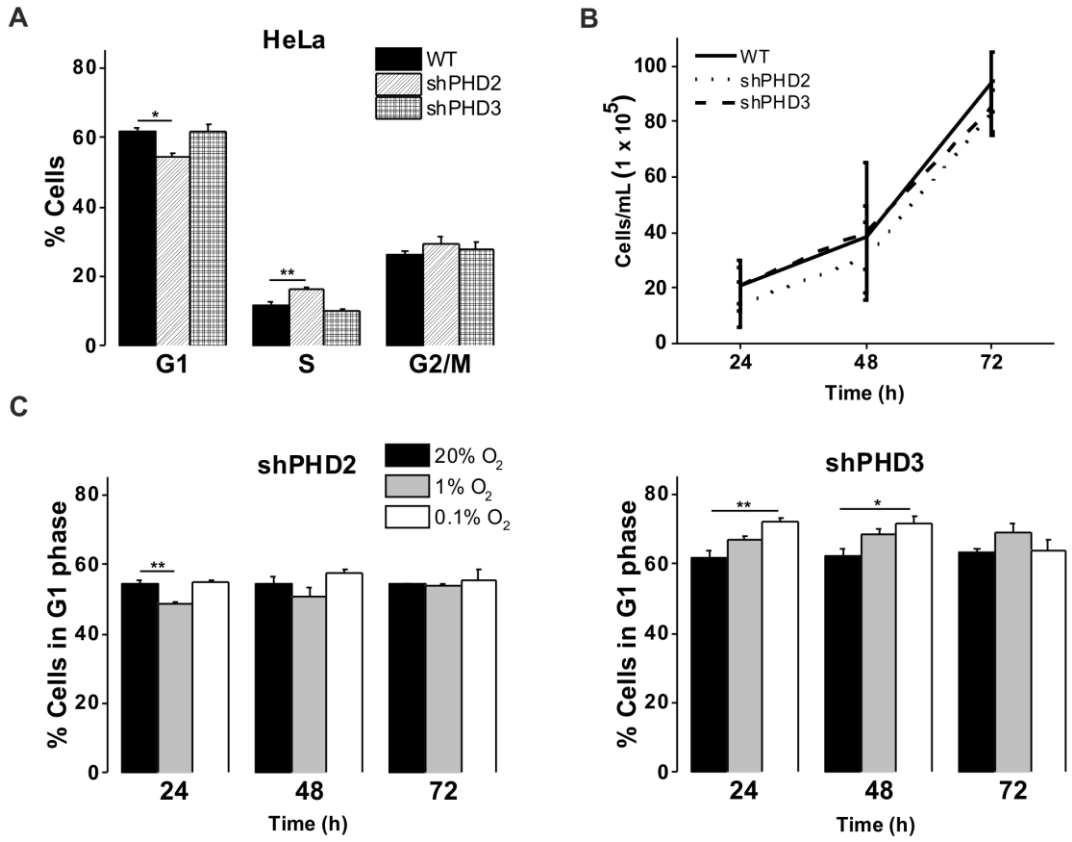

Figure 3.4. PHD3 depletion increases sensitivity to hypoxia. (A) Cell cycle profiles of wild type (WT), shPHD2 and shPHD3 HeLa cells in 20% O_2. Cell cycle profiles were obtained using flow cytometry. **(B)** Cell proliferation in 20% O_2, as measured by cell counting using flow cytometry, did not differ between the three cell lines. **(C).** shPHD2 and shPHD3 cells were incubated in 20%, 1% and 0.1% O_2 for the indicated time points. shPHD3 cells were more sensitive to hypoxia and showed a significant increase in cells in G_1 phase after 24–48 h in 0.1% O_2. Figure shows the mean + SEM of three experiments (A, C) and the mean + SD of two experiments (B). *p < .05, ** p < .01. blot.

3.4 Discussion

We were successful in investigating the effect of different levels of oxygen on cell proliferation in cells cultured as a monolayer. However, our results do not support the hypothesis that physiologically relevant levels of hypoxia cause cell cycle arrest. Even in severe hypoxia, the accumulation of cells in G_1 phase observed in D566 cells was transient and disappeared after 72 h in 0.1% O_2, suggesting that cells can adapt to very low levels of oxygen. In addition, we did not observe any molecular changes associated with cell cycle arrest or cell stress, such as an increase in p21, p27 or p53. We had originally planned to further investigate the relationship between hypoxia and the cell cycle using live cell imaging and mathematical modelling. However, as all of our results indicated that hypoxia does not play a significant role in cell cycle regulation, we decided not to pursue this line of investigation.

We found no increase in p53 in U87 cells, which are *TP53* WT, when cells were exposed to severe hypoxia. Previous research has shown that p53 is stabilised in hypoxia; however, in these studies, cells were exposed to anoxia (<0.02% O_2) (*239, 240*). It is possible that p53 activity is only increased in anoxia, not hypoxia. In line with this hypothesis, Hammond *et al.* reported p53 accumulation at 0.02%, but not 2% O_2 (*241*). However, Pan *et al.* failed to observe p53 accumulation even in 0.02%, unless hypoxia was combined with acidosis or nutrient deprivation (*242*). This picture is further complicated by several reports of hypoxia resulting in the suppression of p53 activity (*243-245*). The relationship between hypoxia and p53 is far from clear, with results varying according to the cell line as well as the severity and duration of hypoxia (for review, see (*246*)).

A factor that further complicates the interpretation of research into hypoxia and cell cycle arrest or cell survival is the practice of serum-starving cells in

order to synchronise them in G_1 phase (*236*). Serum starvation causes stress related morphological and molecular changes, such as cell rounding and an increase in p53 expression and apoptosis, and sensitises tumour cells to DNA-damaging agents (*247, 248*). It is possible that serum starvation has unintended effects when used in combination with an additional stressor such as hypoxia. Therefore, the results of such experiments should be interpreted with caution.

In line with previous research, we found that PHD3 depletion increased sensitivity to hypoxia and caused an accumulation of cells in G_1 phase. Hoegel *et al.* have shown that PHD3 enhances the G_1 to S transition of hypoxic carcinoma cells by decreasing the stability of p27 (*237*). The transient G_1 phase arrest observed in shPHD3 cells mirrored the response of D566 cells incubated in severe hypoxia. We saw no change in p27 mRNA expression in D566 cells; however, we did not examine p27 protein expression. Hoegel *et al.* reported that PHD3 stabilises p27 post-translationally by decreasing the phosphorylation of the protein at serine 10. Therefore, it is possible that changes in p27 protein expression may cause the transient cell cycle arrest observed in D566 cells.

In summary, we have performed a systematic investigation into the effects of low oxygen levels on cell proliferation and survival, the results of which have lead us to conclude that pathophysiological levels of hypoxia (0.1–1% O_2) do not cause cell cycle arrest. The level of oxygen and duration of exposure are important determinants of the cellular response to hypoxia; however, GBM cells are able to proliferate and survive even in severe hypoxia.

Chapter 4:
Characterisation of a glioblastoma multicellular tumour spheroid model

4.1 Introduction

In the last chapter, we established the effects of different oxygen levels on the proliferation and survival of cells cultured as a monolayer. We recognised that this is a poor representation of the solid tumour microenvironment and, having characterised the effects of hypoxia on GBM cells using a simplified system, sought to increase the complexity of the model by culturing cells as multicellular tumour spheroids. Spheroids share important characteristics with solid tumours, such as gradients in oxygen and nutrients (see Chapter 1, section 1.8.1), which made them our preferred model for all further investigations. Several methods can be used to generate spheroids. One approach is to coat tissue culture dishes with substrates that cells struggle to adhere to, such as agar. Another approach is to keep cells in suspension using spinner flasks or rotary cell culture systems. The hanging drop method involves seeding cells in a droplet of media that is suspended in air. Gravity causes the cells to aggregate and, over the course of several days, form a compact spheroid. The main advantages of the hanging drop technique over other methods is that spheroids can be generated quickly and their size and age can be precisely controlled (*249*). This makes the production of homogeneous spheroids possible and allows for more reproducible results.

We wished to characterise GBM spheroids in terms of cell proliferation, survival and indicators of oxygenation and cellular energetics. We anticipated that spheroids would show spatial heterogeneity in these characteristics. Cell proliferation is typically concentrated around the periphery of spheroids, while the cores of spheroids are often necrotic. As the diffusion limit of O_2 in tissue is thought to be 150 μm, we anticipated that spheroids would display a hypoxic core (*70, 71*). We further hypothesised that spheroids would show spatial heterogeneity in markers of cellular energetics, with energy production decreasing as a function of distance from the spheroid periphery. We aimed to investigate cellular energetics in live

spheroids using Perceval High Range (PercevalHR), a fluorescent biosensor that senses ATP:ADP ratio. Perceval was constructed by integrating a circularly permuted monomeric version of the GFP derivative Venus (cpmVenus) into a bacterial regulatory protein (GlnK1) that undergoes a conformational change upon ATP binding. ATP binding alters the excitation spectrum of the construct such that excitation is increased at 490 nm and decreased at 405 nm while ADP binding has the opposite effect. Competition for the binding site means that the fluorescent response depends on the ATP:ADP ratio, allowing the protein to act as a ratiometric sensor (*259*). However, the original sensor saturated at low ATP:ADP ratios (<5:1), which limited its usefulness in mammalian cells. In 2013, Tantama *et al.* reported the development of an optimised version of the sensor, PercevalHR, which senses a greater range of ATP:ADP ratios (0.4–40:1) (*260*).

We also chose to examine the expression of glucose transporter 1 (GLUT1), monocarboxylate transporter-4 (MCT4) and carbonic anhydrase-IX (CAIX) because the expression of these proteins is closely associated with both hypoxia and cellular metabolism**.** GLUT-1 facilitates the transport of glucose across the plasma membrane, while MCT4 exports lactate from glycolytically active cells. The expression of both of these proteins increases in hypoxia in a HIF-1 dependent manner; GLUT-1 expression is also increased by glucose deprivation (*250-254*). CAIX catalyses the hydration of CO_2 into protons and bicarbonate ions, which is thought to facilitate CO_2 excretion. This helps to maintain an alkaline intracellular pH and contributes to maintaining cell survival in the acidic solid tumour microenvironment (*213, 258*). CAIX expression is induced by HIF-1 and the close associated between CAIX and hypoxia has led to it being considered an endogenous marker for hypoxia (*255-257*). We anticipated that the expression of GLUT1, MCT4 and CAIX would be spatially regulated in a manner corresponding to the availability of oxygen and nutrients.

Our aims for this chapter were as follows:

1. To optimise the culture of GBM spheroids.
2. To characterise spheroids in terms of cell proliferation, survival, oxygenation and energetic status.
3. To assess the effects of hypoxia (1% O_2) on the above characteristics.

4.2 Results

4.2.1 Optimisation of spheroid generation

We found that cell culture media contains many small particulates that interfere with spheroid formation (Fig 4.1B). To overcome this problem, we used filtered media when making spheroids. Spheroids were generated by pipetting 50 µl of U87 cell suspension into 96-well hanging drop plates (Fig 4.1A). After three days, when the cells had aggregated and formed a compact spheroid, spheroids were transferred to 35 mm suspension culture dishes. If left in the hanging drop plate, there is a risk of the droplets evaporating or falling off. We aimed to produce spheroids of 400– 500 µm because previous research has suggested that spheroids of this size will experience gradients in nutrients and oxygen (*261, 262*). We found that an initial quantity of 1200 cells per 50 µl droplet produced spheroids of the desired size seven days after seeding (Fig 4.1C, Fig 4.1D).

4.2.2 Choice of method for characterising spheroids

We had hoped to be able to characterise whole spheroids using immunofluorescence followed by lightsheet microscopy. However, we found that nuclear stains and antibodies showed poor penetration under these conditions and, at best, labelled only the outer half of spheroids (Fig 4.2). We also found that the image resolution in the centre of spheroids was poor as the effects of light scattering are increased when imaging at depth, limiting the penetration of light and causing a reduction in resolution and contrast (*263*). Tissue clearing methods can be used to make large samples more permeable and optically transparent (*264, 265*). Following a protocol described by Wenzel, we tried dehydrating spheroids in an ascending ethanol serious (50%, 70%, 85% and 99% ethanol for 5 min each) before clearing them in a 1:1 (v/v) mix of benzyl alcohol/benzyl benzoate (BABB)

(*226*). However, we found that this method was too harsh and caused spheroids to disintegrate. Furthermore, BABB is known to drastically reduce the fluorescence of fluorophores (*265, 266*)**.**

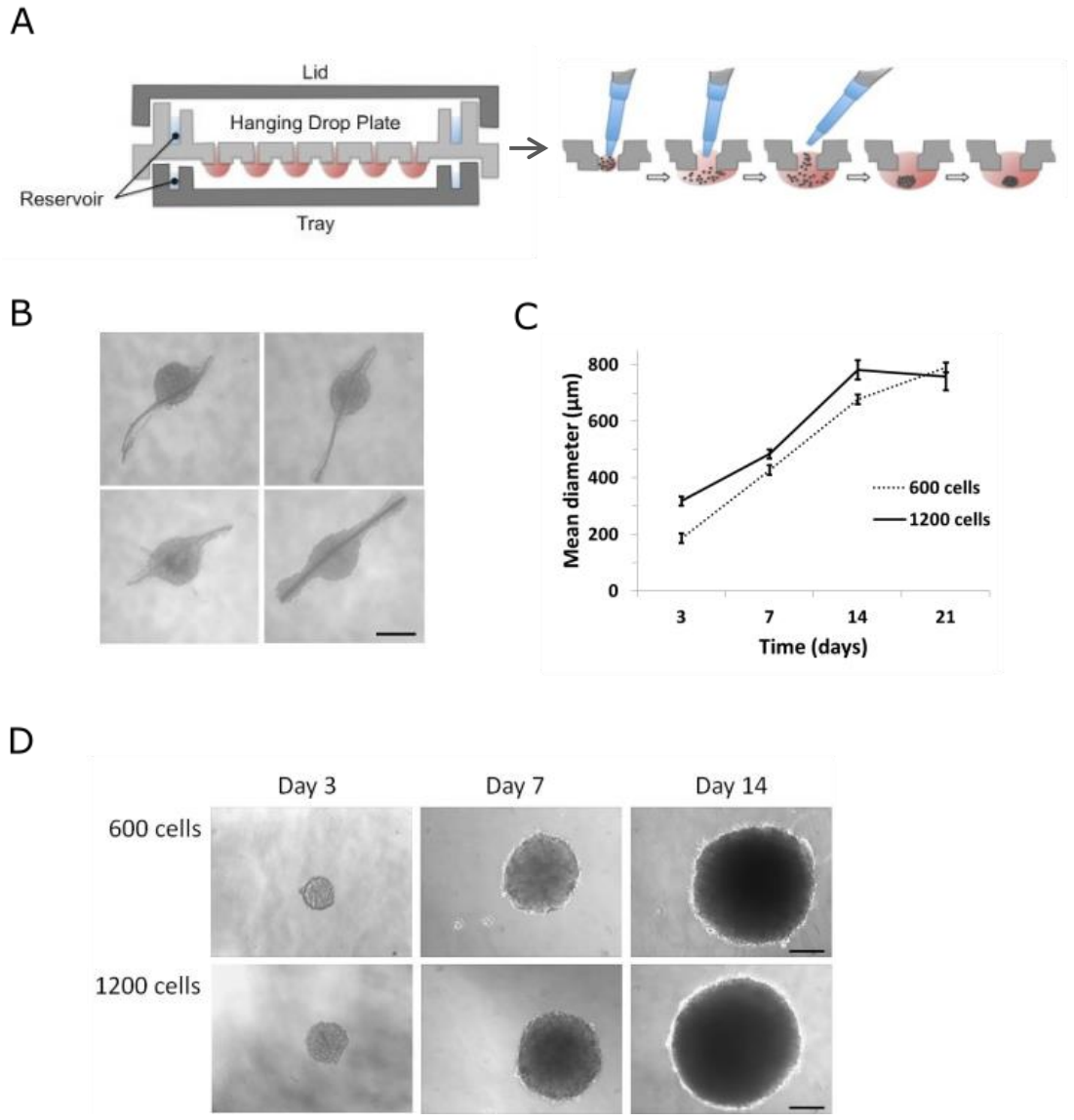

Figure 4.1. Spheroid formation and growth. (A). Cell suspension was pipetted into a 96-well hanging drop plate. The wells are surrounded by a reservoir containing PBS to prevent the evaporation of the hanging drops. At first, cells form a loose aggregate but after three days they form compact spheroids. Adapted from www.3dbiomatrix.com**. (B).** Unfiltered cell culture media contains particulates which cells adhere to. **(C).** Spheroid diameter (average of three measurements per spheroid) at the specified time points was quantified using ImageJ. Figure shows the M + SD of three spheroids (*N* = 1). **(D).** Images of spheroids generated using 600 or 1200 cells at three, seven and 14 days after seeding, Scale bar is 200 µm.

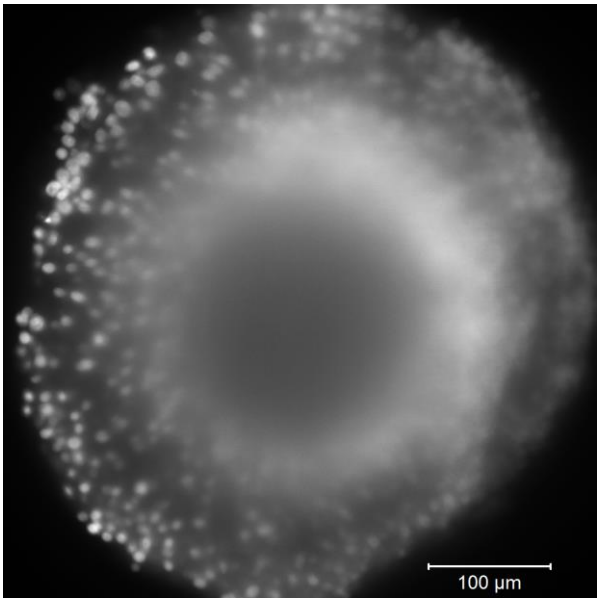

Figure 4.2. Poor penetration of Hoechst in intact spheroids. Whole spheroids were fixed in 4% PFA for 45 min at RT, permeablised as described in Chapter 2, section 2.8.3, then stained with Hoechst 33342 (1:1000) for 45 min. Spheroids were embedded in 1% low-melt agarose and imaged using a 20x objective on a Lightsheet Z.1 (Zeiss) microscope. Fluorescence was excited with a 405 nm laser and emitted light detected using a 490 nm shortpass filter.

There are other clearing methods which are better at preserving fluorescence and may be better tolerated by spheroids, such as CLARITY (*267*). However, these processes can be lengthy and many of the steps require optimisation. We were also concerned about being able to determine whether any changes observed in fluorescence reflected changes in protein expression, or were an artefact of limited solvent or antibody penetration. Although the aim of the current chapter was to develop and characterise a GBM spheroid model, our ultimate aim was to carry out live cell imaging of spheroids. Therefore, we decided not to optimise the imaging of whole immunostained spheroids any further and to overcome the antibody penetration problem by sectioning spheroids before performing immunofluorescence.

4.2.3 Proliferation gradients in spheroids

We characterised the proliferation of cells in spheroids using 5-ethynyl-2´-deoxyuridine (EdU), a thymidine analogue that incorporates into cellular DNA during DNA replication. A terminal alkyne group replaces the methyl group in the 5 position, allowing EdU to be detected by a copper-catalysed reaction between the alkyne group and a fluorescent azide (click chemistry) (*268-270*). The small size of the dye means that, unlike 5-bromo-2´-deoxyuridine staining, DNA does not need to be denatured in order for EdU to be detected (*268*). We found that one-week-old spheroids grown in 20% O_2 showed a proliferation gradient, with the majority of proliferating cells concentrated within 100 μm of the spheroid periphery. The interior of these spheroids contained a mixture of proliferating and quiescent cells (Fig 4.3A). Interestingly, when spheroids were incubated in 1% O_2 for 24 h, proliferating cells were only observed within 100 μm of the spheroid periphery (Fig 4.3A; Fig 4.3B). In two-week-old spheroids grown in 20% O_2, we saw a similar pattern of proliferation to the hypoxic spheroids, with proliferating cells concentrated in a narrow band around the spheroid periphery (Fig 4.3A). This shows that proliferation is affected by the 3D multicellular spheroid environment and, in spheroids, is reduced under conditions of low oxygen.

4.2.4 Spheroid oxygenation status

We characterised the oxygen status of spheroids using pimonidazole hydrochloride (PIMO), a 2-nitroimidazole that is reduced in hypoxic cells. This leads to the formation of stable adducts with thiol groups that can be detected using an antibody. The binding of a similar compound, misonidazole, increases steeply at 10mm Hg (equivalent to 1.3% O_2) and PIMO has been shown to have similar kinetics (*271, 272*). We found an inconsistent pattern of PIMO staining in one-week-old spheroids grown in 20% O_2. A number of spheroids showed small areas of staining in a pattern

clearly indicative of a hypoxic core. However, some spheroids had no PIMO staining at all and, paradoxically, some showed an increase in staining around the periphery. PIMO staining was evident throughout spheroids that had been incubated in 1% O_2 for 24 h, with a slight increase towards the periphery (Fig 4.4A; Fig 4.4B). We were interested in whether hypoxia would affect cell survival in spheroids and so used PI staining to detect the presence of dead cells. One-week-old spheroids grown in 20% O_2 appeared healthy with few PI positive cells; in contrast, spheroids that had been exposed to hypoxia showed had a number of PI-positive cells near their core.

Two-week-old spheroids grown in 20% O_2 showed a donut-like pattern of PI and PIMO staining, with viable, non-hypoxic cells concentrated in the outer 100 μm of spheroids (Fig 4.4C). These spheroids displayed considerable cellular heterogeneity, consisting of proliferating, quiescent, and necrotic cells with varying levels of oxygenation. These results suggest that the one-week-old spheroids are not large enough to develop the hypoxic core that is present in the larger two-week-old spheroids. Furthermore, in the spheroid model, hypoxia appears to reduce cell viability. While the two-week-old spheroids are a good model for tumour tissue in terms of heterogeneity, the large necrotic core means that the viable cell population is relatively small. As we aimed to compare cellular energetics and motility in the core of spheroids with the periphery, it was important that the majority of cells in spheroids were viable. We therefore chose to continue our investigations using the one-week-old spheroids, which contain a larger population of viable cells.

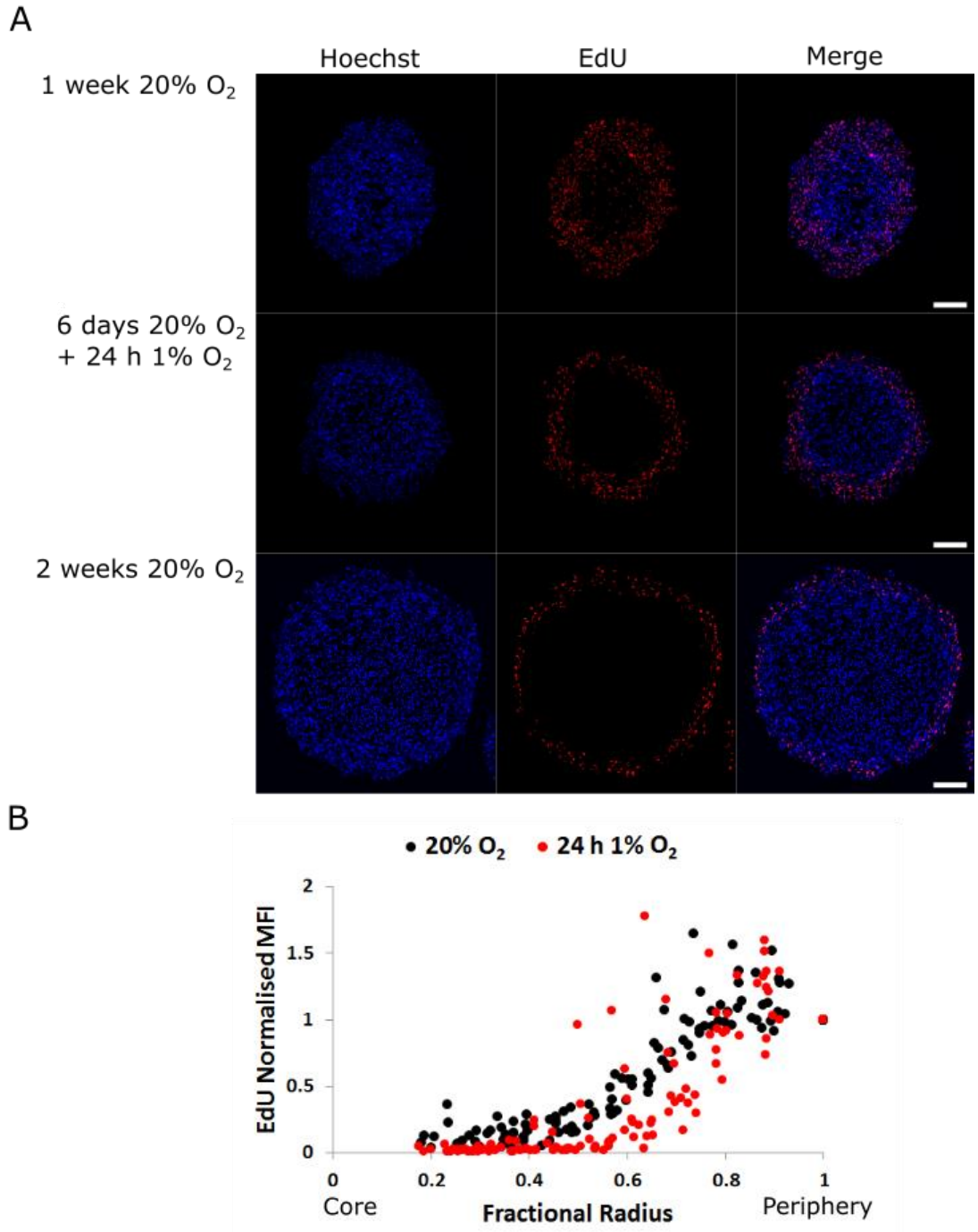

Figure 4.3. Proliferation gradients in spheroids. (A). Representative images of EdU staining in fixed and sectioned spheroids. **(B).** Immunofluorescence was quantified by spatial intensity analysis, as described in Chapter 2, section 2.8.6. The profiles of 12 spheroids incubated in 20% O_2 and 13 spheroids incubated in 1% O_2 (N = 2) are illustrated. The graph shows the normalised mean fluorescence intensity (MFI) plotted against the fractional radius of the spheroid. Scale bar is 100 μm.

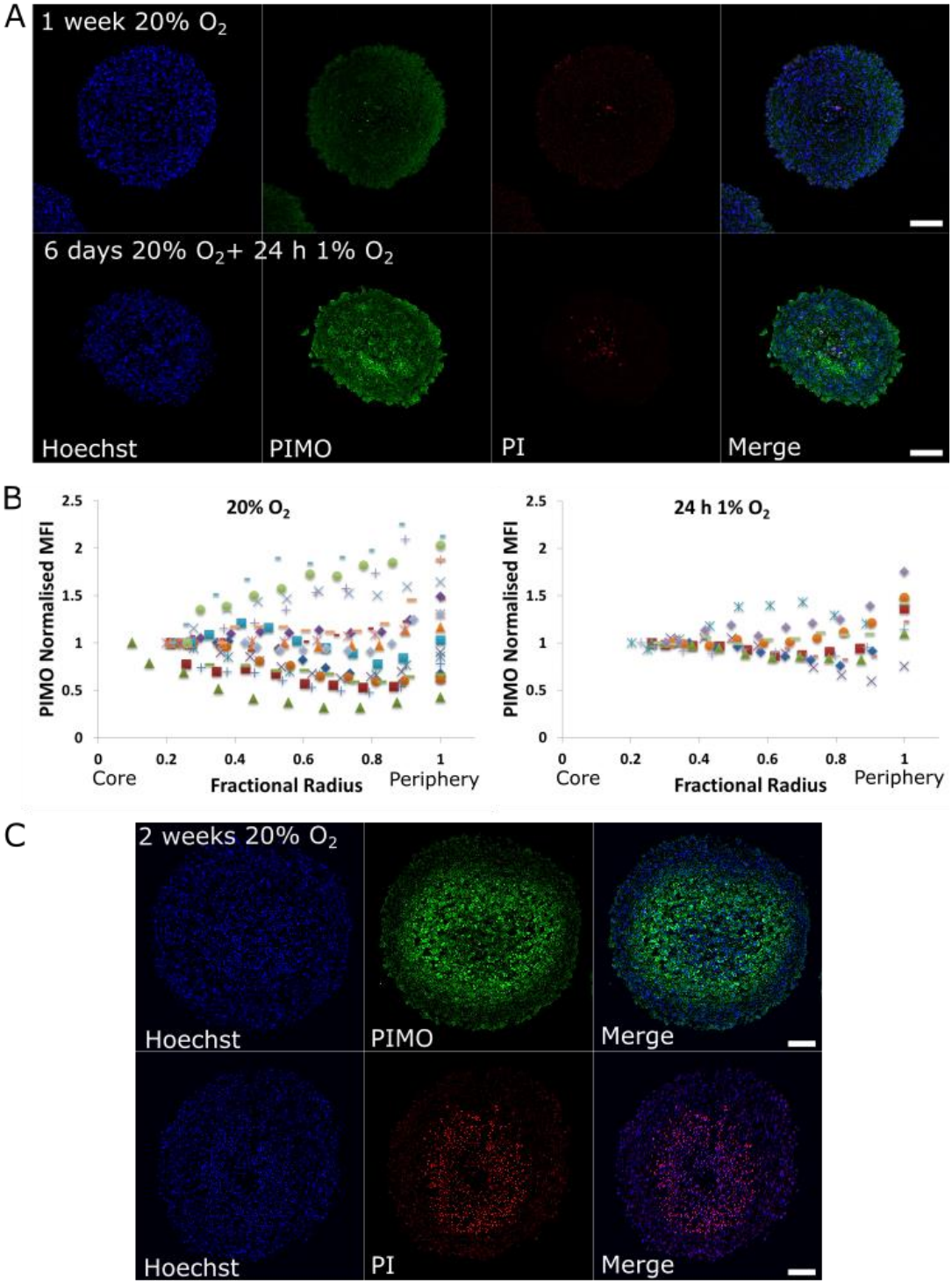

Figure 4.4. Spheroid oxygenation and viability. (A). Representative images of PIMO and PI staining in one-week-old spheroids. **(B).** Immunofluorescence was quantified by spatial intensity analysis. The profiles of 19 spheroids incubated in 20% O_2 (N = 3) and ten spheroids incubated in 1% O_2 (N = 2) are illustrated; each symbol corresponds to the profile of an individual spheroid. The graph shows the normalised mean fluorescence intensity (MFI) plotted against the fractional radius of the spheroid. **(C).** Representative images of PIMO and PI staining in two-week-old spheroids (N = 1). Scale bar is 100 μm.

4.2.5 GLUT-1, MCT4 and CAIX expression in spheroids

We anticipated that the expression of GLUT-1, MCT4 and CAIX might be spatially regulated. We found that GLUT-1 (Fig 4.5A; Fig 4.5C) and CAIX (Fig 4.6B) both showed a homogeneous distribution in one-week-old spheroids cultured in 20% or 1% O_2. MCT4 expression was also generally homogenous, with a slight increase in expression in the peripheral layer of spheroids cultured under both oxygen conditions (Fig 4.5B; Fig 4.5C). We had expected to see an increase in the expression of these proteins in spheroids incubated in hypoxia; however, little difference was observed.

4.2.6 Ratiometric imaging of spheroid energetics

We hypothesised that energy production in spheroids may decrease as a function of distance from the spheroid periphery. To investigate whether cellular energetics are spatially regulated in spheroids, we generated a U87 cell line stably expressing PercevalHR using lentiviral transduction. As PercevalHR is sensitive to changes in pH, it is necessary to monitor and adjust for pH, especially in spheroids where intracellular pH may vary (*260, 273*). We hoped to monitor changes in intracellular pH using Carboxy SNARF-4F 5-(and-6) AM acetate (SNARF), a fluorescent dye that undergoes a pH-dependent wavelength shift. To determine absolute pH values and calibrate the PercevalHR signal, the SNARF signal needs to be calibrated by incubating cells with solutions of varying pH in the presence of the ionophore nigericin. We attempted to carry out the calibration procedure in cells cultured as a monolayer; however, we found that cells would detach almost immediately when incubated in the requisite solutions. This meant that we were unable to perform the calibration and, therefore, unable to exclude the effects of pH from any changes observed in the PercevalHR signal.

Our preliminary experiments indicated that there was little change in the PercevalHR signal throughout one-week-old spheroids grown in 20% O_2. In spheroids exposed to 1% O_2, there was an overall loss of signal at the centre of the spheroid (Fig 4.6B). This loss of signal occurs in the region in which we have seen PI staining, and may therefore be caused by necrosis. However, we did not observe a loss of signal in the core of the two-week-old spheroids, which we know to be necrotic, although there was a change in the ratiometric signal. Further experiments are necessary to determine the cause of the loss of signal in hypoxic spheroids and to confirm whether changes in the ATP:ADP ratio occur in the viable regions of spheroids. However, as we were unsuccessful in correcting for changes in intracellular pH we did not carry out any further investigations using the PercevalHR sensor.

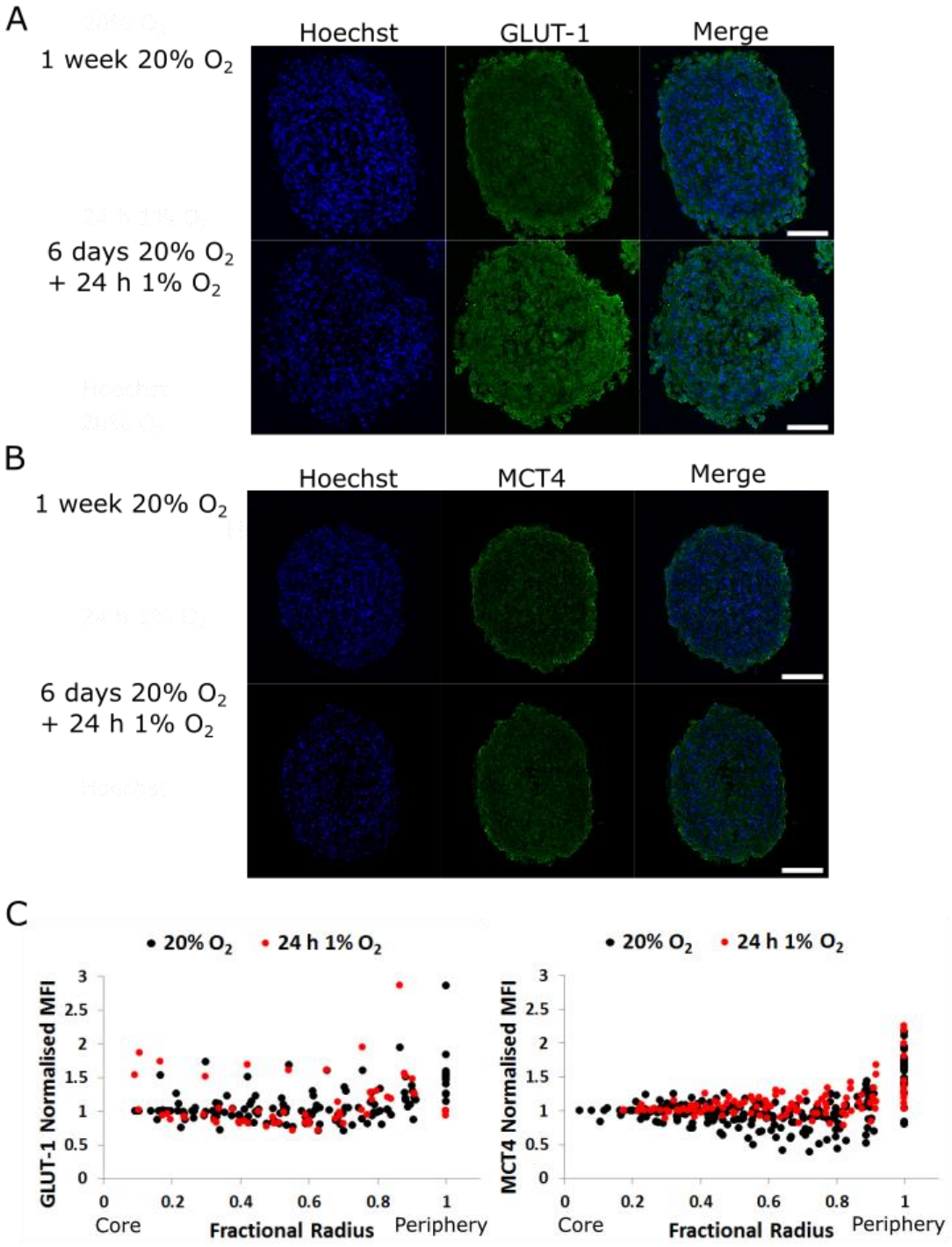

Figure 4.5. GLUT-1 and MCT4 expression in spheroids. (A) GLUT-1 expression and **(B)** MCT4 expression in one-week-old spheroids. **(C).** Immunofluorescence was quantified by spatial intensity analysis. For GLUT-1, the profiles of 23 spheroids incubated in 20% O_2 (N = 3) and 11 spheroids incubated in 1% O_2 (N = 2) are illustrated. For MCT4, the profiles of ten spheroids incubated in 20% O_2 (N = 2) and four spheroids incubated in 20% O_2 (N = 1) are shown. The graph shows the normalised mean fluorescence intensity (MFI) plotted against the fractional radius of the spheroid. Scale bar is 100 μm.

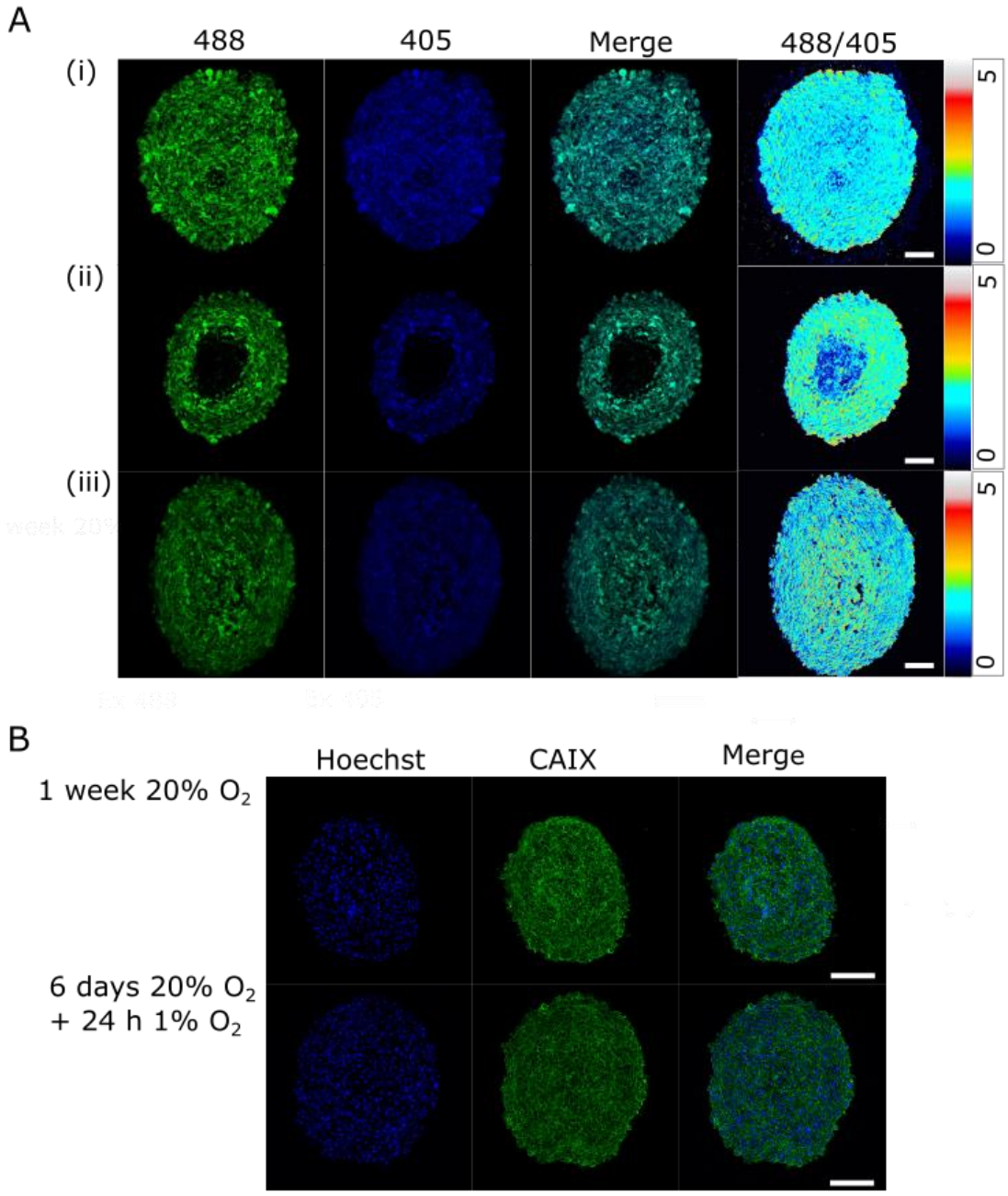

Figure 4.6. PercevalHR and CAIX expression in spheroids. (A). Representative images of U87-PercevalHR spheroids imaged after (i) one week in 20% O_2, (ii) six days in 20% O_2 plus 24 h in 1% O_2 , or (iii) two weeks in 20% O_2 (N = 1). Image shows fluorescence emitted when samples were excited with a 488 nm or 405 nm laser. Emitted fluorescence was collected using a 499-552 nm bandpass filter. Emitted light when excited at 488 nm was divided by the emitted light when excited at 405 nm to produce a ratiometric image. **(B).** Representative images of CAIX expression in one-week-old spheroids (N = 2). Scale bar is 100 μm.

4.3 Discussion

We have optimised the production of GBM spheroids that are ~ 450 μm in diameter after a week in culture and characterised these spheroids in terms of their proliferation, oxygenation and viability under different conditions. The increased quiescence of cells towards the core of spheroids is often presumed to be a result of hypoxia. For example, Laurent *et al.* (*216*) found that actively proliferating cells were localised to the outer 150 μm of spheroids and attributed this phenomenon to a reduction in the supply of oxygen and other nutrients. While some of our one-week-old spheroids did display small regions of hypoxia at their core, this pattern was not consistent enough to explain the proliferation gradient, which itself was very consistent. However, we did see fewer proliferating cells when spheroids were incubated in 1% O_2 for 24 h. In monolayer cultures, we have shown that the proliferation of U87 cells is unaffected by 0.1–1% O_2. Therefore, it is unlikely that hypoxia alone is causing cellular quiescence in spheroids, but it may act as a contributing factor in combination with the added stresses of the 3D spheroid environment. It has previously been shown that EMT6/Ro mouse mammary tumour cells proliferate when exposed to low pH (pH 6.6) or low oxygen (0.8% O_2), but when the two are combined they cease to proliferate (*274*). Similarly, a combination of low oxygen and low glucose results in reduced spheroid volume (*275*). A potential molecular mechanism for the sensing of these microenvironmental changes is p53. Pan *et al.* found that p53 was not induced by hypoxia alone, but responded to the nutrient-deprived and acidic hypoxic microenvironment (*242*).

We found that GLUT-1 was expressed throughout spheroids, with no evidence of a gradient in expression in either oxygen condition. It is unlikely that there were steep gradients in glucose concentrations in our spheroids as uniform glucose distributions have previously been found in spheroids of up to 600 μm in diameter. In larger spheroids, central glucose concentrations

have been found to decline as a function of spheroid size. However, even in spheroids of up to 1600 μm, central glucose concentrations do not fall below 3 μmol/g, which is a concentration sufficient for maintaining cell growth in monolayer cultures (*214*). We found that MCT4 was also expressed throughout spheroids cultured under both oxygen conditions, with a slight increase in expression towards the spheroid periphery. Walenta *et al.* have shown that oncogene-transfected rat embryonic fibroblast spheroids have steep lactate gradients, with very low levels in the outermost layer of cells compared to the rest of the spheroid, and very high levels in the core (*214*). The observed increase in MCT4 expression suggests that the low level of lactate observed at the periphery of spheroids may not just be due to proximity to the spheroid:media interface and enhanced diffusion, but a consequence of the increased extrusion of lactate by MCT4.

As with GLUT-1, we found that CAIX was expressed homogeneously throughout spheroids in both oxygen conditions. CAIX is known to play an important role in the spatial regulation of pH in spheroids. Swietach *et al.* have shown that when CAIX is expressed the intracellular pH gradient in spheroids is reduced; however, the extracellular pH gradient is increased. This effect was evident in spheroids as small as 200 μm (*213, 273*). The strong uniform expression of CAIX in our spheroids may contribute to the maintenance of a more uniform intracellular pH, supporting the viability of cells in the core of the spheroid. We were expecting to see an increase in the expression of CAIX, GLUT-1 and MCT4 in spheroids exposed to hypoxia; however, little to no difference was observed. The relatively high level of expression of these proteins in spheroids under normal oxygen conditions may explain why we did not see any changes in hypoxia. Gliomas are known to be highly glycolytic and overexpress both MCT4 and CAIX, while GLUT-1 expression has been shown to increase significantly in spheroid cultures compared to monolayers (*152, 215, 276-278*). Furthermore, although hypoxia is the most well-known inducer of CAIX, its expression in tumours does not

overlap completely with regions of hypoxia (*257, 278*). CAIX is also regulated by the signalling of proteins known to be dysregulated in GBM, such as EGFR and PI3K, and its expression is increased in dense cultures in a HIF-1α independent manner (*279, 280*).

As the diffusion limit of O_2 in tissue is ~150 μm, we anticipated that spheroids >300 μm would display a hypoxic core (*70, 71*). However, only some of the one-week-old spheroids showed evidence of a hypoxic core and many showed no evidence of hypoxia at all. The variation in oxygenation may be due to variations in spheroid size. Previous reports of the levels of oxygen in the core of spheroids of 400–500 μm, made using microelectrodes, range from 0–8% O_2 (*211, 281*). The level of oxygen in spheroids has also been shown to vary between cell lines as tissue oxygenation is dependent on the comsumption of oxygen as well as the supply (*211, 214*). EMT6/Ro spheroids have been shown to reduce their oxygen consumption as their size increases, reflecting the ability of cells to adapt their metabolic rate to suit their environment (*210*). We have confirmed that the age and size of spheroids are critical; while one-week-old spheroids were healthy with occasional small areas of hypoxia, two-week-old spheroids had large regions of hypoxia and necrosis. It is not clear why PIMO staining was observed at a depth of 100 μm from the spheroid surface in the two-week-old spheroids but not the one-week-old spheroids. One possibility is that these differences reflect changes in oxygen consumption in larger spheroids. We also found the proliferation gradient to be much sharper in two-week-old spheroids. This effect is unlikely to be solely due to gradients in oxygen and nutrients; if this were the case we would expect to see a similar pattern in the one-week-old spheroids. It is possible that older spheroids experience higher concentrations of factors that inhibit growth, such as waste products (*282, 283*).

We saw little PI staining in the one-week-old normoxic spheroids, increased staining in the core of hypoxic spheroids and substantial PI staining in two-week-old spheroids. This is in line with previous investigations, which have found the viable rim in large spheroids to be 100–250 μm in diameter (*214, 284*). It is unlikely that hypoxia alone causes substantial cell death as we have shown that U87 cells can tolerate oxygen concentrations as low as 0.1% O_2 for up to 48 h before viability is affected. However, as with quiescence, hypoxia is likely to be an aggravating factor. Walenta *et al.* found that necrosis in spheroids was preceded by the emergence of anoxia in the core of spheroids followed by a decrease in central ATP, while Monz *et al.* also pinpointed anoxia as the cause of necrosis (*214, 283*). Low levels of oxygen and high levels of lactate, or low levels of both oxygen and glucose, have been shown to have combinatorial effects on the thickness of the viable rim (*275, 283*). Therefore, it is likely that cells are less able to cope with a low oxygen environment when there is a limited supply of glucose and a build-up of lactate. However, necrosis has been shown to emerge despite sufficient oxygen and glucose supply (*210, 211, 285*). Bertuzzi *et al.* carried out mathematical modelling to determine the cause of necrotic core formation. They argued that an insufficient ATP production rate is the underlying cause, as a deficit in ATP predicts the emergence of necrosis much better than either oxygen or glucose alone (*284*).

We were not able to quantify changes in ATP levels using PercevalHR as we were unsuccessful in correcting for pH. However, from our preliminary experiments, changes in the ratiometric signal were only evident in areas that were likely to have been necrotic. Previous research has indicated a steady decline in central ATP with increasing spheroid size prior to the onset of necrosis (*214*). It is possible that more subtle changes in ATP were not detected by PercevalHR because of its limited range. The ratio of total ATP:ADP in mammalian brains is around 10:1; however, the ratio of free ATP:ADP, which is measured by Perceval, is estimated to be nearer to 150:1

due to the increased sequestration of ADP by cellular proteins compared to ATP (*129*). While PercevalHR's range is improved compared to the original sensor, it can only sense ATP:ADP ratios between 0.4 and 40:1 and may not detect less extreme changes. An alternative option would be to use the ATeam indicators, fluorescence resonance energy transfer (FRET)-based indicators which act as a direct measure of ATP level. The sensors are unaffected by pH changes between pH 7.1 and 8.5; however, they are significantly affected by pH values lower than this (*286*). As intracellular pH has been shown to drop from 7.2 at the periphery of spheroids to as low as 6.2 in the core, these sensors would require pH correction to be suitable for use in spheroids (*213*).

In summary, we have successfully determined the starting cell number and culture time necessary to generate spheroids of 200–800 μm. We have characterised spheroids in terms of proliferation, oxygenation and survival. We have also revealed important differences between the effect of hypoxia on cells cultured as spheroids and cells cultured as a monolayer, with stronger effects on proliferation and survival observed in the more complex spheroid model. The combined results of experiments conducted in monolayers and spheroids indicate that the effect of hypoxia on tumour cells is dependent on the level of oxygen and duration of exposure as well as the cellular environment, which is critical because of the synergistic relationship between low oxygen levels and the availability of nutrients and concentration of waste products. The multicellular tumour spheroid model more closely mimics the arrangement of cancer cells and the environment to which they are exposed *in vivo*. We chose to continue to work with this model in the next chapter, in which we investigate cellular invasion in a spheroid model using lightsheet fluorescence microscopy.

Chapter 5:
Live cell imaging of spheroid invasion using lightsheet fluorescence microscopy

5.1 Introduction

The invasion of tumour cells into neighbouring tissue is a hallmark of cancer and a major cause of mortality (*6*). In GBM, the diffuse invasion of cells makes complete surgical resection impossible. As discussed in Chapter 1, the increased expression of integrin αVβ3 in GBM is thought to contribute to this invasive phenotype (*190-192*). Furthermore, GBM has been shown to express a range of cell adhesion molecules (α1, α3, α5, α6β1, αvβ3, ICAM-1, LFA-3, CD44, Lewisx, sialylated Lewisx, and sialylated LewisLewisx) at significantly higher levels than normal brain tissue (*287*). The molecular mechanisms of glioma invasion are a topic of great interest, which may have therapeutic potential. However, the majority of *in vitro* invasion assays are two-dimensional, (for review see (*288*)), and as such are a poor representation of the tumour microenvironment. We aimed to use the multicellular tumour spheroid model, characterised in the previous chapter, to investigate cellular invasion in 3D.

In the typical spheroid invasion assay, spheroids are plated on, or embedded in, ECM in a 96-well plate. The plates are imaged using an inverted microscope and invasion is quantified by measuring the distance that cells have migrated away from the spheroid (*289-292*). While this technique has the advantage of being high-throughput, it only provides information about the movement of cells in the x-y plane and does not provide any information about the migration of cells within spheroids. A further disadvantage is that it is not possible to track the movements of individual cells. The ideal imaging technique would allow us to track the invasion of individual cells in the x, y and z planes, and to track the migration of cells within spheroids, which can provide important information about the effect of the 3D organisation of cells on cell migration.

While it is possible to acquire 3D images using a confocal microscope, the depth penetration is poor. Two-photon microscopy has significantly improved depth penetration compared to confocal microscopy, which, in the past, has made it the most suitable technique for imaging thick samples. However, imaging living samples over long time courses can be challenging due to the effects of photobleaching and phototoxicity (*293*). The development of lightsheet fluorescence microscopy (LSFM), also known as single-plane illumination microscopy (SPIM), has overcome some of these challenges and led to a revolution in the imaging of large (> 1 mm) biological samples. LSFM was developed by Huisken *et al.* in 2004 and uses a plane of light, provided by dual illumination objectives, to provide optical sectioning. The sheet of light illuminates only the focal plane of the detection objective, resulting in reduced photobleaching and phototoxicity compared to confocal microscopy (Fig 5.1A) (*294, 295*). The sample is suspended in a liquid-filled chamber where it can be moved through the light sheet to produce a z-stack (Fig 5.1B). Light is detected by a charge-coupled device (CCD) or CMOS camera, which allows for very fast image acquisition compared to traditional point-scanning confocal laser-scanning microscopy, which measures pixel by pixel. This makes LSFM an ideal technique for imaging cell movement in a large, tightly packed spheroid when z-stacks need to be acquired in rapid succession to facilitate the tracking of cells. To track cells it is necessary to compare images taken at different time points and identify which cells are the same. To do this accurately, the distance moved by an individual cell between subsequent images needs to be less than the distance between neighbouring cells. The ability to track individual cells is crucial to quantifying cell movement and allows us to gain insights into cell behaviour that are not possible with population measurements.

While the seminal paper describing LSFM was published in 2004, it was not until late 2012 that the first commercial instrument, the Lightsheet Z.1 by Zeiss, came onto the market. In 2014, a Lightsheet Z.1 was installed in the

Liverpool Centre for Cell Imaging; it was one of the first commercial instruments to be installed in the UK. We decided to take advantage of this new instrument carry out live cell imaging of spheroid invasion. We aimed to quantify the movements of cells moving within spheroids, as well as the movements of cells invading into ECM. We hypothesised that invading cells would show increased speed or persistence of movement compared to non-invading cells. We further hypothesised that cell motility may be spatially regulated in spheroids, with cells in the core of spheroids showing different characteristics to cells near the spheroid periphery. We also aimed to evaluate the suitability of this technique as a 3D invasion assay by treating spheroids with drugs that are known to alter the invasive capacity of glioma cells.

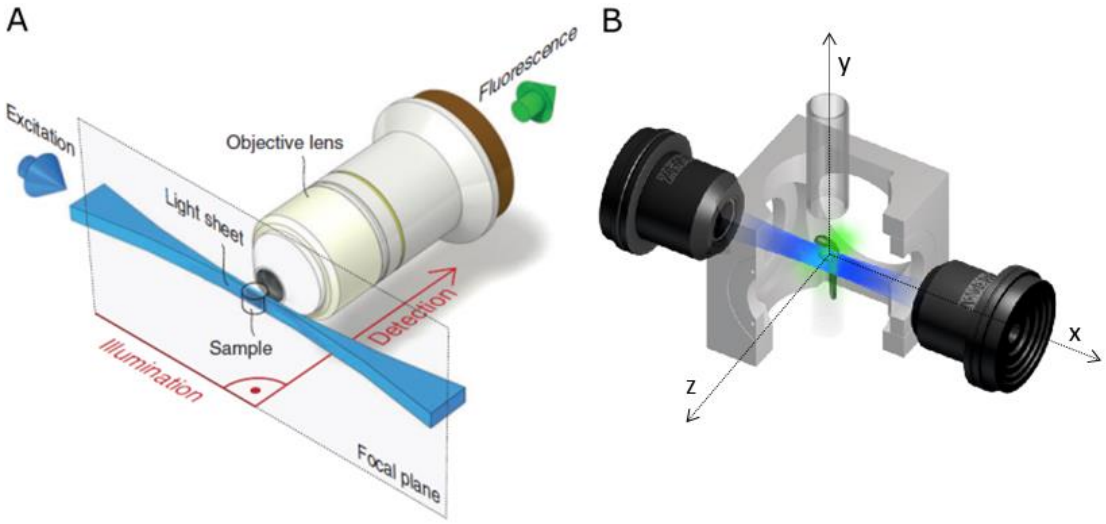

Figure 5.1. Lightsheet fluorescence microscopy. (A). The sample is excited by a sheet of light, shaped by cylindrical lenses, which provides optical sectioning by illuminating only the focal plane. The detection objective is at a 90° angle to the two illumination objectives. Adapted from (*296*). **(B).** Both the sample and detection objective are immersed in a liquid-filled chamber. The sample can be rotated around the y-axis to acquire multiple views. Adapted from (*297*).

5.2 Results

5.2.1 Optimisation of sample preparation

As discussed in the previous chapter, we found that image resolution is reduced in the centre of large spheroids. While resolution can be improved using tissue clearing methods, these techniques are not suitable for live cells. Therefore, we decided to carry out the majority of our experiments using smaller, three-day-old spheroids (around 250 μm in diameter). A nuclear marker is necessary to enable the automated tracking of cells as it facilitates object recognition by the tracking software. We have previously found that nuclear stains show poor penetration in spheroids. Therefore, we decided to create a cell line stably expressing a fluorescent histone H2B nuclear reporter protein by transducing U87 cells with the pHIV-H2BmRFP construct generated by Welm *et al.* (*298*). The use of red-shifted fluorescent proteins (RFPs) results in reduced autofluorescence, light scattering, and phototoxicity, making RFPs the most suitable spectral fluorescent protein variant for live-cell imaging in thick samples (*299*).

We used these cells to form spheroids using the hanging drop method, as previously described. The most typical approach for preparing small samples for imaging using LSFM is to embed them in a hydrogel, such as agarose, which has a refraction index close to that of water. We initially attempted to embed spheroids in 1% low-melt agarose; however, we found that this sample mounting method was not suitable because the cells did not invade. Furthermore, agarose is not an ideal embedding medium because it is not a physiological substrate. We next tried embedding spheroids in collagen IV and MaxGel ECM (Sigma); however, we again found that the cells did not invade. A further problem was that the gel columns were not firm enough to be suspended in the imaging chamber without swaying or disintegrating, making them unsuitable for long time courses.

An alternative to embedding samples in a hydrogel is to contain them in FEP tubing, which has a refraction index close to that of water (*300*). We embedded spheroids in a 1:1 mix of Matrigel and cell culture media plus 25 mM Hepes in an FEP tube (Fig 5.2). As well as creating conditions suitable for stable long-term imaging, a further benefit of this approach is that the sample chamber can be filled with water instead of media. This means that there is no need to dismantle and sterilise the chamber after each use as contamination is not an issue. Furthermore, much smaller volumes of expensive reagents, such as drugs, are required because the volume of the FEP tube is much smaller than the volume of the sample chamber.

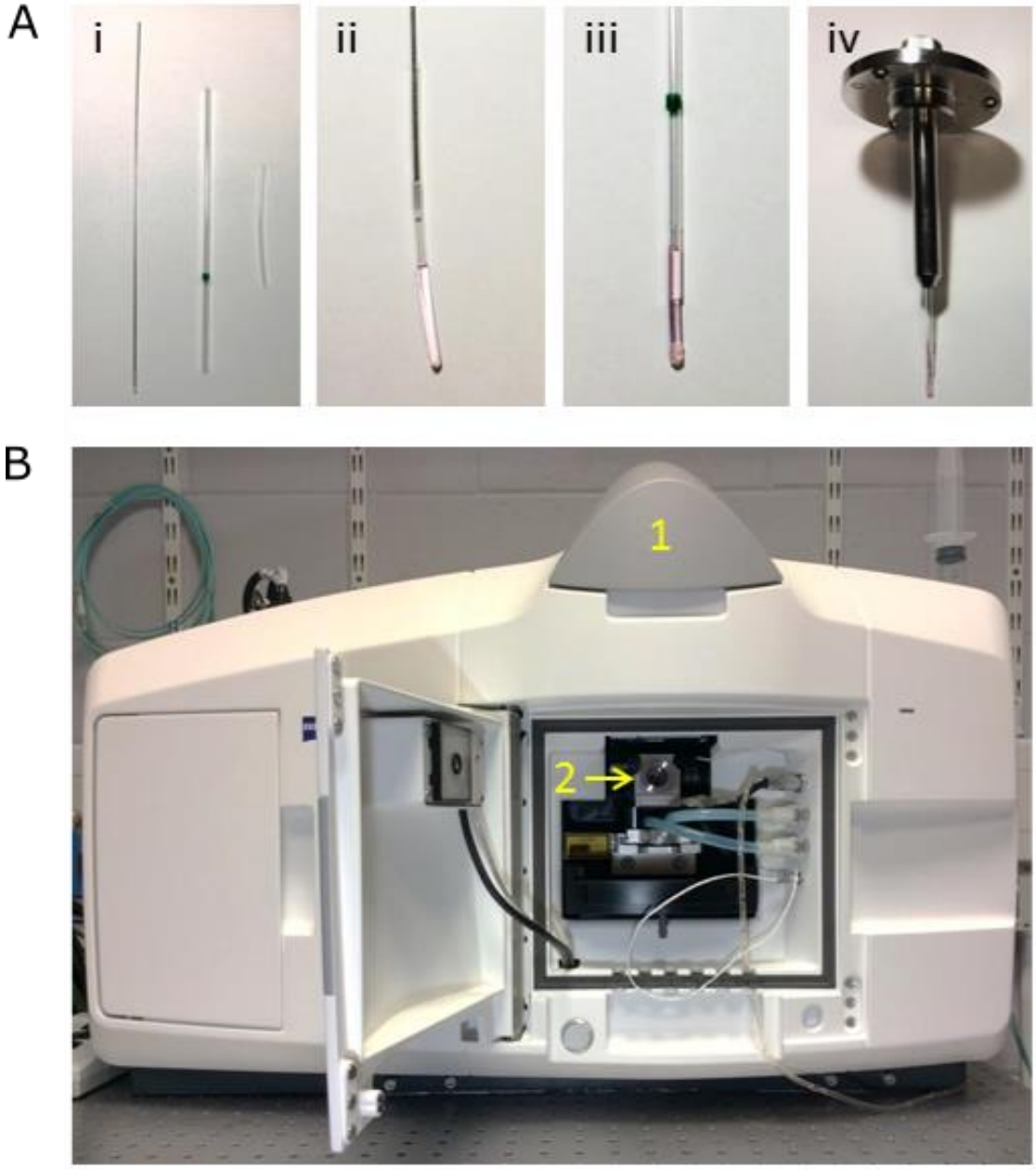

Figure 5.2. Lightsheet sample mounting. (A). Illustration of sample mounting procedure. **(i)** From left to right, Teflon plunger, glass capillary and FEP tube. **(ii).** The Teflon plunger is used to draw the sample into the FEP tube. **(iii).** One end of the FEP tube is inserted into a glass capillary and the other sealed with parafilm**. (iv).** The capillary is mounted within the lightsheet sample holder apparatus. **(B).** Image of Lightsheet Z.1 microscope. **(1)** The sample holder is inserted through the top of the microscope. **(2).** The sample is then lowered into the sample chamber, where it is immersed in water maintained at 37 °C for the duration of the experiment.

5.2.2 Image acquisition and processing

We found that it was difficult to discriminate nuclei from one another in images taken > 150 μm deep into spheroids due to a loss of image resolution. LSFM allows the possibility of taking several z-stacks from different angles in order to achieve good resolution from multiple views. By carrying out multi-view registration, the z-stacks from different angles can be fused to reconstruct an image of the whole spheroid as shown in Video 1. Videos for this chapter are available to view online using the following URL: http://bit.ly/LSFM-RR. However, we chose not to conduct our analyses of invasion of reconstructed spheroids for several reasons. Firstly, the file size would be doubled which would greatly increase the processing time. Secondly, the registration process is imperfect and can result in loss of resolution where the images from different views have been fused. Finally, we felt that imaging whole spheroids was unnecessary as enough cells (800–1200) can be detected in the first half of the spheroid. As such, we chose to image only half of the spheroids.

A further initial challenge was the size of the experiments, up to 250 GB for one 24 h single-channel experiment, which were too large to be opened on any of our image analyses computers. It was necessary to acquire images every 3 min as we found that increasing this time interval led to problems with cell tracking. We tried acquiring images in 8 bit but found that bleaching towards the end of the experiment led to a loss of signal that was exacerbated by the low bit depth. Thus, we opted for acquiring images in 16 bit, then downsampling to 8 bit and performing 2x binning. This was done using a macro in Fiji, which processed each time point individually. A further image registration step was required to correct for sample drift, as we found that by the end of the experiment the sample had often moved towards the edge of the field of view or drifted out of view entirely. Although the file size had been reduced to around 20 GB, we found that the

files were still too large for our analyses computers and that the computers would either fail to open the file or run out of memory before registration was complete. To resolve this issue, we had to order a new computer with more memory (128 GB of RAM). The problems we had because of the size of the data and our initial lack of a suitable computer meant there was a considerable delay between acquiring the data and being able to process it. For a summary of the post-acquisition processing steps and approximate processing times, see Fig 5.3.

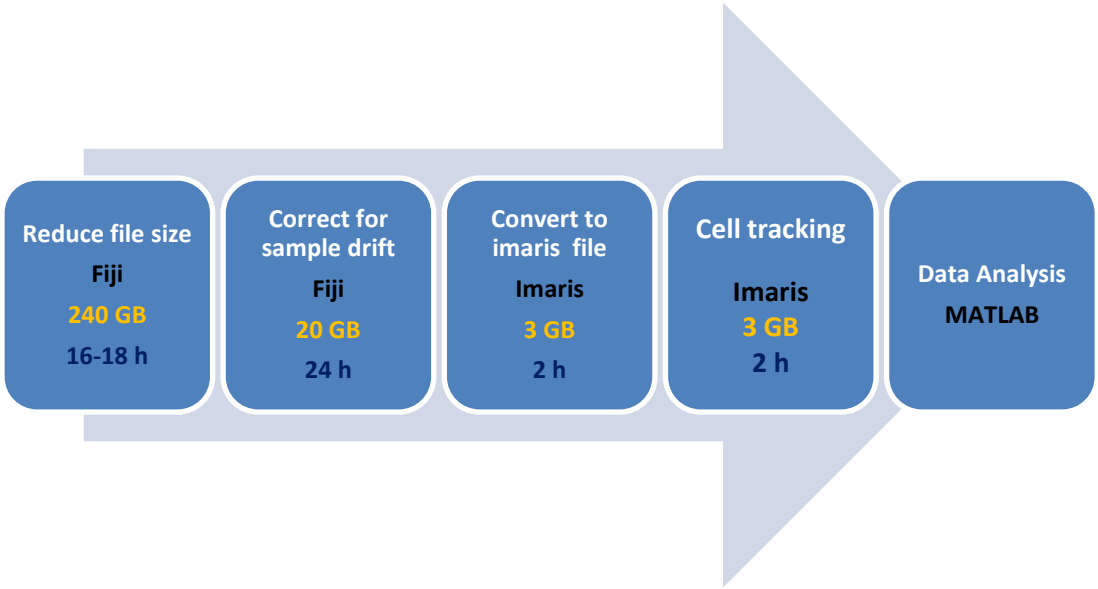

Figure 5.3. Summary of post-acquisition processing steps. Fiji is used to reduce file size by downsampling and binning, and then to register the images to correct for sample drift. The processed images are converted into the native Imaris file format, which compresses the file further. Imaris is used to carry out cell segmentation and tracking and to obtain tracking statistics. The tracking data is then further analysed using Matlab. Approximate file sizes and processing times are shown for small (~250 µm) spheroids; for larger spheroids, the file size is closer to 750 GB and processing times increased accordingly. Additional information about the image processing and analyses is detailed in Chapter 2, section 2.9.

We found that an initial sample drift tended to occur in the first three hours of the experiment, before cells had begun to invade. Therefore, we chose to mount spheroids on the lightsheet microscope immediately after embedding but to delay imaging for three hours after sample mounting, to allow the sample to stabilise. We aimed to image spheroids for 24 h; however, due to problems with the sample drifting out of view towards the end of the experiment, spheroids were imaged for between 16 and 24 h.

5.2.3 Tracking cell movements in three-day-old spheroids

We were successful in carrying out live cell imaging of cell migration and invasion in spheroids for up to 24 h (Fig 5.4A; Video 2 http://bit.ly/LSFM-RR). We defined migration as the movement of cells within the spheroid, invasion as the movement of cells in ECM, and motility as any kind of cell movement. As we wished to quantify these movements, we used the cell tracking software Imaris to track the trajectories of individual nuclei. Further analyses of cell movements were carried out using MATLAB and generated a large number of graphs. While summary statistics and representative beeswarm plots and histograms are included throughout this chapter, the full set of graphs can be viewed online using the image management software Zegami at http://tiny.cc/2016-LSFM-RR. Cell tracking and data analyses methods are described in more detail in Chapter 2, section 2.9.4.

We wanted to obtain information about two characteristics that are important in determining how far a cell moves from its point of origin: cell speed and persistence of movement. To track the movement of objects over time, Imaris carries out image segmentation by identifying the features (e.g. nuclei) in each frame, which are referred to as 'spots'. The tracking algorithm then looks at the spots present at each time point and links together spots that should be part of the same track. The total number of spots in an

experiment is equal to the number of spots identified in each time point summed together; thus, there are many more spots than tracks. While the track data can give us information about the average movements of a cell over the course of the whole experiment, the spot data allows us to take a more detailed look at what is happening. For example, we can calculate the instantaneous spot speed for a given spot by dividing the distance between the preceding and proceeding spots by the time interval. This allows us to obtain the speed of each spot at any one moment in time. We found that spot speeds within a single spheroid were highly variable, ranging from 0.2 to 214 μm/h (Fig 5.4B, C), as were spot speeds within a single track (Fig 5.4B). However, while a few spots were moving very fast, the mean spot speed was 21 μm/h and this was consistent between spheroids (Fig 5.9B).

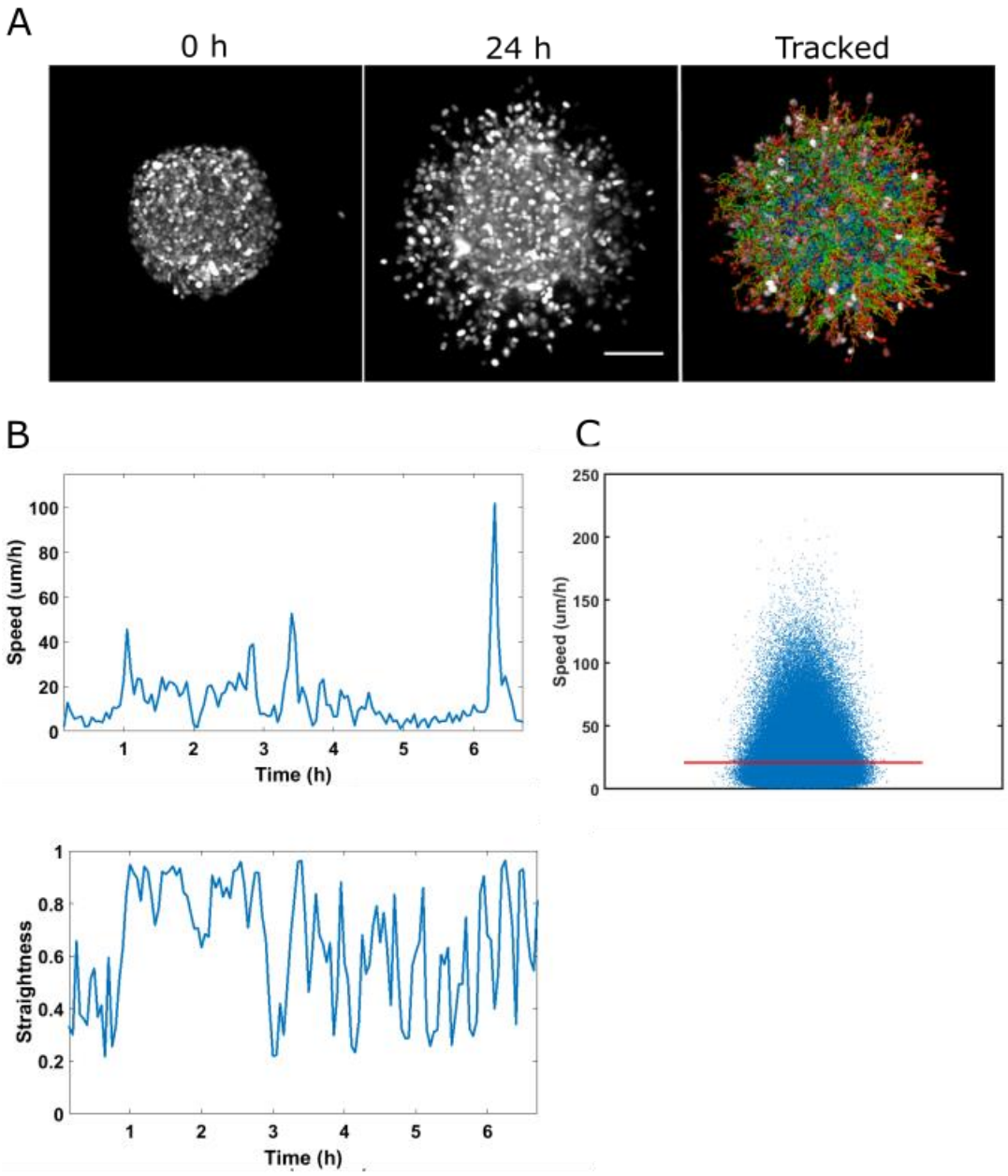

Figure 5.4. Tracking cell movements in three-day-old spheroids. (A). Maximum intensity projection images of a three-day-old U87-H2BmRFP spheroid embedded in 50% Matrigel, imaged at the indicated time points and tracked using Imaris. For imaging parameters, see Chapter 4, section 2.9. Scale bar is 100 µm. **(B).** Spot speed and straightness over a period of 6 h for one randomly selected track. A straightness value of one indicates a direct path of movement while lower values indicate a less direct path. **(C).** Beeswarm plot of the speed of every spot (invading and non-invading) in one spheroid; the line indicates the mean value.

5.2.3.1 Analyses of spot speed and straightness

We hypothesised that spot speed might vary according to whether cells were migrating within the spheroid or invading out into the Matrigel. As a higher proportion of cells have invaded by the end of the experiment, we also hypothesised that spot speed may vary over time. We found that mean spot speed was slightly higher in invading than non-invading cells; however, this difference was not significant (Table 5.1; Fig 5.6B). The distribution of spot speeds also remained consistent throughout the course of the experiment (Fig 5.6A).

$$\text{Track straightness} = \frac{\text{Displacement}}{\text{Track length}}$$

Figure 5.5. Definition of track straightness. Track straightness is calculated by dividing the track displacement by the total length of the track. Track displacement is the distance between the first and last spot position while track length is the total sum of the displacements within the track.

In order to move away from its starting point, a cell needs to persist at moving in a certain direction. Persistence of movement can be measured by examining track straightness; a straightness value of one indicates that a spot is moving 'as the crow flies' while a straightness value closer to zero indicates a less efficient movement (Fig 5.5). We initially examined whether track straightness differed between invading and non-invading cells. However, by looking at a single straightness value for each track we run the risk of overlooking the variability that exists within the data set. As track straightness is akin to the average of spot straightness, it is not possible to look at the variation in spot straightness throughout the experiment and any extreme values will be averaged out. We chose to break track straightness down into windows of five time points (15 min in total) to gain greater insight into the movement of cells.

We found that spot straightness was highly variable over the course of the experiment and that spots frequently changed direction (Fig 5.4B; Video 3, http://bit.ly/LSFM-RR). As with spot speed, we then assessed whether spot straightness varied systematically as a function of spot position or time. There was a small but significant difference between invading and non-invading spots, with invading spots having a higher straightness value (Table 5.1; Fig 5.7B). As with spot speed, spot straightness remained consistent throughout the experiment (Fig 5.7A). From this, we can conclude that invading cells are taking a straighter path of movement than cells migrating within the spheroid but moving at a similar speed. As both spot speed and straightness are consistent over time, we can be confident that spheroids are not adversely affected by the imaging conditions. Although there is an increase in invading cells towards the end of the experiment, this increase is not enough to affect the mean straightness value for the entire spheroid.

Table 5.1 | Three-day-old spheroid spot speed (µm/h) and straightness in non-invading and invading cells. The table shows the mean of three experiments ± SD. Ns = not significant.

	Non-invading	Invading	P value
Spot speed	20.35 ± 1.24	23.83 ± 4.43	ns
Spot straightness	0.64 ± .01	0.71 ± .012	.001

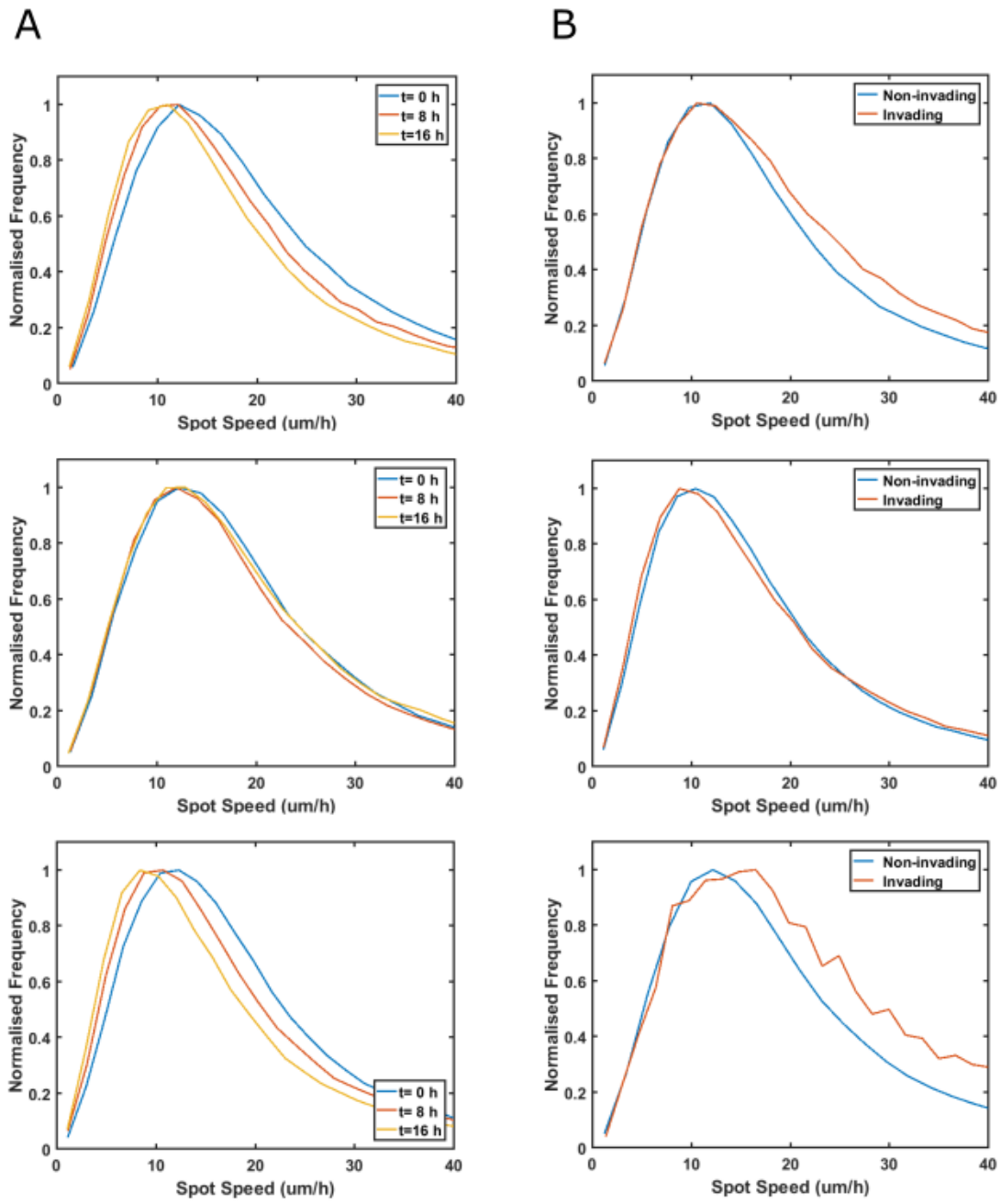

Figure 5.6. Three-day-old spheroid spot speed. (A). Normalised distribution of spot speed (invading and non-invading combined) in three spheroids as a function of time (t) from the start of imaging. **(B).** Normalised distribution of spot speed in invading and non-invading spots across all time points. Non-normalised graphs are available to view using Zegami at http://tiny.cc/2016-LSFM-RR.

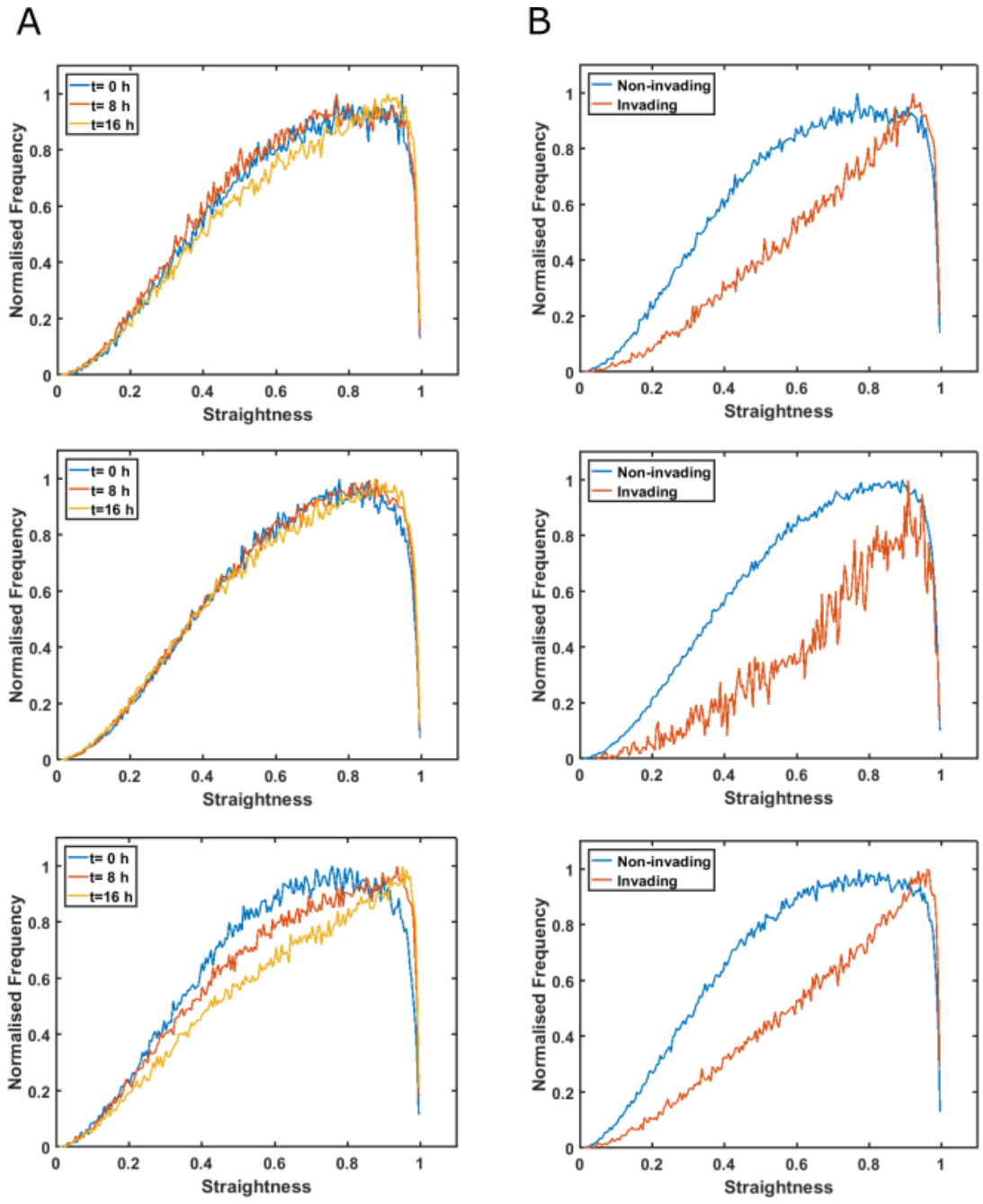

Figure 5.7. Three-day-old spheroid spot straightness (A). Normalised distribution of spot straightness (invading and non-invading combined) in three spheroids as a function of time (t) from the start of imaging. **(B).** Normalised distribution of spot speed in invading and non-invading spots across all timepoints.

5.2.4 The effects of drug treatment on invasion characteristics

To assess the suitability of this technique as an assay for characterising inhibitors of invasion, we treated spheroids with 17-allylamino-17-demethoxygeldanamycin (17-AAG) and cilengitide. Both drugs were added to the cell culture media during sample embedding. 17-AAG inhibits the growth and invasion of glioma cells by inhibiting heat shock protein 90 (HSP90); a chaperone protein that regulates numerous signalling proteins, including those involved in cell proliferation, survival, migration and invasion (*301-304*). Cilengitide is an αvβ3 and αvβ5 integrin inhibitor with anti-tumour activity (*305*). Integrins are known to promote glioma growth and survival, and their central role in cellular adhesion and migration has led to the hypothesis that their inhibition may halt glioma invasion (*306*). However, evidence of the effect of cilengitide on invasion is mixed; while some reports document an anti-invasive effect (*191, 307*), others have found that it acts to promote migration and invasion (*308, 309*).

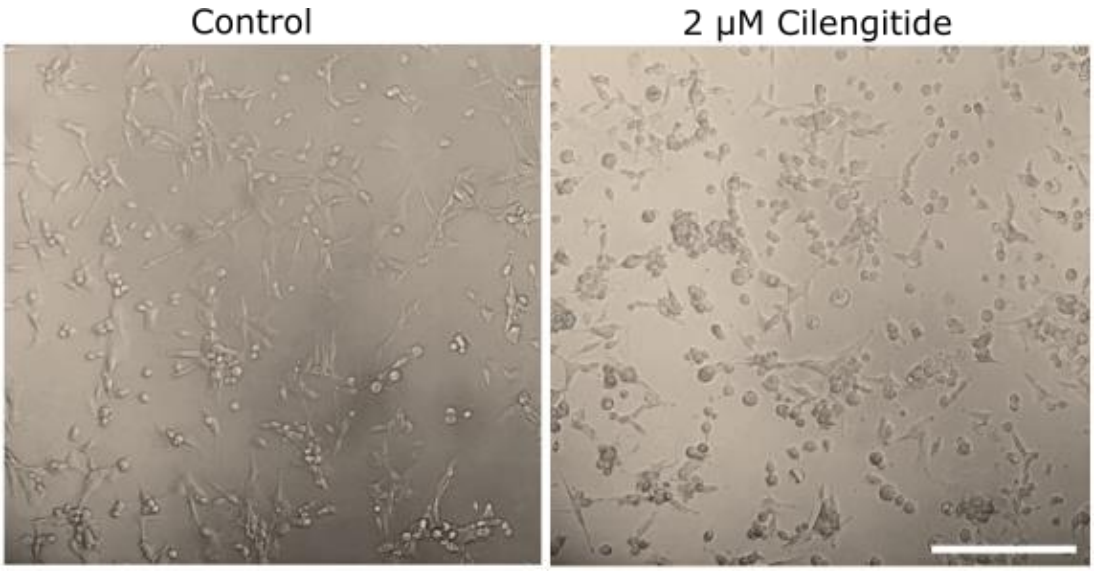

Figure 5.8. The effects of cilengitide treatment on a monolayer culture. Cells treated with 2 µM cilengitide for 24 h showed increased signs of rounding up and detaching from the dish Image is a representative example from one of two experiments. Scale bar is 100 µm.

We found that treatment with 0.5 µM 17-AAG clearly inhibited invasion (Fig 5.9A; Video 4, http://bit.ly/LSFM-RR). In contrast, treatment with 2 µM cilengitide did not inhibit invasion (Fig 5.9A; Video 5, http://bit.ly/LSFM-RR), although this concentration was sufficient to cause detachment in a monolayer culture (Fig 5.8). There was no difference in mean spot speed or straightness between control spheroids and cilengitide treated spheroids (Fig 5.9B). In cilengitide treated spheroids, both mean spot speed and straightness were higher in invading than non-invading spots (Table 5.2). There was no difference in mean spot speed and straightness throughout the experiment. Therefore, cilengitide did not have any effect on migration or invasion out of spheroids. Conversely, in 17-AAG treated spheroids mean spot speed was significantly lower than in control spheroids (Fig 5.9B). While some spots were moving very fast, a higher proportion of spots were moving at a lower speed than in the control spheroids (Fig 5.9C). Mean spot straightness was also significantly lower in 17-AAG treated spheroids (Fig 5.9B). We found no difference in mean spot speed between invading and non-invading spots, although spot straightness was significantly increased in invading spots (Table 5.2). We also found that mean spot speed was significantly slower after 16 h (M = 11.77, SD = 0.57) compared to the beginning of the experiment (M = 17.60, SD = 0.57, p = 03), although there was no difference in spot straightness. This indicates that while 17-AAG treated cells are able to migrate within the spheroid, their speed and straightness of movement are reduced and they are unable to invade into the Matrigel. The reduction in spot speed over time is most likely to be a reflection of the time it takes for the drug to become effective.

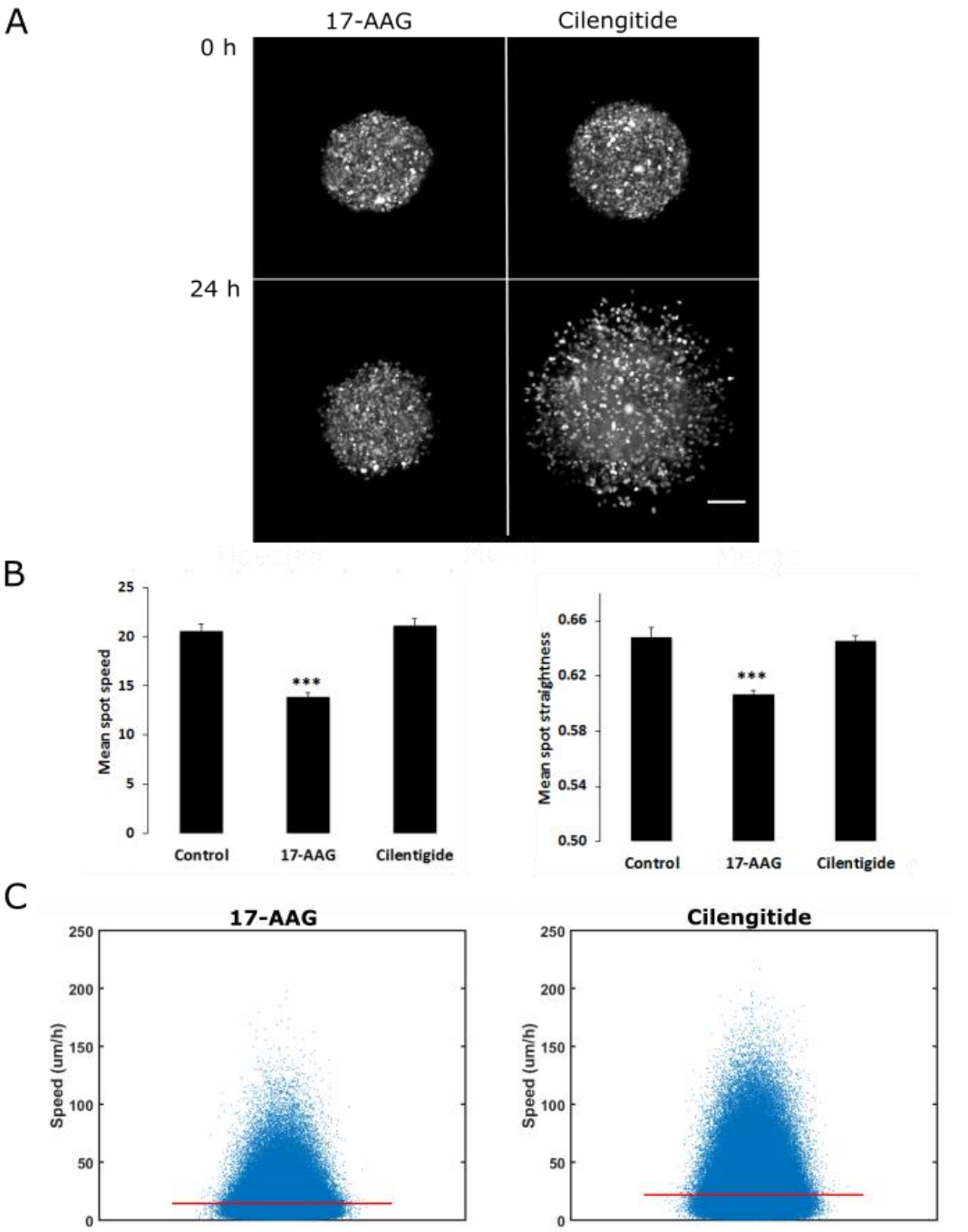

Figure 5.9. Treatment with 17-AAG inhibits invasion in spheroids; cilengitide does not. Three-day-old spheroids were embedded in 50% Matrigel plus 0.5 µM 17-AAG or 2 µM cilengitide and imaged with LSFM. **(A).** Maximum intensity projection images of spheroids at the indicated time points. For imaging parameters, see Chapter 4, section 2.9. Scale bar is 100 µm. **(B).** Spot speed and straightness (invading and non-invading combined) were significantly reduced in spheroids treated with 17-AAG compared to control spheroids. Figure shows mean + SEM of three experiments. **(C).** Beeswarm plots of spot speed in spheroids treated with 17-AAG or cilengitide. Plots are representative examples from one of three experiments. The line indicates the mean value. *** $p \leq 0.001$

Table 5.2 | 17-AAG and cilengitide treated spheroid spot speed (μm/h) and straightness. The table shows the mean of three experiments ± SD. Ns = not significant.

		Non-invading	Invading	P value
Cilengitide	Spot speed	20.66± 1.32	23.64 ± 1.05	.038
	Spot straightness	0.64 ± .01	0.69 ± 0.01	.001
17-AAG	Spot speed	13.79 ± 0.69	16.24 ± 5.19	ns
	Spot straightness	0.60 ± .01	0.70 ± 0.03	.011

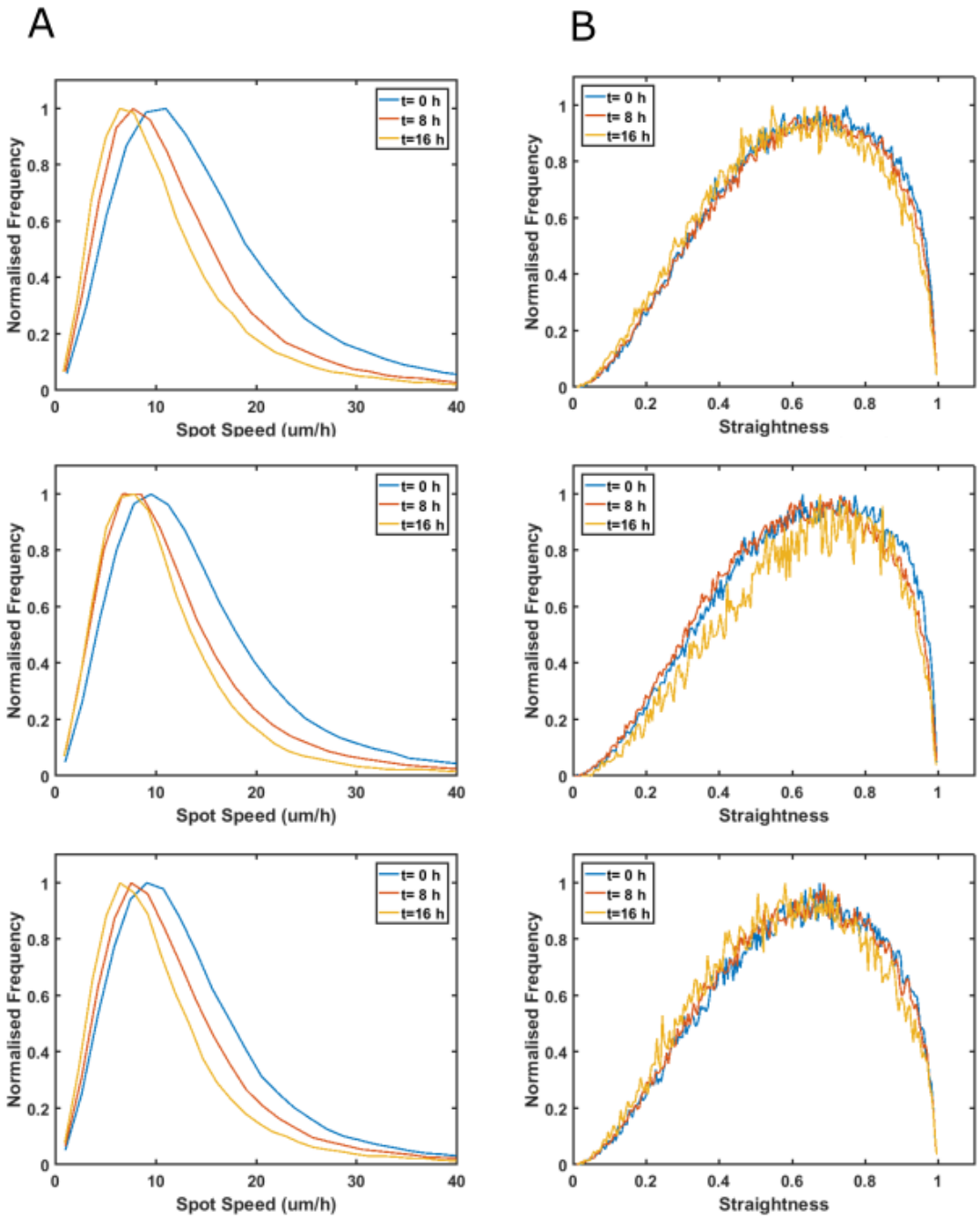

Figure 5.10. 17-AAG treated spheroid spot speed and straightness over time. Normalised distribution of (A) spot speed and (B) spot straightness **in** three spheroids as a function of time (t) from the start of imaging (invading and non-invading spots combined).

5.2.5 Plotting spheroid invasiveness

We wished to find a simple way of comparing the invasiveness of spheroids. From the beeswarm plots of invading spot speed, we can see that both the number and speed of invading spots is reduced in spheroids in which invasion has been inhibited (Fig 5.11A). However, the number of invading spots will vary according to the size of the spheroid. Another way of determining spheroid invasiveness is to plot the normalised cumulative number of spots by distance, over time. In invasive spheroids, the spatial distribution shifts over time as cells invade out into the Matrigel, while in non-invasive spheroids the distribution remains the same (Fig 5.11B).

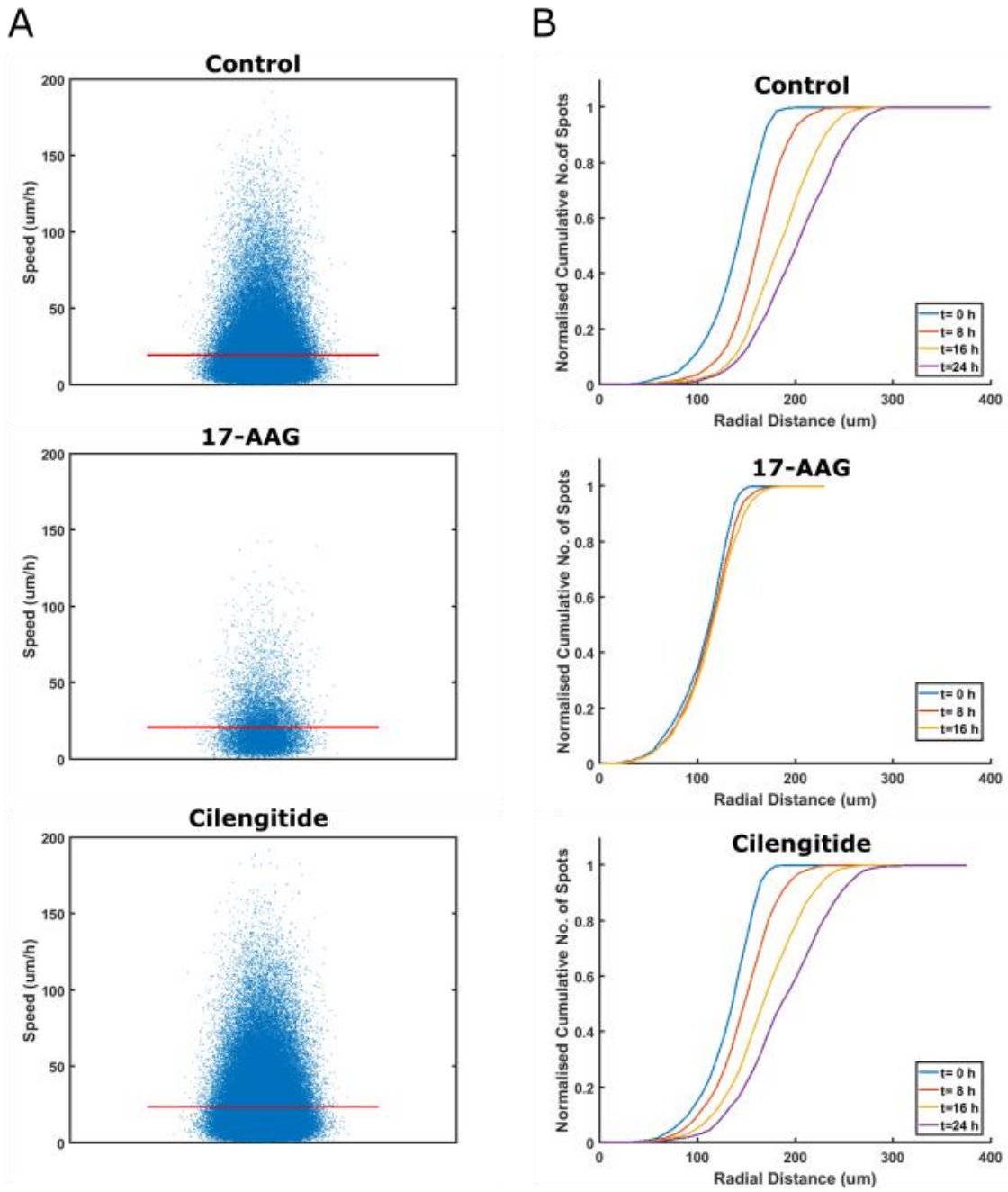

Figure 5.11. Quantifying spheroid invasion. (A). Beeswarm plots of invading spot speed in a single control, 17-AAG or cilengitide treated spheroid. The line indicates the mean value. **(B).** Normalised cumulative number of spots in a single spheroid (invading and non-invading combined) by distance as a function of time (t) from the start of imaging. In the control and cilengitide experiments, the curve shifts to the right over time as cells invade out from the spheroid. In 17-AAG treated spheroids, the curve remains the same because invasion is inhibited.

5.2.6 Imaging larger, hypoxic spheroids

We conducted our initial experiments using three-day-old spheroids as their smaller size allows for increased resolution throughout the spheroid and decreased file size compared to one-week-old spheroids. While smaller spheroids are easier to image, gradients in soluble factors typically do not occur until spheroids reach ~500 μm. To increase the complexity of our model, we next examined invasion in larger, one-week-old spheroids that had been incubated in 1% O_2 for 24 h (Fig 5.12A; Video 6). We have previously shown that, under these culture conditions, proliferation is restricted to the periphery of the spheroid (Chapter 4, Fig 4.3). It is also well known that exposure to hypoxia increases invasiveness (*196, 310*). We wanted to assess whether spot speed and straightness differed between three-day-old spheroids and one-week-old spheroids that had been exposed to hypoxia. We were also interested in whether spot speed and straightness in larger spheroids would vary according to the spatial location of spots.

We found that mean spot speed was significantly lower in one-week-old spheroids compared to three-day-old spheroids (Fig 5.12C, D; Video 7) and invasion reduced (Fig 5.12A, B). We next examined the spatial distribution of spot speeds and found that spot speed was significantly higher in invading than non-invading spots (Table 5.3). To determine whether there was a relationship between spot speed and the position of the spot within the spheroid, we divided spheroids into three regions: core, middle and outer. We found that spot speed did not vary between the three regions (Figure 5.13B) and was consistent throughout the course of the experiment (Fig 5.13A).

We next examined track straightness and found that it was significantly lower in one-week-old spheroids compared to three-day-old spheroids (Fig 5.12D). We again found that mean spot straightness was significantly higher in invading than in non-invading spots, but remained constant throughout

the course of the experiment (Table 5.3; Fig 5.14A). Additionally, we found that mean spot straightness was significantly lower in the inner region of the spheroid, compared to the middle and outer regions (Fig 5.14B). In summary, we conclude that spot speed has been affected by the change in culture conditions compared to the three-day-old spheroids, and that spot straightness is reduced in the core of larger, hypoxic spheroids. An increase in cell stress caused by the oxygen-deprived environment in these spheroids may contribute to the changes in speed and straightness that we have observed.

Table 5.3 | One-week-old spheroid spot speed (μm/h) and straightness in non-invading and invading cells. The table shows the mean of three experiments ± SD.

	Non-invading	Invading	P value
Spot speed	15.95 ± 0.08	19.46 ± 1.18	.007
Spot straightness	0.61 ± 0.02	0.70 ± 0.01	.001

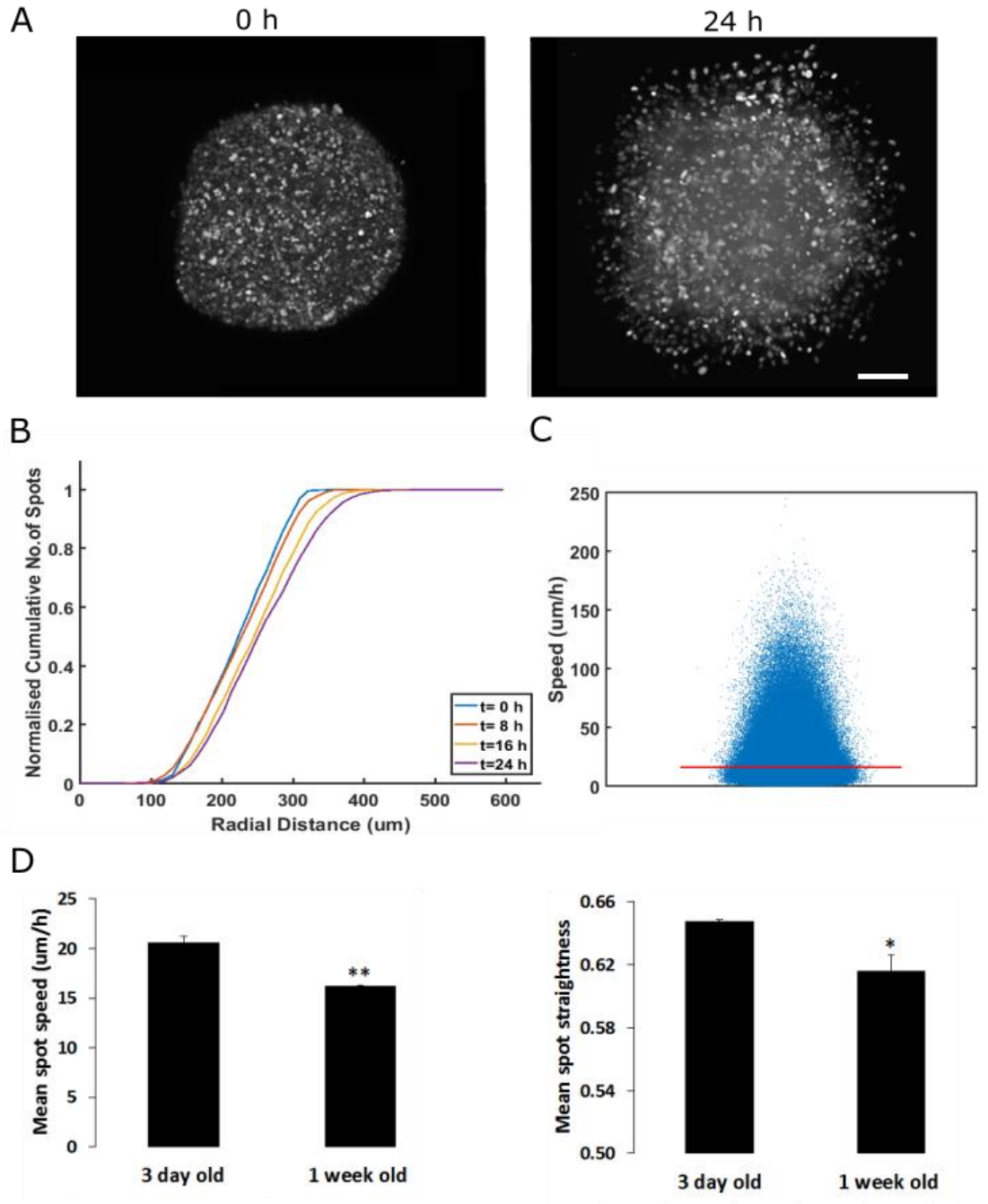

Figure 5.12. Spot speed and straightness are reduced in larger, hypoxic spheroids. Spheroids were cultured for 6 days in 20% O_2 followed by 24 h in 1% O_2. **(A)**. Maximum intensity projection images of one-week-old spheroids imaged at the indicated time points. For imaging parameters, see Chapter 4, section 2.9. Scale bar is 100 µm. **(B).** Spot speed and straightness (invading and non-invading combined) were significantly reduced compared to three-day-old spheroids. Figure shows the mean + SEM of three experiments. **(C).** Beeswarm plot of the speed of every spot in one spheroid (invading and non-invading combined); the line indicates the mean value. **(D).** Mean spot speed and spot straightness in 3 day old and 1 week old spheroids. * $p < .05$, ** $p > .01$.

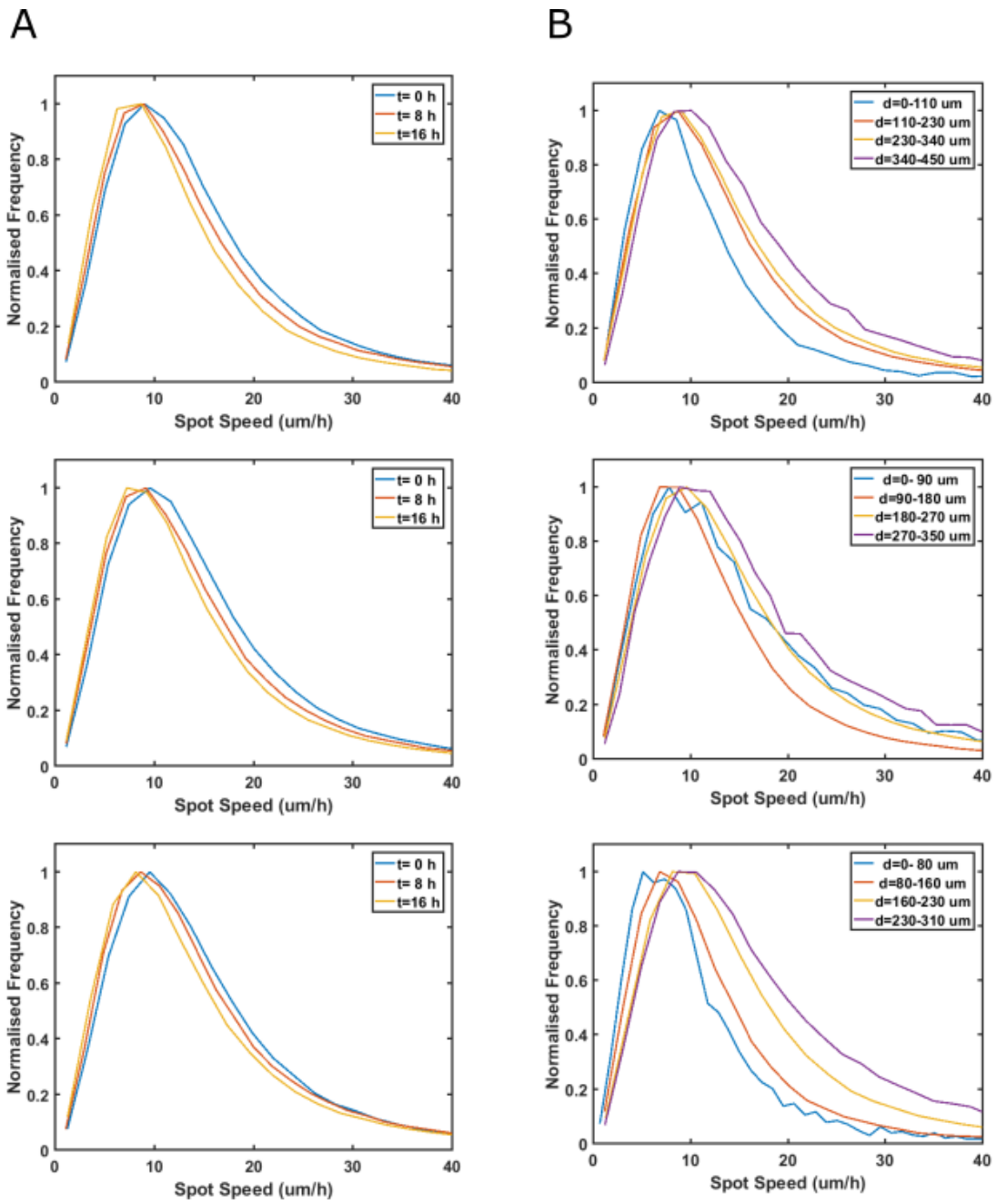

Figure 5.13. One-week-old spheroid spot speed. (A) Normalised distribution of spot speed (invading and non-invading combined) in three spheroids as a function of time (t) from the start of imaging. **(B)** Normalised distribution of spot speed in three spheroids as a function of the starting position of the spot, defined by radial distance (d) from the centre of the spheroid. Spheroids were spatially divided into three regions: core, middle and outer. The region outside of the spheroid boundary, represented by the purple line, indicates invading spots.

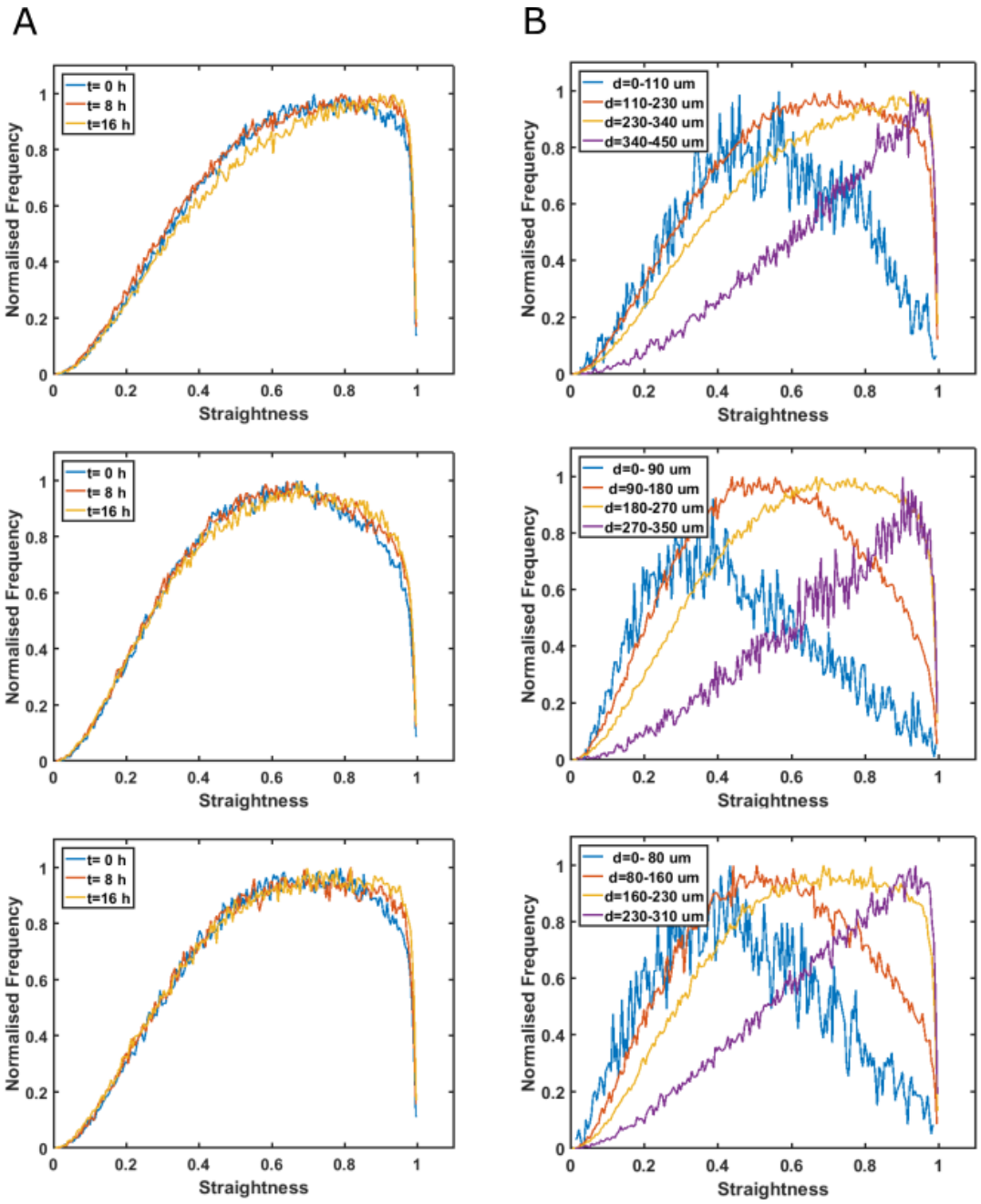

Figure 5.14. One-week-old spheroid spot straightness as a function of time and space. (A). Normalised distribution of spot straightness (invading and non-invading combined) in three spheroids as a function of time (t) from the start of imaging. **(B).** Normalised distribution of spot straightness in three spheroids as a function of the starting position of the spot, defined by radial distance (d) from the centre of the spheroid. Spheroids were spatially divided into three regions: core, middle and outer. The region outside of the spheroid boundary, represented by the purple line, indicates invading spots.

5.2.6.1 The effects of 17-AAG treatment in one-week-old spheroids

We next assessed the response to 17-AAG in one-week-old spheroids that had been incubated in 1% O_2 for 24 h. We wanted to confirm that the effectiveness of 17-AAG was not affected by the increased size of the spheroid. We found that, as in the three-day-old spheroids, 17-AAG effectively inhibited invasion (Fig 5.15A) and that mean spot speed and straightness were decreased compared to untreated spheroids (Fig 5.15B, C). As in the untreated one-week-old spheroids, we found that spot straightness was reduced in the core of the spheroid compared to the outer two regions, while spot speed did not vary (Fig 5.15D). From these results, we can conclude that the effect of 17-AAG is not altered in larger, hypoxic spheroids compared to three-day-old spheroids.

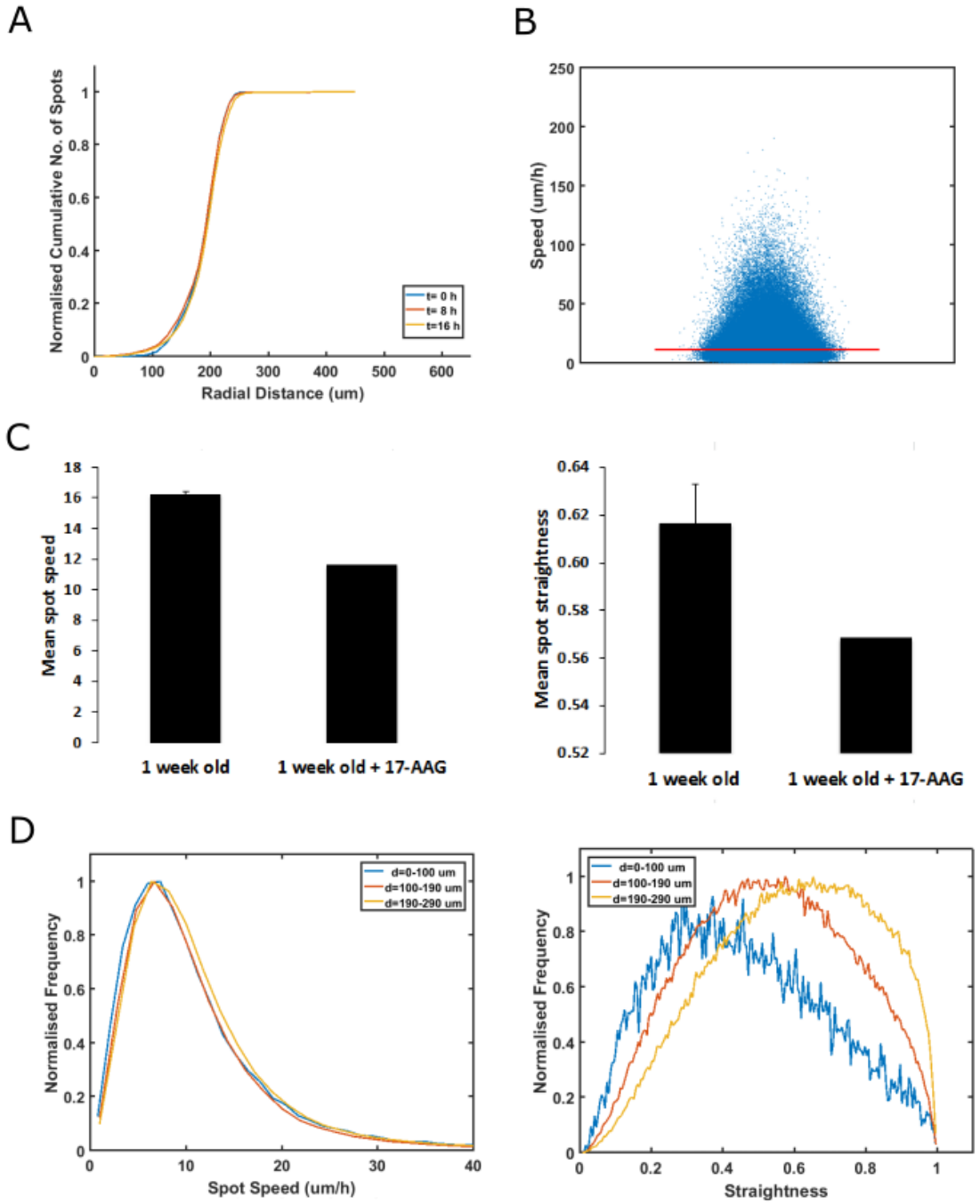

Figure 5.15. 17-AAG inhibits invasion in larger, hypoxic spheroids. Spheroids were cultured for 6 days in 20% O_2 and 24 h in 1% O_2, embedded in 50% Matrigel plus 0.5 µM 17-AAG and imaged for 16 h. **(A).** Normalised cumulative number of spots by distance over time (t) from the start of imaging. **(B).** Beeswarm plot of the speed of every spot (invading and non-invading) in one spheroid; the line indicates the mean value. **(C).** 17-AAG treated spheroid spot speed and straightness (N = 1) were reduced compared to untreated spheroids (N = 3). For untreated spheroids, figure shows the mean + SEM. **(D).** Normalised distribution of spot speed and straightness as a function of the starting position of the spot within the spheroid, defined by radial distance (d) from the centre of the spheroid.

5.3 Discussion

To our knowledge, this is the first use of lightsheet microscopy as a tool for imaging cellular invasion in multicellular tumour spheroids. We have optimised the imaging of spheroids, from sample preparation through to image processing and data analyses. We have shown that it is possible to track the movement of up to 1200 cells per spheroid, and quantify these movements in terms of speed and straightness. While spheroids have previously been used to investigate invasion, these investigations have been limited by the available imaging techniques. We have been able to track the migration of individual cells within spheroids as well as the invasion of cells out of spheroids. We have also been able to collect information about the movement of cells in the z dimension, making this a truly three-dimensional invasion assay.

Our aim was to conduct a feasibility study to assess the suitability of LSFM as a tool for investigating migration and invasion in spheroids; as such, we have not investigated the molecular mechanism of the changes we have detected. It is clear from our results that 17-AAG prevents the invasion of cells into the Matrigel but does not prevent their migration within the spheroid. However, the movement of cells inside 17-AAG treated spheroids is slower and less direct than in control spheroids. 17-AAG affects many signalling proteins through its inhibition of HSP90, including numerous proteins involved in cellular adhesion and motility, making it difficult to pinpoint the mechanism through which invasion is inhibited (*302, 303, 311*). However, it has been shown that treatment with 17-AAG blocks hyaluronic acid-induced MMP-9 secretion, impairing cells ability to degrade the ECM and reducing their invasiveness (*304*). The average pore size of 50% Matrigel is 2 μm and it has been shown that at pore sizes of less than 7 μm cells are unable to migrate unless they are able to degrade the ECM (*312, 313*). The rate-limiting factor is the nucleus, which can only deform to 10% of its

original cross section. This suggests that MMP activity is essential to invasion in our experiments due to the small pore size of the Matrigel. The inhibition of MMP-9 by 17-AAG may provide an explanation for why cells are able to migrate within the spheroid but not invade into the Matrigel; to confirm this hypothesis it would be necessary to use a more specific inhibitor of MMP-9 activity. Although 17-AAG successfully inhibits invasion *in vitro*, it has been unsuccessful in clinical trials due to a poor pharmaceutical and toxicity profile. Second-generation HSP90 inhibitors with improved bioavailability and reduced toxicity are currently under clinical development (*314*).

In contrast to 17-AAG, we found that cilengitide was not effective in inhibiting invasion and, furthermore, we could not detect any differences between spheroids treated with cilengitide and control spheroids. It has been shown that cilengitide reduces cell viability by causing detachment and anoikis. U87 cells are resistant to anoikis and their sensitivity to cilengitide-induced detachment is dependent on the composition of the ECM. While cells cultured on vitronectin-coated plates show increased detachment, cells cultured on collagen or fibronectin-coated plates resist detachment (*315, 316*). Blocking the action of integrins reduces cellular adherence, which can have different effects depending on the environment. Zaman *et al*. have shown that blocking β1 integrin activity retards the movement of cells in high concentrations of Matrigel (>60%); however, invasion speed is significantly increased in lower concentrations of Matrigel (*312*). Several *in vitro* studies have found that cilengitide can increase the speed of migration and invasion (*309, 316*), while studies in animal models have demonstrated an anti-invasive effect (*191, 192*). However, despite promising results in phase II clinical trials, cilengitide did not improve outcomes in a phase III study and is no longer being developed as an anti-cancer drug (*317*). The effect of cilengitide on invasion remains far from clear, although ECM composition may be key in determining its effectiveness. The discrepancies in results

between studies can most likely be explained by the differences in the methods used to investigate invasion.

We have found that cells in three-day-old spheroids are capable of moving up to 214 μm/h, with a mean invading spot speed of 24 μm/h. These findings correlate well with the results of an investigation by Farin *et al.* in which glioma cells were injected into neonatal rat forebrains. Glioma cell invasion was investigated in slice cultures generated from these brains using an inverted microscope. They analysed cells in the infiltrative margins of tumours and found that they reached speeds of over 100 μm/h, with an average speed of 25 μm/h. They also found that cells migrated in a saltatory fashion, with periods of stillness followed by bursts of movement and frequent direction changes (*172*). The similarity of our findings with those of Farin *et al.* suggests that, in certain circumstances, our model could be used as an alternative to investigations in animal models. Indeed, our approach has overcome some of the limitations faced by Farin *et al*. They were unable to track cells within the tumour itself and, as data was collected from a single focal plane, were only able to track the movements of cells in the x-y plane. Alternatives to animal models are necessary not only to fulfil the principles of the 3Rs, but also to improve the translation of results from the bench to the bedside. Crucial physiological differences between humans and animals, and a failure to accurately replicate the disease under investigation, mean that less than 8% of the successes achieved in animal studies are translated to clinical cancer trials (*318*). The use of spheroids in preclinical drug screening assays can lead to more effective selection of compounds, reducing the number of compounds that need to be tested in animals (*220*).

We found that spot straightness was consistently increased in cells that were invading into the Matrigel compared to cells that were migrating within the spheroid. These changes in movement most likely reflect a response to the change in microenvironment. The speed and mode of cellular invasion are

modulated by properties of the ECM such as composition, matrix stiffness and pore size (*312, 313, 319, 320*). At around 10 Pa, 50% Matrigel is much more pliable than brain tissue, which is in the region of 300 Pa (*312, 321*). Although many tumours have been found to be stiffer than the surrounding tissue, gliomas are not. This may be because the unique ECM of the brain means that the gliomas cannot form the filamentous ECM that is common in other tumours (*186, 321*). Matrigel consists mainly of laminin and collagen, which means it does not resemble brain parenchymal ECM but is similar to the vascular basement membrane. Therefore, our model mimics the composition of the ECM encountered by glioma cells during perivascular migration. However, we have not attempted to recreate the mechanical or structural properties of this microenvironment.

We found that cells in one-week-old spheroids that had been incubated in 1% O_2 for 24 h moved slower and less straight than cells in three-day-old spheroids that had been incubated in 20% O_2. This is contrary to what we expected as hypoxia is known to increase the invasiveness of cells (*196*). However, we did not examine the invasiveness of one-week-old spheroids that had not been exposed to hypoxia. It is possible that it is the age and size of the spheroid that causes the reduction in cell speed and straightness, rather than the exposure to hypoxia. We also found that spot straightness was reduced in the core of larger spheroids, although spot speed was unaffected. The change in straightness may reflect a response to the harsher environment found in the core of spheroids, although further investigations would be necessary to confirm whether this is indeed the case.

Wu *et al.* examined the migration of single cells through a 3D collagen matrix and found that, in contrast to 2D migration, 3D migration does not follow a random walk. Rather, cells migrating in 3D show a spatially anisotropic velocity pattern; they move faster along their primary migration axis, defined by the primary direction of migration, than the perpendicular axis (*322*). In

contrast to our results, they found that migration speed and persistence were correlated. However, Wu *et al.* examined the movement of single cells within a matrix, rather than the movement of cells within a large heterogeneous spheroid. The movement of cells within spheroids is a topic of interest that has previously been difficult to examine experimentally. Early experiments by Dorie *et al.* showed that labelled cells and polystyrene microbeads are internalised into the spheroid, suggesting that cells are moving away from the nutrient-rich surface of the spheroid towards the necrotic core (*323*). Mathematical models attempting to explain this finding have concluded that the mechanical pressure of proliferating cells creates pressure gradients, driving cells towards the centre of the spheroid (*324*). The motility of cells within spheroids have been addressed by a number of mathematical models which attempt to explain the typical structure of a large spheroid, where the majority of cells are quiescent but surrounded by a proliferating rim of cells. These models are based on assumptions about pressure gradients, chemotaxis and the relationship between cell cycle status and migration, often obtained from studies conducted in 2D (*324-327*). Furthermore, they fail to take into account important factors such as the composition and mechanical properties of the surrounding ECM. The paucity of experimental data on cell motility in 3D, and in spheroids in particular, has hampered the development of these models and limited their complexity (*328*).

While we have examined the straightness of movement of cells, we have not addressed the directionality of their movements in relationship to the core of the spheroid. The directionality of the cells can be calculated using the spot position information we have collected; however, due to the time-limited nature of this project, we have only been able to carry out limited analyses of the data. Collaboration with mathematicians would be necessary to facilitate the assessment of directionality and enable deeper analyses of the data. A further question of interest is the relationship between proliferation status and invasion. The 'go or grow' hypothesis postulates that cellular

proliferation and invasion are mutually exclusive phenotypes. While proliferation and invasion have been shown to be temporary mutually exclusive, several studies have shown that migratory cells proliferate en route (*172, 329*). Furthermore, some studies have found a positive correlation between proliferation and migration, refuting the idea of a dichotomy between the states of 'go' and 'grow' at the population level (*330*). Using our technique, it is possible to test the relationship between proliferation and motility in spheroids. It is hoped that further analyses of our data by our group and others will address some of the questions that we have as yet been unable to address.

The challenges of manipulating such large files were greater than we expected and resolving these issues was time-consuming. Even when we had tracked the spheroids and no longer had to deal with large image files, we found that data manipulation was slow due to the number of data points, which could exceed half a million for a single spheroid (1200 spots x 460 time points). We conducted 16–24 h time courses as we did not know how spheroids would be affected by the embedding and imaging protocol and how motility might change over time. However, our results indicate that this technique is sensitive enough to detect small changes in motility and that long time courses are not necessary to characterise the effects of anti-invasive drugs. An alternative approach would be to treat spheroids with the compound of interest and then image them for 1–2 h only. This would significantly reduce file size and processing time, increasing the number of spheroids that could be analysed. Another way of reducing the amount of data would be to label only a proportion of the cell nuclei. As well as reducing the number of cells that need to be tracked this would also enable less timepoints to be acquired; as the spheroid would not be as densely packed with labelled cells the time interval between image acquisitions could be increased without detriment to the cell tracking.

We have demonstrated that LSFM is a powerful tool for investigating cellular motility and invasion in 3D. Using the technique we have developed, it is possible to investigate the effect of different aspects of the tumour microenvironment on cellular motility in a spheroid model. It is also possible to gain quantitative information about cell movements in a 3D environment. This technique holds promise as an assay for screening and investigating the mechanism of anti-invasive drugs, contributing to the principles of the replacement and reduction of the use of animals in experimental research. We hope that this technique will be of use to other investigators and will contribute towards furthering our understanding of the mechanisms of invasion and the ways in which it can be inhibited.

Chapter 6:
Discussion

6.1 Revisiting the thesis aims

The overall aim of this thesis was to investigate the effect of the solid tumour microenvironment on GBM cells. More specifically, we sought to understand how cell proliferation is affected by the low oxygen levels that are characteristic of this environment. We performed a systematic investigation into the effect of different oxygen levels on cell proliferation and found that, in monolayer cultures, pathophysiological levels of hypoxia do not affect cell proliferation. These results were unexpected, as previous investigations had indicated that hypoxia causes cell cycle arrest; however, these experiments were carried out in near anoxic conditions. Our results demonstrated the importance of using physiologically relevant conditions when investigating components of the tumour microenvironment.

We then aimed to improve our model by exploring the effect of hypoxia in GBM cells cultured as multicellular tumour spheroids. We had originally hoped to characterise spheroids using LSFM; however, we were unsuccessful in performing immunofluorescence in whole spheroids. Instead, we characterised spheroids by fixing, sectioning and staining them before imaging them with confocal microscopy. We were again surprised by our results when we found that, in the spheroid model, hypoxia is associated with quiescence. Our findings indicate that, in GBM, hypoxia may act as a general stressor rather than a specific regulator of cell cycle. They also suggest the existence of a threshold which, when reached, informs the cell that conditions are unfavourable for proliferation and causes cell cycle arrest. While hypoxia alone does not affect cell proliferation, additional stressors present in the 3D tumour microenvironment cause this critical threshold to be reached.

Lastly, we aimed to use LSFM to carry out live cell imaging of cellular migration and invasion in spheroids. We further aimed to quantify the

movements of cells moving within spheroids, as well as the movements of cells invading into ECM. We also aimed to assess the suitability of this technique as a 3D invasion assay for characterising the effects of drugs that target the invasion process. We were successful in achieving these aims; as far as we are aware, we are the first to carry out live cell imaging of invasion in multicellular tumour spheroids using LSFM. We have developed a novel and truly 3D assay, which can be used to investigate the effect of different environmental factors or therapeutic compounds on cellular invasion.

6.2 The challenges of 3D cell culture

3D cell culture is one of the fastest growing areas in biology (*331*). However, despite the development of the multicellular tumour spheroid model 45 years ago, the overwhelming majority of *in vitro* investigations into cancer cell biology are still carried out in monolayer cultures. A number of factors may have contributed to the slow uptake of 3D cell culture. New methods for culturing cells in 3D are constantly emerging. However, many of these methods, such as magnetic cell levitation, are complicated and have niche applications (*332*). The use of different culture methods by different investigators can limit the usefulness of the results obtained; it is important that a common approach to 3D cell culture is adopted so that results can be compared and replicated. Multicellular tumour spheroids are most well-characterised 3D cell culture model; although, within this approach there are numerous methods for forming spheroids. The choice of culture method can be challenging, especially as the most appropriate method varies according to the cell line used. For example, some cells will readily form spheroids in ultra-low-adherence plates, while others will not. The cost of additional equipment, such as rotary cell culture systems or specialised plates, may also have hindered the uptake of 3D cell culture. The analyses of 3D cell cultures can also be challenging; many assays that have traditionally been used in

monolayer cultures are either not compatible with 3D cell cultures, or require adaptation. Until recently, high-throughput screening (HTS) has been restricted to monolayer cultures (*333*). However, advances in technology have made it possible to automate the production of large numbers of homogeneous spheroids and are leading to an increase in the uptake of this approach (*224, 334-337*).

6.3 Increasing the complexity of 3D cultures

One important aspect of the microenvironment that we did not attempt to replicate in this thesis is the interaction between tumour cells and parenchymal or stromal cells. Such interactions are known to influence important aspects of glioma biology, such as cellular metabolism and invasion (Chapter 1, Section 1.5.1). These interactions can be investigated in monolayers, spheroids, tissue explants or *in vivo* (Fig 6.1). While more complex models are more physiologically relevant, they are also more challenging to investigate. The relevance of cell culture models can also be improved by the use of primary cells. We used primary cells to confirm the results obtained in cell lines in Chapter 3; with more time, we would have liked to have cultured primary cells as spheroids and imaged them using LSFM. We would also have liked to carry out co-cultures of GBM cells and astrocytes in spheroids. However, as immortalised astrocyte cell lines are not available, it is necessary to work with primary cells, which can be difficult to obtain and cannot be maintained in culture. While the use of primary cells and co-cultures are an important step towards increasing the physiological relevance of 3D cell culture models, the inherent heterogeneity of these models means that they are less well suited to HTS.

In vivo investigations in animal models capture aspects of the tumour microenvironment that can be difficult to replicate in cell culture. However,

animal models are costly and fail to replicate many important aspects of human physiology and pathology (*318*). An investigation into the effect of *in vivo* growth on GBM gene expression by Camphausen *et al.* demonstrated the importance of orthotopic conditions. This refers to the transplantation of cells into the organ which they are derived from, which in GBM is the brain. Numerous differences in gene expression occur when cells are transplanted subcutaneously and intracerebrally, with cells grown intracerebrally expressing more genes related to CNS function. Interestingly, U87 and U251 cells have divergent gene expression profiles in monolayer or subcutaneous growth conditions that become more similar when grown intracerebrally. These results demonstrate the importance of the tumour microenvironment on gene expression. The unique microenvironment of the brain means that it is especially important that animal models of GBM are orthotopic. Zebrafish are a popular model organism because of their optical clarity and rapid development and have been imaged extensively using LSFM (*338-340*). Lal *et al.* injected U87 cells into the brains of zebrafish, which they imaged using confocal microscopy (*177*). They observed the migration of GBM cells along blood vessels and found that cells did not metastasise outside the brain, suggesting that zebrafish may be a useful model organism for GBM. As LSFM is the ideal technique for the *in vivo* imaging of zebrafish, an interesting and novel approach would be the use of LSFM to investigate GBM invasion in a zebrafish model.

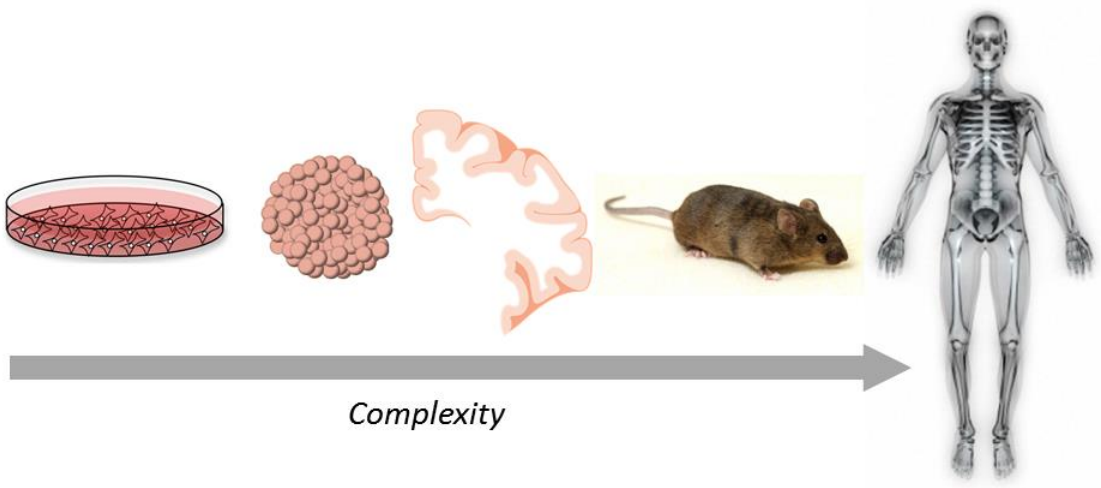

Figure 6.1. Biological models for cancer research. Cancer biology can be investigated in monolayer cell cultures, in 3D cell culture models, in whole organs or sections of organs, in animals, or in humans. Each of these models presents its own challenges and advantages. A more complex model is not necessarily always a better option than a model of lesser complexity, as the most appropriate method is often determined by the hypothesis under investigation. Figure produced using images adapted from (*341-343*).

6.4 Technological advancements in lightsheet microscopy

We were only able to track the movements of around half of the cells present in spheroids, due to a loss of image resolution towards the core of spheroids and the difficulty of fusing multiple sample views. Since the development of LSFM, investigators have been continuously working to improve the spatial resolution and imaging depth penetration of this technique. Increasing the number and type of biological samples that can be imaged, in as natural a setting as possible, is another area of intensive investigation. The standard configuration of a lightsheet microscope, consisting of two excitation objectives mounted perpendicularly to a single detection objective, has been adapted to suit different aims and sample types. Conventionally mounted samples can now be imaged using an inverted lightsheet microscope (iSPIM),

removing the need to embed samples in hydrogels. In an iSPIM set-up, the illumination pillar of an inverted microscope supports a single excitation objective and a detection objective, mounted perpendicular to each other. The excitation and detection objectives are positioned above the sample and the lightsheet is scanned through the sample using a galvanometric mirror (*344*). The spatiotemporal resolution of this approach has been improved by alternating excitation and detection between the two objectives (dual-view illumination SPIM [diSPIM]). This allows for fast acquisition of two views of the sample (Fig 6.2) (*345*). However, it is worth noting that the successful merging of the two views is required in order to achieve improved spatial resolution. Additionally, the acquisition of multiple views by any means will increase the amount of data collected. Another approach to improving the resolution of LSFM is to combine it with two-photon excitation (*346*). Recently, two-photon excitation has been implemented in an iSPIM set-up (*347*). The development of iSPIM means that more types of biological samples can be imaged using LSFM and the advent of 3D printing means that it is easier than ever to make custom-built holders for these samples. Both iSPIM and diSPIM sets-ups are now available to purchase as a kit (*348*).

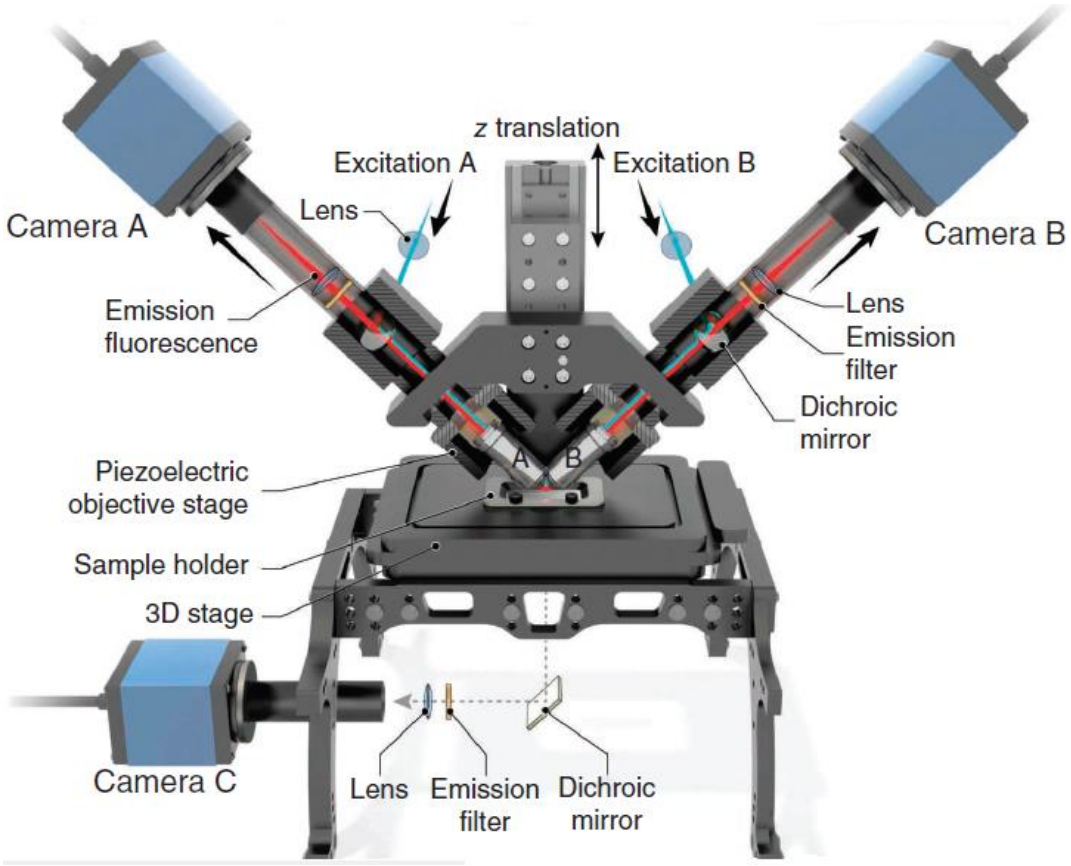

Figure 6.2. Dual-view inverted single plane microscopy (diSPIM). Dual objectives are mounted perpendicular to each other on the illumination pillar of an inverted microscope. Light sheet excitation is produced by objective A and detected on camera B through dichroic mirrors, emission filters and lenses. The piezoelectric stage moves the detection objective in synchronisation with the light sheet. To obtain a second view, excitation is switched to objective A and detection switched to camera B. Adapted by permission from Macmillan Publishers Ltd [Nature Biotechnology] (*345*) © 2013.

LSFM is being used for diverse applications, from single molecule to whole organism imaging (*338, 349, 350*). For optimal imaging conditions, it has become clear that the microscope needs to be adapted to suit the sample of interest. One of the disadvantages of purchasing a commercial, rather than a home-built, lightsheet microscope is that it cannot be adapted to suit different samples or address different questions. However, in multi-user microscopy facilities, commercial microscopes have the advantage of being simple to use. Furthermore, in this scenario, it is not possible to have a purpose-built microscope for each investigator. A major improvement in the

field of LSFM would be the development of an instrument that has the flexibility to image a broad variety of samples, without compromising image quality or sample physiology. One promising approach is swept, confocally-aligned planar excitation (SCAPE) microscopy, which provides light sheet excitation and detection using a single objective. The only component that is required to move is the scanning mirror, allowing for high-speed image acquisition in a variety of biological samples. SCAPE has been used to image whole body movements and muscle and heart contractions in freely moving *Drosophila* larvae, as well as neuronal calcium signalling in the cortex of an awake, behaving mouse (*351*).

6.5 The future: LSFM for 3D high-throughput screening

Conventional LSFM is incompatible with HTS, which requires the analyses of 96-well or 386-well plates. While iSPIM is compatible with tissue culture dishes and plates, it is not suitable for imaging multi-well plates because of their geometry (*352*). Francesco Pampaloni's group, who are based at the Buchmann Institute for Molecular Life Sciences in Frankfurt, are developing an LSFM set-up specifically designed for HTS of 3D cell cultures (*353*). They have pioneered the fabrication of multi-well plates from FEP film and are developing a synthetic hydrogel to support the physiological growth of 3D cell cultures (*354*). This approach is being applied to the production of pancreas organoids for the cellular therapy of type 1 diabetes (http://lsfm4life.eu). As well as contributing to the development of cellular therapies, this technique will change the landscape of drug discovery and toxicity screening in 3D cell cultures. The use of LSFM for HTS is set to become a reality in the near future; however, the enormous amounts of data this will generate will be extremely challenging to deal with.

The efficient processing of lightsheet data requires investment in computing facilities so that processing can be parallelised. Parallel processing can be achieved using multiple computers linked together in a cluster, or by using a single machine capable of general-purpose computing on graphics processing units (GPGPU computing). Neither of these methods was accessible during the course of this project; while the processing of lightsheet data was still possible, it was extremely time-consuming. Even when parallel processing is employed, image processing and data analyses is the main obstacle that needs to be overcome in order to increase the throughput of LSFM. Ideally, image processing and analyses should be carried out in real time. Schmid and Huisken have developed a method of carrying out real-time multiview deconvolution using GPGPU computing, which reduces processing times by a factor of 25 and 75 compared to processing with and without GPU support, respectively (*355*). We have benefited from advancements in image analyses software that allow for straightforward, automated and reproducible image segmentation and cell tracking. Before such technology was available, cell tracking had to be performed manually, which is both challenging and extremely slow. The next logical step would be to develop online image segmentation and tracking. This would represent a major advance in biological imaging and analyses.

An additional challenge posed by the use of LSFM for HTS is the storage of such large amounts of data. Our group are fortunate enough to have access to a 60TB server, which was adequate for this project. However, a server of this size would be nowhere near adequate for the amount of data generated by HTS. The huge amount of data generated by LSFM is forcing the lightsheet microscopy community to reassess what we consider to be raw data. In some cases, it is simply not possible to store all of the raw image files. An alternative option is to keep only the compressed or processed data and then delete the original files (*293*).

6.6 Final remarks

Initially, the aim of this thesis was to carry out an in-depth investigation into the relationship between hypoxia and the cell cycle. However, such relationships must always be considered within the broader context of the cellular environment. Tumours and their microenvironment are characterised by heterogeneity, which is one of the reasons cancer is so difficult to treat. Cancer is not a single disease with a single cause, and the historical approach of treating cancers of the same tissue as one disease is proving to be outdated. Tumours such as GBM can be categorised into different molecular subtypes, reflecting different origins and characteristics, with important implications for treatment. Thus far, despite many attempts to develop new therapies, there has been little progress in treating GBM. Tumour heterogeneity, the challenge of developing compounds that cross the BBB and the diffuse invasion of cells all contribute to the difficulty of treating this disease. As GBM has a diffusely infiltrating pattern from its inception, inhibiting invasion may be a case of 'shutting the stable door after the horse has bolted'. However, as invasiveness is a characteristic common to residual cells, a better understanding of this process may aid the development of therapies that can specifically target residual cells (*39*).

We have developed a 3D invasion assay that can be used to investigate the mechanisms of invasion. Technological and methodological advances mean that, in the near future, this assay could be used in a HTS approach to identify molecules that inhibit invasion and provide information on their mechanism of action. The use of 3D cell cultures for HTS will improve the translation of results from the bed to the bedside and further developments in 3D culture systems may allow future investigators to more closely replicate the solid tumour microenvironment *in vitro*. Modern biology increasing requires a multi-disciplinary approach. This is well illustrated by LSFM, in which the collaboration of physicists, biologists, computational

scientists and image analyses experts is required to get the most from the technique. Indeed, Reynaud *et al*. have commented that LSFM demands "a level of interdisciplinarity previously unseen in the biological sciences"(*293*). However, while the interdisciplinary nature of this technique can be challenging, collaborations between investigators from different backgrounds can lead to novel insights and approaches. The rapid pace of development in the field of lightsheet microscopy will change the landscape of biological imaging for years to come. It has been both challenging and exciting to be a part of the lightsheet microscopy community at a time of such great change.

References

1. J. Ferlay *et al.*, Cancer incidence and mortality worldwide: Sources, methods and major patterns in GLOBOCAN 2012. *International Journal of Cancer* **136**, E359-E386 (2015).
2. Office for National Statistics, Deaths registered in England and Wales (Series DR)(2014). Available from http://www.ons.gov.uk/. Accessed 20 August 2016.
3. M. Quaresma, M. P. Coleman, B. Rachet, 40-year trends in an index of survival for all cancers combined and survival adjusted for age and sex for each cancer in England and Wales, 1971-2011: a population-based study. *Lancet* **385**, 1206-1218 (2015).
4. D. M. Parkin, L. Boyd, L. C. Walker, The fraction of cancer attributable to lifestyle and environmental factors in the UK in 2010 Summary and conclusions. *British Journal of Cancer* **105**, S77-S81 (2011).
5. P. Pisani, D. M. Parkin, N. Munoz, J. Ferlay, Cancer and infection: Estimates of the attributable fraction in 1990. *Cancer Epidemiology Biomarkers & Prevention* **6**, 387-400 (1997).
6. D. Hanahan, R. A. Weinberg, The hallmarks of cancer. *Cell* **100**, 57-70 (2000).
7. D. Hanahan, R. A. Weinberg, Hallmarks of Cancer: The Next Generation. *Cell* **144**, 646-674 (2011).
8. B. Vogelstein, K. W. Kinzler, Cancer genes and the pathways they control. *Nature Medicine* **10**, 789-799 (2004).
9. D. N. Louis *et al.*, The 2007 WHO classification of tumours of the central nervous system. *Acta Neuropathologica* **114**, (2007).
10. T. A. Dolecek, J. M. Propp, N. E. Stroup, C. Kruchko, CBTRUS Statistical Report: Primary Brain and Central Nervous System Tumors Diagnosed in the United States in 2005-2009. *Neuro Oncol* **14 Suppl 5**, v1-v49 (2012).
11. B. Young, J. S. Lowe, A. Stevens, J. W. Heath, in *Wheater's functional histology: A text and colour atlas* (Elsevier, Amsterdam, Netherlands, 2006), Chapter 7: Nervous tissues, pp. 140-144.
12. S. Nag, Morphology and properties of astrocytes. *Methods Mol Biol* **686**, 69-100 (2011).
13. M. V. Sofroniew, H. V. Vinters, Astrocytes: biology and pathology. *Acta Neuropathologica* **119**, 7-35 (2010).
14. M. Santello, C. Cali, P. Bezzi, Gliotransmission and the Tripartite Synapse. *Synaptic Plasticity: Dynamics, Development and Disease* **970**, 307-331 (2012).
15. V. A. Cuddapah, S. Robel, S. Watkins, H. Sontheimer, A neurocentric perspective on glioma invasion. *Nature Reviews Neuroscience* **15**, 455-465 (2014).
16. R. Stupp *et al.*, Radiotherapy plus concomitant and adjuvant temozolomide for glioblastoma. *New England Journal of Medicine* **352**, (2005).

17. H. Ohgaki, P. Kleihues, Population-based studies on incidence, survival rates, and genetic alterations in astrocytic and oligodendroglial gliomas. *Journal of Neuropathology and Experimental Neurology* **64**, 479-489 (2005).
18. S. M. Chang *et al.*, Patterns of care for adults with newly diagnosed malignant glioma. *Jama-Journal of the American Medical Association* **293**, 557-564 (2005).
19. S. Larjavaara *et al.*, Incidence of gliomas by anatomic location. *Neuro-Oncology* **9**, 319-325 (2007).
20. G. Reifenberger, I. Blümcke, T. Pietsch, W. Paulus, in *Oncology of CNS tumors,* J.-C. Tonn, M. Wesphal, J. T. Rutka, Eds. (Springer, Berlin Heidelberg, 2010).
21. H. Ohgaki, P. Kleihues, Epidemiology and etiology of gliomas. *Acta Neuropathologica* **109**, 93-108 (2005).
22. F. de Almeida Sassi, A. Lunardi Brunetto, G. Schwartsmann, R. Roesler, A. L. Abujamra, Glioma revisited: from neurogenesis and cancer stem cells to the epigenetic regulation of the niche. *J Oncol* **2012**, 537861 (2012).
23. I. C. Gibbs, D. Haas-Kogan, S. Terezakis, B. D. Kavanagh, The subventricular zone neural progenitor cell hypothesis in glioblastoma: epiphany, trojan horse, or cheshire fact? *International Journal of Radiation Oncology Biology Physics* **86**, 606-608 (2013).
24. F. A. Siebzehnrubl, B. A. Reynolds, A. Vescovi, D. A. Steindler, L. P. Deleyrolle, The Origins of Glioma: E Pluribus Unum? *Glia* **59**, 1135-1147 (2011).
25. H. Ohgaki, P. Kleihues, Genetic pathways to primary and secondary glioblastoma. *American Journal of Pathology* **170**, 1445-1453 (2007).
26. Y. Yarden, The EGFR family and its ligands in human cancer: signalling mechanisms and therapeutic opportunities. *European Journal of Cancer* **37**, S3-S8 (2001).
27. J. W. Rocco, D. Sidransky, p16(MTS-1/CDKN2/INK4a) in cancer progression. *Experimental Cell Research* **264**, 42-55 (2001).
28. A. J. Levine, p53, the cellular gatekeeper for growth and division. *Cell* **88**, 323-331 (1997).
29. A. Di Cristofano, P. P. Pandolfi, The multiple roles of PTEN in tumor suppression. *Cell* **100**, 387-390 (2000).
30. R. G. W. Verhaak *et al.*, Integrated genomic analysis identifies clinically relevant subtypes of glioblastoma characterized by abnormalities in PDGFRA, IDH1, EGFR, and NF1. *Cancer Cell* **17**, 98-110 (2010).
31. A. Sottoriva *et al.*, Intratumor heterogeneity in human glioblastoma reflects cancer evolutionary dynamics. *Proceedings of the National Academy of Sciences of the United States of America* **110**, 4009-4014 (2013).
32. I. Christensen, N0019653 medio-transverse section. *Welcome Images* (https://wellcomeimages.org/). Accessed August 2016.
33. K. Yamashita *et al.*, MR imaging-based analysis of glioblastoma multiforme: estimation of IDH1 mutation status. *American Journal of Neuroradiology* **37**, 58-65 (2016).
34. A. Claes, A. J. Idema, P. Wesseling, Diffuse glioma growth: a guerilla war. *Acta Neuropathologica* **114**, 443-458 (2007).

35. R. Stupp *et al.*, Effects of radiotherapy with concomitant and adjuvant temozolomide versus radiotherapy alone on survival in glioblastoma in a randomised phase III study: 5-year analysis of the EORTC-NCIC trial. *Lancet Oncology* **10**, (2009).
36. D. A. Reardon, P. Y. Wen, Therapeutic advances in the treatment of glioblastoma: Rationale and potential role of targeted agents. *Oncologist* **11**, (2006).
37. C. P. Haar *et al.*, Drug Resistance in Glioblastoma: A Mini Review. *Neurochemical Research* **37**, 1192-1200 (2012).
38. K. Petrecca, M.-C. Guiot, V. Panet-Raymond, L. Souhami, Failure pattern following complete resection plus radiotherapy and temozolomide is at the resection margin in patients with glioblastoma. *Journal of Neuro-Oncology* **111**, 19-23 (2013).
39. A. Giese, R. Bjerkvig, M. E. Berens, M. Westphal, Cost of migration: Invasion of malignant gliomas and implications for treatment. *Journal of Clinical Oncology* **21**, 1624-1636 (2003).
40. M. E. Hegi *et al.*, MGMT gene silencing and benefit from temozolomide in glioblastoma. *New England Journal of Medicine* **352**, (2005).
41. A. E. Pegg, T. L. Byers, Repair of DNA containing O6-alkylguanine. *Faseb Journal* **6**, 2302-2310 (1992).
42. D. Lau, S. T. Magill, M. K. Aghi, Molecularly targeted therapies for recurrent glioblastoma: current and future targets. *Neurosurgical Focus* **37**, (2014).
43. H. Wang *et al.*, The Challenges and the Promise of Molecular Targeted Therapy in Malignant Gliomas. *Neoplasia* **17**, 239-255 (2015).
44. O. van Tellingen *et al.*, Overcoming the blood-brain tumor barrier for effective glioblastoma treatment. *Drug Resistance Updates* **19**, 1-12 (2015).
45. M. Westphal *et al.*, A phase 3 trial of local chemotherapy with biodegradable carmustine (BCNU) wafers (Gliadel wafers) in patients with primary malignant glioma. *Neuro-Oncology* **5**, 79-88 (2003).
46. W.-k. Xing, C. Shao, Z.-y. Qi, C. Yang, Z. Wang, The role of Gliadel wafers in the treatment of newly diagnosed GBM: a meta-analysis. *Drug Design Development and Therapy* **9**, 3341-3348 (2015).
47. A. Bregy *et al.*, The role of Gliadel wafers in the treatment of high-grade gliomas. *Expert Review of Anticancer Therapy* **13**, 1453-1461 (2013).
48. S. J. Price *et al.*, NICE guidance on the use of carmustine wafers in high grade gliomas: a national study on variation in practice. *British Journal of Neurosurgery* **26**, 331-335 (2012).
49. S. Nag, Morphology and properties of brain endothelial cells. *Methods Mol Biol* **686**, 3-47 (2011).
50. N. J. Abbott, L. Ronnback, E. Hansson, Astrocyte-endothelial interactions at the blood-brain barrier. *Nature Reviews Neuroscience* **7**, 41-53 (2006).
51. R. Suryadinata, M. Sadowski, B. Sarcevic, Control of cell cycle progression by phosphorylation of cyclin-dependent kinase (CDK) substrates. *Bioscience Reports* **30**, 243-255 (2010).
52. C. J. Sherr, Cancer cell cycles. *Science* **274**, 1672-1677 (1996).

53. C. J. Sherr, J. M. Roberts, CDK inhibitors: positive and negative regulators of G(1)-phase progression. *Genes & Development* **13**, 1501-1512 (1999).
54. M. Hollstein *et al.*, Database of p53 gene somatic mutations in human tumors and cell-lines. *Nucleic Acids Research* **22**, 3551-3555 (1994).
55. P. B. S. Lai, T. Y. Chi, G. G. Chen, Different levels of p53 induced either apoptosis or cell cycle arrest in a doxycycline-regulated hepatocellular carcinoma cell line in vitro. *Apoptosis* **12**, 387-393 (2007).
56. M. Kracikova, G. Akiri, A. George, R. Sachidanandam, S. A. Aaronson, A threshold mechanism mediates p53 cell fate decision between growth arrest and apoptosis. *Cell Death and Differentiation* **20**, 576-588 (2013).
57. P. Vaupel, Tumor microenvironmental physiology and its implications for radiation oncology. *Seminars in Radiation Oncology* **14**, 198-206 (2004).
58. N. E. Sounni, A. Noel, Targeting the tumor microenvironment for cancer therapy. *Clin Chem* **59**, 85-93 (2013).
59. M. Egeblad, E. S. Nakasone, Z. Werb, Tumors as Organs: Complex Tissues that Interface with the Entire Organism. *Developmental Cell* **18**, 884-901 (2010).
60. D. Schiffer, *Brain Tumors: biology, pathology, and clinical references*. (Springer, Berlin, ed. 2nd, 1997).
61. D. B. Hoelzinger, T. Demuth, M. E. Berens, Autocrine factors that sustain glioma invasion and paracrine biology in the brain microenvironment. *Journal of the National Cancer Institute* **99**, 1583-1593 (2007).
62. E. I. Fomchenko *et al.*, Recruited cells can become transformed and overtake PDGF-induced murine gliomas in vivo during tumor progression. *Plos One* **6**, (2011).
63. A. M. Katz *et al.*, Astrocyte-specific expression patterns associated with the PDGF-induced glioma microenvironment. *PLoS One* **7**, e32453 (2012).
64. R. Glass *et al.*, Glioblastoma-induced attraction of endogenous neural precursor cells is associated with improved survival. *Journal of Neuroscience* **25**, 2637-2646 (2005).
65. K. Stock *et al.*, Neural precursor cells induce cell death of high-grade astrocytomas through stimulation of TRPV1. *Nature Medicine* **18**, 1232-+ (2012).
66. H. S. Venkatesh *et al.*, Neuronal activity promotes glioma growth through neuroligin-3 secretion. *Cell* **161**, 803-816 (2015).
67. Z. C. Ye, H. Sontheimer, Glioma cells release excitotoxic concentrations of glutamate. *Cancer Research* **59**, 4383-4391 (1999).
68. T. Takano *et al.*, Glutamate release promotes growth of malignant gliomas. *Nature Medicine* **7**, 1010-1015 (2001).
69. H. Sontheimer, A role for glutamate in growth and invasion of primary brain tumors. *Journal of Neurochemistry* **105**, 287-295 (2008).
70. G. Helmlinger, F. Yuan, M. Dellian, R. K. Jain, Interstitial pH and pO(2) gradients in solid tumors in vivo: High-resolution measurements reveal a lack of correlation. *Nature Medicine* **3**, 177-182 (1997).

71. R. H. Thomlinson, L. H. Gray, The histological structure of some human lung cancers and the possible implications for radiotherapy. *British Journal of Cancer* **9**, 539-& (1955).
72. S. Brem, J. Folkman, R. Cotran, Tumor angiogenesis - quantitative method for histologic grading. *Journal of the National Cancer Institute* **48**, 347-& (1972).
73. P. Vajkoczy, M. D. Menger, Vascular microenvironment in gliomas. *Journal of Neuro-Oncology* **50**, 99-108 (2000).
74. Y. Boucher, H. Salehi, B. Witwer, G. R. Harsh, R. K. Jain, Interstitial fluid pressure in intracranial tumours in patients and in rodents. *British Journal of Cancer* **75**, 829-836 (1997).
75. S. K. Hobbs *et al.*, Regulation of transport pathways in tumor vessels: Role of tumor type and microenvironment. *Proceedings of the National Academy of Sciences of the United States of America* **95**, 4607-4612 (1998).
76. X. Kostaras *et al.*, Use of dexamethasone in patients with high-grade glioma: a clinical practice guideline. *Current Oncology* **21**, E493-E503 (2014).
77. J. W. Baish, P. A. Netti, R. K. Jain, Transmural coupling of fluid flow in microcirculatory network and interstitium in tumors. *Microvascular Research* **53**, 128-141 (1997).
78. R. T. Tong *et al.*, Vascular normalization by vascular endothelial growth factor receptor 2 blockade induces a pressure gradient across the vasculature and improves drug penetration in tumors. *Cancer Research* **64**, 3731-3736 (2004).
79. J. Holash *et al.*, Vessel cooption, regression, and growth in tumors mediated by angiopoietins and VEGF. *Science* **284**, 1994-1998 (1999).
80. P. Vaupel, F. Kallinowski, P. Okunieff, Blood-flow, oxygen and nutrient supply, and metabolic microenvironment of human-tumors - a review. *Cancer Research* **49**, (1989).
81. K. Ruan, G. Song, G. Ouyang, Role of Hypoxia in the Hallmarks of Human Cancer. *Journal of Cellular Biochemistry* **107**, (2009).
82. G. L. Semenza, Defining the role of hypoxia-inducible factor 1 in cancer biology and therapeutics. *Oncogene* **29**, (2010).
83. Q. Liu, P. Cao, Clinical and prognostic significance of HIF-1 alpha in glioma patients: a meta-analysis. *International Journal of Clinical and Experimental Medicine* **8**, 22073-22083 (2015).
84. J. R. Flynn *et al.*, Hypoxia-regulated protein expression, patient characteristics, and preoperative imaging as predictors of survival in adults with glioblastoma multiforme. *Cancer* **113**, 1032-1042 (2008).
85. S. Rockwell, I. T. Dobrucki, E. Y. Kim, S. T. Marrison, V. T. Vu, Hypoxia and Radiation Therapy: Past History, Ongoing Research, and Future Promise. *Current Molecular Medicine* **9**, 442-458 (2009).
86. K. M. Comerford *et al.*, Hypoxia-inducible factor-1-dependent regulation of the multidrug resistance (MDR1) gene. *Cancer Research* **62**, 3387-3394 (2002).
87. G. L. Semenza, Targeting HIF-1 for cancer therapy. *Nature Reviews Cancer* **3**, (2003).

88. Y. X. Liu, S. R. Cox, T. Morita, S. Kourembanas, Hypoxia regulates vascular endothelial growth-factor gene-expression in endothelial-cells - identification of a 5'-enhancer. *Circulation Research* **77**, 638-643 (1995).
89. F. Yuan *et al.*, Time-dependent vascular regression and permeability changes in established human tumor xenografts induced by an anti-vascular endothelial growth factor/vascular permeability factor antibody. *Proc Natl Acad Sci U S A* **93**, 14765-14770 (1996).
90. W. N. Tong, F. X. Xiong, Y. Li, L. B. Zhang, Hypoxia inhibits cardiomyocyte proliferation in fetal rat hearts via upregulating TIMP-4. *American Journal of Physiology-Regulatory Integrative and Comparative Physiology* **304**, R613-R620 (2013).
91. C. G. Lee *et al.*, Anti-vascular endothelial growth factor treatment augments tumor radiation response under normoxic or hypoxic conditions. *Cancer Research* **60**, 5565-5570 (2000).
92. M. R. Gilbert *et al.*, A Randomized Trial of Bevacizumab for Newly Diagnosed Glioblastoma. *New England Journal of Medicine* **370**, 699-708 (2014).
93. O. L. Chinot *et al.*, Bevacizumab plus radiotherapy-temozolomide for newly diagnosed glioblastoma. *New England Journal of Medicine* **370**, 709-722 (2014).
94. A. D. Norden *et al.*, Bevacizumab for recurrent malignant gliomas - Efficacy, toxicity, and patterns of recurrence. *Neurology* **70**, 779-787 (2008).
95. A. Narayana *et al.*, Antiangiogenic therapy using bevacizumab in recurrent high-grade glioma: impact on local control and patient survival. *Journal of Neurosurgery* **110**, 173-180 (2009).
96. A. K. Lucio-Eterovic, Y. Piao, J. F. de Groot, Mediators of Glioblastoma Resistance and Invasion during Antivascular Endothelial Growth Factor Therapy. *Clinical Cancer Research* **15**, 4589-4599 (2009).
97. M. E. Hardee, D. Zagzag, Mechanisms of Glioma-Associated Neovascularization. *American Journal of Pathology* **181**, 1126-1141 (2012).
98. A. Carreau, B. El Hafny-Rahbi, A. Matejuk, C. Grillon, C. Kieda, Why is the partial oxygen pressure of human tissues a crucial parameter? Small molecules and hypoxia. *Journal of Cellular and Molecular Medicine* **15**, 1239-1253 (2011).
99. W. E. Hoffman, F. T. Charbel, G. Edelman, Brain tissue oxygen, carbon dioxide, and pH in neurosurgical patients at risk for ischemia. *Anesthesia and Analgesia* **82**, 582-586 (1996).
100. J. Meixensberger, J. Dings, H. Kuhnigk, K. Roosen, Studies of tissue PO2 in normal and pathological human brain cortex. *Acta neurochirurgica. Supplementum* **59**, 58-63 (1993).
101. T. Kayama, T. Yoshimoto, S. Fujimoto, Y. Sakurai, Intratumoral oxygen-pressure in malignant brain-tumor. *Journal of Neurosurgery* **74**, 55-59 (1991).
102. T. Beppu *et al.*, Change of oxygen pressure in glioblastoma tissue under various conditions. *Journal of Neuro-Oncology* **58**, 47-52 (2002).

103. I. R. Whittle, N. Stavrinos, H. Akil, Y. Yau, S. C. Lewis, Assessment of physiological parameters within glioblastomas in awake patients: a prospective clinical study. *British Journal of Neurosurgery* **24**, (2010).
104. D. R. Collingridge, J. M. Piepmeier, S. Rockwell, J. P. S. Knisely, Polarographic measurements of oxygen tension in human glioma and surrounding peritumoural brain tissue. *Radiotherapy and Oncology* **53**, 127-131 (1999).
105. R. Rampling, G. Cruickshank, A. D. Lewis, S. A. Fitzsimmons, P. Workman, Direct measurement of pO2 distribution and bioreductive enzymes in human-malignant brain-tumors. *International Journal of Radiation Oncology Biology Physics* **29**, 427-431 (1994).
106. J. Magat, B. F. Jordan, G. O. Cron, B. Gallez, Noninvasive mapping of spontaneous fluctuations in tumor oxygenation using F-19 MRI. *Medical Physics* **37**, (2010).
107. H. Kimura *et al.*, Fluctuations in red cell flux in tumor microvessels can lead to transient hypoxia and reoxygenation in tumor parenchyma. *Cancer Research* **56**, (1996).
108. M. W. Dewhirst, Relationships between cycling hypoxia, HIF-1, angiogenesis and oxidative stress. *Radiation Research* **172**, (2009).
109. P. Martinive *et al.*, Preconditioning of the tumor vasculature and tumor cells by intermittent hypoxia: Implications for anti-cancer therapies. *Acta Clinica Belgica* **63**, (2008).
110. C.-H. Hsieh, H.-T. Chang, W.-C. Shen, W.-C. Shyu, R.-S. Liu, Imaging the impact of nox4 in cycling hypoxia-mediated U87 glioblastoma invasion and infiltration. *Molecular Imaging and Biology* **14**, (2012).
111. C.-W. Chou *et al.*, Tumor cycling hypoxia induces chemoresistance in glioblastoma multiforme by upregulating the expression and function of ABCB1. *Neuro-oncology* **14**, 1227-1238 (2012).
112. F. Pistollato *et al.*, Intratumoral hypoxic gradient drives stem cells distribution and MGMT expression in glioblastoma. *Stem Cells* **28**, (2010).
113. G. L. Wang, B. H. Jiang, E. A. Rue, G. L. Semenza, Hypoxia-inducible factor-1 is a basic-helix-loop-helix-pas heterodimer regulated by cellular O2 tension. *Proceedings of the National Academy of Sciences of the United States of America* **92**, (1995).
114. M. Ema *et al.*, A novel bHLH-PAS factor with close sequence similarity to hypoxia-inducible factor 1 alpha regulates the VEGF expression and is potentially involved in lung and vascular development. *Proceedings of the National Academy of Sciences of the United States of America* **94**, (1997).
115. Y. Makino, A. Kanopka, W. J. Wilson, H. Tanaka, L. Poellinger, Inhibitory PAS domain protein (IPAS) is a hypoxia-inducible splicing variant of the hypoxia-inducible factor-3 alpha locus. *Journal of Biological Chemistry* **277**, (2002).
116. K. L. Talks *et al.*, The expression and distribution of the hypoxia-inducible factors HIF-1 alpha and HIF-2 alpha in normal human tissues, cancers, and tumor-associated macrophages. *American Journal of Pathology* **157**, 411-421 (2000).

117. L. E. Huang, Z. Arany, D. M. Livingston, H. F. Bunn, Activation of hypoxia-inducible transcription factor depends primarily upon redox-sensitive stabilization of its alpha subunit. *Journal of Biological Chemistry* **271**, (1996).
118. R. K. Bruick, S. L. McKnight, A conserved family of prolyl-4-hydroxylases that modify HIF. *Science* **294**, (2001).
119. A. C. Epstein *et al.*, C. elegans EGL-9 and mammalian homologs define a family of dioxygenases that regulate HIF by prolyl hydroxylation. *Cell* **107**, 43-54 (2001).
120. M. Ivan *et al.*, HIF alpha targeted for VHL-mediated destruction by proline hydroxylation: Implications for O-2 sensing. *Science* **292**, (2001).
121. L. E. Huang, J. Gu, M. Schau, H. F. Bunn, Regulation of hypoxia-inducible factor 1 alpha is mediated by an O2-dependent degradation domain via the ubiquitin-proteasome pathway. *Proceedings of the National Academy of Sciences of the United States of America* **95**, (1998).
122. D. Lando, D. J. Peet, D. A. Whelan, J. J. Gorman, M. L. Whitelaw, Asparagine hydroxylation of the HIF transactivation domain: A hypoxic switch. *Science* **295**, (2002).
123. P. J. Kallio, I. Pongratz, K. Gradin, J. McGuire, L. Poellinger, Activation of hypoxia-inducible factor 1 alpha: Posttranscriptional regulation and conformational change by recruitment of the Arnt transcription factor. *Proceedings of the National Academy of Sciences of the United States of America* **94**, (1997).
124. R. S. Pollenz, C. A. Sattler, A. Poland, The aryl-hydrocarbon receptor and aryl-hydrocarbon receptor nuclear translocator protein show distinct subcellular localizations in hepa 1c1c7 cells by immunofluorescence microscopy. *Molecular Pharmacology* **45**, (1994).
125. Y. S. Chun, M. S. Kim, J. W. Park, Oxygen-dependent and -independent regulation of HIF-1alpha. *Journal of Korean Medical Science* **17**, 581-588 (2002).
126. G. L. Semenza, HIF-1: upstream and downstream of cancer metabolism. *Current Opinion in Genetics & Development* **20**, 51-56 (2010).
127. M. Upadhyay, J. Samal, M. Kandpal, O. V. Singh, P. Vivekanandan, The Warburg effect: Insights from the past decade. *Pharmacology & Therapeutics* **137**, 318-330 (2013).
128. B. Alberts *et al.*, *Molecular biology of the cell*. (Garland Science, New York, ed. 4th, 2002).
129. M. Erecinska, I. A. Silver, ATP and brain-function. *Journal of Cerebral Blood Flow and Metabolism* **9**, 2-19 (1989).
130. O. Warburg, Origin of cancer cells. *Science* **123**, 309-314 (1956).
131. N. Masson, P. J. Ratcliffe, Hypoxia signaling pathways in cancer metabolism: the importance of co-selecting interconnected physiological pathways. *Cancer & metabolism* **2**, 3-3 (2014).
132. S. S. Gambhir, Molecular imaging of cancer with positron emission tomography. *Nature Reviews Cancer* **2**, 683-693 (2002).

133. C. Granchi, D. Fancelli, F. Minutolo, An update on therapeutic opportunities offered by cancer glycolytic metabolism. *Bioorganic & Medicinal Chemistry Letters* **24**, 4915-4925 (2014).
134. R. Moreno-Sanchez *et al.*, Who controls the ATP supply in cancer cells? Biochemistry lessons to understand cancer energy metabolism. *International Journal of Biochemistry & Cell Biology* **50**, 10-23 (2014).
135. R. Moreno-Sanchez, S. Rodriguez-Enriquez, A. Marin-Hernandez, E. Saavedra, Energy metabolism in tumor cells. *Febs Journal* **274**, 1393-1418 (2007).
136. R. Rossignol *et al.*, Energy substrate modulates mitochondrial structure and oxidative capacity in cancer cells. *Cancer Research* **64**, 985-993 (2004).
137. K. Smolkova *et al.*, Mitochondrial bioenergetic adaptations of breast cancer cells to aglycemia and hypoxia. *Journal of Bioenergetics and Biomembranes* **42**, 55-67 (2010).
138. G. Gstraunthaler, T. Seppi, W. Pfaller, Impact of culture conditions, culture media volumes, and glucose content on metabolic properties of renal epithelial cell cultures - Are renal cells in tissue culture hypoxic? *Cellular Physiology and Biochemistry* **9**, 150-172 (1999).
139. H. G. Crabtree, Observations on the carbohydrate metabolism of tumours. *Biochemical Journal* **23**, 536-545 (1929).
140. M. A. Kiebish, X. Han, H. Cheng, T. N. Seyfried, In vitro growth environment produces lipidomic and electron transport chain abnormalities in mitochondria from non-tumorigenic astrocytes and brain tumours. *Asn Neuro* **1**, (2009).
141. A. Wolf, S. Agnihotri, A. Guha, Targeting metabolic remodeling in glioblastoma multiforme. *Oncotarget* **1**, 552-562 (2010).
142. N. C. Denko, Hypoxia, HIF1 and glucose metabolism in the solid tumour. *Nature Reviews Cancer* **8**, 705-713 (2008).
143. C. Sandt, C. Nadaradjane, R. Richards, P. Dumas, V. See, Use of infrared microspectroscopy to elucidate a specific chemical signature associated with hypoxia levels found in glioblastoma. *Analyst* **141**, 870-883 (2016).
144. G. Laurenti *et al.*, Hypoxia induces peroxisome proliferator-activated receptor alpha (PPAR alpha) and lipid metabolism peroxisomal enzymes in human glioblastoma cells. *Journal of Cellular Biochemistry* **112**, 3891-3901 (2011).
145. M. Erecinska, S. Cherian, I. A. Silver, Energy metabolism in mammalian brian during development. *Progress in Neurobiology* **73**, 397-445 (2004).
146. S. N. Vaishnavi *et al.*, Regional aerobic glycolysis in the human brain. *Proceedings of the National Academy of Sciences of the United States of America* **107**, 17757-17762 (2010).
147. G. A. Dienel, N. F. Cruz, Aerobic glycolysis during brain activation: adrenergic regulation and influence of norepinephrine on astrocytic metabolism. *Journal of Neurochemistry* **138**, 14-52 (2016).
148. M. S. Goyal, M. Hawrylycz, J. A. Miller, A. Z. Snyder, M. E. Raichle, Aerobic glycolysis in the human brain is associated with development and neotenous gene expression. *Cell Metabolism* **19**, 49-57 (2014).

149. P. Mergenthaler, U. Lindauer, G. A. Dienel, A. Meisel, Sugar for the brain: the role of glucose in physiological and pathological brain function. *Trends in Neurosciences* **36**, 587-597 (2013).
150. P. Chinnaiyan *et al.*, The metabolomic signature of malignant glioma reflects accelerated anabolic metabolism. *Cancer Research* **72**, 5878-5888 (2012).
151. R. J. DeBerardinis *et al.*, Beyond aerobic glycolysis: Transformed cells can engage in glutamine metabolism that exceeds the requirement for protein and nucleotide synthesis. *Proceedings of the National Academy of Sciences of the United States of America* **104**, 19345-19350 (2007).
152. C. E. Griguer, C. R. Oliva, G. Y. Gillespie, Glucose metabolism heterogeneity in human and mouse malignant glioma cell lines. *Journal of Neuro-Oncology* **74**, 123-133 (2005).
153. P. Tabatabaei, P. Bergstrom, R. Henriksson, A. T. Bergenheim, Glucose metabolites, glutamate and glycerol in malignant glioma tumours during radiotherapy. *Journal of Neuro-Oncology* **90**, 35-39 (2008).
154. I. Marin-Valencia *et al.*, Analysis of Tumor Metabolism Reveals Mitochondrial Glucose Oxidation in Genetically Diverse Human Glioblastomas in the Mouse Brain In Vivo. *Cell Metabolism* **15**, 827-837 (2012).
155. E. A. Maher *et al.*, Metabolism of U-13C glucose in human brain tumors in vivo. *Nmr in Biomedicine* **25**, 1234-1244 (2012).
156. D. Guo, E. H. Bell, A. Chakravarti, Lipid metabolism emerges as a promising target for malignant glioma therapy. *CNS oncology* **2**, 289-299 (2013).
157. K. C. Patra, N. Hay, Hexokinase 2 as oncotarget. *Oncotarget* **4**, 1862-1863 (2013).
158. A. Wolf *et al.*, Hexokinase 2 is a key mediator of aerobic glycolysis and promotes tumor growth in human glioblastoma multiforme. *Journal of Experimental Medicine* **208**, 313-326 (2011).
159. M.-J. Blouin *et al.*, Loss of function of PTEN alters the relationship between glucose concentration and cell proliferation, increases glycolysis, and sensitizes cells to 2-deoxyglucose. *Cancer Letters* **289**, 246-253 (2010).
160. J. Balss *et al.*, Analysis of the IDH1 codon 132 mutation in brain tumors. *Acta Neuropathologica* **116**, 597-602 (2008).
161. M. Sanson *et al.*, Isocitrate dehydrogenase 1 codon 132 mutation is an important prognostic biomarker in gliomas. *Journal of Clinical Oncology* **27**, 4150-4154 (2009).
162. H. Yan *et al.*, IDH1 and IDH2 mutations in gliomas. *New England Journal of Medicine* **360**, 765-773 (2009).
163. L. Dang *et al.*, Cancer-associated IDH1 mutations produce 2-hydroxyglutarate. *Nature* **462**, 739-U752 (2009).
164. P. Koivunen *et al.*, Transformation by the (R)-enantiomer of 2-hydroxyglutarate linked to EGLN activation. *Nature* **483**, 485-U144 (2012).
165. D. Rohle *et al.*, An Inhibitor of Mutant IDH1 Delays Growth and Promotes Differentiation of Glioma Cells. *Science* **340**, 626-630 (2013).

166. J.-A. Losman, W. G. Kaelin, Jr., What a difference a hydroxyl makes: mutant IDH, (R)-2-hydroxyglutarate, and cancer. *Genes & Development* **27**, 836-852 (2013).
167. G. Kalokhe *et al.*, Metastatic glioblastoma: case presentations and a review of the literature. *Journal of Neuro-Oncology* **107**, 21-27 (2012).
168. A. C. Bellail, S. B. Hunter, D. J. Brat, C. Tan, E. G. Van Meir, Microregional extracellular matrix heterogeneity in brain modulates glioma cell invasion. *International Journal of Biochemistry & Cell Biology* **36**, 1046-1069 (2004).
169. W. E. Dandy, Removal of right cerebral hemisphere for certain tumors with hemiplegia - Preliminary report. *Journal of the American Medical Association* **90**, 823-825 (1928).
170. H. J. Scherer, Structural development in gliomas. *The American Journal of Cancer* **XXXIV**, 333-351 (1938).
171. M. Segarra, B. C. Kirchmaier, A. Acker-Palmer, A vascular perspective on neuronal migration. *Mech Dev* **138 Pt 1**, 17-25 (2015).
172. A. Farin *et al.*, Transplanted glioma cells migrate and proliferate on host brain vasculature: A dynamic analysis. *Glia* **53**, 799-808 (2006).
173. F. Winkler *et al.*, Imaging Glioma Cell Invasion In Vivo Reveals Mechanisms of Dissemination and Peritumoral Angiogenesis. *Glia* **57**, 1306-1315 (2009).
174. S. Watkins *et al.*, Disruption of astrocyte-vascular coupling and the blood-brain barrier by invading glioma cells. *Nat Commun* **5**, 4196 (2014).
175. V. Montana, H. Sontheimer, Bradykinin promotes the chemotactic invasion of primary brain tumors. *J Neurosci* **31**, 4858-4867 (2011).
176. J. J. Bernstein, C. A. Woodard, Glioblastoma cells do not intravasate into blood vessels. *Neurosurgery* **36**, 124-132; discussion 132 (1995).
177. S. Lal, J. La Du, R. L. Tanguay, J. A. Greenwood, Calpain 2 is required for the invasion of glioblastoma cells in the zebrafish brain microenvironment. *J Neurosci Res* **90**, 769-781 (2012).
178. L. G. Dubois *et al.*, Gliomas and the vascular fragility of the blood brain barrier. *Frontiers in Cellular Neuroscience* **8**, (2014).
179. A. P. Anzil, Glioblastoma multiforme with exgracranial metastases in absence of previous craniotomy - case report. *Journal of Neurosurgery* **33**, 88-& (1970).
180. M. Lun, E. Lok, S. Gautam, E. Wu, E. T. Wong, The natural history of extracranial metastasis from glioblastoma multiforme. *Journal of Neuro-Oncology* **105**, 261-273 (2011).
181. A. Aspelund *et al.*, A dural lymphatic vascular system that drains brain interstitial fluid and macromolecules. *Journal of Experimental Medicine* **212**, 991-999 (2015).
182. A. Louveau *et al.*, Structural and functional features of central nervous system lymphatic vessels. *Nature* **523**, 337-+ (2015).
183. S. Jimsheleishvili *et al.*, Extracranial glioblastoma in transplant recipients. *Journal of Cancer Research and Clinical Oncology* **140**, 801-807 (2014).
184. C. Muller *et al.*, Hematogenous dissemination of glioblastoma multiforme. *Science Translational Medicine* **6**, (2014).

185. R. G. Thorne, C. Nicholson, In vivo diffusion analysis with quantum dots and dextrans predicts the width of brain extracellular space. *Proceedings of the National Academy of Sciences of the United States of America* **103**, 5567-5572 (2006).
186. E. Ruoslahti, Brain extracellular matrix. *Glycobiology* **6**, 489-492 (1996).
187. R. H. Goldbrunner, J. J. Bernstein, J. C. Tonn, Cell-extracellular matrix interaction in glioma invasion. *Acta Neurochirurgica* **141**, 295-305 (1999).
188. R. O. Hynes, Integrins: bidirectional, allosteric signaling machines. *Cell* **110**, 673-687 (2002).
189. S. M. Weis, D. A. Cheresh, alpha v Integrins in Angiogenesis and Cancer. *Cold Spring Harbor Perspectives in Medicine* **1**, (2011).
190. O. Schnell *et al.*, Expression of integrin avb3 in gliomas correlates with tumor grade and is not restricted to tumor vasculature. *Brain Pathology* **18**, 378-386 (2011).
191. J. Ishida *et al.*, Integrin Inhibitor suppresses bevacizumab-induced glioma invasion. *Translational Oncology* **7**, 292-U305 (2014).
192. M. Onishi *et al.*, Bimodal anti-glioma mechanisms of cilengitide demonstrated by novel invasive glioma models. *Neuropathology* **33**, 162-174 (2013).
193. M. Egeblad, Z. Werb, New functions for the matrix metalloproteinases in cancer progression. *Nature Reviews Cancer* **2**, 161-174 (2002).
194. P. A. Forsyth *et al.*, Gelatinase-A (MMP-2), gelatinase-B (MMP-9) and membrane type matrix metalloproteinase-1 (MT1-MMP) are involved in different aspects of the pathophysiology of malignant gliomas. *British Journal of Cancer* **79**, 1828-1835 (1999).
195. O. Mendez *et al.*, Knock down of HIF-1 alpha in glioma cells reduces migration in vitro and invasion in vivo and impairs their ability to form tumor spheres. *Molecular Cancer* **9**, 10 (2010).
196. S. Fujiwara *et al.*, Silencing hypoxia-inducible factor-1 alpha inhibits cell migration and invasion under hypoxic environment in malignant gliomas. *International Journal of Oncology* **30**, 793-802 (2007).
197. D. Zagzag *et al.*, Hypoxia-inducible factor 1 and VEGF upregulate CXCR4 in glioblastoma: implications for angiogenesis and glioma cell invasion. *Laboratory Investigation* **86**, 1221-1232 (2006).
198. K. D. C. Dahl, S. E. Robertson, V. M. Weaver, M. C. Simon, Hypoxia-inducible factor regulates alpha v ss 3 integrin cell surface expression. *Molecular Biology of the Cell* **16**, 1901-1912 (2005).
199. A. Herrmann *et al.*, Cellular memory of itypoxia elicits neuroblastoma metastasis and enables invasion by non-aggressive neighbouring cells. *Oncogenesis* **4**, (2015).
200. N. Gagliano *et al.*, Glioma-astrocyte interaction modifies the astrocyte phenotype in a co-culture experimental model. *Oncology Reports* **22**, 1349-1356 (2009).
201. D. M. Le *et al.*, Exploitation of astrocytes by glioma cells to facilitate invasiveness: A mechanism involving matrix metalloproteinase-2 and the

urokinase-type plasminogen activator-plasmin cascade. *Journal of Neuroscience* **23**, 4034-4043 (2003).

202. R. Oliveira *et al.*, Contribution of gap junctional communication between tumor cells and astroglia to the invasion of the brain parenchyma by human glioblastomas. *Bmc Cell Biology* **6**, (2005).
203. P. Gabelloni *et al.*, Inhibition of metalloproteinases derived from tumours: new insights in the treatment of human glioblastoma. *Neuroscience* **168**, 514-522 (2010).
204. M. D. Groves *et al.*, Phase II trial of temozolomide plus marimastat for recurrent anaplastic gliomas: A relationship among efficacy, joint toxicity and anticonvulsant status. *Journal of Neuro-Oncology* **80**, 83-90 (2006).
205. B. M. Baker, C. S. Chen, Deconstructing the third dimension - how 3D culture microenvironments alter cellular cues. *Journal of Cell Science* **125**, 3015-3024 (2012).
206. B. Larson, 3D cell culture: a review of current techniques. (2015). Available from http://www.biotek.com/resources/articles/3d-cell-culture-review-of-current-techniques.html. Accessed August 2016.
207. R. Edmondson, A. F. Adcock, L. J. Yang, Influence of Matrices on 3D-Cultured Prostate Cancer Cells' Drug Response and Expression of Drug-Action Associated Proteins. *Plos One* **11**, (2016).
208. R. M. Sutherland, J. A. McCredie, W. R. Inch, Growth of multicell spheroids in tissue culture as a model of nodular carcinomas. *Journal of the National Cancer Institute* **46**, 113-& (1971).
209. R. M. Sutherland, Importance of critical metabolites and cellular interactions in the biology of microregions of tumors. *Cancer* **58**, 1668-1680 (1986).
210. W. Muellerklieser, J. P. Freyer, R. M. Sutherland, Influence of glucose and oxygen-supply conditions on the oxygenation of multicellular spheroids. *British Journal of Cancer* **53**, 345-353 (1986).
211. W. F. Muellerklieser, R. M. Sutherland, Oxygen-tensions in multicell spheroids of 2 cell-lines. *British Journal of Cancer* **45**, 256-264 (1982).
212. L. A. KunzSchughart, K. Groebe, W. MuellerKlieser, Three-dimensional cell culture induces novel proliferative and metabolic alterations associated with oncogenic transformation. *International Journal of Cancer* **66**, 578-586 (1996).
213. P. Swietach, S. Patiar, C. T. Supuran, A. L. Harris, R. D. Vaughan-Jones, The role of carbonic anhydrase 9 in regulating extracellular and intracellular pH in three-dimensional tumor cell growths. *Journal of Biological Chemistry* **284**, 20299-20310 (2009).
214. S. Walenta, J. Doetsch, W. Mueller-Klieser, L. A. Kunz-Schughart, Metabolic imaging in multicellular spheroids of oncogene-transfected fibroblasts. *Journal of Histochemistry & Cytochemistry* **48**, 509-522 (2000).
215. S. Rodriguez-Enriquez *et al.*, Energy metabolism transition in multi-cellular human tumor spheroids. *Journal of Cellular Physiology* **216**, 189-197 (2008).
216. J. Laurent *et al.*, Multicellular tumor spheroid models to explore cell cycle checkpoints in 3D. *Bmc Cancer* **13**, (2013).

217. H. S. Bell, I. R. Whittle, M. Walker, H. A. Leaver, S. B. Wharton, The development of necrosis and apoptosis in glioma: experimental findings using spheroid culture systems. *Neuropathology and Applied Neurobiology* **27**, 291-304 (2001).
218. M. T. Santini *et al.*, MG-63 human osteosarcoma cells grown in monolayer and as three-dimensional tumor spheroids present a different metabolic profile: a H-1 NMR study. *Febs Letters* **557**, 148-154 (2004).
219. P. Hamer *et al.*, The genomic profile of human malignant glioma is altered early in primary cell culture and preserved in spheroids. *Oncogene* **27**, 2091-2096 (2008).
220. S. Breslin, L. O'Driscoll, Three-dimensional cell culture: the missing link in drug discovery. *Drug Discovery Today* **18**, 240-249 (2013).
221. G. M. Thurber, K. D. Wittrup, Quantitative spatiotemporal analysis of antibody fragment diffusion and endocytic consumption in tumor spheroids. *Cancer Research* **68**, 3334-3341 (2008).
222. M. Wartenberg *et al.*, Regulation of the multidrug resistance transporter P-glycoprotein in multicellular tumor spheroids by hypoxiainducible factor-1 and reactive oxygen species. *Faseb Journal* **17**, 503-+ (2003).
223. D. Barbone, T. M. Yang, J. R. Morgan, G. Gaudino, V. C. Broaddus, Mammalian target of rapamycin contributes to the acquired apoptotic resistance of human mesothelioma multicellular spheroids. *Journal of Biological Chemistry* **283**, 13021-13030 (2008).
224. Y. C. Tung *et al.*, High-throughput 3D spheroid culture and drug testing using a 384 hanging drop array. *Analyst* **136**, 473-478 (2011).
225. A. L. Howes *et al.*, The phosphatidylinositol 3-kinase inhibitor, PX-866, is a potent inhibitor of cancer cell motility and growth in three-dimensional cultures. *Molecular Cancer Therapeutics* **6**, 2505-2514 (2007).
226. C. Wenzel, Technical University of Berlin, Berlin (2014).
227. National Centre for the Replacement Refinement & Reduction of Animals and Research. Available from https://www.nc3rs.org.uk/the-3rs. Accessed January 2017.
228. R. H. Kutner, X.-Y. Zhang, J. Reiser, Production, concentration and titration of pseudotyped HIV-1-based lentiviral vectors. *Nature Protocols* **4**, 495-505 (2009).
229. J. Schindelin *et al.*, Fiji: an open-source platform for biological-image analysis. *Nature Methods* **9**, 676-682 (2012).
230. S. Preibisch, S. Saalfeld, J. Schindelin, P. Tomancak, Software for bead-based registration of selective plane illumination microscopy data. *Nature Methods* **7**, 418-419 (2010).
231. A. Sakaue-Sawano *et al.*, Visualizing spatiotemporal dynamics of multicellular cell-cycle progression. *Cell* **132**, 487-498 (2008).
232. J. Bagnall *et al.*, Tight Control of hypoxia-inducible factor-alpha transient dynamics is essential for cell survival in hypoxia. *Journal of Biological Chemistry* **289**, 5549-5564 (2014).

233. R. Richards, M. D. Jenkinson, B. J. Haylock, V. See, Cell cycle progression in glioblastoma cells is unaffected by pathophysiological levels of hypoxia. *Peerj* **4**, (2016).
234. Catalogue of somatic mutation in cancer (COSMIC). [Database; no author]. Available from http://www.sanger.ac.uk/cosmic. Accessed August 2016.
235. N. O. Karpinich, M. Tafani, R. J. Rothman, M. A. Russo, J. L. Farber, The course of etoposide-induced apoptosis from damage to DNA and p53 activation to mitochondrial release of cytochrome c. *Journal of Biological Chemistry* **277**, 16547-16552 (2002).
236. H. Hogel, K. Rantanen, T. Jokilehto, R. Grenman, P. M. Jaakkola, Prolyl Hydroxylase PHD3 Enhances the Hypoxic Survival and G1 to S Transition of Carcinoma Cells. *Plos One* **6**, (2011).
237. H. Hoegel, P. Miikkulainen, L. Bino, P. M. Jaakkola, Hypoxia inducible prolyl hydroxylase PHD3 maintains carcinoma cell growth by decreasing the stability of p27. *Molecular Cancer* **14**, (2015).
238. S. C. Moser *et al.*, PHD1 links cell-cycle progression to oxygen sensing through hydroxylation of the centrosomal protein Cep192. *Developmental Cell* **26**, 381-392 (2013).
239. T. G. Graeber *et al.*, Hypoxia induces accumulation of p53 protein, but activation of a G(1)-phase checkpoint by low-oxygen conditions is independent of p53 status. *Molecular and Cellular Biology* **14**, 6264-6277 (1994).
240. W. G. An *et al.*, Stabilization of wild-type p53 by hypoxia-inducible factor 1 alpha. *Nature* **392**, 405-408 (1998).
241. E. M. Hammond, N. C. Denko, M. J. Dorie, R. T. Abraham, A. J. Giaccia, Hypoxia links ATR and p53 through replication arrest. *Molecular and Cellular Biology* **22**, 1834-1843 (2002).
242. Y. Pan, P. R. Oprysko, A. M. Asham, C. J. Koch, M. C. Simon, p53 cannot be induced by hypoxia alone but responds to the hypoxic microenvironment. *Oncogene* **23**, 4975-4983 (2004).
243. L. Zhang, P. Subarsky, R. P. Hill, Hypoxia-regulated p53 and its effect on radiosensitivity in cancer cells. *International Journal of Radiation Biology* **83**, 443-456 (2007).
244. B. Chen, M. S. Longtine, Y. Sadovsky, D. M. Nelson, Hypoxia downregulates p53 but induces apoptosis and enhances expression of BAD in cultures of human syncytiotrophoblasts. *American Journal of Physiology-Cell Physiology* **299**, C968-C976 (2010).
245. J.-P. J. Cosse, M. Ronvaux, N. Ninane, M. J. Raes, C. Michiels, Hypoxia-Induced Decrease in p53 Protein Level and Increase in c-jun DNA Binding Activity Results in Cancer Cell Resistance to Etoposide. *Neoplasia* **11**, 976-U917 (2009).
246. A. Sermeus, C. Michiels, Reciprocal influence of the p53 and the hypoxic pathways. *Cell Death & Disease* **2**, (2011).
247. N. M. Hasan, G. E. Adams, M. C. Joiner, Effect of serum starvation on expression and phosphorylation of PKC-alpha and p53 in V79 cells:

Implications for cell death. *International Journal of Cancer* **80**, 400-405 (1999).
248. Y. Shi *et al.*, Starvation-induced activation of ATM/Chk2/p53 signaling sensitizes cancer cells to cisplatin. *Bmc Cancer* **12**, (2012).
249. J. M. Kelm, N. E. Timmins, C. J. Brown, M. Fussenegger, L. K. Nielsen, Method for generation of homogeneous multicellular tumor spheroids applicable to a wide variety of cell types. *Biotechnology and Bioengineering* **83**, 173-180 (2003).
250. C. H. Chen, N. Pore, A. Behrooz, F. Ismail-Beigi, A. Maity, Regulation of glut1 mRNA by hypoxia-inducible factor-1 - Interaction between H-ras and hypoxia. *Journal of Biological Chemistry* **276**, 9519-9525 (2001).
251. R. J. Boado, W. M. Pardridge, Glucose deprivation and hypoxia increase the expression of the GLUT1 glucose transporter via a specific mRNA cis-acting regulatory element. *Journal of Neurochemistry* **80**, 552-554 (2002).
252. K. S. Dimmer, B. Friedrich, F. Lang, J. W. Deitmer, S. Broer, The low-affinity monocarboxylate transporter MCT4 is adapted to the export of lactate in highly glycolytic cells. *Biochemical Journal* **350**, 219-227 (2000).
253. M. S. Ullah, A. J. Davies, A. P. Halestrap, The plasma membrane lactate transporter MCT4, but not MCT1, is up-regulated by hypoxia through a HIF-1 alpha-dependent mechanism. *Journal of Biological Chemistry* **281**, 9030-9037 (2006).
254. K. Rosafio, L. Pellerin, Oxygen tension controls the expression of the monocarboxylate transporter MCT4 in cultured mouse cortical astrocytes via a hypoxia-inducible factor-1 alpha-mediated transcriptional regulation. *Glia* **62**, 477-490 (2014).
255. C. C. Wykoff *et al.*, Hypoxia-inducible expression of tumor-associated carbonic anhydrases. *Cancer Research* **60**, 7075-7083 (2000).
256. J. A. Loncaster *et al.*, Carbonic anhydrase (CA IX) expression, a potential new intrinsic marker of hypoxia: Correlations with tumor oxygen measurements and prognosis in locally advanced carcinoma of the cervix. *Cancer Research* **61**, 6394-6399 (2001).
257. N. J. P. Beasley *et al.*, Carbonic anhydrase IX, an endogenous hypoxia marker, expression in head and neck squamous cell carcinoma and its relationship to hypoxia, necrosis, and microvessel density. *Cancer Research* **61**, 5262-5267 (2001).
258. J. Chiche *et al.*, Hypoxia-Inducible carbonic anhydrase ix and xii promote tumor cell growth by counteracting acidosis through the regulation of the intracellular pH. *Cancer Research* **69**, 358-368 (2009).
259. J. Berg, Y. P. Hung, G. Yellen, A genetically encoded fluorescent reporter of ATP:ADP ratio. *Nature Methods* **6**, 161-166 (2009).
260. M. Tantama, J. R. Martinez-Francois, R. Mongeon, G. Yellen, Imaging energy status in live cells with a fluorescent biosensor of the intracellular ATP-to-ADP ratio. *Nature Communications* **4**, (2013).
261. F. Hirschhaeuser *et al.*, Multicellular tumor spheroids: An underestimated tool is catching up again. *Journal of Biotechnology* **148**, 3-15 (2010).

262. L. A. Kunz-Schughart, M. Kreutz, R. Knuechel, Multicellular spheroids: a three-dimensional in vitro culture system to study tumour biology. *International Journal of Experimental Pathology* **79**, 1-23 (1998).
263. E. Gratton, Deeper Tissue Imaging with Total Detection. *Science* **331**, 1016-1017 (2011).
264. D. Zhu, K. V. Larin, Q. Luo, V. V. Tuchin, Recent progress in tissue optical clearing. *Laser & Photonics Reviews* **7**, 732-757 (2013).
265. V. Marx, Optimizing probes to image cleared tissue. *Nature Methods* **13**, 205-209 (2016).
266. K. Becker, N. Jaehrling, S. Saghafi, R. Weiler, H.-U. Dodt, Chemical Clearing and Dehydration of GFP Expressing Mouse Brains. *Plos One* **7**, (2012).
267. K. Chung, K. Deisseroth, CLARITY for mapping the nervous system. *Nature Methods* **10**, 508-513 (2013).
268. A. Salic, T. J. Mitchison, A chemical method for fast and sensitive detection of DNA synthesis in vivo. *Proceedings of the National Academy of Sciences of the United States of America* **105**, 2415-2420 (2008).
269. C. W. Tornoe, C. Christensen, M. Meldal, Peptidotriazoles on solid phase: 1,2,3 -triazoles by regiospecific copper(I)-catalyzed 1,3-dipolar cycloadditions of terminal alkynes to azides. *Journal of Organic Chemistry* **67**, 3057-3064 (2002).
270. V. V. Rostovtsev, L. G. Green, V. V. Fokin, K. B. Sharpless, A stepwise Huisgen cycloaddition process: Copper(I)-catalyzed regioselective "ligation" of azides and terminal alkynes. *Angewandte Chemie-International Edition* **41**, 2596-+ (2002).
271. M. W. Gross, U. Karbach, K. Groebe, A. J. Franko, W. Muellerklieser, Calibration of misonidazole labeling by simultaneous measurement of oxygen-tension and labeling density in multicellular spheroids. *International Journal of Cancer* **61**, 567-573 (1995).
272. S. C. Chou, Y. Azuma, M. A. Varia, J. A. Raleigh, Evidence that involucrin, a marker for differentiation, is oxygen regulated in human squamous cell carcinomas. *British Journal of Cancer* **90**, 728-735 (2004).
273. P. Swietach *et al.*, Tumor-associated carbonic anhydrase 9 spatially coordinates intracellular pH in three-dimensional multicellular growths. *Journal of Biological Chemistry* **283**, 20473-20483 (2008).
274. J. J. Casciari, S. V. Sotirchos, R. M. Sutherland, Variations in tumor-cell growth-rates and metabolism with oxygen concentration, glucose-concentration, and extracellular pH. *Journal of Cellular Physiology* **151**, 386-394 (1992).
275. J. P. Freyer, R. M. Sutherland, Regulation of growth saturation and development of necrosis in EMT6-RO multicellular spheroids by the glucose and oxygen-supply. *Cancer Research* **46**, 3504-3512 (1986).
276. J. Meixensberger, B. Herting, W. Roggendorf, H. Reichmann, Metabolic patterns in malignant gliomas. *Journal of Neuro-Oncology* **24**, 153-161 (1995).

277. V. Miranda-Goncalves *et al.*, Monocarboxylate transporters (MCTs) in gliomas: expression and exploitation as therapeutic targets. *Neuro-Oncology* **15**, 172-188 (2013).
278. M. A. Proescholdt *et al.*, Expression of hypoxia-inducible carbonic anhydrases in brain tumors. *Neuro-Oncology* **7**, 465-475 (2005).
279. S. Kaluz *et al.*, Lowered oxygen tension induces expression of the hypoxia marker MN/carbonic anhydrase IX in the absence of hypoxia-inducible factor 1 alpha stabilization: A role for phosphatidylinositol 3 '-kinase. *Cancer Research* **62**, 4469-4477 (2002).
280. T. Dorai, I. S. Sawczuk, J. Pastorek, P. H. Wiernik, J. P. Dutcher, The role of carbonic anhydrase IX overexpression in kidney cancer. *European Journal of Cancer* **41**, 2935-2947 (2005).
281. W. F. Muellerklieser, R. M. Sutherland, Influence of convection in the growth-medium on oxygen-tensions in multicellular tumor spheroids. *Cancer Research* **42**, 237-242 (1982).
282. E. Marx, W. Muellerklieser, P. Vaupel, Lactate-induced inhibition of tumor-cell proliferation. *International Journal of Radiation Oncology Biology Physics* **14**, 947-955 (1988).
283. B. Monz, U. Karbach, K. Groebe, W. Muellerklieser, Proliferation and oxygenation status of WiDr spheroids in different lactate and oxygen environments. *Oncology Reports* **1**, 1177-1183 (1994).
284. A. Bertuzzi, A. Fasano, A. Gandolfi, C. Sinisgalli, Necrotic core in EMT6/Ro tumour spheroids: Is it caused by an ATP deficit? *Journal of Theoretical Biology* **262**, 142-150 (2010).
285. W. Muellerklieser, J. P. Freyer, R. M. Sutherland, Evidence for a major role of glucose in controlling development of necrosis in emt6/ro multicell tumor spheroids. *Advances in Experimental Medicine and Biology* **159**, 487-495 (1983).
286. H. Imamura *et al.*, Visualization of ATP levels inside single living cells with fluorescence resonance energy transfer-based genetically encoded indicators. *Proceedings of the National Academy of Sciences of the United States of America* **106**, 15651-15656 (2009).
287. M. C. Gingras, E. Roussel, J. M. Bruner, C. D. Branch, R. P. Moser, Comparison of cell-adhesion molecule expression between glioblastoma-multiforme and autologous normal brain-tissue. *Journal of Neuroimmunology* **57**, 143-153 (1995).
288. N. Kramer *et al.*, In vitro cell migration and invasion assays. *Mutation Research-Reviews in Mutation Research* **752**, 10-24 (2013).
289. M. Vinci *et al.*, Advances in establishment and analysis of three-dimensional tumor spheroid-based functional assays for target validation and drug evaluation. *Bmc Biology* **10**, (2012).
290. L. Cheng *et al.*, Elevated invasive potential of glioblastoma stem cells. *Biochemical and Biophysical Research Communications* **406**, (2011).
291. A. M. Stein, T. Demuth, D. Mobley, M. Berens, L. M. Sander, A mathematical model of glioblastoma tumor spheroid invasion in a three-dimensional in vitro experiment. *Biophysical Journal* **92**, 356-365 (2007).

292. S. Blacher *et al.*, Cell Invasion in the Spheroid Sprouting Assay: A Spatial Organisation Analysis Adaptable to Cell Behaviour. *Plos One* **9**, (2014).
293. E. G. Reynaud, U. Krzic, K. Greger, E. H. K. Stelzer, Light sheet-based fluorescence microscopy: more dimensions, more photons, and less photodamage. *Hfsp Journal* **2**, 266-275 (2008).
294. E. H. K. Stelzer, Light-sheet fluorescence microscopy for quantitative biology. *Nature Methods* **12**, 23-26 (2015).
295. J. Huisken, J. Swoger, F. Del Bene, J. Wittbrodt, E. H. K. Stelzer, Optical sectioning deep inside live embryos by selective plane illumination microscopy. *Science* **305**, 1007-1009 (2004).
296. J. Huisken, D. Y. R. Stainier, Selective plane illumination microscopy techniques in developmental biology. *Development* **136**, 1963-1975 (2009).
297. ZEISS Lightsheet Z.1: Light sheet fluorescence microscopy for multiview imaging of large specimens (Carl Zeiss Microscopy GmbH, Germany, 2015). Available from http://www.zeiss.com/microscopy/en_de/light/lightsheet-z-1.html. Accessed September 2016.
298. B. E. Welm, G. J. Dijkgraaf, A. S. Bledau, A. L. Welm, Z. Werb, Lentiviral transduction of mammary stem cells for analysis of gene function during development and cancer. *Cell Stem Cell* **2**, 90-102 (2008).
299. D. M. Shcherbakova, O. M. Subach, V. V. Verkhusha, Red fluorescent proteins: advanced imaging applications and future design. *Angewandte Chemie-International Edition* **51**, 10724-10738 (2012).
300. A. Kaufmann, M. Mickoleit, M. Weber, J. Huisken, Multilayer mounting enables long-term imaging of zebrafish development in a light sheet microscope. *Development* **139**, 3242-3247 (2012).
301. L. Whitesell, S. L. Lindquist, HSP90 and the chaperoning of cancer. *Nature Reviews Cancer* **5**, 761-772 (2005).
302. S. Tsutsumi, K. Beebe, L. Neckers, Impact of heat-shock protein 90 on cancer metastasis. *Future Oncology* **5**, 679-688 (2009).
303. C. M.-E. Sauvageot *et al.*, Efficacy of the HSP90 inhibitor 17-AAG in human glioma cell lines and tumorigenic glioma stem cells. *Neuro-Oncology* **11**, 109-121 (2009).
304. M.-S. Kim *et al.*, 17-allylamino-17-demethoxygeldanamycin down-regulates hyaluronic acid-induced glioma invasion by blocking matrix metalloproteinase-9 secretion. *Molecular Cancer Research* **6**, 1657-1665 (2008).
305. K. Kurozumi, T. Ichikawa, M. Onishi, K. Fujii, I. Date, Cilengitide treatment for malignant glioma: current status and future direction. *Neurologia Medico-Chirurgica* **52**, 539-547 (2012).
306. G. M. D'Abaco, A. H. Kaye, Integrins: Molecular determinants of glioma invasion. *Journal of Clinical Neuroscience* **14**, 1041-1048 (2007).
307. A. Wilisch-Neumann *et al.*, The integrin inhibitor cilengitide affects meningioma cell motility and invasion. *Clinical Cancer Research* **19**, 5402-5412 (2013).

308. G. D. Maurer *et al.*, Cilengitide modulates attachment and viability of human glioma cells, but not sensitivity to irradiation or temozolomide in vitro. *Neuro-Oncology* **11**, 747-756 (2009).
309. P. T. Caswell *et al.*, Rab-coupling protein coordinates recycling of alpha 5 beta 1 integrin and EGFR1 to promote cell migration in 3D microenvironments. *Journal of Cell Biology* **183**, 143-155 (2008).
310. C. Sahlgren, M. V. Gustafsson, S. Jin, L. Poellinger, U. Lendahl, Notch signaling mediates hypoxia-induced tumor cell migration and invasion. *Proceedings of the National Academy of Sciences of the United States of America* **105**, 6392-6397 (2008).
311. W. B. Pratt, D. O. Toft, Regulation of signaling protein function and trafficking by the hsp90/hsp70-based chaperone machinery. *Experimental Biology and Medicine* **228**, 111-133 (2003).
312. M. H. Zaman *et al.*, Migration of tumor cells in 3D matrices is governed by matrix stiffness along with cell-matrix adhesion and proteolysis. *Proceedings of the National Academy of Sciences of the United States of America* **103**, 10889-10894 (2006).
313. K. Wolf *et al.*, Physical limits of cell migration: Control by ECM space and nuclear deformation and tuning by proteolysis and traction force. *Journal of Cell Biology* **201**, 1069-1084 (2013).
314. K. Jhaveri *et al.*, Heat shock protein 90 inhibitors in the treatment of cancer: current status and future directions. *Expert Opinion on Investigational Drugs* **23**, 611-628 (2014).
315. P. Leblond *et al.*, Cilengitide targets pediatric glioma and neuroblastoma cells through cell detachment and anoikis induction. *Anticancer Drugs* **24**, 818-825 (2013).
316. G. D. Maurer *et al.*, Cilengitide modulates attachment and viability of human glioma cells, but not sensitivity to irradiation or temozolomide in vitro. *Neuro Oncol* **11**, 747-756 (2009).
317. R. Stupp *et al.*, Cilengitide combined with standard treatment for patients with newly diagnosed glioblastoma with methylated MGMT promoter (CENTRIC EORTC 26071-22072 study): a multicentre, randomised, open-label, phase 3 trial. *Lancet Oncol* **15**, 1100-1108 (2014).
318. I. W. Y. Mak, N. Evaniew, M. Ghert, Lost in translation: animal models and clinical trials in cancer treatment. *American Journal of Translational Research* **6**, 114-118 (2014).
319. R. H. Goldbrunner *et al.*, ECM dependent and integrin mediated tumor cell migration of human glioma and melanoma cell lines under serum-free conditions. *Anticancer Research* **16**, 3679-3687 (1996).
320. M. Herrera-Perez, S. L. Voytik-Harbin, J. L. Rickus, Extracellular matrix properties regulate the migratory response of glioblastoma stem cells in three-dimensional culture. *Tissue Engineering Part A* **21**, 2572-2582 (2015).
321. K. Pogoda *et al.*, Compression stiffening of brain and its effect on mechanosensing by glioma cells. *New Journal of Physics* **16**, (2014).

322. P.-H. Wu, A. Giri, S. X. Sun, D. Wirtz, Three-dimensional cell migration does not follow a random walk. *Proceedings of the National Academy of Sciences of the United States of America* **111**, 3949-3954 (2014).
323. M. J. Dorie, R. F. Kallman, D. F. Rapacchietta, D. Van Antwerp, Y. R. Huang, Migration and internalization of cells and polystyrene microsphere in tumor cell spheroids. *Exp Cell Res* **141**, 201-209 (1982).
324. D. L. McElwain, G. J. Pettet, Cell migration in multicell spheroids: swimming against the tide. *Bull Math Biol* **55**, 655-674 (1993).
325. M. J. Tindall, C. P. Please, Modelling the cell cycle and cell movement in multicellular tumour spheroids. *Bull Math Biol* **69**, 1147-1165 (2007).
326. G. J. Pettet, C. P. Please, M. J. Tindall, D. L. McElwain, The migration of cells in multicell tumor spheroids. *Bull Math Biol* **63**, 231-257 (2001).
327. K. Pham *et al.*, Density-dependent quiescence in glioma invasion: instability in a simple reaction-diffusion model for the migration/proliferation dichotomy. *Journal of Biological Dynamics* **6**, 54-71 (2012).
328. R. Rangarajan, M. H. Zaman, Modeling cell migration in 3D Status and challenges. *Cell Adhesion & Migration* **2**, 106-109 (2008).
329. A. Corcoran, R. F. Del Maestro, Testing the "Go or Grow" hypothesis in human medulloblastoma cell lines in two and three dimensions. *Neurosurgery* **53**, 174-184 (2003).
330. T. Garay *et al.*, Cell migration or cytokinesis and proliferation? - Revisiting the "go or grow" hypothesis in cancer cells in vitro. *Experimental Cell Research* **319**, 3094-3103 (2013).
331. M. Ravi, V. Paramesh, S. R. Kaviya, E. Anuradha, F. D. P. Solomon, 3D Cell culture systems: Advantages and applications. *Journal of Cellular Physiology* **230**, 16-26 (2015).
332. G. R. Souza *et al.*, Three-dimensional tissue culture based on magnetic cell levitation. *Nature Nanotechnology* **5**, 291-296 (2010).
333. E. Fennema, N. Rivron, J. Rouwkema, C. van Blitterswijk, J. de Boer, Spheroid culture as a tool for creating 3D complex tissues. *Trends in Biotechnology* **31**, 108-115 (2013).
334. J. Friedrich, C. Seidel, R. Ebner, L. A. Kunz-Schughart, Spheroid-based drug screen: considerations and practical approach. *Nature Protocols* **4**, 309-324 (2009).
335. C. Wenzel *et al.*, 3D high-content screening for the identification of compounds that target cells in dormant tumor spheroid regions. *Experimental Cell Research* **323**, 131-143 (2014).
336. F. Monjaret *et al.*, Fully Automated one-step production of functional 3D tumor spheroids for high-content Screening. *Jala* **21**, 268-280 (2016).
337. S. I. Montanez-Sauri, K. E. Sung, J. P. Puccinelli, C. Pehlke, D. J. Beebe, Automation of three-dimensional cell culture in arrayed microfluidic devices. *Jala* **16**, 171-185 (2011).
338. P. J. Keller, A. D. Schmidt, J. Wittbrodt, E. H. K. Stelzer, Reconstruction of zebrafish early embryonic development by scanned light sheet microscopy. *Science* **322**, 1065-1069 (2008).

339. M. B. Ahrens, M. B. Orger, D. N. Robson, J. M. Li, P. J. Keller, Whole-brain functional imaging at cellular resolution using light-sheet microscopy. *Nature Methods* **10**, 413-+ (2013).
340. O. K. Park *et al.*, 3D light-sheet fluorescence microscopy of cranial neurons and vasculature during zebrafish embryogenesis. *Molecules and Cells* **38**, 975-981 (2015).
341. A. Y. Chow, Cell cycle control by oncogenes and tumor suppressors: driving the transformation of normal cells into cancerous Cells. *Nature Education* **3**, 7 (2010).
342. Welcome Images, C0018191. (2003). Available from https://wellcomeimages.org/. Accessed September 2016.
343. B. Campbell, Wellcome Images, B0004170. Available from https://wellcomeimages.org/, 2001. Accessed September 2016.
344. Y. C. Wu *et al.*, Inverted selective plane illumination microscopy (iSPIM) enables coupled cell identity lineaging and neurodevelopmental imaging in Caenorhabditis elegans. *Proceedings of the National Academy of Sciences of the United States of America* **108**, 17708-17713 (2011).
345. Y. C. Wu *et al.*, Spatially isotropic four-dimensional imaging with dual-view plane illumination microscopy. *Nature Biotechnology* **31**, 1032-+ (2013).
346. F. C. Zanacchi, Z. Lavagnino, M. Faretta, L. Furia, A. Diaspro, Light-Sheet Confined Super-Resolution Using Two-Photon Photoactivation. *Plos One* **8**, (2013).
347. Z. Lavagnino *et al.*, 4D (x-y-z-t) imaging of thick biological samples by means of Two-Photon inverted Selective Plane Illumination Microscopy (2PE-iSPIM). *Scientific Reports* **6**, (2016).
348. Applied Scientific Instrumentation. Selective Plane Illumination Microscopy - iSPIM & diSPIM. Available from http://www.asiimaging.com/index.php/products/light-sheet-microscopy/selective-plane-illumination-microscopy-ispim-dispim/. Accessed September 2016.
349. Y. S. Hu, M. Zimmerley, Y. Li, R. Watters, H. Cang, Single-Molecule Super-Resolution Light-Sheet Microscopy. *Chemphyschem* **15**, 577-586 (2014).
350. A. Maizel, D. von Wangenheim, F. Federici, J. Haseloff, E. H. K. Stelzer, High-resolution live imaging of plant growth in near physiological bright conditions using light sheet fluorescence microscopy. *Plant Journal* **68**, 377-385 (2011).
351. M. B. Bouchard *et al.*, Swept confocally-aligned planar excitation (SCAPE) microscopy for high-speed volumetric imaging of behaving organisms. *Nature Photonics* **9**, 113-119 (2015).
352. F. Pampaloni, B.-J. Chang, E. H. K. Stelzer, Light sheet-based fluorescence microscopy (LSFM) for the quantitative imaging of cells and tissues. *Cell and Tissue Research* **360**, 129-141 (2015).
353. F. Pampaloni. Designs, applications, and perspectives of the High-Throughput LSFM. In: Light Sheet Fluorescence Microscopy International Conference; 31 August - 3 September 2016, Sheffield. (2016).

354. F. Pampaloni. Unpublished communication at the Light Sheet Fluorescence Microscopy International Conference; 31 August - 3 September 2016, Sheffield.
355. B. Schmid, J. Huisken, Real-time multi-view deconvolution. *Bioinformatics* **31**, 3398-3400 (2015).

Appendix

A. Fiji macro to reduce lightsheet data file size

```
// -------------------------------------------------
// DOWN-SAMPLE LIGHTSHEET DATA
// -------------------------------------------------
//
// Macro to reduce the size of CZI lightsheet data by loading in one
timepoint at a time and downsampling by decreasing bitdepth and binning.
//
// User is asked for a file, then given a dialog to select the range to
process (this way you can use multiple machines) and how you want to
downsample. Default is 8bit and 2x bin.
//
// A subdirectory of the file's directory is made (called "processed") and
one tif-stack per timepoint is saved in that folder.
//
// A log window shows dimension information as well as the final physical
size which you will need to enter in post-processing software.
//
// Written and Tested in Fiji [http://fiji.sc] 64bit. Paths coded for
Windows (\).
//
//
//     Dave Mason [dnmason@liv.ac.uk]
//     Centre for Cell Imaging [cci.liv.ac.uk]
//     University of Liverpool
//     Written Nov 2015
//     Last Edited Sept 2016
//
//-------------------------------------------------

debugMode=0;

//-------------------------------------------------
//-- PART 1: Open a file
//-------------------------------------------------
path = File.openDialog("Select a File");

if (debugMode==0) {setBatchMode(true);}

dir = File.getParent(path);
name = File.getName(path);
title = File.nameWithoutExtension;

//-- Get dimension info on selected file
run("Bio-Formats Macro Extensions");
Ext.setId(path);

//-- Only process the first series
  Ext.setSeries(0);
  Ext.getSizeX(sizeX);
  Ext.getSizeY(sizeY);
  Ext.getSizeZ(sizeZ);
  Ext.getSizeC(sizeC);
  Ext.getSizeT(sizeT);
  Ext.getDimensionOrder(dimOrder);

//-- Print out dimensions
  print("- - - - - - - - - - - - - - - - - - - - -");
```

```
  print("Input : "+path);
  print("- - - - - - - - - - - - - - - - - - - - -");
  print("Image dimensions: " + sizeX + " x " + sizeY);
  print("Focal plane count = " + sizeZ);
  print("Channel count = " + sizeC);
  print("Time point count = " + sizeT);
  print("- - - - - - - - - - - - - - - - - - - - -");

//-- check for the existence of the output directory and make it if
necessary
outDir=dir+"\\processed";
  if (!File.exists(outDir)){
       print("Output Directory does not exist. Creating...");
         File.makeDirectory(outDir);
  } else{
       print("Output Directory already exists");
  }

//-----------------------------------------------------
//-- PART 2: Request Processing options
//-----------------------------------------------------

Dialog.create("Processing options");
  Dialog.addNumber("Start Timepoint", 1);
  Dialog.addNumber("End Timepoint", sizeT);
    Dialog.addCheckbox("Crop", false);
  Dialog.addNumber("size in X", sizeX);
  Dialog.addNumber("size in Y", sizeY);
  Dialog.addNumber("X offset", 0);
  Dialog.addNumber("Y offset", 0);
  Dialog.addCheckbox("8-bit?", true);
  Dialog.addChoice("Bin Factor", newArray("1","2","4"),"2");
    Dialog.show();
  startT=Dialog.getNumber();
  endT=Dialog.getNumber();
  doCrop=Dialog.getCheckbox();
  Xdim=Dialog.getNumber();
  Ydim=Dialog.getNumber();
  Xoff=Dialog.getNumber();
  Yoff=Dialog.getNumber();
  downsample=Dialog.getCheckbox();
  binFactor=Dialog.getChoice();

  //-- Report Processing options to log
  if (downsample==true){
  print("Downsampling to 8-bit");
  }
  if (binFactor>1){
       print("Binning with Factor "+binFactor);
  }
  print("- - - - - - - - - - - - - - - - - - - - -");

//-----------------------------------------------------
//-- PART 3: Start processing the data
//-----------------------------------------------------

//-- For each timepoint open a single timepoint and process. This prevents
memory overflow on most systems.
for (i=startT; i<=endT; i++){
print("Processing Timepoint "+i);
run("Bio-Formats Importer", "open=["+path+"] autoscale color_mode=Default
specify_range view=Hyperstack stack_order=XYCZT z_begin=1 z_end="+sizeZ+"
z_step=1 t_begin="+i+" t_end="+i+" t_step=1");
if (i==startT){
       //-- On the first image, get the XYZ calibration
       getVoxelSize(width, height, depth, unit);
       }
```

```
//-- Depending upon the choices made, choose how to process
if (downsample==true){
run("8-bit");
}
if (binFactor>1){
run("Bin...", "x="+binFactor+" y="+binFactor+" z=1 bin=Average");
}
if (doCrop==true){
makeRectangle(Xoff, Yoff, Xdim, Ydim);
run("Crop");
}

//-- Save timepoint
saveAs("Tiff", outDir+"\\t"+IJ.pad(i,3)+".tif");
}
print("Original Pixel Size: " + width + " x " + height + " x " + depth + "
("+unit+")");
print("Processed Pixel Size: " + width*binFactor + " x " + height*binFactor
+ " x " + depth + " ("+unit+")");
print("- - - - - - - - - - - - - - - - - - - - - -");
print("Finished");
print("- - - - - - - - - - - - - - - - - - - - - -");
```

B. MATLAB scripts

B.1 Wrapper script (WRAPPER.m)

```
%% WRAPPER SCRIPT TO PROCESS A DIRECTORY TREE
%
%   A wrapper to find Imaris-exported datasets in a directory tree and call
a processing script on each one.
%   Written to accommodate Lightsheet Data Processing script (processData.m)
and figure plotting script (plotFigures.m)
%
%   Must be run from the top level of the directory tree. Make sure any
called scripts are in the same directory. Only directories containing an
"XXXX_Overall.csv" file will be processed.
%
%   Requires a file called Centroids.csv file with header row
(filename,x,y,z,t) for the spheroid centroid position and temporal
calibration (in microns and seconds respectively).
%
%   Written By Dave Mason [dnmason@liv.ac.uk], Centre for Cell Imaging
[cci.liv.ac.uk, University of Liverpool
%
%-------------------------------------------------------------------------
-----------------------
close all
clear all
clc

%-- Regular expression for the script files to include in the dialog
re='^(processData|plotFigures).+(\.m)$';
%-- get a directory listing
d=dir;
d={d.name}.';
f=regexp(d,re,'match');
f=[f{:}].';
%-- Request the filename of the script to run
[selection,ok]=listdlg('ListString',f,'SelectionMode','single','Name','Selec
t a script');

if ok ==0
    disp('ERROR: Script is required');
    return
else
    wrapper_script=f{selection};
end
clearvars re d f selection ok

%-- You can run a custom script by uncommenting the line below:
%wrapper_script='MakeFigs_v3.m';

%-- list all subdirectories in pwd
wrapper_startDir=pwd;
wrapper_dirList=regexp(genpath(wrapper_startDir),['[^;]*'],'match');

%-- Load an array of filenames, centroids, tCalibs
fid=fopen('Centroids.csv');
wrapper_cents=textscan(fid,'%s','Delimiter', ',');
fclose(fid);

%-- IMPORTANT !!! ----------------------------------------------------------
-----------------------
%-- This needs to be adjusted to represent the number of columns (5) and
rows (14) in the CSV.
```

```
wrapper_cents=reshape(wrapper_cents{1,1},5,14);
clearvars fid ans;
%-------------------------------------------------------------------------
-----------------------

%-- go to each level and look for a set of CSV data
for wrapper_i=1:size(wrapper_dirList,2)
cd(wrapper_dirList{wrapper_i}); %-- Does not carry to the new script called
by run. Must re-issue.
if ~isempty(dir('*_Overall.csv')) %-- Use the Overall as a marker as it's
not used in processing

    %-- file exists so call the script in this directory

    disp('-------------------------------------------------------------------
------')
    disp([datestr(datetime) ' - FOUND TRACKING DATA IN:'])
    disp(wrapper_dirList{wrapper_i})
    disp('-------------------------------------------------------------------
------')

    if exist(fullfile(wrapper_startDir,wrapper_script),'file')
        run(fullfile(wrapper_startDir,wrapper_script));
    else
        disp('ERROR: Cannot find script file. Make sure a copy is in the
starting directory!');
        return
    end

end %-- Data files exist

end %-- All subdirs loop

cd(wrapper_startDir);
close all
clearvars
disp('-------------------------------------------------------------------------
--')
disp([datestr(datetime) ' - WRAPPER IS FINISHED'])
disp('-------------------------------------------------------------------------
--')
```

B.2 Data processing script (ProcessData.m)

```
%% POST-PROCESSING SCRIPT FOR LIGHTSHEET DATA TRACKED IN IMARIS
%
%   Script to calculate various stats from Imaris tracking data output.
%
%   USAGE:
%   ======
%   Can be run stand alone or through the WRAPPER script.
%
%
%   Written By Dave Mason [dnmason@liv.ac.uk]
%   Centre for Cell Imaging [cci.liv.ac.uk]
%   University of Liverpool
%   Written: May 2016
%   Latest update: September 2016
%
%-------------------------------------------------------------------------
-----------------------
%% -- Load in the data
clearvars -except wrapper_*
close all

%-- Store the warning state, then turn off all warnings
w=warning;
warning('off','all');

%-- if called from WRAPPER, PWD is the location of the script, so CD into
the active data directory
if exist('wrapper_i','var')
    cd(wrapper_dirList{wrapper_i});
end

%-- Find the _Overall.csv file and use the filename as an anchor from which
to find the base name
inFileDir=dir('*_Overall.csv');
inFile=inFileDir.name;
clearvars inFileDir;

%-- Rename the file so you can run the same script in the same directory
structure and not double-up processing
movefile(inFile,strrep(inFile,'_Overall.csv','_Overall_RUNNING.csv'));

if exist('wrapper_i','var')
%-- RUNNING FROM WRAPPER SCRIPT

    %-- Find index of this folder
    centIndex=strcmp(inFile,wrapper_cents);
    centIndex=find(centIndex(1,:));

    %-- Pull the coordinates and time calibration

centrePosXYZ=[str2num(wrapper_cents{2,centIndex}),str2num(wrapper_cents{3,ce
ntIndex}),str2num(wrapper_cents{4,centIndex})];
    tCalib=str2num(wrapper_cents{5,centIndex});
    clearvars centIndex;
else
%-- RUNNING STAND-ALONE

    %-- Get user input for centroid position
    inCentroid=inputdlg({'Centroid X position','Centroid Y
position','Centroid Z position','Time Interval (s)'},'Enter Parameters',1);

    if isempty(inCentroid)
        disp('Error! Centroid Coordinates Required for processing');
```

```
        return
    end


centrePosXYZ=[str2num(inCentroid{1}),str2num(inCentroid{2}),str2num(inCentro
id{3})];
    tCalib=str2num(inCentroid{4});
end
clearvars inCentroid;

%-- Sanity check
if isempty(centrePosXYZ) || isempty(tCalib)
    disp('Error! Centroid Coordinates Required for processing');
    return
end


%% -- Drop a timestamp
disp([datestr(datetime) ' - Starting Import ------------------------------
'])

%% -- Import the Data

disp([datestr(datetime) ' - Importing Spot Position'])
data_sPos = xlsread(strrep(inFile,'_Overall.csv','_Position.csv'));
disp([datestr(datetime) ' - ... done'])

disp([datestr(datetime) ' - Importing Spot Speed'])
data_sSpeed = xlsread(strrep(inFile,'_Overall.csv','_Speed.csv'));
disp([datestr(datetime) ' - ... done'])

disp([datestr(datetime) ' - Importing Track Position'])
data_tPosStart =
xlsread(strrep(inFile,'_Overall.csv','_Track_Position_Start.csv'));
disp([datestr(datetime) ' - ... done'])

disp([datestr(datetime) ' - Importing Track Straightness'])
data_tStraight =
xlsread(strrep(inFile,'_Overall.csv','_Track_Straightness.csv'));
disp([datestr(datetime) ' - ... done'])

disp([datestr(datetime) ' - Importing Mean Track Speed'])
data_tSpeedMean =
xlsread(strrep(inFile,'_Overall.csv','_Track_Speed_Mean.csv'));
disp([datestr(datetime) ' - ... done'])


%% -- Drop a timestamp
disp([datestr(datetime) ' - Import Complete, Starting Processing ----------
'])

%% -- Match Spot Speed to Radial Distance
t1=tic;
disp([datestr(datetime) ' - Processing Spot Speed vs Radial Distance'])

%-- Correct speed from um/1s to um/tCalib
data_sSpeed(:,1)=data_sSpeed(:,1)/tCalib;
%-- Turn it into um/hour
data_sSpeed(:,1)=data_sSpeed(:,1)*3600;

%-- Preallocate array
arrLen=length(data_sPos(:,1));
%-- columns (for each feature): 1=distance from centre, 2=Speed,
3=Straightness
calc_SpotData=zeros([arrLen 3]);
h1 = waitbar(0,'Initialising...');
%-- Loop through position file and collate corresponding speed value
```

```
for i=1:arrLen;
    %-- Update waitbar every 100 feats
        if mod(i, 100) == 0
            waitbar(i/arrLen,h1,sprintf('%0.2f%% done analysing Spot
Parameters',(i/arrLen)*100));
        end
    %-- Calculate the absolute distance of the spot from the centre
    calc_SpotData(i,1)=sqrt(((centrePosXYZ(1)-
data_sPos(i,1))^2)+((centrePosXYZ(2)-data_sPos(i,2))^2)+((centrePosXYZ(3)-
data_sPos(i,3))^2));
    searchTID=data_sPos(i,8);
    searchT=data_sPos(i,7);
    %-- Look up and record the corresponding speed, final '1' is not
necessary (for first value) but added for clarity
    calc_SpotData(i,2)=data_sSpeed(data_sSpeed(:,5)==searchTID &
data_sSpeed(:,4)==searchT,1);
end
close(h1);

%-- Concat the Time and Track ID values onto the array
calc_SpotData=horzcat(calc_SpotData,data_sPos(:,7),data_sPos(:,8));


disp([datestr(datetime) ' - Finished processing '
num2str(length(calc_SpotData(:,1))) ' tracks in '
sprintf('%0.f%',toc(t1)/60) ' minutes.'])


%% -- Match Track Straightness to Radial Distance
t1=tic;
disp([datestr(datetime) ' - Processing Track Straightness vs Radial
Distance'])

%-- Preallocate array
arrLen=length(data_tPosStart(:,1));
%-- columns (for each feature): 1=distance from centre, 2=Speed,
3=straightness
calc_TrackData=zeros([arrLen 4]);
h1 = waitbar(0,'Initialising...');
%-- Loop through position file and collate corresponding speed value
for i=1:arrLen;
    %-- Update waitbar
    waitbar(i/arrLen,h1,sprintf('%0.2f%% done analysing Track
Parameters',(i/arrLen)*100));

    %-- Pull the distance from the spot values (first spot in a track)
    calc_TrackData(i,1)=calc_SpotData(
find(calc_SpotData(:,5)==data_tPosStart(i,7),1));

    calc_TrackData(i,4)=data_tPosStart(i,7); %-- Record the track number

    searchTID=data_tPosStart(i,7);
    %-- Look up and record the corresponding track speed and straightness
    calc_TrackData(i,2)=data_tSpeedMean(data_tSpeedMean(:,4)==searchTID,1);
    calc_TrackData(i,3)=data_tStraight(data_tStraight(:,4)==searchTID,1);
end
close(h1);

disp([datestr(datetime) ' - Finished processing '
num2str(length(calc_TrackData(:,1))) ' tracks in '
sprintf('%0.f%',toc(t1)/60) ' minutes.'])

%% -- Calculate the instantaneous Straightness of spots

disp([datestr(datetime) ' - Processing Spot Straightness'])
t1=tic;
```

```
%-- What window should be used to calculate the spots? Note that there is no
edge processing. Edge values are zeroed
windNum=5;

h1=waitbar(0,'Initialising...');

for i=1:length(calc_SpotData(:,1))

    %-- Check to make sure that there are features two forward and two back
    missingFeats=0;
    for j=[-2 -1 1 2] %-- THIS NEEDS TO BE CORRECTED IF windNum IS ALTERED
        if isempty(data_sPos(data_sPos(:,8)==calc_SpotData(i,5) &
data_sPos(:,7)==calc_SpotData(i,4)+j,1:3));
            missingFeats=1;
            break %-- found one, so don't bother searching the others
        end
    end

    % If any are absent, skip to the next spot
    if missingFeats==1;
        continue
    end

    %-- calculate $windNum sets of coordinates
    c=zeros(windNum,3);
    for j=1:windNum
        c(j,:)=data_sPos(data_sPos(:,8)==calc_SpotData(i,5) &
data_sPos(:,7)==calc_SpotData(i,4)+(j-3),1:3);
    end

    %-- Should only have got here if there are indeed windNum sets of coords
in 'c'

    %-- Calculate the end-to-end displacement
    c1=sqrt( (c(1,1)-c(windNum,1))^2 + (c(1,2)-c(windNum,2))^2 + (c(1,3)-
c(windNum,3))^2);

    %-- Calculate the path length (ahead)
    c2=0;
    for j=1:windNum-1
        c2=c2+sqrt( (c(j,1)-c(j+1,1))^2 + (c(j,2)-c(j+1,2))^2 + (c(j,3)-
c(j+1,3))^2);
    end

    %-- Record the straightness
    calc_SpotData(i,3)=c1/c2;

    %-- update the waitbar every 100 tracks (every 1 slows processing too
much)
    if mod(i, 100) == 0
    waitbar(i/length(calc_SpotData(:,1)),h1,sprintf('%0.2f%% done analysing
Spot Parameters',(i/length(calc_SpotData(:,1)))*100));
    end
end
close(h1);

disp(['Finished processing ' num2str(length(calc_SpotData(:,1))) ' spots in
' sprintf('%0.f%',toc(t1)/60) ' minutes.'])
clearvars i xrand missingFeats searchT searchTID j h1 t1 zzz_yVals h51 c c1
c2;


%% -- Calculate the Cumlulative Distribution by distance over time

disp([datestr(datetime) ' - Processing Cumulative Distribution by
Distance'])
```

```
binNum=50;
numPointsArray=[1 160 320 480]; %-- Timepoints are hardcoded for comparison
of data between experiments

%-- Set up array with bins
calc_CDF(:,1)=[0:(max(calc_SpotData(:,1))*1.1)/binNum:max(calc_SpotData(:,1)
)*1.1];

%-- concat T and tID columns onto outSpotData
calc_SpotData=horzcat(calc_SpotData,data_sPos(:,7),data_sPos(:,8));

%-- Figure out how many bins we have
arrLen=length(calc_CDF(:,1));

%-- Do numPoints worth of timepoints
for j=numPointsArray;
%-- Loop through position file and collate corresponding speed value
for i=1:arrLen;

    %-- For each bin step, calculate the cululative number of spots within
that range

calc_CDF(i,find(numPointsArray==j)+1)=length(calc_SpotData(calc_SpotData(:,1
)<calc_CDF(i,1) & calc_SpotData(:,4)==j) );

end %-- i loop

end %-- j loop


%-- Normalise the data in Y for comparison
calc_CDFnorm(:,1)=calc_CDF(:,1);

for j=2:length(calc_CDF(1,:))

    calc_CDFnorm(:,j)=(calc_CDF(:,j)-
min(calc_CDF(:,j)))/(max(calc_CDF(:,j))-min(calc_CDF(:,j)));

end

disp([datestr(datetime) ' - ... done'])
clearvars i j;

%% -- Refine Data matrices to 'OUTSIDE' spots only
disp([datestr(datetime) ' - Refining to outer tracks'])
%-- Calculate the 10 furthest out in the first frame and use the mean as the
in/out boundary
tmp1=sort(calc_SpotData(calc_SpotData(:,4) == 1),1,'descend');
eventHorizon=mean(tmp1(1:10,1));
clearvars tmp1;

%-- Refine the Event Horizon here (add 5% to distance)
eventHorizon=eventHorizon*1.05;

%-- Now refine the outSpotData to only include the values outside the
boundary
%-- Find the indices
tmp_ind=calc_SpotData(:,1)>eventHorizon;
%-- Pull the rows based on the indexing
calc_SpotData_outside=calc_SpotData(tmp_ind,:);
clearvars tmp_ind;

%-- Now refine the outTrackData to only include the values outside the
boundary
%-- Find the indices
tmp_ind=calc_TrackData(:,1)>eventHorizon;
%-- Pull the rows based on the indexing
```

```
calc_TrackData_outside=calc_TrackData(tmp_ind,:);
clearvars tmp_ind;

disp([datestr(datetime) ' - ... done'])

%% -- Finished
%-- Save the workspace variables using the base filename
save(strrep(inFile,'_Overall.csv','_MATLAB_data.mat'));
% -- rename the Input file so that the dataset won't be re-analysed
movefile(strrep(inFile,'_Overall.csv','_Overall_RUNNING.csv'),strrep(inFile,
'_Overall.csv','_Overall_DONE.csv'));
%-- set the warning state back to original
warning(w);
%-- Let the user know we're done
disp([datestr(datetime) ' - Finished ------------------------------------
']);
```

B.3 Figure plotting script (PlotFigures.m)

```
%% POST-PROCESSING SCRIPT FOR LIGHTSHEET DATA TRACKED IN IMARIS - PLOT
FIGURES
%
% Script to plot figures from post-processed lightsheet data
%
%
% Written By Dave Mason [dnmason@liv.ac.uk]
% Centre for Cell Imaging [cci.liv.ac.uk]
% University of Liverpool
% Written: May 2016
% Latest update: September 2016
%
%-------------------------------------------------------------------------
-----------------------

%-- Usual tidy up before IMPORT
clearvars -except wrapper_*
close all

if exist('wrapper_i','var')
    %-- if called from WRAPPER, PWD is the location of the script, so CD
into the active data directory
    cd(wrapper_dirList{wrapper_i});
end

%-- Get the mat file
    tA=dir('*MATLAB_data.mat');

%-- load the CDF array
load(tA.name, '-regexp', '^(?!wrapper_)...');
inFile=tA.name;
clearvars tA

%- Store the warning state, then turn off all warnings
w=warning;
warning('off','all');

%% -- GLOBAL VARIABLES FOR PLOTTING ----------------------------------------
%-------------------------------------------------------------------------

axisFontSize=20;            %-- Size of Font used in Axis labels. Default =
12
axisLineWidth=2;            %-- Axis line width. Default = 0.5
plotLineThickness=2;        %-- Default = 0.5
plotLineThicknessHisto=2;   %-- Default = 0.5 (You might want a thinner line
for histograms cf CDF graphs)
plotMarkerSize=2;           %-- Default = 6
sameAxes=1;                 %-- [0/1] Use consistant axis scaling [1] or
autoscale [0]?

bigSpheroids=0;             %-- [0/1] Determines how the
SpotSpeed/SpotStraightness by Distance bins are calculated.
                            %         [0]= Use 2 bins (in/out) for distance
graphs [1]= Use 6 bins for distance (3 in / 3 out)
minSpots=1000;              %-- Need at least this many Spots to plot a line
graph - prevents crappy-looking normalised histograms

%-- OUTPUTS ---------------------------------------------------------------
saveFIG=1;          %-- [0/1] Save a matlab FIG file?
savePNG=0;          %-- [0/1] Save a PNG file?
addGraphTitle=0;    %-- [0/1] Add a title to the graphs (IE "Spot Speed by
Radial Distance" &c.)
```

```
addFileNameTitle=0; %-- [0/1] Do you want to add a FileName title to each
plot? Recomended to TURN OFF for fig files as it changes the axis layout


%% -- Cumlulative Distribution by distance over time - CURVES

%-- CDF GRAPH ---------------------------------------------------------------
fig01=figure('Color',[1 1 1]);
set(gcf,'position',[100 100 800 600]) %-- Set the figure position and size
of the figure

movegui(gcf,'center') %-- Do this to make sure that the figure isn't cut off
(or including other windows) when exporting
hold on;
for j=2:length(calc_CDF(1,:))
plot(calc_CDF(:,1),calc_CDF(:,j),'LineWidth',plotLineThickness)
end
xlabel('Radial Distance (um)');
ylabel('Cumulative Number of Features');
if sameAxes==1
    xlim([0 400]);
end
if addGraphTitle==1
    title(['Spatial Distribution of Features by Time']);
end
set(gca,'fontsize',axisFontSize, 'LineWidth',axisLineWidth)
%-- Create the legend string
numPointsArray=[1 160 320 480]; %-- provide time points
legendStr = num2str(floor(numPointsArray'*3/60), 't=%2d h');
legend(legendStr,'Location','SE');

if addFileNameTitle==1
%-- Add a FileName title
set(gca, 'OuterPosition', [0 0 1 .95]);
ha = axes('Position',[0 0 1 1],'Xlim',[0 1],'Ylim',[0
1],'Box','off','Visible','off','Units','normalized', 'clipping' , 'off');
text(0.5, 1,inFile,'HorizontalAlignment','center','VerticalAlignment',
'top','interpreter','none','FontSize',12)
end

%-- NORMALISED CDF GRAPH ----------------------------------------------------
fig02=figure('Color',[1 1 1]);
set(gcf,'position',[100 100 800 600]) %-- Set the figure position and size
of the figure
movegui(gcf,'center') %-- Do this to make sure that the figure isn't cut off
(or including other windows) when exporting
hold on
for j=2:length(calc_CDFnorm(1,:))
plot(calc_CDFnorm(:,1),calc_CDFnorm(:,j),'LineWidth',plotLineThickness)
end
ylim([0 1.1]);
xlabel('Radial Distance (um)');
ylabel('Norm Cumulative Number of Features');
if sameAxes==1
    xlim([0 400]);
end
if addGraphTitle==1
    title(['Spatial Distribution of Features by Time']);
end
set(gca,'fontsize',axisFontSize, 'LineWidth',axisLineWidth)
%-- Create the legend string
numPointsArray=[1 160 320 480]; %-- provide time points
legendStr = num2str(floor(numPointsArray'*3/60), 't=%2d h');
legend(legendStr,'Location','SE');

if addFileNameTitle==1
%-- Add a FileName title
```

```
set(gca, 'OuterPosition', [0 0 1 .95]);
ha = axes('Position',[0 0 1 1],'Xlim',[0 1],'Ylim',[0
1],'Box','off','Visible','off','Units','normalized', 'clipping' , 'off');
text(0.5, 1,inFile,'HorizontalAlignment','center','VerticalAlignment',
'top','interpreter','none','FontSize',12)
end

%% -- Spot Speed by Time - ALL - LINE HISTOGRAM

fig06=figure('Color',[1 1 1]);
set(gcf,'position',[100 100 800 600]) %-- Set the figure position and size
of the figure
movegui(gcf,'center') %-- Do this to make sure that the figure isn't cut off
(or including other windows) when exporting
fig07=figure('Color',[1 1 1]);
set(gcf,'position',[100 100 800 600]) %-- Set the figure position and size
of the figure
movegui(gcf,'center') %-- Do this to make sure that the figure isn't cut off
(or including other windows) when exporting

binNum=100; %-- How smooth should the distribution be?
numPointsArray=[1 160 320 480]; %-- provide time points

for j=1:length(numPointsArray)-1;
[freq,bins]=hist(calc_SpotData(calc_SpotData(:,4)<numPointsArray(j+1) &
calc_SpotData(:,4)>=numPointsArray(j),2),binNum);
figure(fig06);
plot(bins,freq,'LineWidth',plotLineThicknessHisto);
hold on
freqNorm=(freq-min(freq))/(max(freq)-min(freq));

figure(fig07);
plot(bins,freqNorm,'LineWidth',plotLineThicknessHisto);
hold on

end

figure(fig06);
xlabel('Spot Speed (um/h)');
if sameAxes==1
    xlim([0 150]);
end
ylabel('Frequency');
if addGraphTitle==1
    title('Distribution of Spot Speed by Timepoint');
end
set(gca,'fontsize',axisFontSize, 'LineWidth',axisLineWidth);
%-- Create the legend string
legendStr = num2str(floor(numPointsArray'*3/60), 't=%2d h');
legend(legendStr,'Location','SE');

if addFileNameTitle==1
%-- Add a FileName title
set(gca, 'OuterPosition', [0 0 1 .95]);
ha = axes('Position',[0 0 1 1],'Xlim',[0 1],'Ylim',[0
1],'Box','off','Visible','off','Units','normalized', 'clipping' , 'off');
text(0.5, 1,inFile,'HorizontalAlignment','center','VerticalAlignment',
'top','interpreter','none','FontSize',12)
end

figure(fig07);
ylim([0 1.1]);
xlabel('Spot Speed (um/h)');
if sameAxes==1
    xlim([0 150]);
end
ylabel('Normalised Frequency');
```

```
if addGraphTitle==1
    title('Normalised Distribution of Spot Speed by Timepoint');
end
set(gca,'fontsize',axisFontSize, 'LineWidth',axisLineWidth);
%-- Create the legend string
legendStr = num2str(floor(numPointsArray'*3/60), 't=%2d h');
legend(legendStr,'Location','SE');

if addFileNameTitle==1
%-- Add a FileName title
set(gca, 'OuterPosition', [0 0 1 .95]);
ha = axes('Position',[0 0 1 1],'Xlim',[0 1],'Ylim',[0
1],'Box','off','Visible','off','Units','normalized', 'clipping' , 'off');
text(0.5, 1,inFile,'HorizontalAlignment','center','VerticalAlignment',
'top','interpreter','none','FontSize',12)
end

%% -- Spot Speed by Space - ALL - LINE HISTOGRAM

fig08=figure('Color',[1 1 1]);
set(gcf,'position',[100 100 800 600]) %-- Set the figure position and size
of the figure
movegui(gcf,'center') %-- Do this to make sure that the figure isn't cut off
(or including other windows) when exporting
fig09=figure('Color',[1 1 1]);
set(gcf,'position',[100 100 800 600]) %-- Set the figure position and size
of the figure
movegui(gcf,'center') %-- Do this to make sure that the figure isn't cut off
(or including other windows) when exporting

binNum=100; %-- How smooth should the distribution be?
numPointsArray=[0 100 200 300 400]; %-- provide spatial bins

%-- this is for big spheroids.
if bigSpheroids==1
    %-- Break down into 3 in and 3 out
    numPointsArray=round([0:eventHorizon/3:eventHorizon*2],-1);
else
    %-- Just use in / out
    numPointsArray=round([0:eventHorizon:eventHorizon*2],-1);
end

for j=1:length(numPointsArray)-1;
[freq,bins]=hist(calc_SpotData(calc_SpotData(:,1)<numPointsArray(j+1) &
calc_SpotData(:,1)>=numPointsArray(j),2),binNum);

    if sum(freq)>minSpots %-- only plot if there are enough values for a
reasonable graph

        figure(fig08);
        plot(bins,freq,'LineWidth',plotLineThicknessHisto);
        hold on

        freqNorm=(freq-min(freq))/(max(freq)-min(freq));

        figure(fig09);
        plot(bins,freqNorm,'LineWidth',plotLineThicknessHisto);
        hold on

    end

end
figure(fig08);
xlabel('Spot Speed (um/h)');
if sameAxes==1
    xlim([0 150]);
end
```

```
ylabel('Frequency');
if addGraphTitle==1
    title('Distribution of Spot Speed by Radial Distance')
end
set(gca,'fontsize',axisFontSize, 'LineWidth',axisLineWidth);
legendCell = cellstr([num2str(numPointsArray', 'd=%-d-')
num2str(circshift(numPointsArray,[0 -1])', ' %-d um')]);
legend(legendCell,'Location','NE');

if addFileNameTitle==1
%-- Add a FileName title
set(gca, 'OuterPosition', [0 0 1 .95]);
ha = axes('Position',[0 0 1 1],'Xlim',[0 1],'Ylim',[0
1],'Box','off','Visible','off','Units','normalized', 'clipping' , 'off');
text(0.5, 1,inFile,'HorizontalAlignment','center','VerticalAlignment',
'top','interpreter','none','FontSize',12)
end

figure(fig09);
ylim([0 1.1]);
xlabel('Spot Speed (um/h)');
if sameAxes==1
    xlim([0 150]);
end
ylabel('Normalised Frequency');
if addGraphTitle==1
    title('Normalised Distribution of Spot Speed by Radial Distance')
end
set(gca,'fontsize',axisFontSize, 'LineWidth',axisLineWidth);

legend(legendCell,'Location','NE');

if addFileNameTitle==1
%-- Add a FileName title
set(gca, 'OuterPosition', [0 0 1 .95]);
ha = axes('Position',[0 0 1 1],'Xlim',[0 1],'Ylim',[0
1],'Box','off','Visible','off','Units','normalized', 'clipping' , 'off');
text(0.5, 1,inFile,'HorizontalAlignment','center','VerticalAlignment',
'top','interpreter','none','FontSize',12)
end

%% -- Spot Straightness by Time - ALL - LINE HISTOGRAM

fig10=figure('Color',[1 1 1]);
set(gcf,'position',[100 100 800 600]) %-- Set the figure position and size
of the figure
movegui(gcf,'center') %-- Do this to make sure that the figure isn't cut off
(or including other windows) when exporting
fig11=figure('Color',[1 1 1]);
set(gcf,'position',[100 100 800 600]) %-- Set the figure position and size
of the figure
movegui(gcf,'center') %-- Do this to make sure that the figure isn't cut off
(or including other windows) when exporting


binNum=200; %-- How smooth should the distribution be?
numPointsArray=[1 160 320 480]; %-- provide time points

for j=1:length(numPointsArray)-1;
[freq,bins]=hist(calc_SpotData(calc_SpotData(:,4)<numPointsArray(j+1) &
calc_SpotData(:,3)~=0 & calc_SpotData(:,4)>=numPointsArray(j),3),binNum);
figure(fig10);
plot(bins,freq,'LineWidth',plotLineThicknessHisto);
hold on
freqNorm=(freq-min(freq))/(max(freq)-min(freq));

figure(fig11);
```

```
plot(bins,freqNorm,'LineWidth',plotLineThicknessHisto);
hold on

end

figure(fig10);
xlabel('Straightness');
if sameAxes==1
    xlim([0 1.1]);
end
ylabel('Frequency');
if addGraphTitle==1
    title('Distribution of Spot Straightness by Timepoint');
end
set(gca,'fontsize',axisFontSize, 'LineWidth',axisLineWidth);
%-- Create the legend string
legendStr = num2str(floor(numPointsArray'*3/60), 't=%2d h');
legend(legendStr,'Location','NW');

if addFileNameTitle==1
%-- Add a FileName title
set(gca, 'OuterPosition', [0 0 1 .95]);
ha = axes('Position',[0 0 1 1],'Xlim',[0 1],'Ylim',[0
1],'Box','off','Visible','off','Units','normalized', 'clipping' , 'off');
text(0.5, 1,inFile,'HorizontalAlignment','center','VerticalAlignment',
'top','interpreter','none','FontSize',12)
end

figure(fig11);
ylim([0 1.1]);
xlabel('Straightness');
if sameAxes==1
    xlim([0 1.1]);
end
ylabel('Normalised Frequency');
if addGraphTitle==1
    title('Normalised Distrib^N of Spot Straightness by Timepoint');
end
set(gca,'fontsize',axisFontSize, 'LineWidth',axisLineWidth);
%-- Create the legend string
legendStr = num2str(floor(numPointsArray'*3/60), 't=%2d h');
legend(legendStr,'Location','NW');

if addFileNameTitle==1
%-- Add a FileName title
set(gca, 'OuterPosition', [0 0 1 .95]);
ha = axes('Position',[0 0 1 1],'Xlim',[0 1],'Ylim',[0
1],'Box','off','Visible','off','Units','normalized', 'clipping' , 'off');
text(0.5, 1,inFile,'HorizontalAlignment','center','VerticalAlignment',
'top','interpreter','none','FontSize',12)
end

%% -- Spot Straightness by Space - ALL - LINE HISTOGRAM

fig12=figure('Color',[1 1 1]);
set(gcf,'position',[100 100 800 600]) %-- Set the figure position and size
of the figure
movegui(gcf,'center') %-- Do this to make sure that the figure isn't cut off
(or including other windows) when exporting
fig13=figure('Color',[1 1 1]);
set(gcf,'position',[100 100 800 600]) %-- Set the figure position and size
of the figure
movegui(gcf,'center') %-- Do this to make sure that the figure isn't cut off
(or including other windows) when exporting

binNum=200; %-- How smooth should the distribution be?
```

```
numPointsArray=[0 100 200 300 400]; %-- provide spatial bins

%-- this is for big spheroids.
if bigSpheroids==1
    %-- Break down into 3 in and 3 out
    numPointsArray=round([0:eventHorizon/3:eventHorizon*2],-1);
else
    %-- Just use in / out
    numPointsArray=round([0:eventHorizon:eventHorizon*2],-1);
end

for j=1:length(numPointsArray)-1;
[freq,bins]=hist(calc_SpotData(calc_SpotData(:,1)<numPointsArray(j+1) &
calc_SpotData(:,3) ~=0 & calc_SpotData(:,1)>=numPointsArray(j),3),binNum);

    if sum(freq)>minSpots %-- only plot if there are enough values for a
reasonable graph

        figure(fig12);
        plot(bins,freq,'LineWidth',plotLineThicknessHisto);
        hold on

        freqNorm=(freq-min(freq))/(max(freq)-min(freq));

        figure(fig13);
        plot(bins,freqNorm,'LineWidth',plotLineThicknessHisto);
        hold on
    end
end
figure(fig12);
xlabel('Straightness');
if sameAxes==1
    xlim([0 1.1]);
end
ylabel('Frequency');
if addGraphTitle==1
    title('Distrib^N of Spot Straightness by Radial Distance')
end
set(gca,'fontsize',axisFontSize, 'LineWidth',axisLineWidth);

legendCell = cellstr([num2str(numPointsArray', 'd=%-d-')
num2str(circshift(numPointsArray,[0 -1])', ' %-d um')]);
legend(legendCell,'Location','NW');

if addFileNameTitle==1
%-- Add a FileName title
set(gca, 'OuterPosition', [0 0 1 .95]);
ha = axes('Position',[0 0 1 1],'Xlim',[0 1],'Ylim',[0
1],'Box','off','Visible','off','Units','normalized', 'clipping' , 'off');
text(0.5, 1,inFile,'HorizontalAlignment','center','VerticalAlignment',
'top','interpreter','none','FontSize',12)
end

figure(fig13);
ylim([0 1.1]);
xlabel('Straightness');
if sameAxes==1
    xlim([0 1.1]);
end
ylabel('Normalised Frequency');
if addGraphTitle==1
    title('Normalised Distribution of Spot Straightness by Radial Distance')
end
set(gca,'fontsize',axisFontSize, 'LineWidth',axisLineWidth);
legend(legendCell,'Location','NW');

if addFileNameTitle==1
```

```
%-- Add a FileName title
set(gca, 'OuterPosition', [0 0 1 .95]);
ha = axes('Position',[0 0 1 1],'Xlim',[0 1],'Ylim',[0
1],'Box','off','Visible','off','Units','normalized', 'clipping' , 'off');
text(0.5, 1,inFile,'HorizontalAlignment','center','VerticalAlignment',
'top','interpreter','none','FontSize',12)
end

pause(3); %-- Have no idea why this is required but without it the axes get
borked when running the whole script

%% -- Spot Speed - ALL - LINE HISTOGRAM

fig14=figure('Color',[1 1 1]);
set(gcf,'position',[100 100 800 600]) %-- Set the figure position and size
of the figure
movegui(gcf,'center') %-- Do this to make sure that the figure isn't cut off
(or including other windows) when exporting

binNum=100; %-- How smooth should the distribution be?

[freq,bins]=hist(calc_SpotData(:,2),binNum);
plot(bins,freq,'LineWidth',plotLineThickness); %-- because there's only one
use the thicker line

xlabel('Speed (um/h)');
if sameAxes==1
    xlim([0 150]);
end
ylabel('Frequency');
ylim([0 max(freq)*1.05]);
if addGraphTitle==1
    title('Distrib^N of Spot Speed')
end
set(gca,'fontsize',axisFontSize, 'LineWidth',axisLineWidth);

if addFileNameTitle==1
%-- Add a FileName title
set(gca, 'OuterPosition', [0 0 1 .95]);
ha = axes('Position',[0 0 1 1],'Xlim',[0 1],'Ylim',[0
1],'Box','off','Visible','off','Units','normalized', 'clipping' , 'off');
text(0.5, 1,inFile,'HorizontalAlignment','center','VerticalAlignment',
'top','interpreter','none','FontSize',12)
end


%% -- Spot Straightness - ALL - LINE HISTOGRAM

fig15=figure('Color',[1 1 1]);
set(gcf,'position',[100 100 800 600]) %-- Set the figure position and size
of the figure
movegui(gcf,'center') %-- Do this to make sure that the figure isn't cut off
(or including other windows) when exporting

binNum=100; %-- How smooth should the distribution be?

[freq,bins]=hist(calc_SpotData(calc_SpotData(:,3) ~=0,3),binNum);
plot(bins,freq,'LineWidth',plotLineThickness); %-- because there's only one
use the thicker line

xlabel('Straightness');
if sameAxes==1
    xlim([0 1.1]);
end
ylabel('Frequency');
ylim([0 max(freq)*1.05]);
if addGraphTitle==1
```

```
    title('Distrib^N of Spot Straightness')
end
set(gca,'fontsize',axisFontSize, 'LineWidth',axisLineWidth);

if addFileNameTitle==1
%-- Add a FileName title
set(gca, 'OuterPosition', [0 0 1 .95]);
ha = axes('Position',[0 0 1 1],'Xlim',[0 1],'Ylim',[0
1],'Box','off','Visible','off','Units','normalized', 'clipping' , 'off');
text(0.5, 1,inFile,'HorizontalAlignment','center','VerticalAlignment',
'top','interpreter','none','FontSize',12)
end

%% -- Spot Speed - ALL - BEEHIVE

xrand=0.1.*randn(size(calc_SpotData,1),1)+1;

%-- Plot the graph
fig16=figure('Color',[1 1 1]);
set(gcf,'position',[100 100 800 600]) %-- Set the figure position and size
of the figure
movegui(gcf,'center') %-- Do this to make sure that the figure isn't cut off
(or including other windows) when exporting

plot(xrand,calc_SpotData(:,2),'.','MarkerSize',plotMarkerSize);
xlim([0 2]);
set(gca,'fontsize',axisFontSize, 'LineWidth',axisLineWidth,'XTick', [])

ylim([0 250]);
ylabel('Speed (um/h)');
if addGraphTitle==1
    title('Spot Speed (All Cells)','FontSize',12);
end
hold on
plot([0.4 1.6],[mean(calc_SpotData(:,2)) mean(calc_SpotData(:,2))],'r-
','LineWidth',1, 'HandleVisibility','off');

if addFileNameTitle==1
%-- Add a FileName title
set(gca, 'OuterPosition', [0 0 1 .95]);
ha = axes('Position',[0 0 1 1],'Xlim',[0 1],'Ylim',[0
1],'Box','off','Visible','off','Units','normalized', 'clipping' , 'off');
text(0.5, 1,inFile,'HorizontalAlignment','center','VerticalAlignment',
'top','interpreter','none','FontSize',12)
end


%% -- Spot Straightness - ALL - BEEHIVE

%-- Prepare the data for plotting (strip zeros)
zzz_yVals=calc_SpotData(calc_SpotData(:,3)~=0,3);
xrand=0.1.*randn(size(zzz_yVals,1),1)+1;

%-- Plot the graph
fig17=figure('Color',[1 1 1]);
set(gcf,'position',[100 100 800 600]) %-- Set the figure position and size
of the figure
movegui(gcf,'center') %-- Do this to make sure that the figure isn't cut off
(or including other windows) when exporting

plot(xrand,zzz_yVals,'.','MarkerSize',plotMarkerSize);
xlim([0 2]);
set(gca,'fontsize',axisFontSize, 'LineWidth',axisLineWidth,'XTick', [])

ylabel('Straightness');
if addGraphTitle==1
    title('Spot Straightness (All Cells)','FontSize',12);
```

```
end
hold on
meanStraight=mean(zzz_yVals);
plot([0.4 1.6],[mean(zzz_yVals) mean(zzz_yVals)],'r-','LineWidth',1,
'HandleVisibility','off');

if addFileNameTitle==1
%-- Add a FileName title
set(gca, 'OuterPosition', [0 0 1 .95]);
ha = axes('Position',[0 0 1 1],'Xlim',[0 1],'Ylim',[0
1],'Box','off','Visible','off','Units','normalized', 'clipping' , 'off');
text(0.5, 1,inFile,'HorizontalAlignment','center','VerticalAlignment',
'top','interpreter','none','FontSize',12)
end



%% -- NOW DO THE SAME AGAIN BUT WITH INVADING ONLY -------------------------
% -- Spot Speed by Time - INVADING - LINE HISTOGRAM

fig30=figure('Color',[1 1 1]);
set(gcf,'position',[100 100 800 600]) %-- Set the figure position and size
of the figure
movegui(gcf,'center') %-- Do this to make sure that the figure isn't cut off
(or including other windows) when exporting
fig31=figure('Color',[1 1 1]);
set(gcf,'position',[100 100 800 600]) %-- Set the figure position and size
of the figure
movegui(gcf,'center') %-- Do this to make sure that the figure isn't cut off
(or including other windows) when exporting


binNum=100; %-- How smooth should the distribution be?
numPointsArray=[1 160 320 480]; %-- provide time points

for j=1:length(numPointsArray)-1;
[freq,bins]=hist(calc_SpotData_outside(calc_SpotData_outside(:,4)<numPointsA
rray(j+1) & calc_SpotData_outside(:,4)>=numPointsArray(j),2),binNum);
figure(fig30);
plot(bins,freq,'LineWidth',plotLineThicknessHisto);
hold on
freqNorm=(freq-min(freq))/(max(freq)-min(freq));

figure(fig31);
plot(bins,freqNorm,'LineWidth',plotLineThicknessHisto);
hold on

end

figure(fig30);
xlabel('Spot Speed (um/h)');
if sameAxes==1
    xlim([0 150]);
end
ylabel('Frequency');
if addGraphTitle==1
    title('Distribution of Invading Spot Speed by Timepoint');
end
set(gca,'fontsize',axisFontSize, 'LineWidth',axisLineWidth);
%-- Create the legend string
legendStr = num2str(floor(numPointsArray'*3/60), 't=%2d h');
legend(legendStr,'Location','SE');

if addFileNameTitle==1
%-- Add a FileName title
set(gca, 'OuterPosition', [0 0 1 .95]);
```

```
ha = axes('Position',[0 0 1 1],'Xlim',[0 1],'Ylim',[0
1],'Box','off','Visible','off','Units','normalized', 'clipping' , 'off');
text(0.5, 1,inFile,'HorizontalAlignment','center','VerticalAlignment',
'top','interpreter','none','FontSize',12)
end

figure(fig31);
ylim([0 1.1]);
xlabel('Spot Speed (um/h)');
if sameAxes==1
    xlim([0 150]);
end
ylabel('Normalised Frequency');
if addGraphTitle==1
    title('Normalised Distribution of Invading Spot Speed by Timepoint');
end
set(gca,'fontsize',axisFontSize, 'LineWidth',axisLineWidth);
%-- Create the legend string
legendStr = num2str(floor(numPointsArray'*3/60), 't=%2d h');
legend(legendStr,'Location','SE');

if addFileNameTitle==1
%-- Add a FileName title
set(gca, 'OuterPosition', [0 0 1 .95]);
ha = axes('Position',[0 0 1 1],'Xlim',[0 1],'Ylim',[0
1],'Box','off','Visible','off','Units','normalized', 'clipping' , 'off');
text(0.5, 1,inFile,'HorizontalAlignment','center','VerticalAlignment',
'top','interpreter','none','FontSize',12)
end

%% -- Spot Speed by Space - INVADING - LINE HISTOGRAM

fig32=figure('Color',[1 1 1]);
set(gcf,'position',[100 100 800 600]) %-- Set the figure position and size
of the figure
movegui(gcf,'center') %-- Do this to make sure that the figure isn't cut off
(or including other windows) when exporting
fig33=figure('Color',[1 1 1]);
set(gcf,'position',[100 100 800 600]) %-- Set the figure position and size
of the figure
movegui(gcf,'center') %-- Do this to make sure that the figure isn't cut off
(or including other windows) when exporting

binNum=100; %-- How smooth should the distribution be?
numPointsArray=[0 100 200 300 400]; %-- provide spatial bins

for j=1:length(numPointsArray)-1;
[freq,bins]=hist(calc_SpotData_outside(calc_SpotData_outside(:,1)<numPointsA
rray(j+1) & calc_SpotData_outside(:,1)>=numPointsArray(j),2),binNum);

        figure(fig32);
        plot(bins,freq,'LineWidth',plotLineThicknessHisto);
        hold on

        freqNorm=(freq-min(freq))/(max(freq)-min(freq));

        figure(fig33);
        plot(bins,freqNorm,'LineWidth',plotLineThicknessHisto);
        hold on

end
figure(fig32);
xlabel('Spot Speed (um/h)');
if sameAxes==1
    xlim([0 150]);
end
ylabel('Frequency');
```

```
if addGraphTitle==1
    title('Distribution of Invading Spot Speed by Radial Distance')
end
set(gca,'fontsize',axisFontSize, 'LineWidth',axisLineWidth);
%-- Create the legend string
legendCell = cellstr([num2str(numPointsArray', 'd=%-d-')
num2str(circshift(numPointsArray,[0 -1])', ' %-d um')]);
legend(legendCell,'Location','NE');

if addFileNameTitle==1
%-- Add a FileName title
set(gca, 'OuterPosition', [0 0 1 .95]);
ha = axes('Position',[0 0 1 1],'Xlim',[0 1],'Ylim',[0
1],'Box','off','Visible','off','Units','normalized', 'clipping' , 'off');
text(0.5, 1,inFile,'HorizontalAlignment','center','VerticalAlignment',
'top','interpreter','none','FontSize',12)
end

figure(fig33);
ylim([0 1.1]);
xlabel('Spot Speed (um/h)');
if sameAxes==1
    xlim([0 150]);
end
ylabel('Normalised Frequency');
if addGraphTitle==1
    title('Normalised Distribution of Invading Spot Speed by Radial
Distance')
end
set(gca,'fontsize',axisFontSize, 'LineWidth',axisLineWidth);

legend(legendCell,'Location','NE');

if addFileNameTitle==1
%-- Add a FileName title
set(gca, 'OuterPosition', [0 0 1 .95]);
ha = axes('Position',[0 0 1 1],'Xlim',[0 1],'Ylim',[0
1],'Box','off','Visible','off','Units','normalized', 'clipping' , 'off');
text(0.5, 1,inFile,'HorizontalAlignment','center','VerticalAlignment',
'top','interpreter','none','FontSize',12)
end

%% -- Spot Straightness by Time - INVADING - LINE HISTOGRAM

fig34=figure('Color',[1 1 1]);
set(gcf,'position',[100 100 800 600]) %-- Set the figure position and size
of the figure
movegui(gcf,'center') %-- Do this to make sure that the figure isn't cut off
(or including other windows) when exporting
fig35=figure('Color',[1 1 1]);
set(gcf,'position',[100 100 800 600]) %-- Set the figure position and size
of the figure
movegui(gcf,'center') %-- Do this to make sure that the figure isn't cut off
(or including other windows) when exporting


binNum=200; %-- How smooth should the distribution be?
numPointsArray=[1 160 320 480]; %-- provide time points

for j=1:length(numPointsArray)-1;
[freq,bins]=hist(calc_SpotData_outside(calc_SpotData_outside(:,4)<numPointsA
rray(j+1) & calc_SpotData_outside(:,3)~=0 &
calc_SpotData_outside(:,4)>=numPointsArray(j),3),binNum);
figure(fig34);
plot(bins,freq,'LineWidth',plotLineThicknessHisto);
hold on
freqNorm=(freq-min(freq))/(max(freq)-min(freq));
```

```
figure(fig35);
plot(bins,freqNorm,'LineWidth',plotLineThicknessHisto);
hold on

end

figure(fig34);
xlabel('Straightness');
if sameAxes==1
    xlim([0 1.1]);
end
ylabel('Frequency');
if addGraphTitle==1
    title('Distrib^N of Invading Spot Straightness by Timepoint');
end
set(gca,'fontsize',axisFontSize, 'LineWidth',axisLineWidth);
%-- Create the legend string
legendStr = num2str(floor(numPointsArray'*3/60), 't=%2d h');
legend(legendStr,'Location','NW');

if addFileNameTitle==1
%-- Add a FileName title
set(gca, 'OuterPosition', [0 0 1 .95]);
ha = axes('Position',[0 0 1 1],'Xlim',[0 1],'Ylim',[0
1],'Box','off','Visible','off','Units','normalized', 'clipping' , 'off');
text(0.5, 1,inFile,'HorizontalAlignment','center','VerticalAlignment',
'top','interpreter','none','FontSize',12)
end

figure(fig35);
ylim([0 1.1]);
xlabel('Straightness');
if sameAxes==1
    xlim([0 1.1]);
end
ylabel('Normalised Frequency');
if addGraphTitle==1
    title('Normalised Distrib^N of Invading Spot Straightness by
Timepoint');
end
set(gca,'fontsize',axisFontSize, 'LineWidth',axisLineWidth);
%-- Create the legend string
legendStr = num2str(floor(numPointsArray'*3/60), 't=%2d h');
legend(legendStr,'Location','NW');

if addFileNameTitle==1
%-- Add a FileName title
set(gca, 'OuterPosition', [0 0 1 .95]);
ha = axes('Position',[0 0 1 1],'Xlim',[0 1],'Ylim',[0
1],'Box','off','Visible','off','Units','normalized', 'clipping' , 'off');
text(0.5, 1,inFile,'HorizontalAlignment','center','VerticalAlignment',
'top','interpreter','none','FontSize',12)
end

%% -- Spot Straightness by Space - INVADING - LINE HISTOGRAM

fig36=figure('Color',[1 1 1]);
set(gcf,'position',[100 100 800 600]) %-- Set the figure position and size
of the figure
movegui(gcf,'center') %-- Do this to make sure that the figure isn't cut off
(or including other windows) when exporting
fig37=figure('Color',[1 1 1]);
set(gcf,'position',[100 100 800 600]) %-- Set the figure position and size
of the figure
movegui(gcf,'center') %-- Do this to make sure that the figure isn't cut off
(or including other windows) when exporting
```

```
binNum=30; %-- How smooth should the distribution be?

numPointsArray=[0 100 200 300 400]; %-- provide spatial bins

for j=1:length(numPointsArray)-1;
[freq,bins]=hist(calc_SpotData_outside(calc_SpotData_outside(:,1)<numPointsA
rray(j+1) & calc_SpotData_outside(:,3) ~=0 &
calc_SpotData_outside(:,1)>=numPointsArray(j),3),binNum);
figure(fig36);
plot(bins,freq,'LineWidth',plotLineThicknessHisto);
hold on

freqNorm=(freq-min(freq))/(max(freq)-min(freq));

figure(fig37);
plot(bins,freqNorm,'LineWidth',plotLineThicknessHisto);
hold on

end
figure(fig36);
xlabel('Straightness');
if sameAxes==1
    xlim([0 1.1]);
end
ylabel('Frequency');
if addGraphTitle==1
    title('Distrib^N of Invading Spot Straightness by Radial Distance')
end
set(gca,'fontsize',axisFontSize, 'LineWidth',axisLineWidth);
%-- Create the legend string
legendCell={'d=0-100 um';'d=100-200 um';'d=200-300 um';'d=300-400
um';'d=400-500 um'};
legend(legendCell,'Location','NW');

if addFileNameTitle==1
%-- Add a FileName title
set(gca, 'OuterPosition', [0 0 1 .95]);
ha = axes('Position',[0 0 1 1],'Xlim',[0 1],'Ylim',[0
1],'Box','off','Visible','off','Units','normalized', 'clipping' , 'off');
text(0.5, 1,inFile,'HorizontalAlignment','center','VerticalAlignment',
'top','interpreter','none','FontSize',12)
end

figure(fig37);
ylim([0 1.1]);
xlabel('Straightness');
if sameAxes==1
    xlim([0 1.1]);
end
ylabel('Normalised Frequency');
if addGraphTitle==1
    title('Normalised Distrib^N of Invading Spot Straightness by Radial
Distance')
end
set(gca,'fontsize',axisFontSize, 'LineWidth',axisLineWidth);
legend(legendCell,'Location','NW');

if addFileNameTitle==1
%-- Add a FileName title
set(gca, 'OuterPosition', [0 0 1 .95]);
ha = axes('Position',[0 0 1 1],'Xlim',[0 1],'Ylim',[0
1],'Box','off','Visible','off','Units','normalized', 'clipping' , 'off');
text(0.5, 1,inFile,'HorizontalAlignment','center','VerticalAlignment',
'top','interpreter','none','FontSize',12)
end
```

```
pause(3); %-- Have no idea why this is required but without it the axes get
borked

%% -- Spot Speed - INVADING - LINE HISTOGRAM

fig38=figure('Color',[1 1 1]);
set(gcf,'position',[100 100 800 600]) %-- Set the figure position and size
of the figure
movegui(gcf,'center') %-- Do this to make sure that the figure isn't cut off
(or including other windows) when exporting

binNum=100; %-- How smooth should the distribution be?

[freq,bins]=hist(calc_SpotData_outside(:,2),binNum);
plot(bins,freq,'LineWidth',plotLineThickness); %-- because there's only one
use the thicker line

xlabel('Speed (um/h)');
if sameAxes==1
    xlim([0 150]);
end
ylabel('Frequency');
ylim([0 max(freq)*1.05]);
if addGraphTitle==1
    title('Distrib^N of Invading Spot Speed')
end
set(gca,'fontsize',axisFontSize, 'LineWidth',axisLineWidth);

if addFileNameTitle==1
%-- Add a FileName title
set(gca, 'OuterPosition', [0 0 1 .95]);
ha = axes('Position',[0 0 1 1],'Xlim',[0 1],'Ylim',[0
1],'Box','off','Visible','off','Units','normalized', 'clipping' , 'off');
text(0.5, 1,inFile,'HorizontalAlignment','center','VerticalAlignment',
'top','interpreter','none','FontSize',12)
end


%% -- Spot Straightness - INVADING - LINE HISTOGRAM

fig39=figure('Color',[1 1 1]);
set(gcf,'position',[100 100 800 600]) %-- Set the figure position and size
of the figure
movegui(gcf,'center') %-- Do this to make sure that the figure isn't cut off
(or including other windows) when exporting

binNum=100; %-- How smooth should the distribution be?

[freq,bins]=hist(calc_SpotData_outside(calc_SpotData_outside(:,3)
~=0,3),binNum);
plot(bins,freq,'LineWidth',plotLineThickness); %-- because there's only one
use the thicker line

xlabel('Straightness');
if sameAxes==1
    xlim([0 1.1]);
end
ylabel('Frequency');
ylim([0 max(freq)*1.05]);
if addGraphTitle==1
    title('Distrib^N of Invading Spot Straightness')
end
set(gca,'fontsize',axisFontSize, 'LineWidth',axisLineWidth);

if addFileNameTitle==1
%-- Add a FileName title
set(gca, 'OuterPosition', [0 0 1 .95]);
```

```
ha = axes('Position',[0 0 1 1],'Xlim',[0 1],'Ylim',[0
1],'Box','off','Visible','off','Units','normalized', 'clipping' , 'off');
text(0.5, 1,inFile,'HorizontalAlignment','center','VerticalAlignment',
'top','interpreter','none','FontSize',12)
end

%% -- Spot Speed - INVADING - BEEHIVE

xrand=0.1.*randn(size(calc_SpotData_outside,1),1)+1;

%-- Plot the graph
fig40=figure('Color',[1 1 1]);
set(gcf,'position',[100 100 800 600]) %-- Set the figure position and size
of the figure
movegui(gcf,'center') %-- Do this to make sure that the figure isn't cut off
(or including other windows) when exporting

plot(xrand,calc_SpotData_outside(:,2),'.','MarkerSize',plotMarkerSize);
xlim([0 2]);
set(gca,'fontsize',axisFontSize, 'LineWidth',axisLineWidth,'XTick', [])

ylabel('Speed (um/h)');
if addGraphTitle==1
    title('Spot Speed (Invading)','FontSize',axisFontSize);
end
hold on
plot([0.4 1.6],[mean(calc_SpotData_outside(:,2))
mean(calc_SpotData_outside(:,2))],'r-','LineWidth',1,
'HandleVisibility','off');

if addFileNameTitle==1
%-- Add a FileName title
set(gca, 'OuterPosition', [0 0 1 .95]);
ha = axes('Position',[0 0 1 1],'Xlim',[0 1],'Ylim',[0
1],'Box','off','Visible','off','Units','normalized', 'clipping' , 'off');
text(0.5, 1,inFile,'HorizontalAlignment','center','VerticalAlignment',
'top','interpreter','none','FontSize',12)
end


%% -- Spot Straightness - INVADING - BEEHIVE

%-- Prepare the data for plotting (strip zeros)
zzz_yVals=calc_SpotData_outside(calc_SpotData_outside(:,3)~=0,3);
xrand=0.1.*randn(size(zzz_yVals,1),1)+1;

%-- Plot the graph
fig41=figure('Color',[1 1 1]);
set(gcf,'position',[100 100 800 600]) %-- Set the figure position and size
of the figure
movegui(gcf,'center') %-- Do this to make sure that the figure isn't cut off
(or including other windows) when exporting

plot(xrand,zzz_yVals,'.','MarkerSize',plotMarkerSize);
xlim([0 2]);
set(gca,'fontsize',axisFontSize, 'LineWidth',axisLineWidth,'XTick', [])

ylabel('Straightness');
if addGraphTitle==1
    title('Spot Straightness (Invading)','FontSize',axisFontSize);
end
hold on
plot([0.4 1.6],[mean(zzz_yVals) mean(zzz_yVals)],'r-','LineWidth',1,
'HandleVisibility','off');

if addFileNameTitle==1
%-- Add a FileName title
```

```
set(gca, 'OuterPosition', [0 0 1 .95]);
ha = axes('Position',[0 0 1 1],'Xlim',[0 1],'Ylim',[0
1],'Box','off','Visible','off','Units','normalized', 'clipping' , 'off');
text(0.5, 1,inFile,'HorizontalAlignment','center','VerticalAlignment',
'top','interpreter','none','FontSize',12)
end



%% -- Save the figures and tidy up

if saveFIG==1
%-- Save the figures as fig files
savefig(fig01,strrep(inFile,'_MATLAB_data.mat','_ALL_CDF.fig'));
savefig(fig02,strrep(inFile,'_MATLAB_data.mat','_ALL_CDF_norm.fig'));
savefig(fig06,strrep(inFile,'_MATLAB_data.mat','_ALL_SPEED_byTime.fig'));
savefig(fig07,strrep(inFile,'_MATLAB_data.mat','_ALL_SPEED_byTime_Norm.fig')
);
savefig(fig08,strrep(inFile,'_MATLAB_data.mat','_ALL_SPEED_bySpace.fig'));
savefig(fig09,strrep(inFile,'_MATLAB_data.mat','_ALL_SPEED_bySpace_Norm.fig'
));
savefig(fig10,strrep(inFile,'_MATLAB_data.mat','_ALL_STRAIGHT_byTime.fig'));
savefig(fig11,strrep(inFile,'_MATLAB_data.mat','_ALL_STRAIGHT_byTime_Norm.fi
g'));
savefig(fig12,strrep(inFile,'_MATLAB_data.mat','_ALL_STRAIGHT_bySpace.fig'))
;
savefig(fig13,strrep(inFile,'_MATLAB_data.mat','_ALL_STRAIGHT_bySpace_Norm.f
ig'));
savefig(fig14,strrep(inFile,'_MATLAB_data.mat','_ALL_SPEED.fig'));
savefig(fig15,strrep(inFile,'_MATLAB_data.mat','_ALL_STRAIGHT.fig'));
savefig(fig16,strrep(inFile,'_MATLAB_data.mat','_ALL_SPEED_BH.fig'));
savefig(fig17,strrep(inFile,'_MATLAB_data.mat','_ALL_STRAIGHT_BH.fig'));
%-- Invading
savefig(fig30,strrep(inFile,'_MATLAB_data.mat','_INV_SPEED_byTime.fig'));
savefig(fig31,strrep(inFile,'_MATLAB_data.mat','_INV_SPEED_byTime_Norm.fig')
);
savefig(fig32,strrep(inFile,'_MATLAB_data.mat','_INV_SPEED_bySpace.fig'));
savefig(fig33,strrep(inFile,'_MATLAB_data.mat','_INV_SPEED_bySpace_Norm.fig'
));
savefig(fig34,strrep(inFile,'_MATLAB_data.mat','_INV_STRAIGHT_byTime.fig'));
savefig(fig35,strrep(inFile,'_MATLAB_data.mat','_INV_STRAIGHT_byTime_Norm.fi
g'));
savefig(fig36,strrep(inFile,'_MATLAB_data.mat','_INV_STRAIGHT_bySpace.fig'))
;
savefig(fig37,strrep(inFile,'_MATLAB_data.mat','_INV_STRAIGHT_bySpace_Norm.f
ig'));
savefig(fig38,strrep(inFile,'_MATLAB_data.mat','_INV_SPEED.fig'));
savefig(fig39,strrep(inFile,'_MATLAB_data.mat','_INV_STRAIGHT.fig'));
savefig(fig40,strrep(inFile,'_MATLAB_data.mat','_INV_SPEED_BH.fig'));
savefig(fig41,strrep(inFile,'_MATLAB_data.mat','_INV_STRAIGHT_BH.fig'));
end

if savePNG==1
%-- Save the figures as PNG files
saveas(fig01,strrep(inFile,'_MATLAB_data.mat','_ALL_CDF.png'));
saveas(fig02,strrep(inFile,'_MATLAB_data.mat','_ALL_CDF_norm.png'));
saveas(fig06,strrep(inFile,'_MATLAB_data.mat','_ALL_SPEED_byTime.png'));
saveas(fig07,strrep(inFile,'_MATLAB_data.mat','_ALL_SPEED_byTime_Norm.png'))
;
saveas(fig08,strrep(inFile,'_MATLAB_data.mat','_ALL_SPEED_bySpace.png'));
saveas(fig09,strrep(inFile,'_MATLAB_data.mat','_ALL_SPEED_bySpace_Norm.png')
);
saveas(fig10,strrep(inFile,'_MATLAB_data.mat','_ALL_STRAIGHT_byTime.png'));
saveas(fig11,strrep(inFile,'_MATLAB_data.mat','_ALL_STRAIGHT_byTime_Norm.png
'));
saveas(fig12,strrep(inFile,'_MATLAB_data.mat','_ALL_STRAIGHT_bySpace.png'));
```

```
saveas(fig13,strrep(inFile,'_MATLAB_data.mat','_ALL_STRAIGHT_bySpace_Norm.pn
g'));
saveas(fig14,strrep(inFile,'_MATLAB_data.mat','_ALL_SPEED.png'));
saveas(fig15,strrep(inFile,'_MATLAB_data.mat','_ALL_STRAIGHT.png'));
saveas(fig16,strrep(inFile,'_MATLAB_data.mat','_ALL_SPEED_BH.png'));
saveas(fig17,strrep(inFile,'_MATLAB_data.mat','_ALL_STRAIGHT_BH.png'));
%-- Invading
saveas(fig30,strrep(inFile,'_MATLAB_data.mat','_INV_SPEED_byTime.png'));
saveas(fig31,strrep(inFile,'_MATLAB_data.mat','_INV_SPEED_byTime_Norm.png'))
;
saveas(fig32,strrep(inFile,'_MATLAB_data.mat','_INV_SPEED_bySpace.png'));
saveas(fig33,strrep(inFile,'_MATLAB_data.mat','_INV_SPEED_bySpace_Norm.png')
);
saveas(fig34,strrep(inFile,'_MATLAB_data.mat','_INV_STRAIGHT_byTime.png'));
saveas(fig35,strrep(inFile,'_MATLAB_data.mat','_INV_STRAIGHT_byTime_Norm.png
'));
saveas(fig36,strrep(inFile,'_MATLAB_data.mat','_INV_STRAIGHT_bySpace.png'));
saveas(fig37,strrep(inFile,'_MATLAB_data.mat','_INV_STRAIGHT_bySpace_Norm.pn
g'));
saveas(fig38,strrep(inFile,'_MATLAB_data.mat','_INV_SPEED.png'));
saveas(fig39,strrep(inFile,'_MATLAB_data.mat','_INV_STRAIGHT.png'));
saveas(fig40,strrep(inFile,'_MATLAB_data.mat','_INV_SPEED_BH.png'));
saveas(fig41,strrep(inFile,'_MATLAB_data.mat','_INV_STRAIGHT_BH.png'));
end

clearvars i j xrand zzz_yVals;
```

Thesis output

i. Publications

Richards, R., Mason, D., & Sée, V. Imaging glioblastoma cell invasion using multicellular tumour spheroids and light sheet fluorescence microscopy. *In preparation.*

Richards, R., Jenkinson, M. D., Haylock, B. J. & Sée, V. Cell cycle progression in glioblastoma cells is unaffected by pathophysiological levels of hypoxia. *PeerJ*, 2016, 4:e1755.

Sandt, C., Nadaradjane, C., Richards, R., Dumas, P. & Sée. V. Use of infrared microspectroscopy to elucidate a specific chemical signature associated with hypoxia levels found in glioblastoma. *Analyst*, 2016, 141 (3): 870-83.

ii. Talks

Imaging cellular invasion using multicellular tumour spheroids and light sheet microscopy. *Light Sheet Fluorescence Microscopy International Conference,* 31 August – 3 September 2016, Sheffield, UK.

Multicellular tumour spheroid models & the tumour microenvironment. *Liverpool Centre for Cell Imaging Annual Workshop,* 21-22 September 2015, Liverpool, UK. Best short talk prize awarded.

iii. Poster presentations

North West Cancer Research Centre Scientific Symposium, Liverpool, March 2016.

Liverpool Technology Directorate Showcase Event, April 2014.

Genes and Cancer 30th Anniversary Meeting, Cambridge, March 2014.

British Neuro-oncology Society Conference: Contemporary Approaches to Paediatric and Adult Brain Tumours, Liverpool, 2014.

Liverpool Cancer Research UK Centre Annual Meeting, Liverpool, 2014.